

Development of a Multi-Laser, Multi-Channel XUV
Spectrometer Facility Based on the Dual Laser Plasma
Technique.

A Thesis for the Degree of
Doctor of Philosophy.

By

Laurence Kiernan, B.Sc.

School of Physical Sciences
Dublin City University

Research Supervisor

Prof. E. T. Kennedy, B.Sc., Ph.D., C.Phys., F.Inst.P.

March 1994

I hereby certify that this material, which I now submit for assessment on the programme of study leading to the award of Doctor of Philosophy, is entirely my own work and has not been taken from the work of others save and to the extent that such work has been cited and acknowledged within the text of my work.

Signed : Laura Viesman

Date : 28/03/94

Candidate

To Fiona and my parents

“The theory with atoms having more than one electron, it is such a
great misery”

Wolfgang Pauli 1923

Development of a Multi-Laser, Multi-Channel XUV Spectrometer Facility Based on the Dual Laser Plasma Technique.

Abstract

Growing interest in the fields of core excited atomic, molecular and solid species has resulted in a demand for a compact, low cost laboratory source in the XUV (Extreme Ultra Violet) region of the spectrum. In contrast to the optical spectra of the valence electrons, which can mainly be described by the one-electron picture of the central field approximation, inner shell excitations are characterised by strong many electron effects causing the breakdown of the simple one-electron picture. Photoabsorption experiments provide valuable information on these many-electron correlation effects in atoms, excited atoms and ions. The measurement of photoionization cross sections of free ions pose considerable experimental difficulties, as a suitable absorbing column, of adequate density, must be produced and back lit by a bright, synchronised XUV continuum emitting source. Through the work reported in this thesis, a multi-laser, multi-channel spectrometer facility, for the measurement of photoionization cross sections of free atoms, excited atoms and ions, in the XUV has been developed.

The facility is based on the DLP (Dual Laser Plasma) technique, whereby the absorbing column is produced by the ablation of spectroscopically pure targets, *in vacuo*, by either a flashlamp pumped dye laser (≈ 1 J in 2.5 μ s) or by a Q-switched ruby laser (≈ 1.5 J in 30 ns). The synchronised XUV continuum source is generated by tightly focusing the output of a Nd:YAG laser (≈ 1 J in 15 ns) on a metal of high atomic number. Selection and isolation of the absorbing species of interest is achieved by an appropriate combination of laser type, target irradiation, spatial probing position of absorbing target and temporal separation of laser optical pulses. The continuum XUV radiation passes through the absorbing column and is collected by a toroidal mirror which efficiently couples the light into a 2.2 m grazing incidence spectrometer. The spectrometer is equipped with an MCP (Micro Channel Plate) self scanning diode array detector.

The performance, capabilities and reliability of the facility have been demonstrated through the undertaking of a varied programme of XUV photoemission and photoabsorption experiments. The XUV photoabsorption characteristics of aluminium thin films, helium, argon, and free metal atoms and ions in the transition regions of the Periodic Table have been recorded. Where possible comparisons have been drawn against a background of recent significant experiments in the field.

The ions of the alkaline earth elements, calcium and barium, represent some of the few atomic systems for which there exist absolute photoionization cross section measurements in the XUV energy region. Both isonuclear sequences have been examined using the DLP spectrometer facility. In order to illustrate the unique advantages offered by the present experimental system, considerable emphasis has been placed on the less well explored spectra of calcium and its ions in the energy region corresponding to excitation from the 3p subshell. New photoabsorption results are presented for singly and doubly ionized calcium and a tentative analysis of the strongest features of the spectra, based on existing calculations and our own multi-configurational Hartree-Fock calculations, is proposed.

Photoabsorption studies, also in the energy region corresponding to 3p electron excitation, have been initiated along the zinc isonuclear sequence as far as Zn^{3+} . For neutral zinc, Zn^+ and Zn^{2+} the 3d subshell remains closed and excitations of the type $3p \rightarrow ns$ have been found to predominate. The symmetric nature of the resonance profiles is evidence of the weak interaction of these discrete states with the underlying 3d continua. The relatively large width of the resonances can be interpreted as being mostly due to the non-radiative decay of the 3p core hole, through both super and normal Coster-Kromg decay processes. The spectral signature of the 'transition metal-like' Zn^{3+} $3p \rightarrow 3d$ resonance transition is dramatically different, the asymmetric nature of which indicates substantial interaction between the direct photoionization process of the 3d subshell and the discrete state. The main resonances in the spectra of Zn^+ , Zn^{2+} and Zn^{3+} have been parametrised and compared with calculations based on both single particle and collective models.

Operating at the limits of resolution and dynamic range of the present experimental system, we have recorded the first observation of a photon-induced triply excited state, $2s^22p$, of atomic lithium. Such highly correlated states are of considerable theoretical interest as they represent a very unusual situation where all three electrons reside in the same $n=2$ shell. This experiment represents the first step in the photoionization studies of this fundamental atomic system in which the motion of the three electrons in the field of the nucleus is so highly correlated. In addition we have measured, also for the first time, using photoelectric registration, the helium-like $Li^+ 2snp$ doubly excited series. In both cases Fano parameters for the main resonances have been extracted after removal of the folded instrument response function.

Table of Contents

Chapter 1 Introduction.

1.1. Development of Spectroscopy — A Historical Perspective	2
1.1.1. Photoionization in the VUV.	4
1.2. Stimulus for Spectroscopic Investigation in the Energy Region of Subvalence Electron Excitation.	6
1.3. The Role of Laser Produced Plasmas in Spectroscopy.	8
1.3.1. Introduction.	8
1.3.2. Review of General Properties of Plasmas.	9
1.3.3. Atomic Processes in Laser Produced Plasmas.	10
(i) Bound — Bound Transitions.	10
(ii) Free — Bound Transitions.	11
(iii) Free — Free Transitions.	12
1.3.4. Generation and Evolution of Laser Produced Plasmas.	13
1.4. Spectroscopic Investigation of the Structure of Atoms, Excited Atoms and Ions, in the XUV.	16
1.4.1. Photoemission Studies.	16
1.4.2. Photoabsorption Studies.	20
1.4.3. Evolution of the Dual Laser Plasma Technique.	26
1.5. References.	33

Chapter 2 Construction, Integration and Characterisation of the Multi-Channel, Multi-Laser XUV Spectrometer Facility.

2.1. Introduction.	39
2.2. Implementation of Experimental System.	40
2.2.1. General Features of Experimental Setup.	40
2.2.2. Description of Laser Systems.	43
(i) The Ruby Laser.	43
(ii) The Nd:YAG Laser.	44
(iii) The Dye Laser.	45
2.2.3. Synchronisation of Lasers.	47
2.2.4. The Target Chamber.	49
2.2.5. The Toroidal Mirror Chamber.	51
2.2.6. Optical Characteristics of Toroidal Mirror.	56
2.2.7. Grazing Incidence Spectrometer.	59

2.2.8. The Multi-Channel Photoelectric Detection System.	62
2.2.9. Spectrometer System Performance.	65
(i) Resolving Power.	65
(ii) Calibration.	68
2.3. References.	71
2.3.1. General References.	71

Chapter 3

Application of DLP Spectrometer Facility to XUV Photoabsorption Studies.

3.1. Introduction.	74
3.2. Suitability of Experimental System for Photoabsorption Studies of Thin Films, Gases, Free Metal Atoms and Ions in the XUV.	75
3.2.1. Characterisation of Backlighting Continuum Source.	75
3.2.2. Thin Film Photoabsorption Measurements in the XUV.	77
3.2.3. XUV Photoabsorption Spectrum of Helium.	78
3.2.4. Inner-Shell Photoabsorption Spectra of the First Row Transition Metals; Comparison with Synchrotron Data.	80
3.3. XUV Photoabsorption of Free Ions : Photoabsorption Studies in the Transition Regions of the Periodic Table.	84
3.3.1. Xenon Isoelectronic Sequence.	84
3.3.2. Calcium and its Ions in the XUV.	91
(i) Neutral Calcium.	91
(ii) Singly Ionized Calcium.	95
(iii) Argon-Like Calcium.	106
3.4. References.	114

Chapter 4

Photoabsorption Spectrum of Atomic Zinc and its Ions (Znⁿ⁺ :n=1,2,3), in the Region of 3p Electron Excitation.

4.1. Introduction.	119
4.2. Review of Work to Date on Subvalence Excitations of Atomic Zinc.	120
4.2.1. Excitation from 3d Subshell.	120
4.2.2. Excitation from 3s Subshell.	121
4.2.3. Excitation from 3p Subshell.	121
4.3. Photoabsorption of Zn I, in the Region of 3p Excitation.	126
4.4. Photoabsorption Spectrum of Zn II, in the Region of 3p Excitation.	131
4.5. Photoabsorption Spectrum of Zn III, in the Region of 3p Excitation.	134
4.6. Photoabsorption Spectrum of Zn IV, in the Region of 3p Excitation.	136

4 7 Summary and Conclusions	138
4 8 References	142

Chapter 5

Photoabsorption Studies Along the Lithium Isonuclear Sequence in the Region of Single and Multiple K-Shell Electron Excitation.

5 1 Introduction	145
5 2 Collisional Experiments on Multiply Core Excited States in the Lithium Isonuclear Sequence	146
5 3. Previous Photoabsorption Measurements of the K-Shell Spectra of Atomic Lithium and its Ions	150
5 4 Optimisation Requirements of Experimental Technique to Observe Double K-Shell Electron Resonances	153
5 5 Measurement of the $1s^2 (1S^e) \rightarrow 2s2p (1P^o)$ Resonance of Singly ionized Lithium	156
5 6 Measurement of the Triply Excited $1s^2 2s (2S^e) \rightarrow 2s^2 2p (2P^o)$ Resonance of Neutral Lithium	162
5 7 References	171

Chapter 6

Summary and Conclusions.

6 1 Summary and Conclusions	175
6 2 Suggestions for Future Work	179

Appendix A

System Mechanical Drawings.

A1 Legend

A2-A18 Drawings

Chapter 1

Introduction

1.1. Development of Spectroscopy—A Historical Perspective.

The beginnings of spectroscopy were laid in the seventeenth century when Newton proved that white light contains light of all the colours. This he did by demonstrating that a spectrum produced by one prism, if passed through a second prism, can either be recombined into white light or dispersed through greater angles, but undergoes no further change in colour. Previously it was thought that the prism somehow introduced the colours. The nature of light, however, remained controversial for 150 years, with Newton on one hand supporting a corpuscular theory, Hooke and Huygens on the other, a wave theory. Early in the nineteenth century Young had apparently settled the matter with his interference experiments.

Subsequent to Newton's discovery and study of the spectrum of the sun, over two and a half centuries ago, there was a period of almost one hundred years entirely concerned with emission spectroscopy. However, in 1802 Wollaston reported the presence of dark bands in the continuum emission spectrum of the sun and, after a more detailed study by Fraunhofer in 1814, Brewster, in 1820 was able to ascribe them to absorption of radiation within the sun's atmosphere. Another forty years passed before Kirchoff and Bunsen showed that one of these dark bands in the emission spectrum of the sun corresponded exactly to the yellow emission band obtained when sodium vapour is heated in a flame. Their work enabled Kirchoff to determine the fundamental relationship between emission and absorption spectra: any species that can be excited to emit radiation at a particular wavelength will also absorb radiation at that wavelength. Thus a new technique could be added to the already well-established one of emission spectroscopy and the work of Bunsen and Kirchoff was continued and placed on a sound theoretical basis by the physicists and astronomers of the early twentieth century.

The nineteenth century saw spectroscopy in rapid advance; Stokes in about 1862 used quartz optics, a spark source and fluorescence detection to reach 1830 \AA , a record that lasted for almost 50 years. Perhaps the greatest technical break-through, however, was the discovery of photography by Niepce and Daguerre in 1839 which made possible the recording of spectra in the ultra-violet as well as the visible. Also of great importance to spectroscopy was Rowland's invention of the concave diffraction grating in 1882, since it led to the determination of precise wavelengths of spectrum lines in the sun and laboratory sources. As a result, series were discovered in spectra, the first in 1885 by Balmer, who gave a simple formula for the positions of the best known

lines in the spectrum of hydrogen.

Probably the greatest contribution to the discovery of the extreme ultraviolet was the work outlined in no less than forty seven papers between 1885 and 1903 by Victor Schumann. In rapid succession he made three discoveries, all breakthroughs. The first was the use of fluorite instead of quartz for prisms and lenses, enabling him to reach 1820 Å. Secondly, he recognised the ultraviolet absorbing character of gelatine, thus inventing the Schumann plate containing almost no gelatine and sensitive all the way through the extreme ultraviolet. He also realised that air below 1850 Å soon becomes opaque and constructed the first vacuum spectrograph which could operate down to 1300 Å.

The reemission by an atom of radiation as fluorescence after the absorption of light from a suitable source was first reported in 1905 when Wood succeeded in exciting atomic fluorescence of the D lines of sodium vapour. He used an evacuated test tube containing sodium vapour as the atom reservoir and a gas flame containing sodium chloride as the illuminating source. The result was predicted by the classical theory of light in the same way as the resonance of standing waves observed for sound, vibrating strings, etc. Wood, therefore, termed this fluorescence “resonance radiation” a name which is still used today for the atomic fluorescence of resonance lines such as the D lines. Similar work was carried out with other readily volatile elements, enclosed cells again being used to contain the atomic vapour, and was mainly concerned with fundamental studies of atomic spectra.

In the same year that Wood, inspired by the classical theory of light, coined the phrase resonance radiation, Einstein correctly explained a phenomenon first discovered by Hertz in 1885, whereby matter, under the action of electromagnetic radiation, was seen to emit electrons. This process, called the photoeffect, was suggested by Einstein in 1905 to be due to the fact that light is absorbed and emitted in fixed amounts, or quanta, and propagates as photons rather than continuously, thus reviving Newton's corpuscular hypothesis. This was a very important contribution to the idea that electromagnetic waves are at the same time a flux of photons. The photoeffect was explained in terms of a process whereby an electron in a metal absorbs a photon leading to a subsequent increase in its kinetic energy. If this becomes sufficiently high, the electron can leave the metal. The same process, of course, may take place in an isolated or free atom.

The release of electrons by free atoms, due to their interaction with photons : also called photoionization, is one of the fundamental processes in the interaction of photons with matter. The study of this process has provided the impetus for a large number of theoretical approaches to obtain an improved understanding of atomic

properties and to gain a deeper insight into the dynamics of excitation and deexcitation. Without a detailed understanding of the atomic photoionization mechanism it is impossible to explain the interaction of radiation with complex natural objects such as molecules, biological structures, and solids.

Photoabsorption is one of the most widespread processes in nature. The investigation of not only the cross section for the process but also the energy and angular distributions of electrons ejected from the atom supplies extremely valuable information on the electronic structure of various substances. A photon couples to an atom comparatively weakly without disturbing the structure of its ground or excited states. As the photon is absorbed a transition is made between two atomic states, the energy or angular frequency of the incoming photon determining to which excited state the atom is promoted.

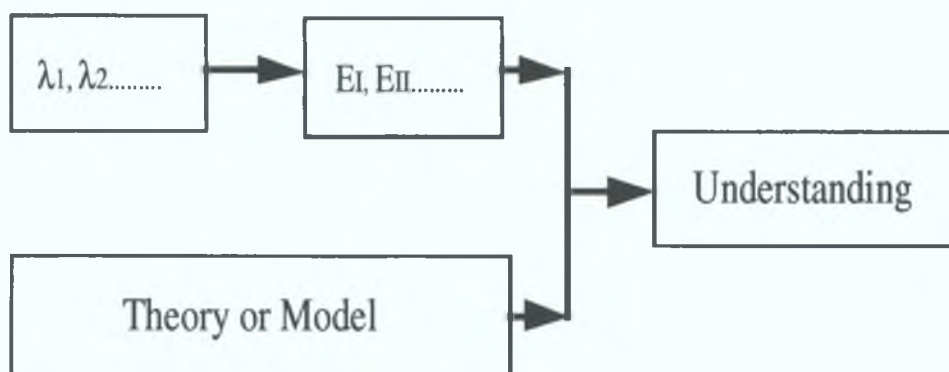


Figure 1.1. Schematic representation of the spectroscopic process.

By measuring fundamental quantities such as the wavelengths of the transitions of interest the energy level structure of the system can be mapped out. Spectroscopic investigations can be of a fundamental or applied nature, in fundamental spectroscopy experimentally determined energy levels, transition probabilities, etc. are employed for obtaining an understanding of the studied systems using adequate theories or models. This process is schematically illustrated in figure 1.1.

1.1.1 Photoionization in the VUV

For the use of electromagnetic radiation at wavelengths $\lambda \leq 2000 \text{ \AA}$, as discovered by Schumann, it becomes necessary to work under vacuum conditions due

to atmospheric absorption. The spectral region $\lambda \leq 2000 \text{ \AA}$ is therefore generally called the vacuum ultraviolet (VUV). Below $\lambda \sim 2 \text{ \AA}$ the atmosphere becomes transparent again: wavelengths of about 2 \AA can therefore be regarded as the lower-wavelength limit of the VUV. Wavelengths between 2 \AA and 300 \AA are often referred to as the soft x-ray range, figure 1.2 summarises the photon wavelength or energy region encompassed by the term VUV.

Photoionization studies of metallic vapours started with the investigation of Cs irradiated by Ultra-Violet (UV) photons in the range $2500\text{-}3500 \text{ \AA}$ by Foote and Mohler in 1925, which were soon followed by the first measurements of absolute photoionization cross-sections for Cs and Rb between 2200 and 3200 \AA by Mohler and Boeckner in 1929. The spectral range was extended to the VUV by the development of continuum light sources such as the He discharge lamp which allowed the systematic study of inner-shell excitation processes which characterise the electronic transitions resulting from the interaction of VUV photons with atoms. Beutler and Guggenheimer in the 1930's performed photoabsorption measurements for the first time below 1200 \AA on some of the more easily vapourizable elements such as Hg, Cd, Zn, K, Cs, Rb, and Tl.

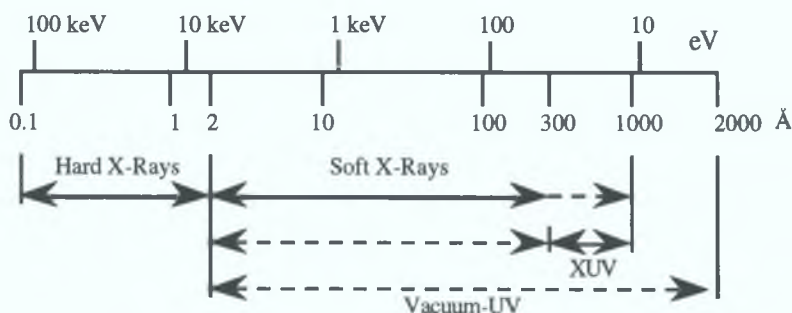


Figure 1.2. Breakdown of the electromagnetic spectrum in the VUV region

The use of photoelectron spectroscopy after VUV excitation (Villesov *et al.* 1961, Turner and Al-Jobourg 1962) and the development of synchrotrons as the ideal featureless continuum VUV source (Madden and Codling 1963) were the next important steps which accelerated the rapidly increasing number of experiments in the field of core excitation and photoionization. Whereas the earlier experiments in photoabsorption were limited to total cross-sectional measurements, the intense and well collimated monochromatized photon beams of the synchrotron radiation facilities enabled the development of various experimental techniques like energy- (angular,

spin) resolved electron spectroscopy, ion spectroscopy or fluorescence spectroscopy to study the different decay products.

1.2. Stimulus for Spectroscopic Investigation in the Energy Region of Subvalence Electron Excitation.

Photoabsorption, within the bounds of the dipole approximation, is a superior method for an investigation of atomic structure when compared with other processes such as elastic and inelastic scattering of electrons, protons and ions. In all of these other processes the target atom gets strongly deformed, most weakly by the fast electron, and so direct information is provided only on the structure of the compound system. It should be pointed out that the atom is a many body system, for which the interaction among its constituents-the electron-nuclear attraction and interelectron repulsion-is known with very high accuracy. In this sense the atom is a unique object in nature, permitting us to trace how its structure changes under increasing number of constituents from the simplest case of hydrogen to more complex atoms.

In contrast to the optical spectra of the valence electrons, which can mainly be described by the one-electron picture of the central field approximation, the inner-shell excitation is characterised by strong many-electron effects causing the break-down of the simple one electron picture. This simple one electron picture was derived from the model employed by Stoble in 1930 to describe the behaviour of the photoionization cross section for hydrogen, this being the simplest, two body system. The relationship between photon frequency and cross section proved quite distinctive: when the energy of the incident photon is coincident with the ionization potential of the electron, ie the minimum energy required to remove the electron from the atom to a point at infinity with zero kinetic energy, there appears a finite jump in the cross section - termed the threshold. For increasing photon energy above threshold the cross section decreases rapidly as $(\text{Photon Energy})^{-7/2}$, such behaviour is called 'hydrogen-like'. It was assumed for a number of years that this description would be adequate in dealing with more complex multi-electron atoms and that one would observe a finite leap at each new threshold corresponding to ionization from a deeper lying electron shell, giving their spectra a saw-toothed appearance, see figure 1.3.

Initially, due to the lack of experimental data available and the narrow band of photon energies investigated, the hydrogen-like model seemed to be adequate in describing the features observed. In the mid 1960's this situation changed dramatically

when Lukirskii and Zimkina in the USSR and Ederer and his colleagues (PRL 1964 eg Xenon) in the USA obtained photoabsorption measurements in the region from tens to hundreds of electron-volts. Their data was in complete contradiction with the hydrogen model predictions.

In some cases, for example, it was observed that the photoionization cross section increased beyond an ionization threshold (delayed onset) before subsequently decreasing. The words 'delayed onset' refer to the fact that, in an optical spectrum, the signal due to photoionization is normally large near threshold, decreasing monotonically as the energy increases. Likewise, with the experimental resolution available in the X-ray range, the absorption edges due to photoionization of inner-shells appear to be quite sharp. In the energy range of subvalence excitation, however, the photoionization signal can be low at threshold, building up as the energy increases, and the actual maximum frequently occurs tens of eV above the ionization limit.

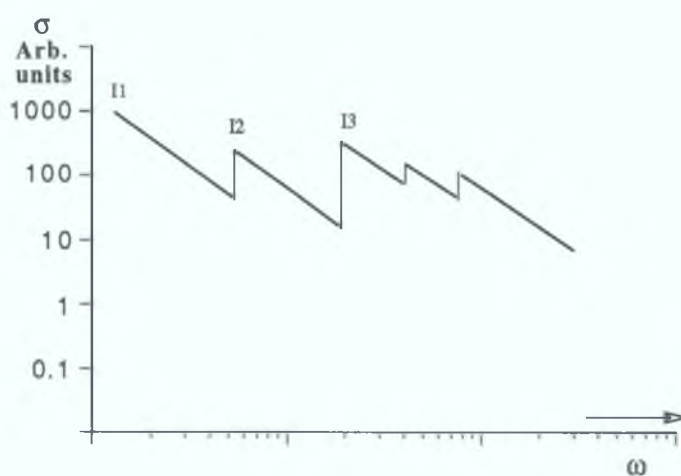


Figure 1.3. Schematic representation of photoionization cross section in the hydrogen approximation where σ is measured in arbitrary units and I_1, I_2, I_3 are ionization potentials of electrons with decreasing principle quantum numbers.

These experimental results demonstrated the inadequacy of the hydrogen-like model for at least the outer and intermediate shells of multi-electron systems whose excitation energies are bounded by the VUV photon range. The deviation of the photoionization cross section from the simple hydrogenic case displays how and to what extent interelectron or electron-electron correlation effects manifest themselves in the atomic structure of a multi electron atom. It should be noted that correlation effects

have also been observed in solid state, ionic and molecular absorption spectra (JP Connerade 1978a, 1987).

1.3. The Role of Laser Produced Plasmas in Spectroscopy.

1.3.1 Introduction.

The interest in atomic and molecular photoionization has moved continuously towards a deeper understanding of the role and importance of correlation effects in photoionization. More specifically this has been accomplished in most cases by critical comparison between theoretical results, which include correlation effects, and improved and extended sets of experimental data. Electron-electron interaction phenomena such as delayed onset of absorption (eg Ederer, 1964), giant resonances (M.Meyer *et al.* , 1986), and single photon/multi electron excitations (Kiernan *et al.* 1994), have all provided impetus for an increasing number of experiments in the Extreme-Ultraviolet (XUV) energy region. This growing interest in the fields of core excited atomic, molecular and solid species has resulted in a demand for compact, low cost XUV continuum light sources. One such source is the Laser Produced Plasma (LPP) which, by suitable choice of target material, can be used to produce a clean line-free continuum from 40-2000 Å (Fischer *et al.* 1984 and Bridges *et al.* 1986). The conversion of laser light into UV radiation and X-rays can be very high. Conversion efficiencies of 40% and higher have been reported (Rosen *et al.* 1981, Mead *et al.* 1981, Caro *et al.* 1984 and Bijkerk and Shevelko 1991).

To date most of the work in XUV photoabsorption experiments has been concentrated on measurements using stable species such as solids (eg Zimkina *et al.* 1967), inert gases (eg Madden and Codling 1963, Schmidt 1992) and easily vapourizable metal elements (eg Mehlmann *et al.* 1978). There is very little known about the photoabsorption of free ions due to the technical difficulties in producing adequately high densities of ions suitable for absorption studies. LPP's have proven to be versatile sources for the study of the emission spectra of highly ionized atoms (see for example the review by Martinson 1989). The results from isonuclear and isoelectronic sequences in such spectra combined with scaled and *ab-initio* multi configurational calculations have yielded a great deal of basic atomic data together with

many insights into the effects of increasing ionization and nucleus occupancy. There are many refractory and highly corrosive species for which vapours cannot easily be produced and that act aggressively towards conventional soft X-ray optic components. It is precisely in these two areas of ionic (eg Jannitti and Nicolosi 1987) and refractory atom absorption (eg Carroll and Costello 1986, Hansen *et al.* 1989), that the LPP has made its' niche.

1.3.2. Review of General Properties of Plasmas.

Plasma is generally regarded as the fourth state of matter. Although in our immediate environment its occurrence is rare, on the cosmological scale it is reckoned to make up about 99% of all matter in the Universe whether as stellar, interstellar or intergalactic material (Carroll & Kennedy 1981).

There are an enormous variety of conditions under which matter becomes an ionized gas or "plasma". In general for atoms to be ionized the temperature must normally be greater than a few eV ($1\text{eV}\approx 10^4\text{ K}$). In magnetic fusion machines such as the tokamak, the plasma density is $10^{12} - 10^{14}$ electrons or ions per cubic centimetre; in LPPs, usually formed when the output pulse from a high power laser (typical irradiance of $\sim 10^{16}\text{ W m}^{-2}$) is focused onto a solid target *in vacuo*, the densities are usually much higher, $10^{17} - 10^{22}$ per cm^3 . Inter stellar plasmas have much lower densities, a few particles per cm^3 , whereas much higher densities, $\sim 10^{25}$ per cm^3 , can be found in stellar interiors. All these plasmas consist of ionized atoms and much interest centres on the various excitation/ionization mechanisms and on their spatial and temporal behaviour.. For example, the analysis of atomic emission lines can reveal plasma conditions such as electron temperature or the locations of impurity atoms (eg Fawcett 1984); this information can then be used to improve the performance of a plasma machine.

Atomic processes play an important role in the energy balance of a plasma, be it in a fusion machine or in a star. For example, electron-ion collisions limit electron thermal conduction and photon-ion interactions limit the radiative heat conduction. The opacity coefficient is an average atomic absorption cross-section which describes how radiant energy flows out of a star. At present, our understanding of stellar structure depends upon opacity data which come from theoretical models of atoms in plasmas.

High-charge ions are very unstable in the presence of ordinary matter. For example, when a high-charge ion comes in contact with a solid surface, it tears electrons from the solid and releases an impressive amount of energy, up to hundreds of keV, as the electrons recombine with the ion. This creates a sort of atomic scale ‘microplasma’. Jean-Pierre Briand (1990,1991) of the Université de Paris has studied such recombination events for Ar^{17+} and Ar^{18+} ions, observing that the rates for filling the outer shells are faster than those for filling the inner shells. The result is a sort of “hollow atom” in which the L and M shells have filled before the K shell refills. These recombination kinetics are revealed by high resolution spectroscopy of the K-shell X-ray emission.

Finally, one may broadly state that a plasma is matter in a state of ionization. The plasma system is assumed to remain overall neutral, with the electron density n_e balancing the ion density of the various charge states.

$$n_e = \sum_z n_z z \quad (1.1)$$

1.3.3. Atomic Processes in Laser Produced Plasmas.

(i) Bound-Bound Transitions.

When an atom or ion makes a transition from one bound state to another, the energy of the emitted or absorbed photon is well defined. In the absence of perturbations the transition gives rise to a spectral line whose profile depends upon the lifetime of the final state, and on the velocity distribution of the atoms concerned which causes a distribution of Doppler shifts. Emission follows excitation, which may be caused by collisions with other particles or by the absorption of photons.



Collisional excitation by energetic electrons is a very important process, and the spectrum of the line radiation depends on the electron temperature (or velocity distribution) and density. In a cool partially-ionized gas ($T_e=1$ eV) much of the line

radiation is in the infrared and visible regions of the spectrum. As the temperature rises, atoms can be raised to more energetic excited states and thus tend to emit lines of shorter wavelengths. When $T_e \sim 10$ eV nearly all of the atoms will be ionized and

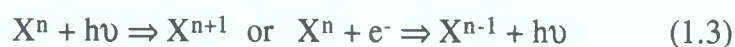
	Electron emits	Electron absorbs	Photon is absorbed
FF	Bremstrahlung	Inverse Bremstralung	I.B. or joule heating
BF	Radiative recombination	Photoelectric effect	Photoionization
BB	Line emission	Line absorption	Line absorption

Figure 1.4. Summary of the nine radiative cross-sections which can be broadly classified as FF(free-free), Fb(free-bound) and BB(bound-bound) transitions.

multiple ionization of many electron atoms occurs. The reduced screening of the nuclear charge in multiply-ionized atoms leads to larger energy differences between bound states, so that line radiation is emitted mostly at shorter wavelengths in the far ultraviolet and X-ray regions of the spectrum.

(ii) Free-Bound Transitions.

Photoionization can occur when an incident photon has sufficient energy to remove an electron from an atomic system thus leaving it in a higher stage of ionization. Conversely, when a free electron is captured by an n-times ionized atom and makes a transition to a bound state of the (n-1)-times ionized atom, the surplus energy may be emitted as a photon.



The emission is known as recombination or free-bound radiation. For a particular final bound state, the emission spectrum is a continuum with a fairly sharp low-frequency cut-off. The cut-off is known as the recombination limit, and corresponds to the minimum energy required to ionize the atom from the bound state. The profile of

the continuum depends on the free electron velocity distribution and on the (velocity dependent) capture cross section into the bound state. Each bound state has its own continuum, and these overlap: they may differ greatly in intensity.

Recombination may also occur without the emission of radiation if two free electrons collide with the ion simultaneously. One electron is captured while the other carries away the surplus energy. This ‘three-body’ recombination is in competition with radiative recombination and becomes more probable as the density rises.

(iii) Free-Free Transitions.

Free-free radiation, or bremsstrahlung, occurs when a free electron collides with another particle and makes a transition to another free state of lower energy, with the emission of a photon; see figure 1.5. The spectrum associated with this scattering process is continuous. Electron-electron collisions do not produce radiation except at relativistic velocities. In a hot plasma the dominant interactions are those between electrons and ions.

In the inverse process a photon is absorbed by the ion-electron system and the electron is raised from a lower level in the continuum to a higher one. Essentially the energy of the incoming photon is converted into an increase in the kinetic energy of the free electron. Both bremsstrahlung and inverse bremsstrahlung are of major importance

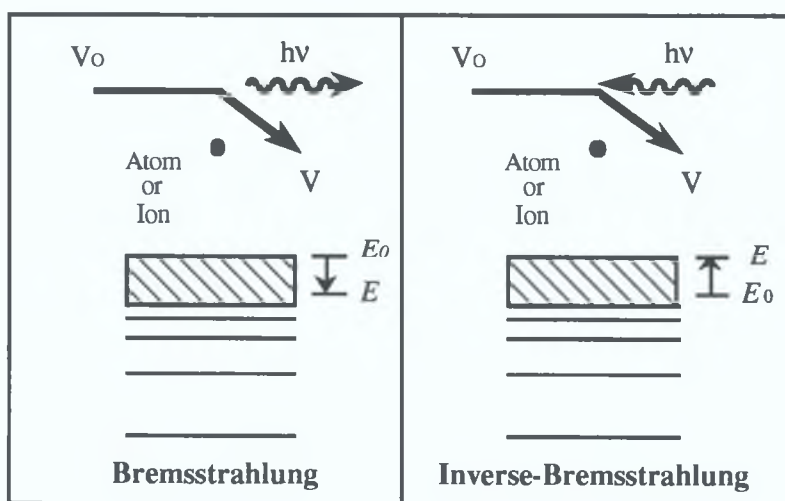


Figure 1.5. Schematic illustrations of the bremsstrahlung emission of a photon of energy $h\nu = E_0 - E$ during a free electron's collision with a point charge Ze , and of the opposite process—inverse bremsstrahlung.

in laser produced plasmas. One should also note that for every plasma process outlined above, there exists an exact inverse process—this symmetry of plasma kinetics is an inherent assumption in any model describing plasma equilibrium.

1.3.4. Generation and Evolution of Laser Produced Plasmas.

The black-body emitter is the simplest type of continuum light source. The shape of the radiation spectrum emitted from a hole in the side of a perfect black-body cavity is described by the Planck formula,

$$M_{\lambda} = 8\pi hc^2 \lambda^{-5} \left[1 / (\exp(hc/\lambda kT) - 1) \right] \quad (1.4)$$

where M_{λ} , in units of $W m^{-3}$, is defined as the spectral radiant exitance, λ is the wavelength of the radiation, T is the cavity temperature and the rest of the symbols have their usual meanings. From figure 1.6 it can be seen that in order to obtain emission extending into the EUV and soft X-ray regions of the spectrum it is necessary to raise the temperature of the thermal source to $T \approx 10^5 - 10^6$ K. The curves in figure 1.6 have been calculated by converting equation (1.4) to its frequency form ($M\nu$). Dividing the frequency dependent form by 4π yields the quantity $L\nu(0)$ which is the spectral radiance normal to the cavity aperture, ie

$$L\nu(0) = M\nu/\pi = 2 \times 10^{-3} \nu^3 / c^2 \left[1 / (\exp(h\nu/kT) - 1) \right] \quad (1.5)$$

Figure 1.6 also illustrates the energy form of the Wien displacement law which describes the linear shift of energy position of maximum photon flux with increasing black-body temperature.

By integrating equation (1.5) with respect to wavelength the total radiation emitted by a black-body source may be determined (i.e. the Stefan-Boltzmann Law = $\sigma T^4 W m^{-2}$ where $\sigma = 5.67 \times 10^{-8} W m^{-2} K^{-4}$). For a black-body source emitting in the EUV at a temperature of 10^6 K, approximately $5 \times 10^{16} W m^{-2}$ of radiant power is produced. Thus to generate a black-body at such a temperature would require an extremely powerful heating source to both initially reach the required temperature and then to sustain this temperature against huge radiation losses. High power pulsed lasers are ideal candidates for this role. The spectrum of radiation emitted from a LPP crudely approximates that of a black-body continuum at an equivalent temperature. For

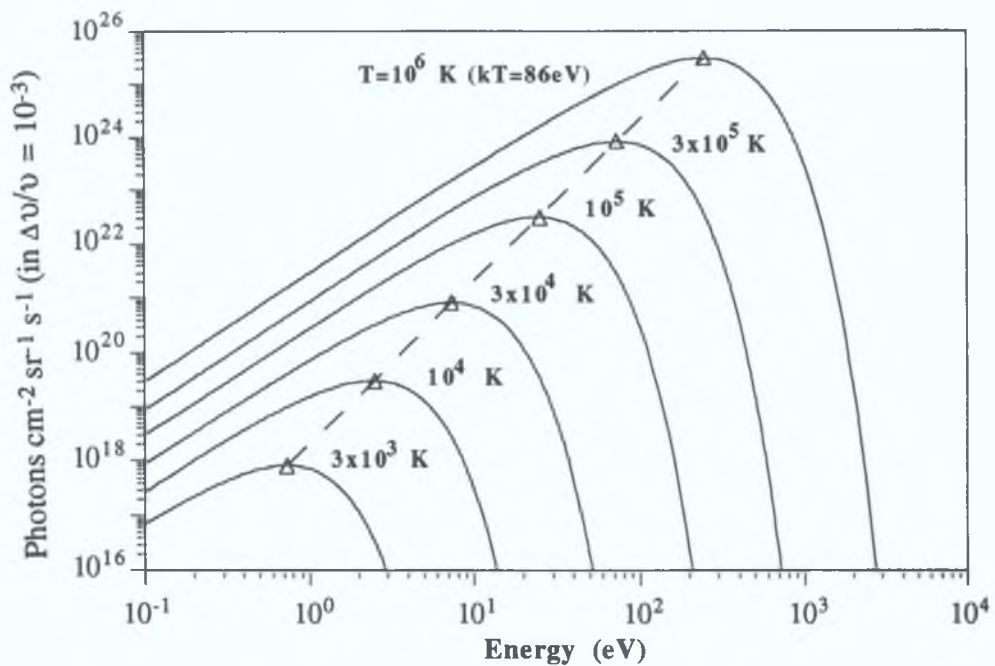


Figure 1.6. Black-body spectra at various cavity temperatures with the straight line indicating Wien's displacement law.

example a Nd:YAG laser (0.8 J in 15 ns) can deliver 5.3×10^7 W of power. When focused to a spot, typically 100 μm in diameter, this corresponds to an irradiance of 2×10^{16} W m^{-2} . Assuming a moderate conversion efficiency of 15%, 3.2×10^{15} W m^{-2} of black body radiation will be generated. From the Stefan-Boltzmann law this corresponds to a black body temperature of approximately 5×10^5 K. At this temperature, from figure 1.6, about 10^{24} photons $\text{cm}^{-2} \text{sr}^{-1} \text{s}^{-1}$ in a bandwidth of $\Delta\nu/\nu = 10^{-3}$ will be emitted. This figure is in good agreement with the values quoted by Bijkerk and Shevelko (1991) in their detailed inter comparison between the source characteristics of a black body radiator and various types of laser generated plasmas.

Much effort has been concentrated on the design and construction of powerful laser systems and intricate target geometries for fusion research. Sigel *et al.* (1987), have reported experiments where they have attempted to generate perfect high temperature black-body radiation inside laser-heated gold cavities. This type of experimental configuration is used for the investigation of high temperature Planck radiation for specialised applications such as X-ray driven Inertial Confinement Fusion (ICF), where a thin walled spherical shell is placed inside the cavity. The spherical shell usually contains a deuterium-tritium mixture which is subsequently imploded either directly, by laser irradiation or indirectly by black-body XUV radiation. At stagnation of the implosion the deuterium-tritium mixture is heated by converging

shock waves to fusion temperature, implosion densities can range from 1 to 50 gcm⁻³ and the pressure can reach 10⁹ bar. However for more general studies of LPP's it is not necessary to use such powerful lasers or indeed such complicated targets.

To produce a laser-plasma on the surface of a solid target an irradiance in excess of 10⁹ W cm⁻² is required. This power density is easily within the range of small

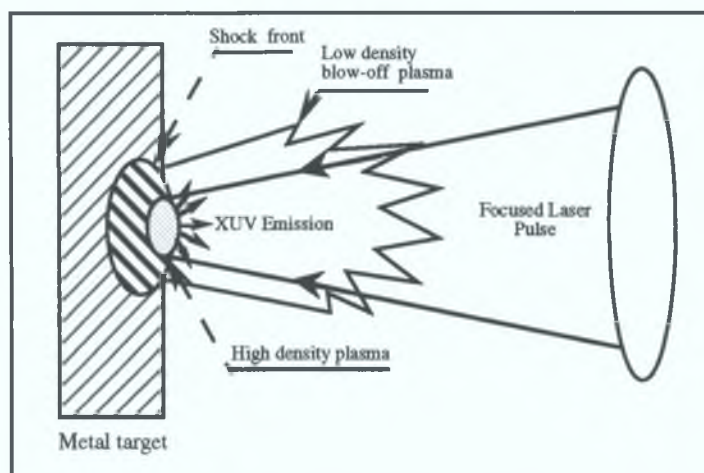


Figure 1.7. Schematic representation of the interaction of a high power pulsed laser with a solid target.

commercial Q-switched, or 'Giant Pulsed', flashlamp pumped solid-state, eg Ruby and Nd:YAG, lasers. Such lasers typically deliver 1-2 J of optical energy in a single pulse lasting 10-30 ns which corresponds to approximately 10⁷-10⁸ W of radiant power. The smallest spot-size to which the laser beam can be focused is theoretically diffraction limited and depends on the mode structure within the beam and on the quality of the focusing optics. Focal spot diameters of less than 100 μm are readily obtained, which corresponds to an irradiance of at least 10¹¹ W cm⁻² for a typical commercially available system.

When attempting to describe the initial formation and resulting evolution of a plasma generated by the interaction of laser light with various solid targets, a distinction arises between processes responsible for plasma initiation in the case of conductors and insulators. In the case of metals the leading edge of the focused laser pulse penetrates only to a very short depth, typically less than one wavelength (Prokhorov 1990). The sudden heating and ionization of the target surface produced by the interaction of the extremely intense electric field (10⁹-10¹² V m⁻¹), set up by the laser light, and the conduction electrons in the metal leads to the formation of a low temperature, expanding plasma close to the surface. For insulators, however, the situation is quite different — the lack of conduction electrons means that the ionization

potentials of such materials are substantially greater than the laser photon energy. Yet, under the action of a sufficiently large photon flux, possibly through processes such as Multi Photon Ionization (MPI), non-linear effects or interaction with impurities at the target surface, plasmas are indeed formed.

The localised low temperature plasma that is thus created, in both sets of materials, strongly absorbs the incoming laser light through the spectrally continuous process of inverse-bremsstrahlung, resulting in a sharp increase in the average kinetic energy of the free electrons. These fast “seed” electrons, in turn through collisional ionization accelerate the electron density to a value which very rapidly approaches that of critical opacity causing the reflection of laser light away from this region of the plasma. The absorption of energy through inverse-bremsstrahlung has a dramatic heating effect on the plasma which causes a hydrodynamic expansion, this leads to a decrease in the electron density allowing the laser light to replenish material lost from the focal volume. In this way a steady state, self-regulating plasma flow is established on a timescale ≈ 50 -100 ps, which lasts until the end of the laser pulse. The pressure of the hot dense plasma drives a strong shock wave into the solid as illustrated in figure 1.7. Through this rocket-like process the shock wave travels at a velocity similar to the plasma blow off velocity. The spectral qualities of the light emitted from such LPP's will be discussed in the following section.

1.4. Spectroscopic Investigation of the Structure of Atoms, Excited Atoms and Ions, in the XUV.

1.4.1. Photoemission Studies.

Progress in the investigation of the light emitted by ionized matter has gone hand in hand with the technological advances associated with XUV light sources. Until the early 1960's the most popular source was the electric spark discharge. This normally consists, in its simplest form, of a pair of electrodes, separated by a few mm under vacuum. The electrodes are connected through a capacitor (typically 0.3-0.5 μ F) to a high voltage supply (50-80 kV), producing a discharge current of up to 50 kA. By introducing a variable inductance in the circuit the distribution of ion stages emitted from the source can be altered. The vacuum spark is a fairly simple and inexpensive light source for highly ionized atoms and has provided an extremely important contribution to the study of isoelectronic sequences in such species. For example, Edlén (1942) through measurements of the XUV spectra of highly stripped iron atoms

showed that forbidden transitions between closely spaced levels produce lines agreeing in wavelength with solar coronal lines. The coronal temperature and density, thus predicted ($\approx 10^6$ K), was far higher than anyone had imagined and had a tremendous impact on astrophysics at that time.

The instability and poor ion stage selectivity of early spark sources rendered them unsuitable for use with photoelectric registration. Numerous improvements were made through new plasma triggering mechanisms and the insertion of an insulating surface, to guide the spark (Vodar B. and Astoin N. 1950), enhancing the performance of these devices. It was observed through the addition of a third electrode, used as a plasma insertion trigger (Ballofet *et al.* 1961, also Lucatoro *et al.* 1979), that a pure continuum spectrum is emitted close to the anode when the anode is made of gold or, best of all, uranium. This continuum extends from about 150 to 600 Å, however the BRV (Ballofet, Romand and Vodar) source suffers from a limited electrode lifetime and a low repetition rate.

Edlén (1963) concludes in his review of laboratory light sources in the VUV that, 'for wavelengths shorter than 500 Å and for very high ionization stages a spark in high vacuum remains the only practicable light source'. However, only a few years later the technique of Beam Foil spectroscopy was shown to yield spectra of highly ionised atoms. Kay (1963) and Bashkin (1964) realised the atomic physics potential of fast ions from particle accelerators. In a typical experiment the accelerated ions of the element to be studied are produced with a well defined energy (velocity) usually by passing through a magnetic analyser. The ions with a typical velocity of 10^6 ms⁻¹, pass a 50 nm thick carbon foil, in which very abrupt excitation occurs (the passage time is $\approx 10^{-14}$ s). Ions of different charge states are formed. An electron can also be picked up and a neutral or excited atom is then formed. These excited states then decay after passing through the foil and since the velocity of the particles is known a well-defined time scale is obtained and the lifetime of the excited state of interest can be measured directly. A more extensive discussion of the beam-foil method can be found in a monograph by Bashkin (1976).

LPP's have been in use as XUV light sources for almost three decades. Spectral line radiation as well as continuum radiation is generally emitted from such plasmas and their value as XUV light sources was recognised soon after the development of high power lasers. In one of the first experiments Fawcett *et al.* (1966) used a Q-switched ruby laser ($\lambda=0.694$ μm) which gave pulses of 8 J energy with a duration of 30 ns. The laser output was focused on Fe and Ni metal targets at a power density of 10^{12} W cm⁻². Spectral studies of the plasmas, thereby formed, showed

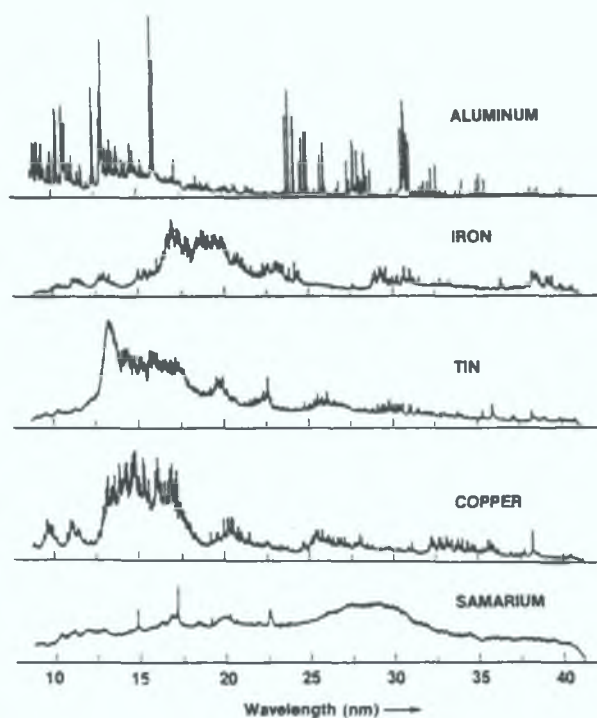


Figure 1.8. Emission spectra from laser produced plasmas of various metal targets. The transition from predominantly line emission in the low-Z metals to pure continuum in the rare earths is well illustrated (after Bridges *et al.* 1986).

transitions in Fe XV, Fe XVI, Ni XVII and Ni XVIII. Besides consisting of only a few and, to a great extent controllable, ion stages the spectra showed no impurity lines (C, N, O etc) which are usually present in spark spectra. Breton and Popular (1973) used both Nd:glass and ruby lasers with Ta targets to produce intense radiation in the region of 1215 Å ; their studies include measurements of the absolute spectral intensity of the generated radiation, its angular distribution (also Gerritsen *et al.* 1986) and its dependence on laser power.

A lot of materials were investigated and although continuum emission from LPP's was frequently noted, little effort was made to develop it as a pulsed continuum source for time resolved absorption spectroscopy. This was mainly due to the fact that most of the elements investigated spectroscopically in the early work were light elements of astrophysical interest, the spectra of which consisted normally of a weak continuum overlaid by a much stronger line spectrum : see, for example, Al spectrum in figure 1.8.

However, as part of a study of the spectra of W, Ta and U plasmas produced with a ruby laser, Ehler and Weissler (1966) noted the predominance of continuum emission in the VUV above 400 Å. Subsequent analysis of high resolution work on the heavier elements from strontium (Z=38) to uranium (Z=92), and in particular the rare

earth elements from Sm (Z=62) to Yb (Z=70) by Carroll *et al.* (1978), (1980) and O'Sullivan *et al.* (1981) revealed that strong essentially line free continua are emitted by these elements throughout the VUV: see figure 1.8.

In order to explain the origin of these very pure continua the dominant ionic species of the plasma under consideration must be determined. According to the theory of Colombant and Tonon (1973) the excitation process in LPP's is considered to be dominated by collisional processes while the de-excitation occurs primarily through radiation (the 'Collisional Radiative' model). On this basis the distribution of ion stages in the plasma can be determined from the target composition and the irradiance and wavelength of the laser pulse (a comprehensive review of various approaches to the problems of plasma diagnostics is given by Carroll and Kennedy (1981)). Application of this model to a ruby driven ($10^{11} \text{ W cm}^{-2}$) rare earth plasma yields an electron density (n_e) of $\approx 10^{21} \text{ cm}^{-3}$ at an electron temperature (T_e) of $\approx 50 \text{ eV}$, with a dominant ion stage of 11. The main source of XUV continuum under these conditions will be through recombination with bremsstrahlung contributing only 20%, or so, to the overall continuum.

Because the spectra from many-electron ions are often too complex for the usual line by line analysis, various statistical methods have been developed. The most sophisticated is the method of unresolved transition arrays developed in the 1980s by Jacques Bauche *et al.* (1986) and (1988), at the Laboratoire Aimé Cotton, Orsay, France. This method permits clear identification of certain transitions of high charge ions. An unresolved transition array is a cluster of lines that result from transitions between states belonging to a specific initial and final configuration. Each pair of configurations generates one UTA, which is characterised by an average energy E_{Av} and a width δE .

$$E_{Av} = \sum \omega_{ij} (E_i - E_j) \quad (1.6)$$

$$\delta E = \left(\sum \omega_{ij} (E_i - E_j)^2 \right)^{1/2} \quad (1.7)$$

The sum runs over all states in the initial and final configurations. E_i and E_j are the energy levels of the states i and j , and ω_{ij} is the strength of the transition $i \rightarrow j$. This method has been applied to a large variety of laser plasma spectra and one can identify many features with enough confidence to determine the average ionisation state from the spectrum. For example, Tragin *et al.* (1988), at the Ecole Polytechnique, Palaiseau, France, have identified UTA spectra from nickel-like ions of Au, Ta, W, Re,

Pt, Hg and Pb — this corresponds to ions from atoms which have lost 50 or more electrons through sequential electron-impact ionization.

In the case of the rare earth elements under consideration here, the occupancy of the 4f subshell is dependent on Z and ion stage. With increasing ionization the binding energy of the 4f electrons increases more rapidly than that of the 5s or 5p electrons resulting in level crossing between all of these levels. Emission transitions between configurations, instead of yielding a relatively modest number of lines as in conventional spectra, generate thousands of very closely spaced lines in broad UTA's. Consequently the oscillator strengths for these lines are so weakened that they are submerged in the background continuum (a more detailed discussion is given by O'Sullivan 1983). There is an element of serendipity in the fact that the output of the ruby and Nd:YAG lasers used to generate such continuum emitting plasmas just meet the requirements necessary to produce the particular ion stages responsible for the observed emission. The advantages associated with the use of such a high purity continuum source for high resolution photoabsorption spectroscopy will be discussed in terms of the other techniques available in the following section.

1.4.2. Photoabsorption Studies.

The attenuation of light passing through an atomic vapour column is an important manifestation of the interaction of electromagnetic radiation with free atoms. In the VUV regime the attenuation is determined by the excitation of bound electrons into discrete or, through the process of photoionization, continuum orbitals. Beer's Law describes the intensity I transmitted through a vapour column of length l ,

$$I = I_0 \exp(-\sigma_a n l) \quad (1.8)$$

where I_0 is the intensity of the incident photon beam, σ_a the total cross section and n the density of the target atoms.

Most of the inner-shell or core excited states, resulting from the interaction of a photon, within the VUV energy range, with a target atom have very short lifetimes against decay into an ion plus one or two electrons. This final ionic state occurs primarily through the radiationless processes of Auger or Coster-Kronig decay (Crasemann *et al.* 1984). Hence these transitions are usually only observed through photoabsorption studies. The technique of photoabsorption spectroscopy also has the

added advantage in that transitions arise from a known ground state thus easing the process of spectral assignment. This technique, however, is more demanding in terms of system costs and technical complexity when compared with photoemission studies. Relatively few elements have been investigated in this way when compared with the more established techniques, outlined above, of emission spectroscopy.

Figure 1.9 summarises the overall general system requirements for an experimental set-up for photoabsorption spectroscopy. This simplified set-up can be broken down into four individual subsystems,

- (i) a background light source yielding an emission continuum;
- (ii) a dispersing instrument for the energy range of interest;
- (iii) a sample cell in which the species of interest, whether transient or stable, is generated and contained;
- (iv) a detector to register the light transmitted through the sample.

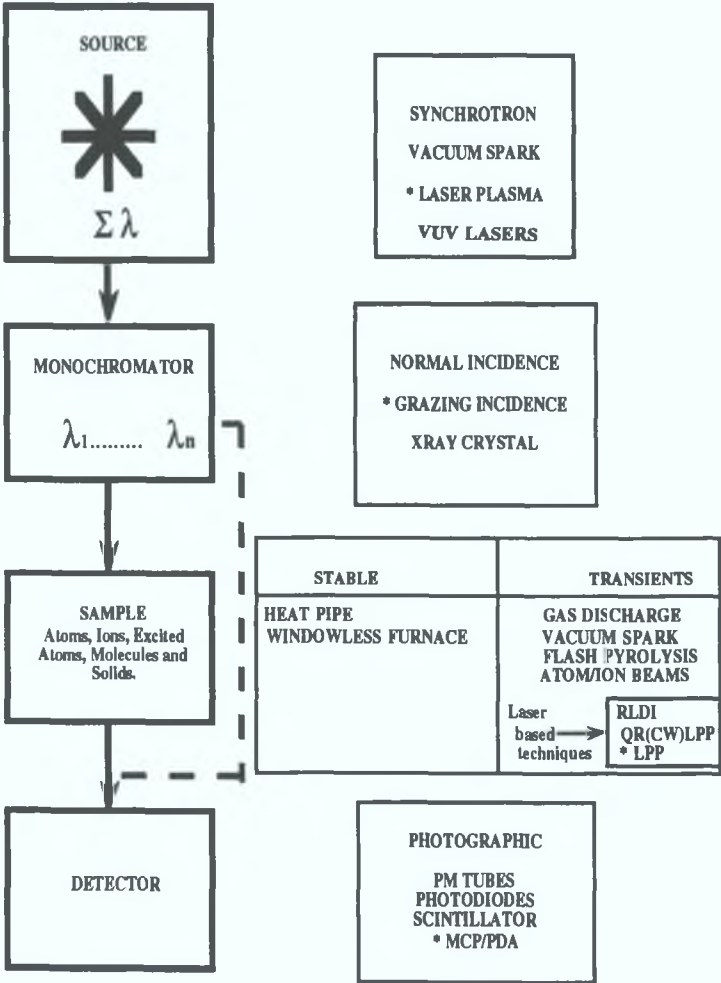


Figure 1.9. General system requirements for XUV photoabsorption studies.

During the last two decades synchrotrons have been increasingly used as sources of continuum radiation for photoabsorption experiments. Synchrotrons were originally the tool of the nuclear physicist, studying the interaction of high energy electrons (or protons) with matter. As synchrotrons of higher energy were built, the major loss mechanism in such devices, the emission of radiation as the charged particle undergoes a centripetal acceleration ($\approx 10^{16}$ g for electrons with a velocity close to c in an orbit radius of 1m) became an increasingly important ‘problem’. It is, in fact, this loss mechanism which sets an upper limit to the energies achievable in synchrotrons. Initially the radiation was obtained “parasitically” from the machines constructed for nuclear physics experiments, but soon after realising the potential of such a light source machines dedicated for light generation only, were constructed.

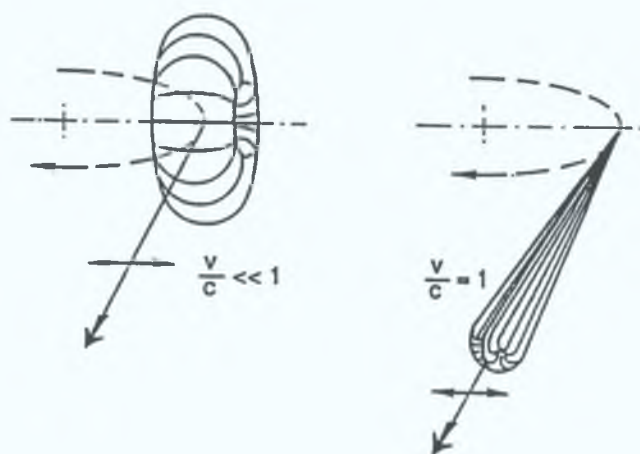


Figure 1.10. Radiation emission pattern of electrons in circular motion: left part for $V/c \ll 1$; right part for $V/c \approx 1$ (after Codling 1973).

The emission pattern of synchrotron light is determined essentially by that of a single circulating electron. For a slow electron moving with a velocity V along a circle of radius R (angular velocity $\omega_0 = V/R$), the energy of the emitted radiation is $h \omega_0/2\pi$ and one obtains a spatial radiation distribution of a circulating dipole, as shown in the left part of figure 1.10. The intensity pattern is proportional to $\text{Sin}^2 \phi$ with ϕ being the angle between the centripetal force and the observer. In an electron storage ring the electrons have a near relativistic velocity along a macroscopic circle (within the bending magnets). In this case one must transform the emission pattern from the left part of figure 1.10, which is still valid in the frame of the moving electron, into the laboratory

frame. This transformation yields the radiation emission pattern shown on the right hand side of figure 1.10. Practically all the radiation is pressed into the forward direction, tangential with respect to the circular trajectory of the relativistic electron. This natural collimation is one of the attractive features of this source also the spectrum associated with this process spans the whole range from the infrared to the hard X-ray regime.

Early photoabsorption experiments using synchrotron light (reviewed in detail by Codling 1973) were primarily concerned with the measurement of the total photoabsorption cross sections of noble gases in the VUV. This was usually achieved by back-filling the spectrometer with the gas, under investigation, to produce an absorbing column of atoms. This necessitated, to meet the Ultra-High Vacuum (UHV) requirements of the storage ring, the insertion of both baffles and a differential pressure stage between the spectrometer and the tangentially mounted beamline. To measure the absorption spectra of metal elements in vapour phase required much effort in the areas of furnace and heat pipe technology. Connerade (1978b) has reviewed most of the different designs. The metal vapour is generally contained in a metal, graphite or ceramic tube that withstands the high temperatures and the liquid and gaseous metals. Typical pressures range between 0.1 and 10 mbar, temperatures of up to 2400 K have been achieved. A buffer gas (eg He) or thin film windows, of well known cross section, are often used to prevent the metal atoms from escaping from the hot zone. The marriage of these technologies guaranteed the major role played by synchrotrons in photoabsorption experiments performed on neutral vapours.

Growing interest in the field of inner-shell excitation of atoms and molecules, largely stimulated by increasing numbers of synchrotron radiation facilities, led to a considerable demand for a laboratory continuum source operating in the VUV and in particular the XUV region of the spectrum. By far the most cost effective and versatile alternative is the LPP. The laser plasma XUV source is most suitable for applications requiring very high instantaneous fluxes or single, short pulse experiments. The peak brightness of a LPP source can be three orders of magnitude higher than for electron storage rings. In experiments requiring the accumulation of particularly short wavelength radiation, synchrotron facilities, being quasi-continuous, are at an advantage. However as excimer and solid-state lasers move up into the kilo pulses per second regime at energies above 100 mJ per pulse, the average power gap will be narrowed.

Very few ionic species have been studied in photoabsorption due to the formidable challenge of obtaining a sufficiently high ion density in the absorbing column, the transient nature of which requires that the generation of the ionic

absorption sample has to be synchronised with a bright backlighting continuum source. Several techniques have been developed to provide such photoabsorption data on ions in the XUV. Using two synchronised vacuum spark discharges Mehlmann (1974) and Esteva (1974) recorded the VUV and XUV absorption spectra of Be^+ and Mg^+ . The spark discharges were oriented in a mutually orthogonal configuration. One of the sources used a uranium anode to produce the backlighting continuum which was synchronised with the second anode, the tip of which was fabricated from the element under investigation. By varying the inter-discharge time delay it was shown to be possible to obtain time resolved spectra of Be and Mg ions. In another approach Cantu *et al.* (1977) employed a technique based on the idea of vapourising a finely divided metal powder compound contained in a quartz glass absorption tube using a powerful flashlamp. The flashlamp pulse was synchronised with a BRV source, which yielded the backlighting continuum. The K-shell photoabsorption spectra of neutral Li and Li^+ were recorded using this technique.

One of the most successful and widely applied methods, in terms of laser based techniques for generating an absorbing column of ions, is that of RLDI (Resonant-Laser Driven Ionization). The absorbing column is created through the interaction of a high power pulsed dye laser with a metal vapour contained in a conventional heatpipe. Lucatorto and McIlrath (1976) discovered that if the laser was tuned to the first resonance absorption line of the vapour, almost 100 % ionization could be achieved within 1.5 μs of laser initiation. The ionization mechanism has been the subject of a number of papers, for example Lucatorto and McIlrath (1980) and more recently Clark and Lucatorto (1987). In general it is believed that the resonantly excited atoms in the vapour become initially ionized either by multi-photon absorption or by collisions with other atoms. This results in a small number of free electrons being produced which become rapidly heated by super elastic collisions with excited atoms within the vapour. When these free electrons acquire sufficient energy, electron impact ionization occurs producing a cascade of seed electrons over the cycle of the laser pulse. By suitable timing of a VUV pulse with respect to the dye laser pulse the absorption spectra of various mixtures of ground state, excited and ionized atoms can be recorded. The absorption spectra of Li^+ , Li^* (even parity states) McIlrath and Lucatorto (1977), Na^+ Sugar *et al.* (1979), Ba-Ba^{2+} Lucatorto *et al.* (1981) and Ca^+ , Ca^* Sonntag *et al.* (1986) have been recorded using this method. The application of RLDI is, however, limited to those species for which reasonable vapour pressures can be achieved in heatpipes. Further, its extension to more than singly and in some cases doubly ionized species is limited by the need for pulsed dye lasers tuned to resonance lines which

rapidly move into the UV with increasing charge state. This trend is illustrated for the alkali metals in figure 1.11.

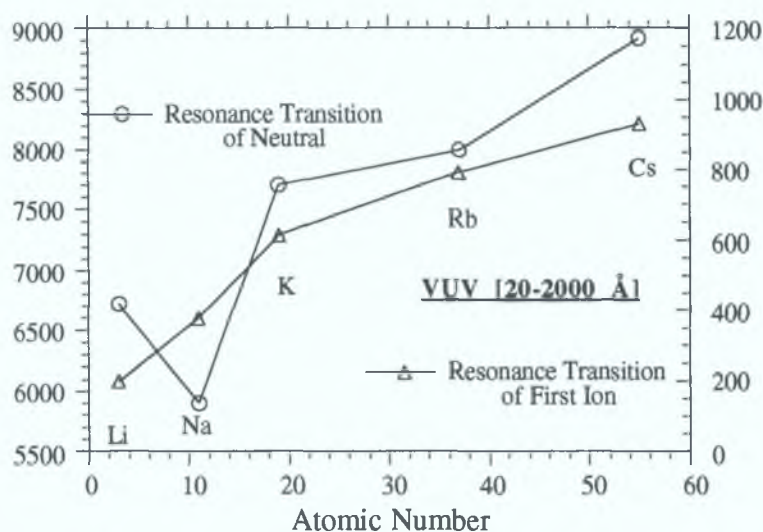


Figure 1.11. Plot showing how the wavelength of the first resonance line rapidly moves to shorter wavelength with increasing ionization for the case of the alkali metals, illustrating the limitations of RLDI.

Recently an investigation has been undertaken by Veza and Sansonetti (1992), at the National Institute of Standards and Technology, into the resonant ionization of alkali metal vapour by laser radiation tuned to the lowest $nP - mD$ atomic transition. Through a process, termed QRLPP (Quasi Resonant Laser Plasma Production), they observed excitation and subsequent ionization of Li vapour with as little as 1 mW of CW dye laser power. Ionization was found to occur only for vapour densities exceeding a critical value of $3.6 \times 10^{15} \text{ cm}^{-3}$. To determine the mechanism by which ionization takes place they measured not only ion production but also the absorption of the pump beam in the Li vapour, the visible and near infra-red spectrum of the Laser Induced Fluorescence (LIF) and the absorption of a second independently tunable probe laser in the excited Li vapour. They conclude from their measurements that the mechanism by which ionization occurs involves a combination of molecular and atomic radiative and collisional processes that can be divided into three stages. First a small seed population of Li atoms in the 2p level are created through collisional energy transfer between laser excited Li molecules and ground state atoms. Second, the seed 2p atoms are rapidly excited to 3d levels by resonant laser light. Each 3d atom can undergo an inverse pooling reaction with a ground state atom returning two new 2p

atoms to the process. This results in strong absorption of the laser power in the vapour and the development of a large steady state population of 2p and 3d atoms. Finally, 3d atoms are photoionized by absorption of a single photon from the resonant laser.

1.4.3. Evolution of The Dual Laser Plasma Technique.

A laser based technique which surmounts the limitations associated with resonant pumping of a metal vapour to produce an absorbing column of atoms, excited atoms and ions is the DLP or Dual Laser Plasma technique. This involves the generation of both absorbing species and a synchronized bright backlighting continuum source using a pair of laser plasmas formed by focusing high power pulsed lasers on suitable metal targets. As the degree of ionization in the absorbing plasma is to a certain extent controllable and is primarily only limited by the laser irradiance, the DLP technique can be used to measure photoabsorption cross sections of ions in low, medium and high stages of ionization. It can also be used to measure the photoabsorption spectra of refractory metal vapours which cannot be created in adequate density by conventional furnaces. Over the past two decades the DLP technique has evolved dramatically and has established itself to be a most unique, versatile and effective means of producing both a continuum source and an absorbing medium for inner shell photoabsorption spectroscopy of atoms and ions.

In one of the earliest experiments using the DLP technique, Carillon *et al.* (1970) measured the time resolved continuum absorption of one Al plasma by a second Al plasma, a schematic of the experimental setup is shown in figure 1.12. The spectra of Al laser plasmas are dominated by line emission in the XUV, see figure 1.8, but there also exist some narrow wavelength regions ($\leq 10 \text{ \AA}$) of continuum emission originating mainly from bremsstrahlung. This emission was used to measure relative continuum absorption at $\approx 98 \text{ \AA}$ of the second Aluminium plasma as a function of distance from the core. Their observation showed that at longer inter-plasma delays absorption decreased smoothly with distance indicating the dominance of inverse-bremsstrahlung as the absorption mechanism. At longer time delays the absorption was modulated at distances $\geq 0.3 \text{ mm}$ which was explained in terms of the photoionization contribution by ions of lower charge state formed by recombination in the outer regions of the plasma. This setup, however, was limited by the source used and unwanted emission from the fore plasma, as a result important information on the fore plasma could not be obtained.

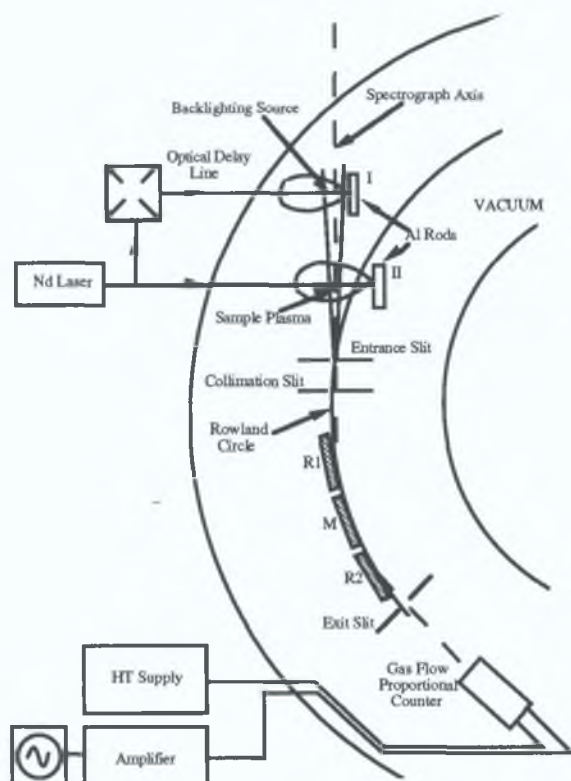


Figure 1.12. Schematic diagram of the Experimental setup by Carillon *et al.*(1970).

Realising the potential of the DLP technique and the inherent problem of the source used by Carillon and his co-workers, Carroll and Kennedy (1977) performed, for the first time, a controlled two plasma experiment with a broad continuum laser plasma backlighting source. In their experimental setup, see figure 1.13, the output of a Q-switched ruby laser was split and directed onto two targets through two

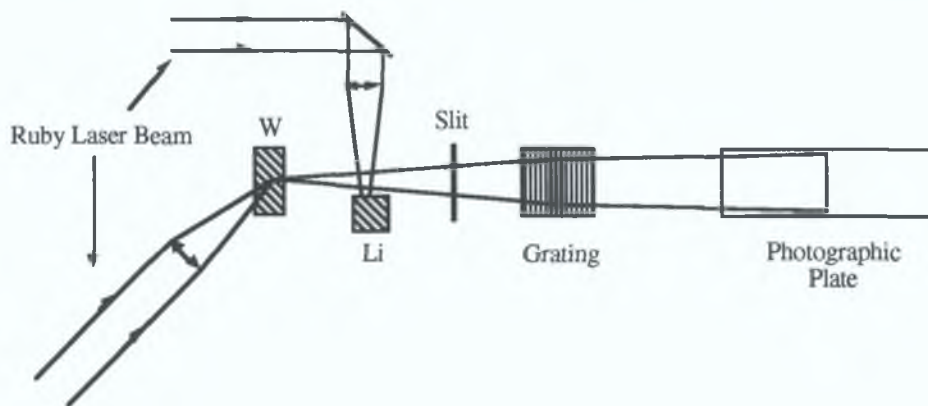


Figure 1.13. Schematic of DLP experimental setup used by Carroll and Kennedy (1977) to measure the singly and doubly core excited states of He-like Li^+ .

independent focusing geometries. One part of the laser beam was focused onto a cylindrical tungsten rod to provide the backlighting continuum while the other part was directed onto a second target, in this case lithium, oriented parallel to the optical axis of grazing incidence spectrograph. Thus the expansion of the sample plasma was in the plane of the slit of the spectrograph and enabled the recording of spatially resolved and magnified spectra. Both resonant single electron transitions, $1s^2 \rightarrow 1snp$ and double electron excitation from the ground state, $1s^2 \rightarrow 2snp$, of Li^+ were observed for the first time in photoabsorption. These measurements, in particular of the doubly excited states, represented an important extension of the helium-like series first observed in the pioneering experiments, using synchrotron light, of Madden and Codling (1965).

The direct measurement of relative photoabsorption cross sections from spectra recorded on photographic plates is a difficult process that requires both great care and patience. A major improvement to the DLP technique in this regard, was made by the group of Janitti *et al.* with the incorporation of a real time photoelectric detection system, a detailed description of which is given by Janitti *et al.* (1987). A schematic of their experimental setup is shown in figure 1.14. The two plasmas are generated by splitting a ruby laser beam (8 J in 20 ns) into two beams, which are suitably delayed (up to 150 ns) with respect to one another by following different optical paths. The continuum emission from the backlighting plasma, which is oriented 'end-on' to the spectrometer, is efficiently collected and focused by a toroidal mirror working at grazing incidence, on the entrance slit of a grazing incidence spectrometer. This dramatically reduces the number of laser shots needed to record a spectrum and also

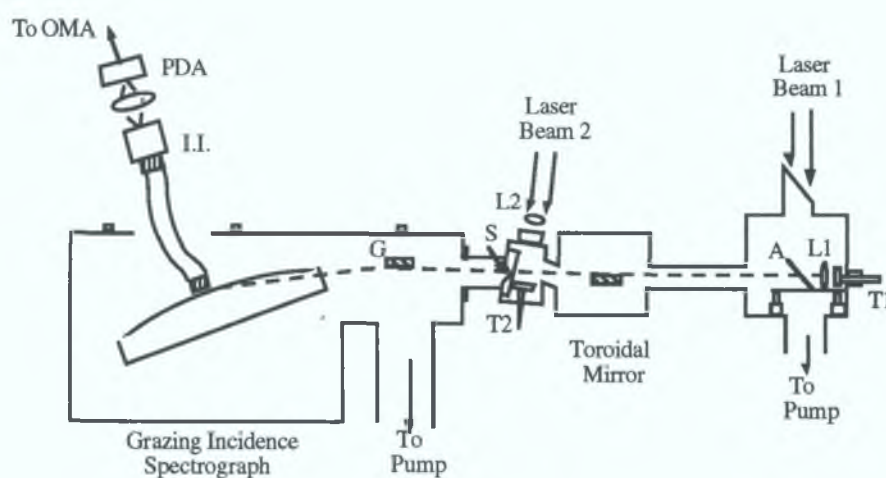


Figure 1.14. Schematic diagram of the DLP experimental setup used by Jannitti *et al.* (1987) employing a combination of toroidal optics and photoelectric detection.

helps to compensate for the astigmatism introduced by the concave grating. The spectrum is formed on a scintillator coated cylindrical face-plate matching the Rowland circle of the spectrometer. The light emitted by the scintillator is relayed from the vacuum chamber via a flexible fiber optic bundle to an image intensifier and then to a Photodiode Array (PDA) of 512 pixels, coupled with an Optical Multichannel Analyser (OMA). This detection system facilitates several types of data processing such as foreground plasma emission subtraction and deconvolution of smeared spectra due to a known system response function. Using this system Janitti *et al.* have published a series of papers on the photoabsorption spectra in the XUV of the light ions Be²⁺ (1984a), B⁺ (1986), B²⁺ - B³⁺ (1984b), Be-Be³⁺ (1987), C²⁺ - C⁴⁺ (1990) and most recently C⁺ (1993).

The application of the DLP technique to the investigation of the photoabsorption spectra of neutral species, in particular highly refractory elements was realised through the work of Costello (1986). The DLP technique used by Costello used two independent time synchronised lasers. As a result it was possible to increase the power density on the sample target and a variable time delay (0.25—100 μ s) could be introduced through sophisticated synchronisation electronics, the operation of which is outlined by Costello *et al.* (1988). It was found that by suitable adjustment of target irradiance and inter-plasma delay, strong absorption in neutral species could be observed. An investigation was undertaken into the photoabsorption spectrum of atomic thorium, Carroll and Costello (1986), which is a highly refractory metal ($m_p \approx 1750^\circ$ C, $b_p \approx 4790^\circ$ C), in the region of the 5d subvalence excitation. The elucidation of the atomic spectrum represented a stringent test of the collective models used to describe this complicated atomic system. Although the spectra of solid thorium, Cukier *et al.* (1978), and ThF₄ vapour, Connerade *et al.* (1980), were already known at that time, the sensitivity of the innershell absorption spectra to environment made the observation of the spectrum of the free atom an important goal.

Cromer *et al.* (1985), at the National Bureau of Standards, constructed a unique VUV spectrometer facility designed for high resolution photoabsorption studies of both stable and transient species, the latter being generated through the process of RLDI. The previous RLDI experimental setup used a BRV type source and photographic detection. The main disadvantages of this system were the relatively long duration of the continuum pulse (≈ 60 ns) and the difficulty in obtaining reliable photometric data from Schumann-type photographic emulsions. They replaced the BRV source with an LPP the temporal profile of which is determined essentially by the length of the pulse of the generating laser, in this case about 25 ns. To register the light transmitted through the sample cell they employed the use of a Channel Electron Multiplier Array

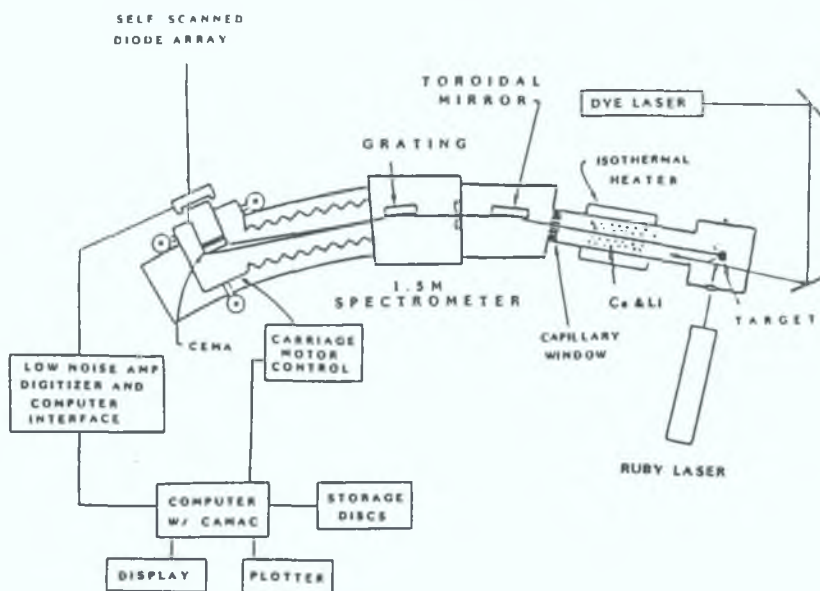


Figure 1.15. Schematic of layout of spectrometer for time resolved absorption studies of dye laser excited or ionized atoms (after Sonntag *et al.* 1986).

(CEMA), aligned tangentially to the Rowland circle of the spectrograph, coupled to a linear self-scanned diode array, figure 1.15 shows the overall layout of the apparatus. The CEMA detector was specially designed for sensitivity and high resolution and was based on detector designs used to observe the line emission spectra of tokamak plasmas. The VUV light, dispersed by the grating into its constituent wavelengths, produces photoelectrons at the front surface of the CEMA, these photoelectrons are multiplied by a factor of up to 10^4 in a microchannel plate and proximity focused onto a phosphor-coated fiber optic bundle. The cascade of electrons from the microchannel plate create visible photons through their interaction with the phosphor and are then detected on a linear diode array (Sonntag *et al.* 1986).

Cooper *et al.* (1989) used this experimental setup in conjunction with the RLDI technique to examine the VUV spectra of Mn and Mn^+ in the region of 3p subshell excitation. Previous high resolution photoabsorption measurements carried out on part of the transition metal series using a heat-pipe generated vapour column and a synchrotron source by Bruhn *et al.* (1982) revealed marked differences between the spectra of Cr and Mn. Cr was shown to be the only member of the iron-group elements with a set of well developed Rydberg series. This was thought to be due to the existence of an unpaired 4s electron in the ground state of Cr, $3p^63d^104s$, strongly inhibiting the Auger decay from the Rydberg levels and thus increasing the lifetime of the excited states. In order to investigate this hypothesis the 3p spectrum of Mn^+ , which

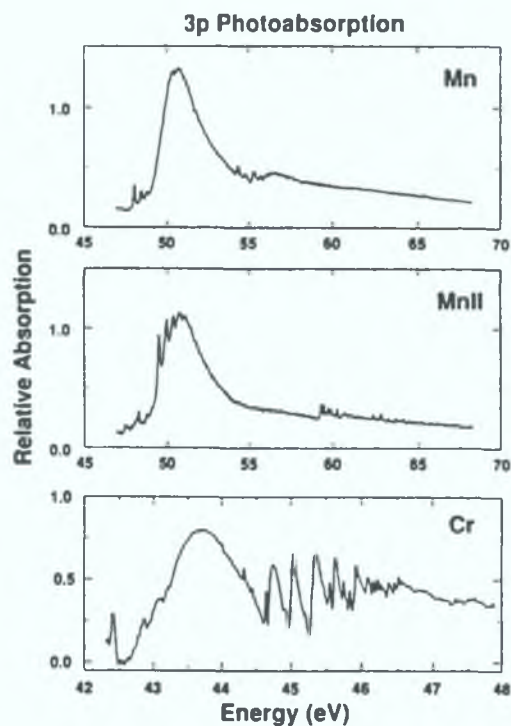


Figure 1.16. Relative photoabsorption cross sections for neutral manganese, singly ionized manganese and chromium in the region of 3p excitation (after Cooper *et al.* 1989).

is isoelectronic with Cr, needed to be measured. From the photoabsorption spectra shown in figure 1.16, it is obvious that there is very little similarity between the spectra of Mn^+ and Cr. These measurements proved that the anomalous behaviour of the 3p spectrum of Cr is due to a unique relationship between its energy levels and not to the previously supposed fact that Cr has an unpaired 4s electron.

In a further series of experiments by Costello *et al.* (1991), performed in collaboration with the group at the National Bureau of Standards, the photoabsorption spectra of Cr, Cr^+ , Mn and Mn^+ were recorded in the region of 3p excitation. This was achieved by modifying the RLDI setup to exploit the DLP technique, where the sample absorber was generated by focusing the output of a flash lamp pumped dye (R6G) laser, 1 J in 1 μs , on Cr and Mn metallic targets. This represented the first attempt to qualitatively compare results obtained through the three complementary approaches of RLDI, DLP and conventional heat-pipe techniques. Figure 1.17 shows the photoabsorption spectra of Mn and Mn^+ obtained using the DLP technique by Costello *et al.* (1991). This ionic data is in excellent agreement with the data acquired in earlier RLDI experiments; see figure 1.16. The success in separating the two ion stages of Mn by varying the inter-laser time delay stimulated experiments to record the photoabsorption spectrum of singly ionized Cr.

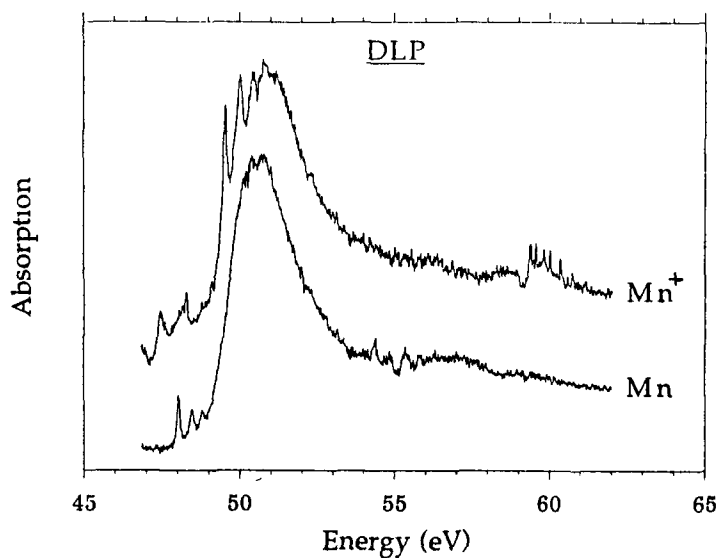


Figure 1.17 Absorption spectra of neutral and singly ionized Mn recorded using the DLP technique at the National Bureau of Standards facility by Costello *et al* (1991)

Through the experience gained and the promise shown in operating this temporary DLP setup in collaboration with the group at the Nation Bureau of Standards, it was decided by the Laser Plasma Group at Dublin City University to develop a permanent and dedicated multi laser, multi channel, high resolution VUV spectrometer system. The technical implementation of this project, which will be outlined in detail in the following chapter, has resulted in the establishment of a currently unique facility that possesses both the capability and versatility to record time resolved photoabsorption spectra of neutral, excited and ionic laser produced species.

1.5 References.

- Ballofet G., Romand J. and Vodar B., C.R. Accad. Sci., **252**, 4139, (1961).
- Bashkin S., Nucl. Instrum. Methods, **28**, 88, (1964).
- Baskin S. (ed.), "Beam-Foil Spectroscopy", Springer-Verlag, (1976).
- Bauche J., Bauche-Arnout C. and Klapisch M., Physica Scripta, **37**, 659, (1986).
- Bauche J., Bauche-Arnout C. and Klapisch M., Adv. in Atom. and Molec. Phys. **23**, 131, (1988)
- Beutler H. and Guggenheimer K., Z. Phys., **87**, 176, (1934).
- Bijkerk F. and Shevelko A. P., SPIE Vol. **1503** Eximer Lasers and Applications III, 381, (1991).
- Breton C. and Popular R., J. Opt. Soc. Am., **63**, 1225, (1973).
- Briand J. P., 15th Intl. Conf. on Xray and Inner Shell Processes, AIP Conf. Proc., 513, (1990)
- Briand J. P., de Billy L., Charles P., Desclaux J. P., Briand P., Geller R., Bliman S. and Ristori C., Z. Phys. D., **21**, S 123, (1991).
- Bridges J. M., Cromer C. L. and McIlrath T. J., App. Opt., Vol **25**, No. 13 (1986).
- Bruhn R., Schmidt E., Schröder H. and Sonntag B. F., J. Phys. B: Atm. Mol. Opt. Phys., **15**, 2807, (1982).
- Cantu A. M., Parkinson W. H., Tondello G. and Tozzi G. P., J. Opt. Soc. Am., **67**, 1030, (1977).
- Carillon A., Jaégle P. and Dhez P., Phys, Rev. Lett., **25**, 140, (1970).
- Caro R. G., Wang J. C., Young J. F. and Harris S. E., Phys. Rev. A, Vol **30**, **3**, 1407, (1984).
- Carroll, P. K. and Costello. J. T., Phys. Rev. Lett. **57**, 1581 (1986).

- Carroll P. K. and Kennedy E. T., Phys. Rev. Lett., **38**, 1068, (1977).
- Carroll, P. K. and Kennedy, E. T., Contemp. Phys., Vol. **22**, no.1, 61-96 (1981).
- Carroll, P. K., Kennedy E. T. and O'Sullivan G., Opt. Lett., **2**, 72, (1978).
- Carroll, P. K., Kennedy E. T. and O'Sullivan G., Appl. Opt., **19**, 1454 , (1980).
- Clark C. W. and Lucatorto T. B., "Giant Resonances in Atoms, Molecules and Solids", (NATO ASI series B Vol 151), Plenum, (1987).
- Codling K., Rep. Prog. Phys., **36**, 541, (1973).
- Colombant D. and Tonon G. F., Appl. Phys., **44**, 3524, (1973).
- Connerade J. P., "The Non-Rydberg Spectroscopy of Atoms", Contemp. Phys. **10**, 415, (1978a).
- Connerade J. P., Nuc. Instr. Meth., **152**, 271, (1978b).
- Connerade J. P., Pantelouris M., Baig M. A., Martin M. A. P. and Cukier M. J., J. Phys., **13**, L357, (1980).
- Connerade J. P., "Giant Resonances in Atoms, Molecules and Solids", (NATO ASI series B Vol 151), Plenum, (1987).
- Cooper J. W., Clark C. W., Cromer C. L., Lucatorto T. B., Sonntag B. F., Kennedy E. T. and Costello J. T., Phys. Rev. A., Vol. **39**, No. 11, 6074, (1989).
- Costello J. T., "XUV Emission and Absorption Spectroscopy of Laser Produced Plasmas", PhD Thesis, National University of Ireland, (1986).
- Costello J., Lynham W. G. and Carroll P. K., J. Physique. Colloq., **C1**, C1-243, Supplément au n^o3, Tome 49, (1988).
- Costello J. T., Kennedy E. T., Sonntag B. F. and Clark C. W., Phys. Rev. A., Vol. **43**, No. 3, (1991).
- Costello J. T., Mosnier J-P. and Kennedy E. T., Physica Scripta., Vol. **T34**, 77, (1991).

Crasemann B., Chen M. H. and Mark H., J. Opt. Soc. Am. B., Vol. 1, No. 2, (1984).

Cromer C. L., Bridges J. M., Roberts J. R. and Lucatorto T. B., Appl. Opt., Vol. 24, 2996, (1985).

Cukier M., Dhez P., Gauthe B., Jaégle P., Wehenkel C. and Combet-Farnoux F., J. Physique. Lett., 39, L319, (1978).

Domke M., Remmers G. and Kaindl G., Phys. Rev. Lett. 69, 1171 (1992).

Ederer D. L. Phys. Rev. Lett. 13, 760, (1964).

Ederer D. L. and Tomboulin D. H., Phys. Rev. A 133, 1525, (1964).

Edlén B., Z. Astrophys., 20, 30 (1942).

Edlén B., Rep. Prog. Phys., 26, 181 (1963).

Ehler A. W. and Weissler G. L., Appl. Phys. Lett., 8, 89, (1966).

Esteva J. M. and Mehlmann G., Astrophys. J., 193, 747, (1974).

Fawcett B. C., J. Opt. Soc. Am. B., Vol. 1, No. 2, 195, (1984).

Fawcett B. C., Gabriel A. H., Irons F. E., Peacock N. J. and Saunders P. A. H., Proc. Phys. Soc., 88, 1051, (1966).

Fischer J., Kuhne M. and Wende B., Appl. Opt. 23, 4252 (1994).

Footo P. D. and Mohler F. L., Phys. Rev, 26, 195, (1925)

Gerritsen H. C., van Brug H., Bijkerk F., and van der Wiel M. J., J. Appl. Phys., 59, (7), (1986).

Hansen J. E., Brilly J., Kennedy E. T. and O'Sullivan G., Phys. Rev. Lett. 63, 1934, (1989).

Jannitti E., Nicolosi P. and Tondello G., Physica, 124C, 139 (1984a).

Jannitti E., Nicolosi P. and Tondello G., Opt. Commun., 50, 225 (1984b).

- Jannitti E., Pinzhong F. and Tondello G., *Physica Scripta*, **33**, 434, (1986).
- Jannitti E., Nicolosi P. and Tondello G., *Physica Scripta*, **36**, 93, (1987)
- Jannitti E., Nicolosi P. and Tondello G., *Physica Scripta*, **41**, 458, (1990).
- Jannitti E., Gaye M., Mazzoni M., Nicolosi P. and Villoresi P., *Phys. Rev. A.*, **47**, 4033, (1993).
- Kay L., *Phys. Lett.*, **5**, 36, (1963).
- Kühne M. and Wende B., *Phys E:Sci. Instrum.*, Vol. **18**, (1985).
- Lucatoro T. B. and McIlrath T. J., *Phys. Rev. Lett.*, **37**, 428, (1976).
- Lucatoro T. B. and McIlrath T. J., *Appl. Opt.*, **19**, 3948 (1980).
- Lucatoro T. B., McIlrath T. J. and Mehlman G., *Appl. Opt.*, **18**, 2916, (1979)
- Lucatoro T. B., McIlrath T. J., Sugar J. and Younger S. M., *Phys. Rev. Lett.*, **47**, 16, (1981).
- Lukirskii A. P. and Zimkina T. M. *Bull. Acad. Sci. USSR Phys. Ser.* **27**, 808, (1963).
- Madden R. P. and Codling K., *Phys. Rev. Lett.*, **10**, 516, (1963).
- Madden R. P. and Codling K., *Astrophys. J.*, **141**, 364 (1965).
- Martinson I., *Rep. Prog. Phys.* **52**, 157 (1989).
- Mead W.C., Campbell E. M., Estabrook K. G., Turner R. E., Kruer W. L., Lee P. H. Y., Pruett B., Rupert V. C., Tirsell K. G., Stradling G.L., ZE F., Max C. E., and Rosen M. D., *Phys. Rev. Lett.* **47**, 1289 (1981).
- Mehlmann G. and Esteva J. M., *Astrophys. J.*, **18**, 191, (1974).
- Mehlmann G., Ederer D. L., Saloman E. B. and Cooper J. W., *J. Phys. B:Atom. Molec. Phys.*, Vol **11**, No. 22, (1978).
- Meyer M., Prescher Th., v.Raven E., Richter M., Schmidt E., Sonntag B., Wetzal H. E., *Zeitschrift für Physik D-At. Mol. and Clust.* **2**, 347 (1986)

- Mohler F. L. and Boeckner C., J. Res. Nat. Bur. Stand., **3**, 303, (1929)
- O'Sullivan G., J. Phys. B: Atm. Mol. Opt. Phys., **16**, 3291, (1983).
- O'Sullivan G., Carroll P. K., McIlrath T. J. and Ginter M. L., Appl. Opt., Vol **20**, No. 17, 3043, (1981).
- Prokhorov A. M., Konov V. I., Ursu I and Mihailescu I. N., " Laser Heating of Metals", The Adam Hilger Series on Optics and Optoelectronics, (1990).
- Rosen M. D., Phillion D. W., Rupert V. C., Mead W. C., Kruer W. L., Thompson J. J., Kornblum H. N., Slivinsky V. W., Caporaso G. J., Boyle M. J., and Tirsell K. G., Phys. Fluids **22**, 2020 (1979).
- Schmidt V., Rep. Prog. Phys., **55**, 1483, (1992).
- Sigel R., Plasma Phys. and Controlled Fusion, **29**, 1261, (1987).
- Sonntag B. F. and Zimmermann P., Rep. Prog. Phys., **55**, 911, (1992).
- Sonntag B. F., Cromer C. L., Bridges Y. M., McIlrath T. J. and Lucatorto T. B., in *Short Wavelength Coherent Radiation: Generation and Applications (Monterey, California 1986)*, AIP Conf. Proc. No. 147, edited by Attwood T. and Bokor Y. (AIP, New York, 1986), p.412.
- Sugar J., Lucatorto T. B., McIlrath T. J. and Weiss A. W., Opt. Lett., **4**, 4, (1979)
- Tragin N., Physica Scripta **37**, 72 (1988)
- Turner D. W. and Al-Jobour M. I., J. Chem. Phys., **37**, 3007, (1962).
- Veza D. and Sansonetti C. J., Z. Phys. D.-atm.,mol. and clus., **22**, 463, (1992).
- Vodar B., Astoin N., Nature, **166**, 1029, (1950).
- Vilesov F. I., Kurbatov B. L. and Terenin A. N., Dokl. Akad. Nauk SSR, **138**, 1329 and **140**, 797 (1962).
- Zimkina T. M., Fomichev V. A., Gribovskii S. A., Zhukova I. I., Sov. Phys.- Solid State, Vol. 9, No. 5, 1128, (1967)

Chapter 2
Construction, Integration and
Characterisation of the Multi-Channel,
Multi-Laser XUV Spectrometer Facility.

2.1. Introduction.

The main aim of this chapter is to describe, in some detail, the individual system components which have been integrated together to form this facility. To this end, the chapter commences with a brief overview of the general operating characteristics of the experimental setup which has been used to measure all the XUV photoabsorption spectra illustrated in the remainder of this thesis. The multi-laser capability of the present experimental system represents a marked improvement on previous DLP (Dual Laser Plasma) arrangements, increasing the available optical flux delivered to the target material under investigation. This results in a generally brighter continuum emitting backlighting plasma and a larger density of absorbing species in the primary absorbing fore plasma. As will be outlined in the following chapters, the type of laser used to generate the absorbing column determines the degree of ionization observed. The operating principals of the three types of high power pulsed lasers, ruby, Nd YAG and dye, in use at this laboratory are briefly described. In order to probe the temporal evolution of the expanding fore plasma, generated normally with the dye or ruby lasers, it is necessary to synchronise their optical pulses with that of the Nd YAG laser which generates the backlighting continuum emitting plasma. For short inter-laser time delays this can be achieved optically by increasing the optical path length of the pulse from the second laser. This is not, however, very practical if the inter-laser delays are large or if the optical pumping cycles of the lasers involved are of different lengths. For these reasons we chose to employ the use of electronic delay generating circuits.

An improved target chamber design renders the possibility of measuring the spatial, as well as temporal, dependence of the XUV absorption through the plume of the fore plasma. The increase in spectrometer speed, resulting from the efficient coupling of the XUV light into the entrance slit of the spectrometer using a toroidal mirror and the significant improvement offered by the multi-channel photoelectric detection system permits for the first time the capability to record single laser shot spectra. The last section of this chapter outlines the resolution performance and calibration of the detection system.

2.2. Implementation of Experimental System.

2.2.1. General Features of Experimental Setup.

The overall layout of the apparatus developed to perform photoabsorption studies of neutral, excited and ionic species in the XUV region of the spectrum is shown schematically in figure 2.1. This experiment is based on the DLP (Dual Laser Plasma) technique and permits the measurement of both space and time resolved spectra of laser produced plasmas.

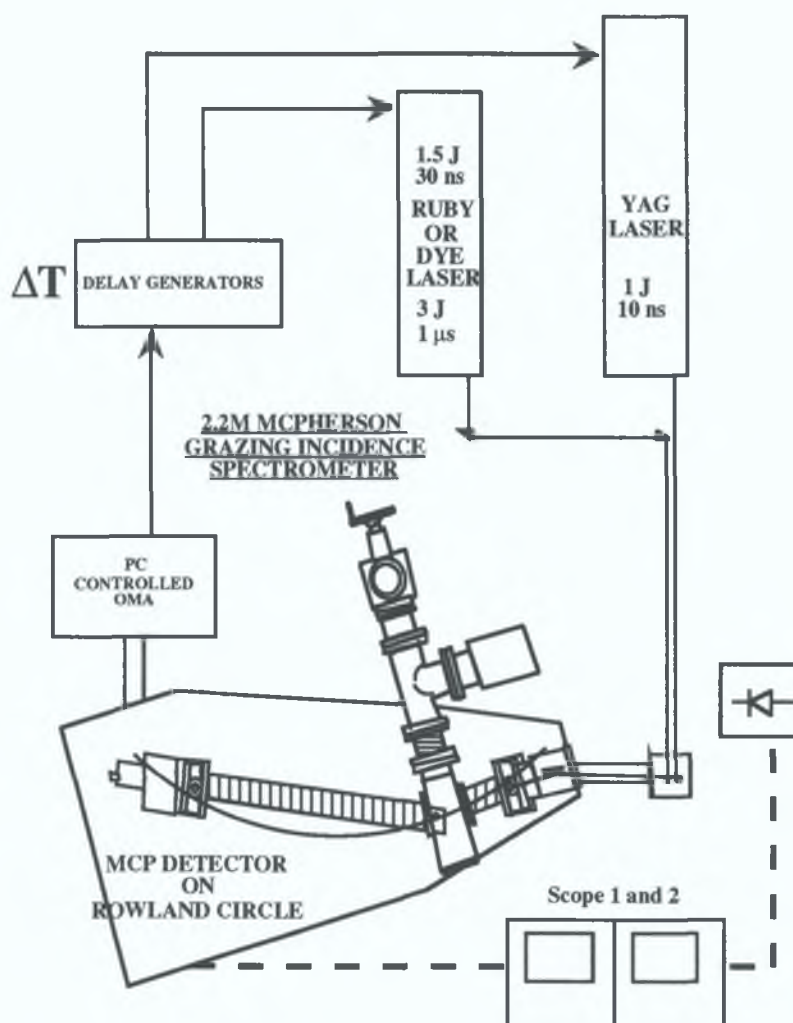


Figure 2.1 Schematic showing general features of DLP experimental setup.

As mentioned in chapter one, any photoabsorption experiment has four main elements, firstly, a source of continuum emission, secondly, a spectrometer appropriate to the spectral region of interest, thirdly, a sample cell and finally a detector to register

the light transmitted through the sample. In this particular arrangement the absorbing species is sequenced between the source and the spectrometer. The capability of this facility to perform photoabsorption studies of neutral, excited and ionic species is achieved through the inter combination of three laser systems incorporated in the setup.

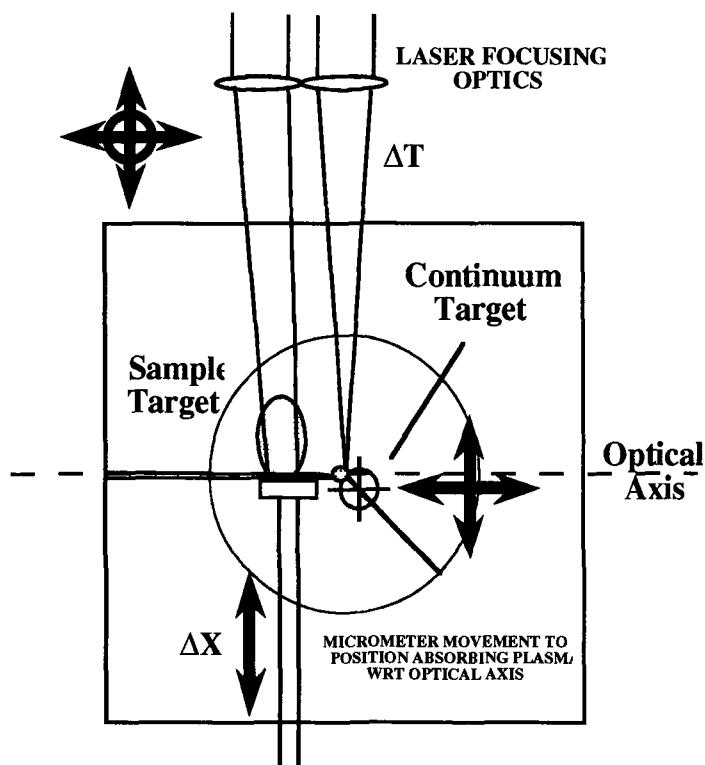


Figure 2.2 Schematic of target chamber illustrating the DLP technique

The absorbing column is produced by the ablation of spectroscopically pure targets *in vacuo* by either a flash lamp pumped dye laser ($\approx 3 \text{ J}$ in $1 \mu\text{s}$) or by a Q-switched ruby laser ($\approx 1.5 \text{ J}$ in 30 ns) focused in either point or line geometries by a spherical or cylindrical lens respectively. The use of the long pulse duration dye laser generally yields a relatively cool absorbing plasma suitable for the investigation of neutrals or low ionized species, the Q-switched ruby laser enables higher ionization stages to be studied. Discrimination of absorbing species is achieved by an appropriate combination of spatial position, temporal resolution and target irradiation. The absorber target is generally flat, the front surface of which is parallel to the optical axis of the system (see figure 2.1). This results in a transverse expansion of the plasma across the optical axis. Backlighting is provided by an XUV continuum emitting plasma created by tightly focusing the output of a synchronised Nd Yag laser ($\approx 1 \text{ J}$ in 10 ns) on a tungsten or tantalum cylindrical target. The radiation from the backlighting plasma passes through the laser generated absorbing column and is then collected by a toroidal

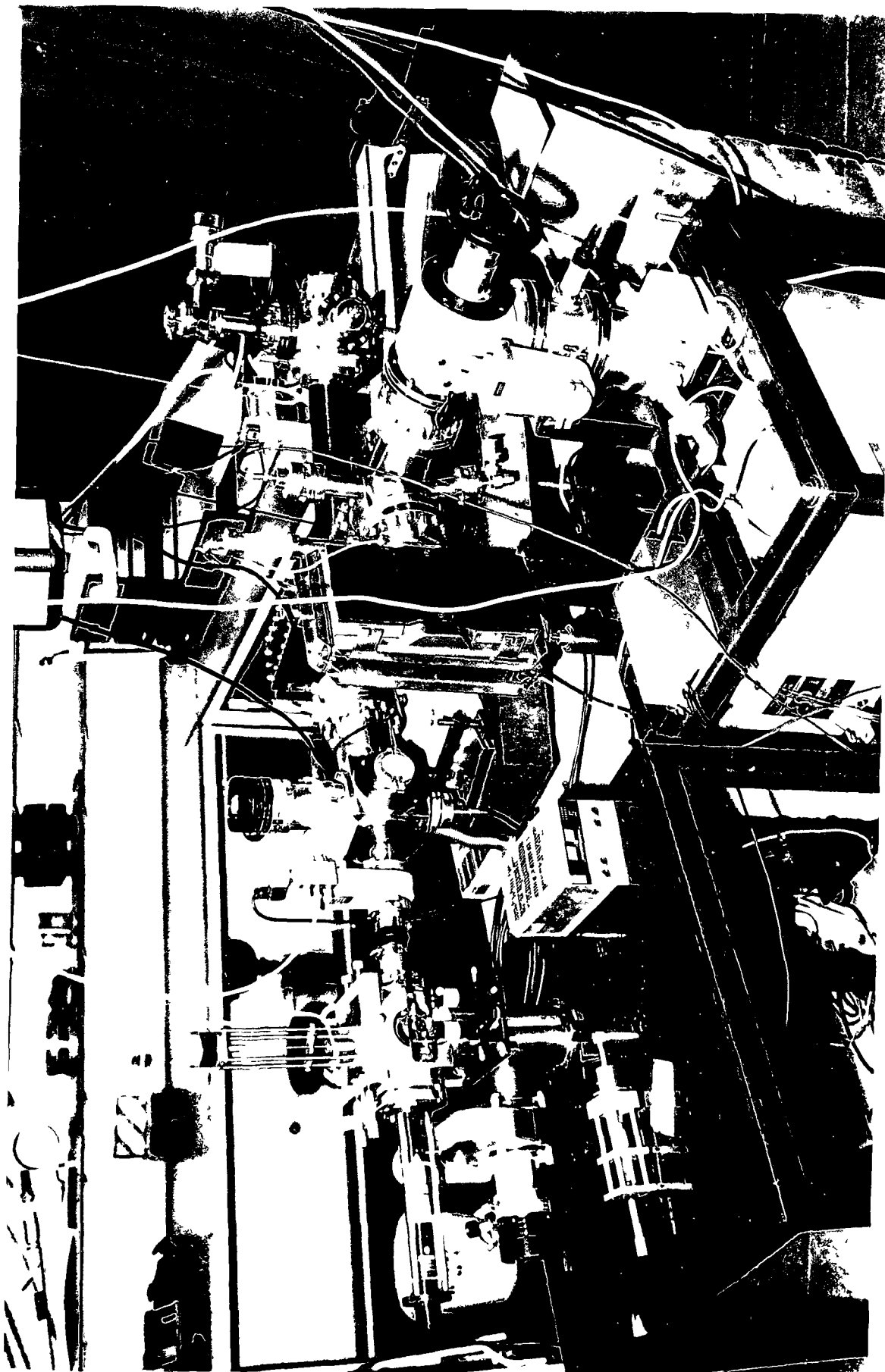


Plate 2.1 Front view of DLP spectrometer system showing the plasma target chamber, on the left , coupled to the toroidal mirror chamber and grazing incidence spectrometer

mirror which efficiently couples the light into a 2.2 metre grazing incidence spectrometer. The XUV light is dispersed into its constituent wavelengths along the Rowland circle of the spectrometer. This particular spectrometer is equipped with a Micro Channel Plate (MCP) image intensifier the output of which is proximity focused through a fibre optic face plate onto a self scanning diode array detector. After each laser shot the video signal from the detector is displayed on a digitising scope. A second fast scope, with up to 2 ns temporal resolution, is used to monitor the inter-laser time delay and any variations in relative intensity, from shot to shot, of the laser optical pulses. The synchronised video signal from the detector is digitised and stored in an Optical Multichannel Analyser (OMA) after each laser shot. If there is a jitter in the inter-laser time delay or in relative intensity the scan can be discarded by the user before accumulation takes place. The accumulated data is then down-loaded onto a PC where the spectra can be processed and stored. The operational characteristics and construction of the individual components, mechanical, optical and electronic, which together make up the facility are detailed in the following sections. Detailed mechanical drawings are included in the appendix A for further reference.

2.2.2. Description of Laser Systems.

(i) The Ruby Laser.

The ruby laser takes its place in history as the first working laser to be demonstrated. The active medium is a cylindrical crystal of synthetic ruby (Al_2O_3) doped with roughly 0.05% by weight of chromium ions (Cr^{3+}). The ends of the rod are polished flat and parallel. High standards of flatness and parallelism are demanded: the flatness over the entire end face should vary by no more than a quarter of a wavelength and both surfaces should be parallel to within a few seconds of arc. The ruby laser in use in this laboratory is a standard JK lasers model QSR2/6 system 2000, which can be operated in free running or Q-switched mode.

The laser consists of a single oscillator which produces an output of approximately 1J in 30 ns at 0.694 μm . The oscillator is optically pumped by two close coupled linear flash lamps with pulse duration 1500 μs . The ruby rod and flash lamps are placed at the respective foci of an elliptical reflector to ensure that as much light as possible is pumped into the rod. The ruby absorbs pumping energy in the blue-green region of the spectrum, the absorption of green light raises the chromium ions into a broad band of upper levels from which they relax very quickly to the upper level of the

laser transition: see figure 2.3. This is a metastable state with a 3 ms lifetime. A population inversion is established between this state and the ground state. In free running mode the output pulse occurs in a series of relaxation spikes superimposed on the fluorescent background. Q-switching is made possible through the insertion of a Pockel cell-polariser combination in the laser cavity. A high voltage (≈ 2.7 kV) is applied across the Pockel cell which causes the plane of polarisation of the light beam to be rotated. Cavity oscillations cannot take place between beams of different polarisations thus laser action is inhibited. In this way population inversion builds up far above its normal threshold value. On removal of the high voltage the plane of polarisation reverts to its original state and oscillation proceeds producing a Q-switched pulse of short duration and high peak power .

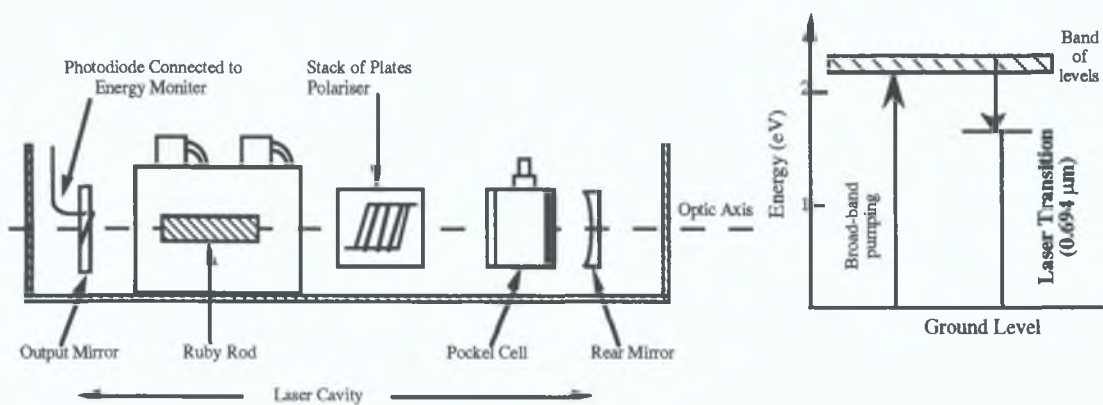


Figure 2.3. Schematic of ruby laser head and the energy level diagram associated with the optical pumping to lasing cycle.

(ii) The Nd:YAG Laser.

This type of solid state laser is now superceding the ruby as the most widely used doped-insulator laser, the host material is a crystal of yttrium-aluminium-garnate (YAG, $Y_2Al_5O_{12}$) doped with neodymium (Nd^{3+}) ions. Optical pumping raises the ions into a large number of levels around 2 eV (see figure 2.4), with non-radiative relaxation into the upper laser level. The advantage of the Nd:YAG over ruby is its lower threshold and higher gain. The implications of this are that the laser runs cooler, can be made smaller for a given energy and can be operated at relatively high repetition rates up to 50 kHz.

The Nd:YAG laser in use at this laboratory is a pulsed SL800 oscillator/amplifier system supplied by Spectron Laser Systems. It can be operated in both free running

and Q-switched mode, the mechanism of Q-switching being similar to the electro-optical shutter outlined in the description of the ruby laser. Operated in Q-switched mode the output is about 1J in 15 ns at a fundamental lasing wavelength of 1.064 μm . Figure 2.4 shows a schematic of the laser head indicating the relative positions of the main optical components.

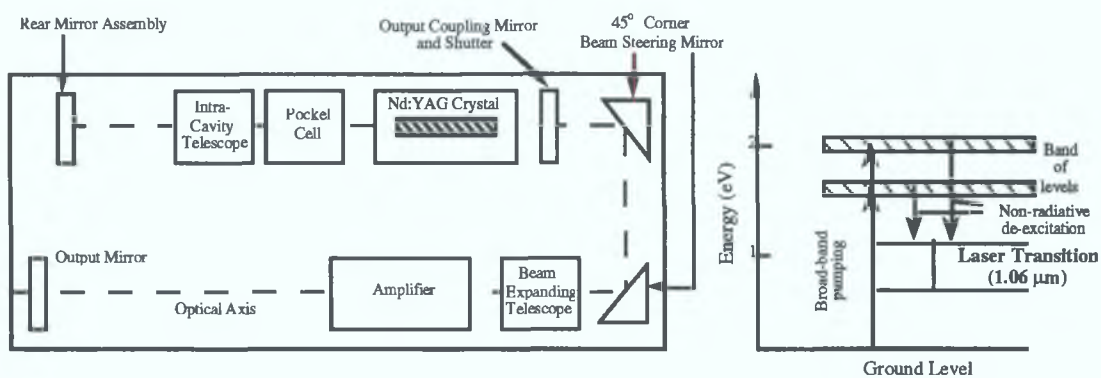


Figure 2.4. Schematic of Nd:YAG laser head and its 4 level energy architecture.

(iii) The Dye Laser.

While fixed frequency lasers have found important applications in, e.g., measurement techniques, information transmission, holography and material processing, tunable lasers are of greatest interest for atomic and molecular spectroscopy. Using different types of tunable lasers the wavelength range 320 nm to tens of μm can be covered by direct laser action, and the tunability region of an individual laser can be considerably extended using non-linear optical effects.

Laser action in organic dyes was discovered independently by Sorokin *et al.* and Schäfer *et al.* in 1966. Since then, several hundreds of dyes have been shown to have suitable properties for use as laser media. One of the most common laser dyes is Rhodamine 6G dissolved in a methanol — distilled water solution. We usually employ a solution of approximately 5×10^{-5} molar R6G dissolved in methanol + 5-10% distilled water. The general level structure of an organic dye is shown in figure 2.5. The transitions relevant for laser action occur between two lower electronic singlet states. The ground state, as well as the excited state is split into a continuous structure of smeared energy sublevels due to the interaction with the solvent. Normally the molecules are Boltzmann distributed on the lowest sublevels of the ground state. The molecules can be optically excited to the next singlet band where they relax very quickly ($\approx 10^{-12}$ s) through radiationless transitions to the lowest level of the excited

state, from where the molecules return to the sublevels of the ground state with a lifetime of about 1 ns, emitting fluorescent light. If the dye is pumped sufficiently strongly, a population inversion between the lowest sublevel of the upper excited state and the sublevels of the ground state is obtained.

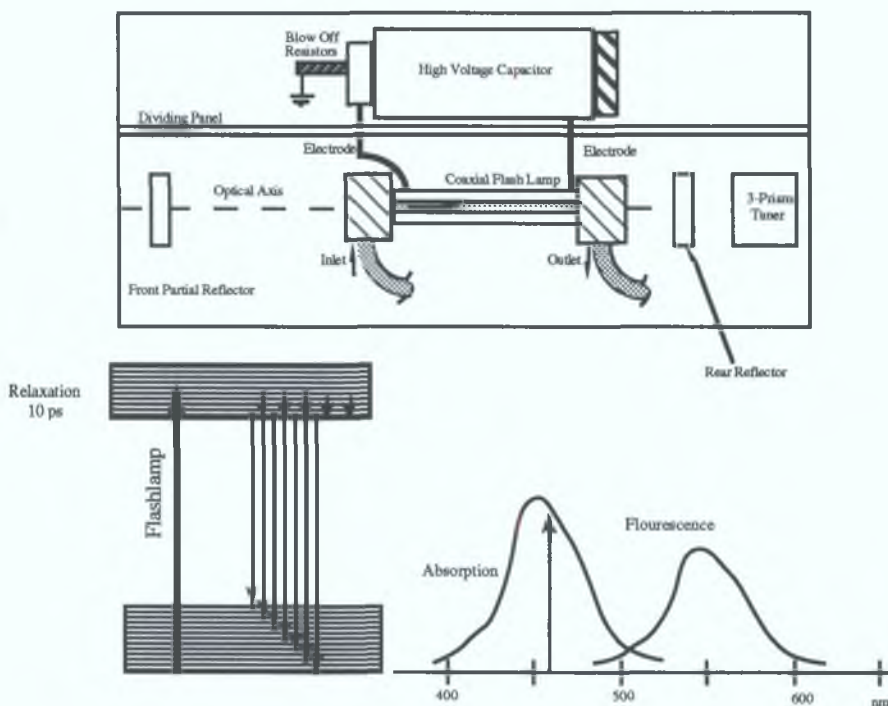


Figure 2.5. Schematic of the dye laser head, the general level structure of an organic dye in a solvent and the absorption and fluorescence bands of Rhodamine 6G.

The dye laser in use at this laboratory is a 40 kV flash lamp pumped model HVD 500A supplied by Candela Laser Corporation. The active medium is circulated around the laser head through a bubble filter to prevent any air bubbles forming inside the cavity. The dye solution is contained in a metal reservoir, capable of holding up to 20 L of solution, which has a water cooled primary heat exchanger controlling the temperature of the dye. The fluid pumping circuit has a bypass valve leading to a reusable kidney which permits the separation and recycling of the solvent from the dye solution. The laser cavity is separated from the high voltage capacitor (see figure 2.5), spark gap and blow off resistors by a metal dividing panel which reduces the risk of damage to any of the optical components if the flash lamp fails to discharge. The voltage across the capacitor is controlled by a regulator and is held off by a spark gap which is purged with a continuous flow of nitrogen gas (at approx. 5 psi) to prevent pre-firing. The output of the laser is typically 2-3 J broadband with a pulse duration of

about $0.8 \mu\text{s}$ (FWHM). Frequency-selective feedback can be achieved with this laser system by replacing the back reflector with a tunable tri-prism mount. Through prism rotation, controlled by an external micrometer drive, the laser can be continuously tuned over the fluorescence band of the dye.

2.2.3. Synchronisation of Lasers.

In order to obtain time resolved photoabsorption measurements of the sample plasma, generated by focusing the output of the dye or Q-switched ruby lasers onto a metal target, it is necessary to synchronise these two lasers with respect to the backlighting continuum generated by the Nd:YAG laser. The time interval between firing the sample laser and the Nd:YAG is introduced using a digital multi-channel delay system. The advantages associated with using an electronically generated delay over, for example, increasing the optical path length of the probe laser beam, are obvious when one considers the distance which would be travelled by a photon over a typical inter-laser delay of $1 \mu\text{s}$ ($\approx 300 \text{ m}$). Each delay generator employs the use of a 4145-2 programmable time delay card which is commercially available from Evans Electronics. These cards operate on TTL logic and have a delay range of 0-999.99 μs in 0.01 μs intervals, with a maximum jitter of $\pm 0.003 \mu\text{s}$ at each output. The required delay is dialled up on thumbwheel switches in units of 10 ns. Each delay generator is designed as a stand alone unit with an onboard power supply and is contained in a

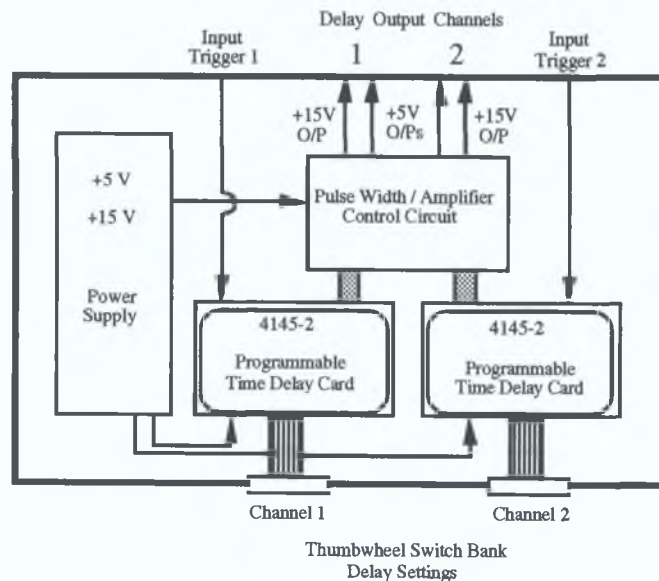


Figure 2.6. Schematic of a multi-channel digital delay generator (after Hopkins 1992).

shielded metal case to help reduce the effects of noise. In order to match the triggering requirements of the various different types of laser flash lamp circuitry each delay generator unit has two delay cards providing four possible outputs at various set voltages. A schematic of a typical delay generator unit is shown in figure 2.6.

To illustrate the timing sequence in a typical DLP experimental setup, where the ruby laser is being used to generate the sample plasma, there follows a short description of the various delays and inter-connections which must be employed to successfully synchronise both lasers and maintain optimum output. A master pulse is derived from the spectrometer detection system when it is ready to integrate the optical data. This signal is applied simultaneously to both input channels of delay generator (A). O/P (output)(1) is connected to the flash lamp trigger of the YAG and O/P (2) to

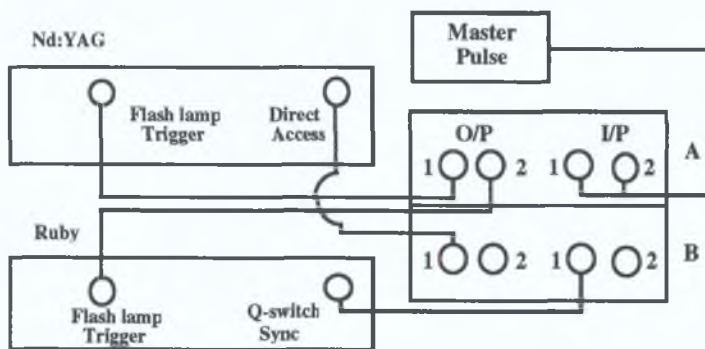


Figure 2.7. Outline of inter-connections between delay generator units and lasers.

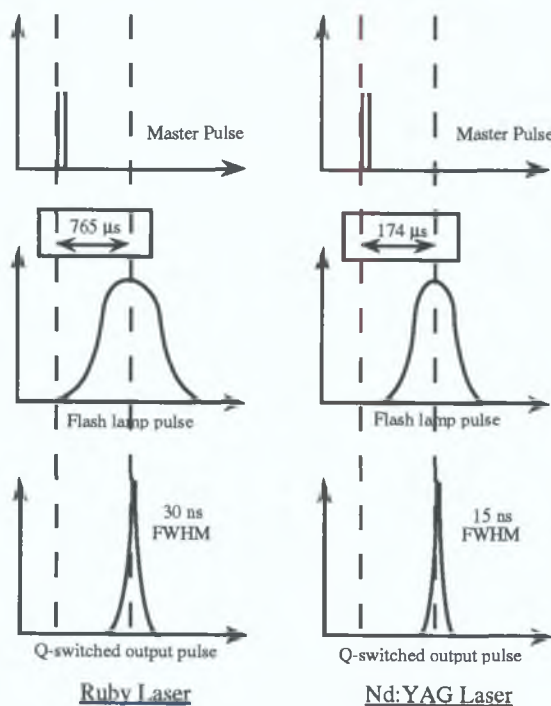


Figure 2.8. Timing diagrams for ruby and Yag lasers, where time=0 is initiated by the master pulse.

the flash lamp trigger of the ruby laser: see figure 2.7. The Q-switched pulse of the ruby arrives approx. 765 μ s after the leading edge of the master pulse. In order for the Q-switched output of the YAG to coincide with the ruby a delay of approx. 591 μ s must be added before the flash lamp is triggered since there is an inherent delay of 174 μ s between the arrival of the YAG Q-switched O/P and the master pulse: see figure 2.8. Thus one delay generating unit with two channels should be enough to control the ruby-YAG inter-laser time delay. Unfortunately, due to a problem with the high voltage Krytron switch which controls the Pockel cell of the ruby, a large jitter of up to ± 50 ns was observed between the flash lamp trigger and the Q-switched output. However, by introducing another delay line, unit (B) channel (1) figure 2.8, between the Q-switched Sync pulse of the ruby and the direct access to the Pockel cell driver of the YAG, the time delay between ruby and YAG optical pulses is thereby maintained regardless of the position of the ruby pulse with respect to the master pulse. The optical O/P of the dye laser is stable with respect to the master pulse therefore only one delay unit with two channels is required where a dye-YAG DLP experiment is being performed.

Both the ruby and YAG lasers have permanently mounted, continuous wave, HeNe alignment lasers which enable the safe and precise positioning of the high power Q-switched output without firing. A removable semiconductor diode laser mounted on the optical rail inside the cavity is used to align the output beam of the dye laser. First the burn pattern is recorded on a piece of polaroid, located some distance from the laser. Then the diode laser is inserted in the laser cavity, close to the rear reflector. The output beam of the diode is made coincident with the burn pattern and hence is aligned with respect to the output of the dye resonator. Right angled prisms, operating under the condition of total internal reflection, direct the high power laser pulses toward a pair of focusing optics located just in front of the laser plasma target chamber.

2.2.4. The Target Chamber.

The cubic target chamber used in this DLP experimental setup was machined from a solid piece of stainless steel. This material is particularly suitable for high vacuum due to its stability and extremely low out-gassing rate. Three large diameter holes, mutually perpendicular, were drilled through the cube presenting the possibility of six user ports. Each side of the cube has four M4 blind tapped holes, of a standard pitch circle diameter, for securing the flanges. The cube is machined very smooth on all six faces providing a suitable sealing surface for conventional O-ring connections. The cube is bolted on top of a 23 cm high support column, also made from stainless steel, which has been drilled out to a diameter of 7.1 cm. Two vacuum ports have been

welded onto the column, one Dn 25 for a pirani pressure gauge, and the other Dn 63 which connects a 50 L/s turbo molecular pump through a high vacuum gate valve. Thus high conductance is maintained leading to a very quick turn around time (typically less than 5 mins starting from atmospheric pressure).

Clamped around the support column is a platform for the laser focusing optics. The optical components have been omitted from figure 2.9 for clarity. The lenses used are generally of two types biconvex and cylindrical, a 10 cm focal length biconvex lens tightly focuses the YAG laser beam on a cylindrical continuum emitting target: see figure 2.2. The absorbing plasma is generated using either a biconvex or cylindrical lens, producing a point or line plasma respectively, depending on the material and ion stage of interest. Each lens is held in a spring loaded clamp mounted on an optical post. Independent linear translational stages provide movement in three perpendicular directions for each focusing optic.

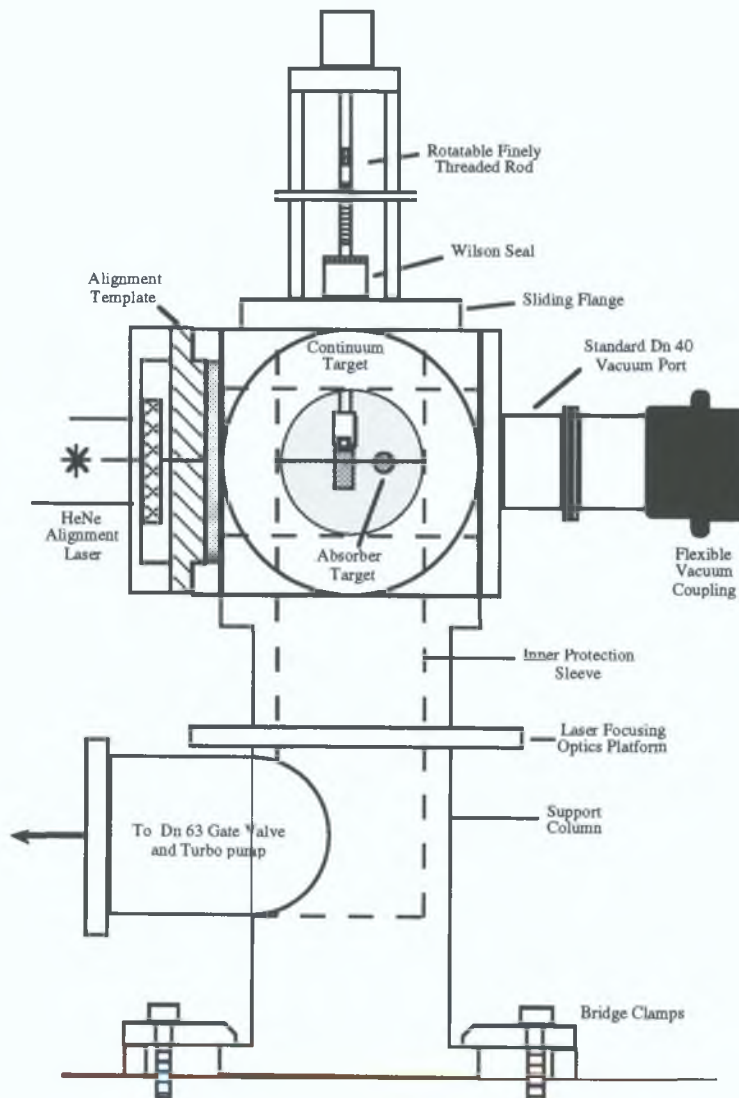


Figure 2.9. Schematic front view of DLP target chamber and support column.

The cylindrical continuum target, usually tungsten or tantalum, is held in a 0.5 cm diameter collet chuck which is screwed into the base of a rotatable vacuum feed-through. The feed-through is threaded, of fine pitch, above the Wilson seal resulting in a helical path for the focal spot on rotation of the shaft. The shaft can be rotated manually or by means of a computer controlled stepper motor. The Wilson seal is mounted on top of an o-ring sealed sliding flange which can be pushed across the top face of the cube under vacuum, enabling approximate positioning of the continuum target with respect to the optical axis. The absorber target is located approximately 15 mm downstream from the continuum target and is secured on the end of a vacuum feed-through. This feed-through is a standard sliding type which has been modified to provide micrometer movement of the absorber on and off the optical axis, yielding the possibility of measurement of space resolved photoabsorption spectra of the expanding plasma: see figure 2.2. In order to protect the inside of the cube from excessive accumulation of target debris, an inner sleeve (shown as a dashed rectangular box in figure 2.9), is inserted into the cube and support column. This has a 15 mm diameter hole along the optical axis and a 50 mm diameter hole perpendicular to the optical axis in the direction of the front window. A metal cylinder extends out from the sleeve and touches the inner surface of the window. Window contamination can occur quite quickly, depending on the type of target in the chamber and the ablation rate. The primary concern in the design of the window flanges was therefore, ease of replacement - in terms of both cost and mechanical complexity.

The base of the support column is bolted onto a solid optical table by means of bridge clamps individually fastened by M8 screws. The top of the table is made from a flat piece of steel 10 mm thick which has some M8 threaded holes to secure the bridge clamps. The advantage of these type of clamps is that the chamber—column ensemble can be bolted to the table without the exact alignment of two sets of M8 holes. The height and level of the table is adjustable, however, the use of a flexible vacuum coupling, between the exit port of the cube and the rest of the system, ensures that any slight misalignment of components will be prevented from causing a serious vacuum leak or mechanical stress at the point of connection.

2.2.5 The Toroidal Mirror Chamber.

The target chamber is separated from the toroidal mirror chamber by a pneumatically operated Dn 40 gate valve. The use of this gate valve enables the target chamber to be independently vented and ensures a quick turn around time between target changes. Also, because the valve is AC mains voltage activated i.e. mains on —

valve open, in the event of a power failure while the system is operational, the valve will close automatically before the turbo molecular pumping systems start to de-accelerate appreciably. This reduces the risk of a pressure burst damaging the detector which must be maintained in a UHV (Ultra High Vacuum) environment.

While the system is running there is a pressure gradient ($10^{-5} \rightarrow 10^{-7}$ mbar) between the source and detector, due mainly to the high number of o-ring seals used in construction. During plasma generation we observed a transient pressure fluctuation of between one and two orders of magnitude in the target chamber. It was then decided to install a differential pressure barrier between the source and the toroidal mirror to prevent pressure equalisation from occurring over the entire system : see figure 2.10.

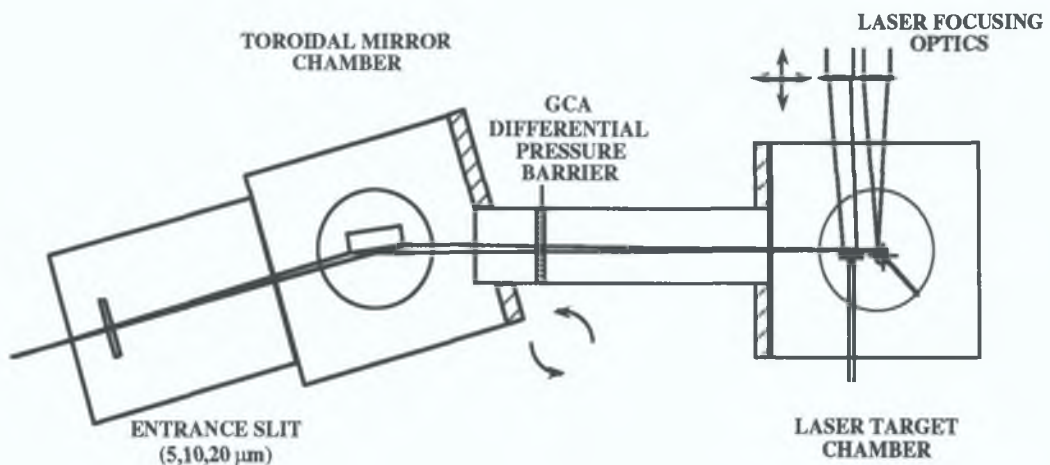


Figure 2.10. Schematic view from above, showing relative position of differential pressure barrier with respect to target and toroidal mirror chambers.

Traditional techniques for separating different pressure regions while transmitting VUV radiation have included thin-film windows and differentially pumped slits. As windows, thin-films have several drawbacks:

- (i) capable of withstanding only a small pressure differential ≈ 10 mbar at most ;
- (ii) limited spectral transmission window ;
- (iii) vulnerable to contamination and corrosion ;
- (iv) easily destroyed.

Differentially pumped slits have the main disadvantage of only providing a small spatial aperture, reducing, for example the available input photon flux into a spectrometer. The use of GCAs (Glass Capillary Array) has been shown to provide a superior alternative. These devices have become commercially available at reasonable cost due to the advances made in the manufacturing of micro channel plate intensifiers. GCAs

consist of glass capillaries of very small diameters (pore sizes from 10 to 50 μm are available), tightly packed in arrays giving large spatial apertures. Soda lime glass is used as the basic standard matrix material due to its mechanical and chemical stability. GCAs are manufactured to give an open area of 50% or greater. Lucatorto *et al.* (1979) describe a mathematical procedure for determining the light transmission and gas flow characteristics (in both molecular and viscous flow regimes), which are both largely dependent on the diameter to length ratio (L/D) of such devices.

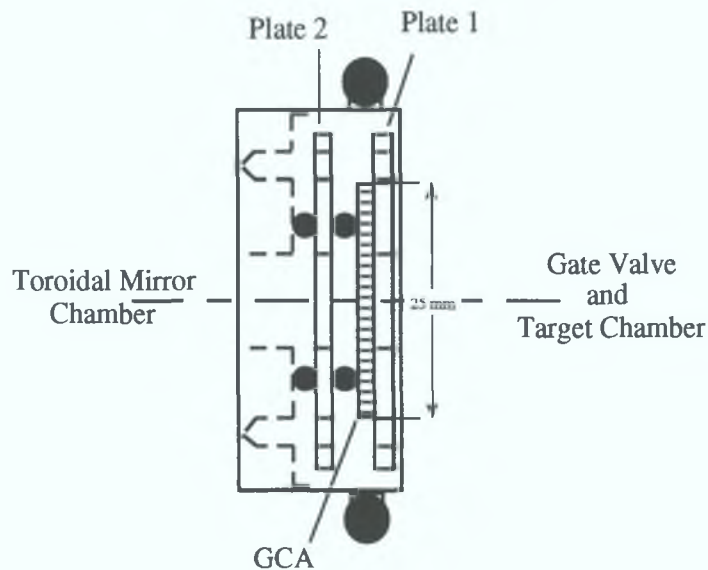


Figure 2.11. O-ring sealed flange for mounting the GCA on a standard Dn 40 vacuum port.

The GCA used in this system has been manufactured by the Galileo Electro-Optics Corporation, has a diameter of 25 mm, pore size 50 μm and a thickness of 2 mm ($\Rightarrow L/D=40$). It is mounted inside a standard Dn 40 vacuum port between the pneumatically operated gate valve and the toroidal mirror chamber. The coupling flange design consists of three main components, excluding the GCA itself. There are two circular plates and a recessed open cylinder which has three tapped holes, at 120° to one another, on the low vacuum side to attach the two plates: see figure 2.11. Each plate has a 10 mm hole in the centre allowing light to pass along the optical axis of the system. Plate 1 is bolted to plate 2 compressing an o-ring between the GCA and plate 2, thus simultaneously separating the two pressure zones and safely sandwiching the array. In addition, plate 2 has three levelling screws which permits some degree of rotational adjustment of the GCA with respect to the optical axis, without mechanically stressing the glass matrix. Alignment is achieved by monitoring the back reflection of the HeNe alignment laser mounted on the target chamber: see figure 2.8.

The toroidal mirror chamber acts as the interface between the light generating part of the system and the spectrometer. The entire chamber, which consists of a cube joined on the end of a cylinder was fashioned from a single solid piece of stainless steel. The centre has been bored out to a diameter of 90 mm along the optical axis and two holes, diameter 71 mm, have been bored perpendicular to the optical axis, providing access to five user ports. It has its own independent turbo molecular pumping system which maintains a pressure of approximately 1×10^{-6} mbar. The chamber is coupled to the entrance slit assembly of the spectrometer via a rotatable collar flange which is of conflat type construction. The entire unit weighs about 6 kg and applies a considerable moment of force to the slit housing. To counteract this force an adjustable support with vibration isolation was designed to fit between the granite base of the spectrometer and the underneath of the cylindrical part of the chamber.

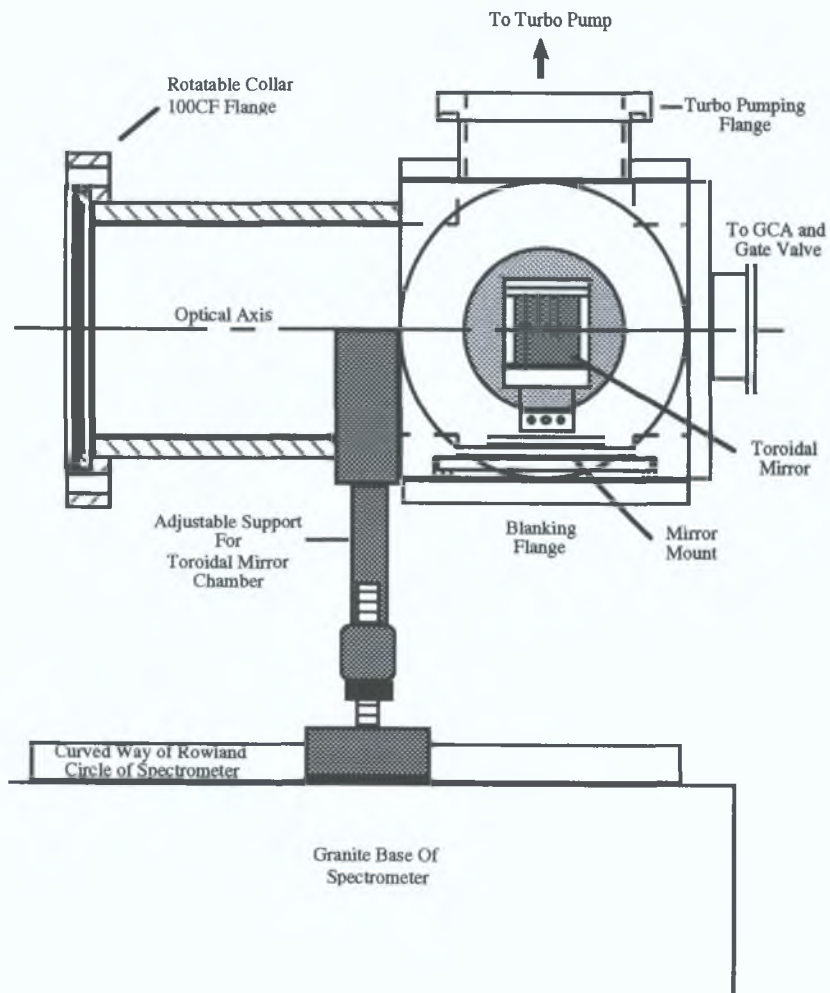


Figure 2.12. Side view of toroidal mirror chamber which is located between the GCA and the entrance slit assembly of the spectrometer.

Located inside the cubic part of the chamber is the toroidal mirror and its associated mount. From figure 2.12 it can be seen that the base plate of the mirror mount is fixed metal to metal above an o-ring sealed flange. This prevents any drift in alignment between venting and pumping cycles. The base has three layers, one fixing layer, a centering layer and a rotatable plate which can be incremented in 1° steps. Attached to the rotating plate is a micrometer stage which provides translational on-axis adjustment of the mirror. The mirror itself is secured by two jaw clamps onto an Oriel® minimount which has independent angular adjustment in two planes around the axis of the mirror. This movement is accomplished by two ultrafine thread (80 threads per inch) thumbnuts in a stable kinematic support structure. The assembled mount, minus the mirror, was baked at 200°C for 72 hours to reduce the outgassing rate of the non-high vacuum elements bringing the ultimate pressure down to an acceptable level.

In order to facilitate the initial process of instrument alignment three templates were designed which defined the optical axis of the compound optical system. Templates 2 and 3, shown in figure 2.13 bolt onto to opposite faces of the plasma target chamber. These templates have 0.5 mm holes drilled through their centres and guide the HeNe alignment laser through the centre of the cube. The template on

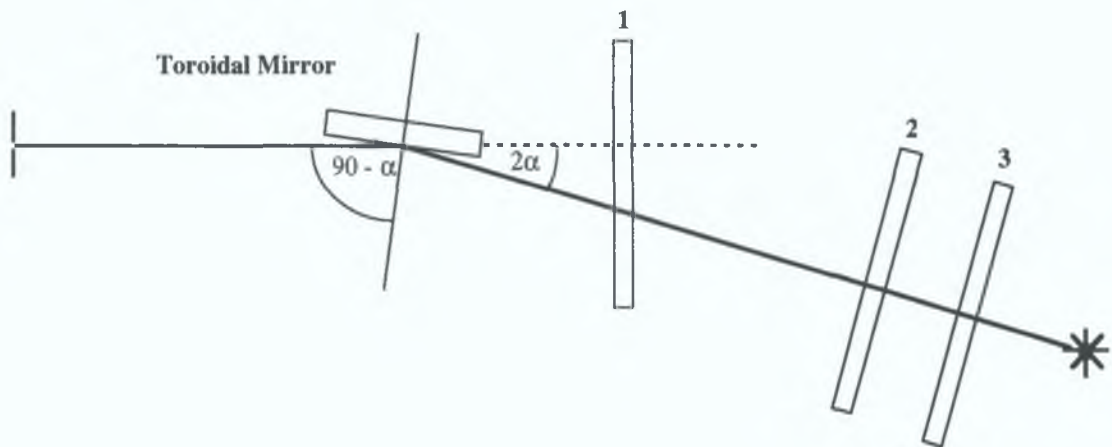


Figure 2.13. Schematic drawing illustrating positions of templates in the initial alignment process.

the toroidal mirror chamber, 1, has two alignment holes, both 0.5 mm in diameter. One passes through the centre of the template and the other defines a ray that emanates from the centre of the toroidal mirror cube at 16° , or 2α where α is the grazing angle, to the straight through ray (indicated as a dashed line in figure 2.13). The templates on the target chamber, when aligned with template 1 ensure that the target chamber is at the right height and orientation with respect to the toroidal mirror. The toroidal mirror was inserted in the mount and rotated 8° with respect to the optical axis of the spectrometer

and fixed in position. The reflected image of the HeNe alignment laser on the entrance slit was adjusted into position by small movements of the adjustment screws on the mirror mount until the transmitted intensity of the diffraction pattern was maximised. The final alignment was retro checked by back projection using a semiconductor laser diode from the spectrometer side of the entrance slit. This alignment procedure proved more than adequate as it is possible to make fine adjustments to the position of the plasma light source by simply moving the target holder *in situ* or by traversing the focusing optics to move the focal spot of the laser across the surface of the cylindrical target.

2.2.6. Optical Characteristics of Toroidal Mirror.

In the region of the XUV, spectroscopic instruments generally employ the use of a spherical, or concave grating, as dispersing, collecting and focusing element. One of the most popular concave grating configurations is that of the Rowland circle mounting. Prof. H. A. Rowland, in 1882, discovered that if a concave grating is placed tangentially to a circle of a diameter equal to the radius of curvature of the grating such that the grating centre lies on the circumference, the spectrum of an illuminated point lying on the circle will be focused on this circle. The optical properties of such gratings have been extensively studied in detail by Beutler (1945) and Namioka (1959). At wavelengths below 300 Å, the reflectivity at near-normal incidence drops to such low values that it becomes necessary to use the grating at grazing incidence in order to obtain acceptable values for the efficiency.

The major aberration of a concave mirror is astigmatism, and this imperfection is inherited by the concave diffraction grating. Astigmatism results in a point on the entrance slit being imaged into a vertical line; that is focusing is achieved only in the horizontal, or meridional plane. In this respect a concave grating working at grazing incidence resembles a cylindrical lens whose axis is parallel to the grooves. The length of the astigmatic image, z , is given by the expression (Samson 1967),

$$z = l \left[\cos \beta / \cos \alpha \right] + L \left[\sin^2 \beta + \sin \alpha \tan \alpha \cos \beta \right] \quad (2.1)$$

where α and β are the angles of incidence and diffraction, measured in the plane of dispersion respectively. The first term in the expression gives the contribution due to an entrance slit of finite vertical length l , and the second term is the astigmatism produced

by a point on the entrance slit. L represents the length of the ruled lines illuminated. Equation 2.1 illustrates that, for values of α and β typical of the XUV region ($80\text{-}89^\circ$) there is little or no focusing in the sagittal plane of the grating. This leads to reduced illumination along the Rowland circle, which results in a considerable decrease in speed, and loss of spatial resolution at the source. Fortunately the focusing properties of toroidal optics can be used to help resolve these problems.

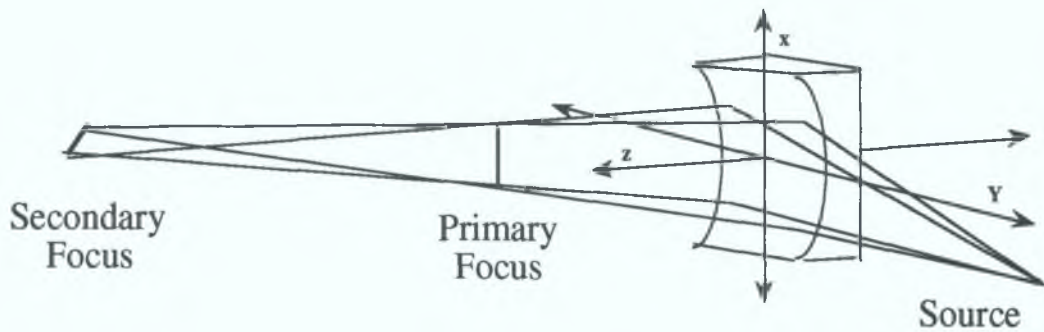


Figure 2.14. Schematic of focusing characteristics of a toroidal mirror, indicating the positions of the primary and secondary foci.

The surface of a torus has two distinct radii of curvature, R (major radius) and r (minor radius), in the Y and X planes respectively: see figure 2.14. A section of the inner surface of the torus replicated on a glass substrate and metallicly coated (in our case gold) produces a concave toroidal mirror. The vertical and horizontal focusing properties, i.e. the relative positions of the primary and secondary foci, of the toroidal mirror can be independently controlled by variation of the two radii and the angle of incidence, ϕ , that the source exacts with the mirror normal (Hopkins 1992).

From the complete analysis, by Beutler and Namioka, of the properties of a concave grating, it was shown that the grating should be illuminated with converging light in the sagittal plane in order to obtain stigmatic focusing at the diffracted image. This can be achieved by using a toroidal mirror in front of the spectrometer between the light source and the entrance slit. The resulting compound optical system is stigmatic at one wavelength only, determined by the position of the virtual source for the grating, i.e. the position of the secondary focus of the toroidal mirror. Because, in this particular case, the spectrometer has an image intensifier detection system, it was decided that the mirror should be designed such that the resulting line lengths along the Rowland circle would be uniform as a function of wavelength. The use of a stigmatic imaging system would otherwise produce a 'hot spot' on the Rowland circle leading to a possible situation where the detector could be saturated.

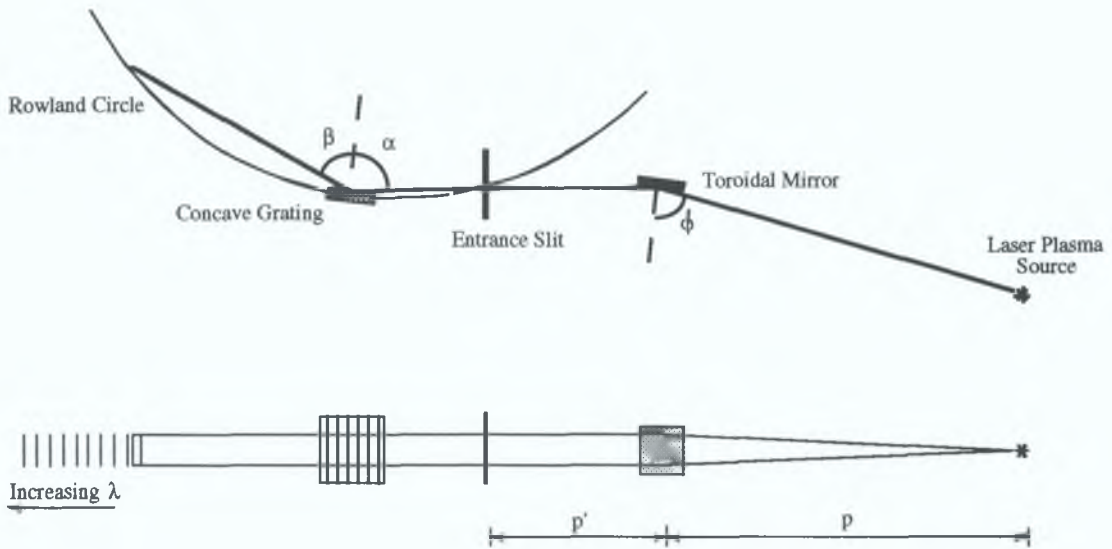


Figure 2.15. Illustration showing compound optical system of toroidal mirror and concave grating of grazing incidence spectrometer.

$$[p]^{-1} + [p']^{-1} = 2 [R \cos \phi]^{-1} \quad (2.2)$$

and

$$[p]^{-1} + [p'']^{-1} = 2 [\cos \phi] [r]^{-1} \quad (2.3)$$

Equations 2.2 and 2.3 describe the inter-dependence of the various optical parameters, where ϕ is the angle of incidence, p source to mirror distance, p' mirror to entrance slit distance and p'' is the mirror to secondary image distance: see figure 2.15. The values of the major, R , and minor, r , radii of curvature control the positions of the primary and secondary images respectively. Table 2.1 summarises the final optical parameters of the toroidal mirror used in this experimental setup. The source distance, p , was fixed at suitable value such that the blow off during laser plasma generation did not result in mirror contamination. The primary focal distance, p' , was optimised by ray tracing with various values of R (major radius) substituted into a system containing reasonable estimates for all parameters. The final value chosen was a trade-off between lengthening the image and admitting more light into the system. As mentioned above, the secondary image was formed at infinity, thus the value of the minor radius of curvature, r , was derived from equation 2.3

Source Distance p	400 mm	Primary Focal Length p'	230 mm
Incident Angle ϕ	82°	Secondary Focal Length p''	∞
Major Radius R	2099 mm	Minor Radius r	111.34 mm

Table 2.1. Summary of optical parameters of toroidal mirror

2.2.7. Grazing Incidence Spectrometer.

As mentioned in the previous section, when working at wavelengths corresponding to the soft x-ray region of the spectrum it becomes necessary to operate reflection gratings at grazing incidence due to the poor reflectivity of most optical surfaces at such short wavelengths. The instrument used throughout this work is a McPherson model 247M8, 2.217 m grazing incidence VUV monochromator and conforms to a Rowland circle mounting for concave gratings. The complete optical system, stainless steel ways, grating chamber, entrance slit assembly and detector chamber are mounted on a granite base plate. This plate provides a dimensionally stable base for the optics, and has the added advantage of providing excellent damping for unwanted vibration. The stainless steel curved way is fixed to the base plate and then machined to the Rowland circle radius. A machining tolerance of $\pm 4 \mu\text{m}$ is maintained along the entire operating surface of the ways.

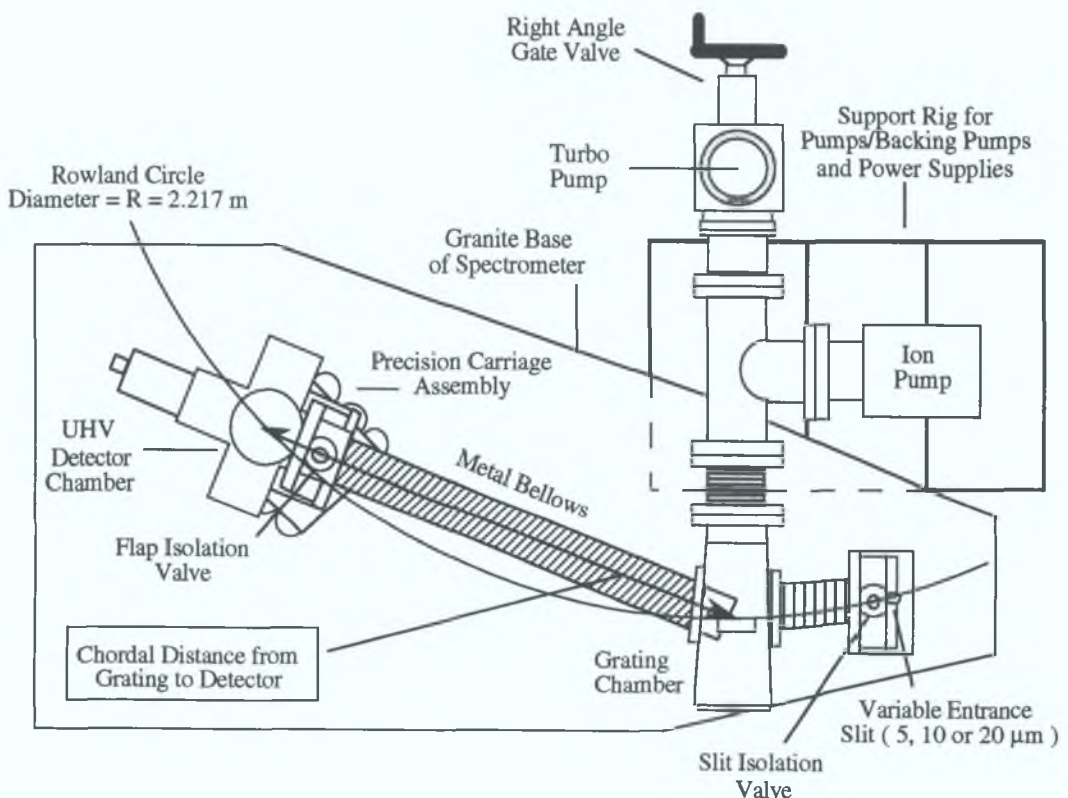


Figure 2.16. Planar view of grazing incidence spectrometer.

The exit slit assembly has been removed and a multichannel detector chamber installed in its place. This chamber houses an MCP detector, flap isolation valve, pressure gauge ports and is attached by means of an adjustable mount to the carriage

assembly. The carriage assembly utilises a recirculating ball bearing system, assuring smooth and accurate movement over the entire tracking range. Correct angular orientation of the scanning detector assembly to the beam is maintained through all wavelengths by a straight edge bar. The bar is built in an upside down “U” configuration and houses the wavelength drive screw. A manual scanning knob and mechanical counter assembly is attached on the end of the precision drive screw and straight edge assembly. Rotation of the knob moves the multichannel detector assembly along the Rowland circle. The mechanical counter reading is in inches and indicates the chordal distance from the centre of the grating to the approximate centre of the detector array. The detector chamber can be moved across the Rowland circle, i.e. perpendicular to the point of tangent, via an adjustable translation stage. The adjustment is controlled by a micrometer and two locking screws. Loosening one screw and tightening the other screw moves the detector across the circle. The detector chamber can also be rotated about the face of the MCP which allows the user to maintain the spectrum at a specific pixel number while translating the chamber across the circle. An isolation valve is attached between the detector chamber and the metal bellows. A flap type valve is controlled by a rotatable knob on top of the unit. Rotating the knob clock-wise, approximately 25 turns, will close the valve and counter-clock-wise will open the valve. A support frame has been designed to carry cooling lines to the detector system, which clamps onto the detector chamber and protects the valve from being opened too far by limiting its vertical movement. Otherwise damage could occur to the Wilson type seal on the valve actuator shaft. A stainless steel, o-ring sealed bellows connects the detector scanning assembly and the main vacuum chamber which contains the grating.

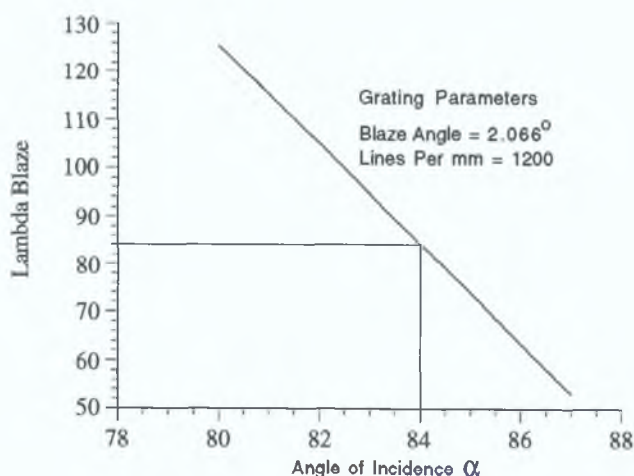


Figure 2.17. Plot of the variation of blaze wavelength (\AA) with angle of incidence for the 1200 lines per mm grating used in this set of experiments.

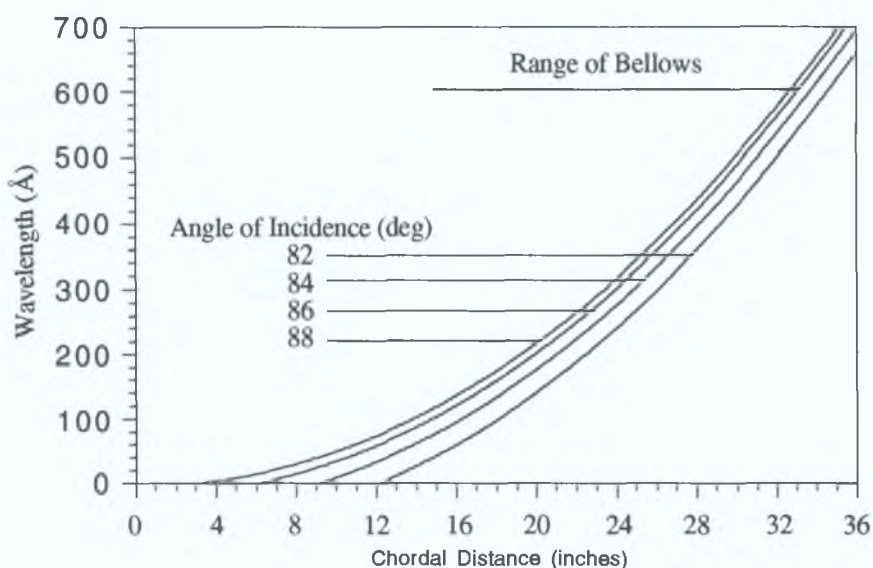


Figure 2.18. Plot of the wavelength ranges possible with a 1200 lines per mm grating at angles of grazing incidence from 82° to 88° .

The main vacuum chamber is made from stainless steel, O-ring sealed and conforms to good vacuum practice. This chamber is connected by means of short bellows to the entrance slit assembly. Although in a fixed position while in operation, this assembly is easily moved along the curved way for setting angles of incidence from 82° to 87° , with positive stops in $1/2^\circ$ increments. For this series of experiments the entrance slit was maintained on the Rowland circle at an angle of incidence of 84° to the grating normal. The grating used was concave with a gold coating, ruled at 1200 lines per mm and blazed at an angle of $2^\circ 4'$ ($\lambda_{\text{blaze}} = 84.34 \text{ \AA}$), figure 2.17 shows the dependence of λ_{blaze} on the angle of incidence α . The grating assembly is kinematically mounted and can be removed and replaced, or other grating assemblies placed in position without further alignment. The effective range of the instrument is determined by the grating being used, the length of bellows between the scanning detector chamber and the main vacuum chamber, and the angle of incidence between the slit source and the grating normal. Figure 2.18 summarises the wavelength ranges possible with the 1200 lines per mm grating at various angles of incidence. The wavelength range is inversely proportional to the number of ruled lines per mm. When substituting a grating not previously aligned, micrometers provide for fine adjustments on all axes. All motions, except focus, pivot on a ball bearing at the centre of the grating mount.

The ultimate operating pressure of the spectrometer is driven by the UHV requirements of the MCP detector. The MCP must not be operated at pressures greater

than 2×10^{-6} mbar. The vacuum pumping system is connected to the main grating chamber by means of a vibration damped bellows terminated with 100 mm (inner diameter) conflat type flanges. There are two types of vacuum pumps in use. A 240 l/s turbo molecular pump, backed by a two stage rotary, is employed to evacuate the system starting from atmospheric pressure (having vented and backfilled the instrument with dry nitrogen). When the pressure has reached approximately 1×10^{-5} mbar the ion pump is switched on. After the ion pump discharge has stabilised the turbo pumping system is isolated from the spectrometer via a right angled gate valve and switched off. The ion pump brings the ultimate pressure down in the detector chamber to approximately 2×10^{-7} mbar, well below the minimum operating requirements. The ion pump is a getter type pump and as such has no need of a backing pump, and when operated in a UHV environment it can be safely left running for years without deterioration in performance. The entire pumping system is supported on a specially designed rig, the height of which can be adjusted before mating to the main vacuum chamber. The performance characteristics of the spectrometer system as an entity, i.e. including detector response, are discussed in section 2.1.9. of this chapter, entitled 'spectrometer system performance'.

2.2.8. The Multichannel Photoelectric Detection System.

For many of the early years, integrating detectors in the form of photographic plates were the basic tool of the spectroscopist. In more recent times, in order to gain the advantages of direct electronic detection, people have turned increasingly to the use of scanning instruments with single channel outputs to electronic detectors such as photomultipliers or photodiodes. It was long recognised that array or multichannel detectors would be a powerful and welcome tool if they could be built with sufficient resolution, sensitivity and dynamic range. The operational characteristics of MCPs meet all of the fore mentioned requirements.

Originally developed as an amplification element for image intensification devices, MCPs have direct sensitivity to charged particles and energetic photons. The MCP is the result of a fortuitous convergence of technologies. Experience gained in the area of secondary emission in dynode electron multipliers in the 1960's and from earlier work on the technique of creating resistive surfaces in lead glass, together laid the foundation for the development of this device. The most important advance came through size reduction techniques achieved by glass fibre drawing techniques which form the basis of fiber optic device fabrication. A detailed description of the MCP manufacturing process is given by Wiza (1979).

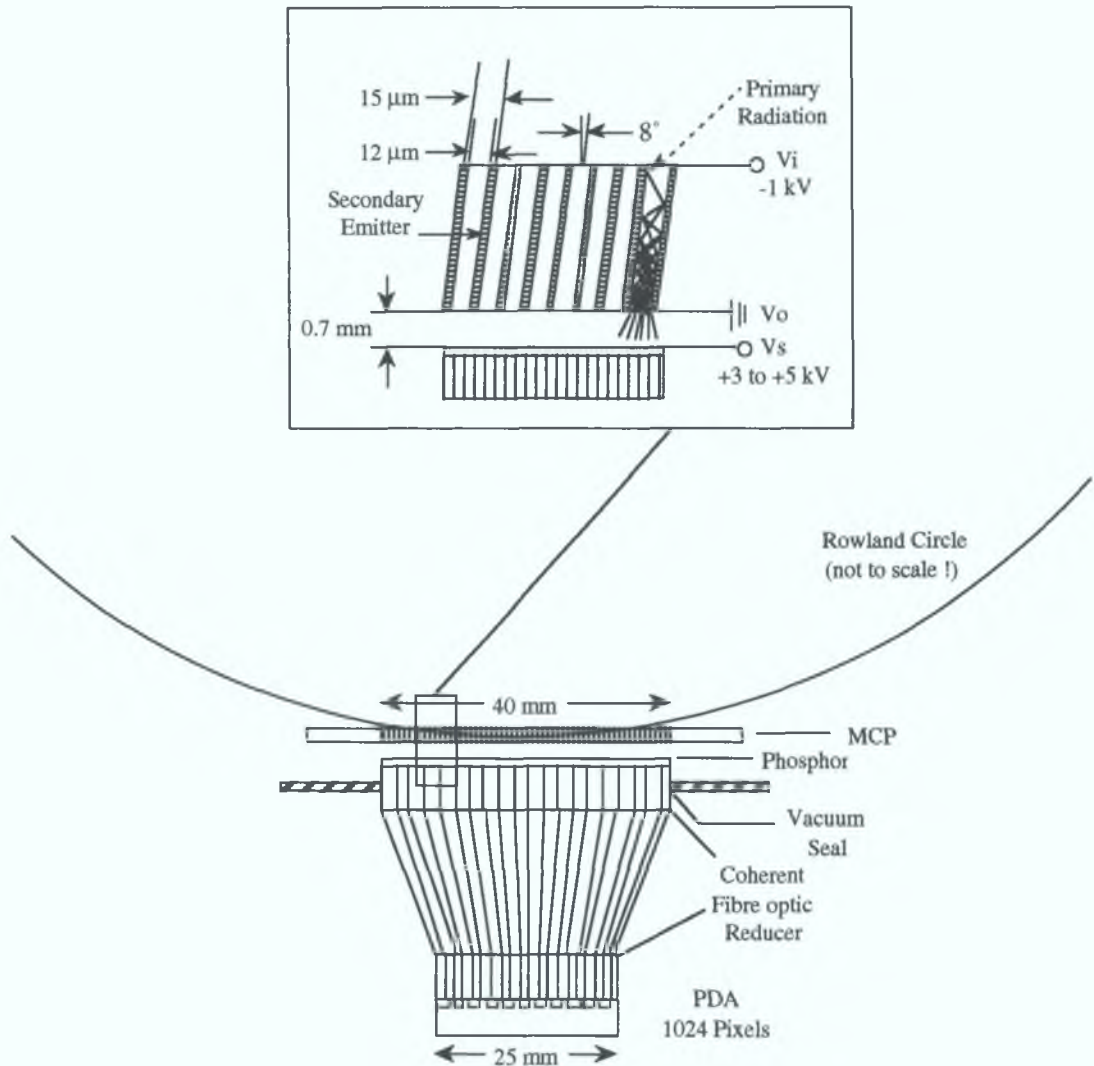


Figure 2.19. Diagram of MCP detector system installed in the grazing incidence spectrometer, the upper half of the figure is an expanded view of the signal intensification region.

An MCP can be considered as an array of miniature electron multipliers oriented parallel to one another. The device used in this apparatus was supplied by Galileo Electro-Optics Corporation and has channel diameters of $12\ \mu\text{m}$ on $15\ \mu\text{m}$ centres. The active area of the matrix is $12.5\ \text{cm}^2$ and presents approximately 40 mm of spectral coverage at the Rowland circle. The channel axes are biased at an angle of 8° to the surface normal. The QE (quantum efficiency) of a standard MCP is 10-20% for normal incidence photons with energies above 15 eV. The OAR (Open Area Ratio) of the MCP can be increased on the input side through chemical funneling. By increasing the area of the open channels, the detection efficiency will increase proportionally. Standard MCPs typically will have OARs greater than 50%; however, chemical funneling can

produce OARs of 70% or greater (Callcott *et al.* 1988). This is particularly important in the grazing incidence regime where geometrical shadowing can prevent incident photons from penetrating far into the channels. In addition, surface photocathode coatings such as CsI improve QE and extend the sensitivity to shorter wavelengths. The channel matrix is manufactured from lead glass, treated in such a way as to optimise the secondary emission characteristics of each channel and to render the walls semiconducting so as to allow charge replenishment from an external voltage source. Thus each channel can be considered to be a continuous dynode structure which acts as its own dynode resistor chain. Parallel electrical contact to each channel is provided by the deposition of a metallic coating on the front and rear surfaces of the MCP, which serve as input and output electrodes. The input electrode (V_i in figure 2.19) is biased up to -1 kV with respect to the output electrode (V_o). This helps to prevent any back-emitted electrons from leaving the array. The typical gain is about 1×10^4 , depending on MCP voltage, the amplified signal emerges as a bunch of electrons which are then accelerated across a vacuum gap (width = 0.7 mm, $E_{\text{field}} = 6 \times 10^4 \text{ Vcm}^{-1}$) by a positive potential difference of about 4 kV (Vs) and proximity focused on a phosphor coated fibre optic bundle. The fibre optic bundle is mounted on a bakable UHV flange and is tapered from 40 down to 25 mm, resulting in a demagnification factor of 1.6. Thus the visible photon signal produced by the phosphor is carried from the vacuum region to a self-scanned 1024 pixel ($25 \mu\text{m} \times 2.5 \text{ mm}$) PDA (Photo Diode Array).

The analog video signal from the PDA is controlled and read by an EG&G® Princeton Applied Research 1461 Detector Interface which forms the heart of the OMA system. The interface is a desktop size device designed to acquire data from a light detector. The detector sends an analog signal signal through a shielded cable to its controller, mounted in a slot of the interface. The controller converts this signal to digital information that can be used by the interface. In addition, the controller governs all aspects of detector operation including, scanning, triggering and temperature control. The digitised data is stored in the interface's on board memory (32K RAM) and can be accessed by an external host computer. The external computer not only accepts data, but also controls the entire data acquisition process. This control is maintained by means of a set of special commands that the microprocessor based interface interprets and executes. Parallel communication between interface and PC is achieved through an IEEE-488 GPIB (General Purpose Instrument Bus) and a GPIB connector. A menu driven software package, to control the data acquisition process, was developed in house (Shaw 1994). This software allows the user to adjust the data acquisition parameters, such as total number of scans, inter-scan delay and detector integration time in remote mode. Flexibility of data storage is also provided, for example, the user can choose between running in continuous mode and accumulating all scans in

memory, or single shot mode where after each scan (which synchronises the laser pulses) a choice is made whether or not to add the resultant data to memory. This decision to run in continuous or single shot mode is usually determined by the stability of the inter-laser time delay which is monitored by a fast optical sensor connected to a Hewlett Packard HP 545402A digitising scope with a time base resolution of up to 2 ns/div. The digital information stored in the interface unit is then downloaded through the GPIB to the PC where it is stored in standard ASCII file format for further data processing.

2.2.9. Spectrometer System Performance.

(i) Resolving Power.

The resolving power and reciprocal dispersion (see figure 2.20) of an instrument are closely related quantities. While the dispersion determines the separation of two wavelengths, the resolving power determines whether this separation can be distinguished. Each monochromatic beam itself forms a diffraction pattern, the principal maxima of which are represented by the order number m . Between such maxima, secondary maxima exist whose intensities decrease as the number of ruled lines, N , exposed to the incident radiation increases. In practice these secondary maxima are very much weaker than the principal maxima. If we use Rayleigh's criterion, two lines of equal intensity will just be resolved when the maximum of one falls on the minimum of the other. The resolving power is defined as $\lambda/\Delta\lambda = mN$ (for a plane grating), where $\Delta\lambda$ is the minimum wavelength separation which can be resolved. Mack *et al.* (1932) have shown that a slit width W gives rise to an image width on the focal curve, of a concave grating in a Rowland mount, corresponding to a wavelength interval $\Delta\lambda = Wd/R$, where d is the inter groove spacing and R is the radius of curvature of the grating. Slit widths of 10 and 20 μm , combined with a 1200 lines/mm grating, were used throughout this series of experiments which gives rise to an instrumental line width of between 0.0375 and 0.075 \AA .

In order to critically assess the performance of the instrument, in terms of its resolution, it was decided to examine the wavelength separation of some well known closely spaced lines in the emission spectrum of a laser produced aluminium plasma. Using a 1200 lines/mm grating the wavelength range of the spectrometer is approximately 80 to 500 \AA , limited by the available length of bellows.

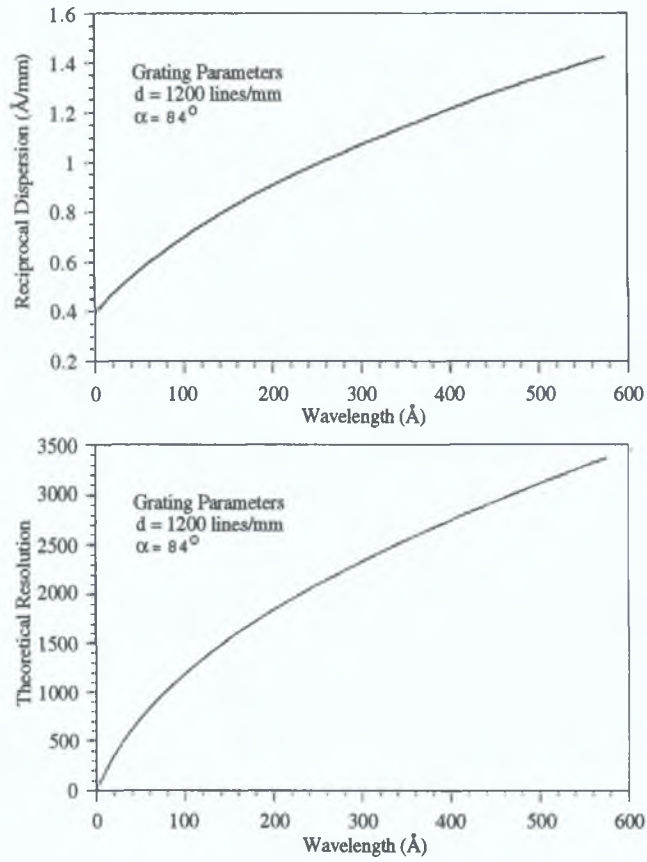


Figure 2.20. Plots of reciprocal dispersion ($\text{\AA}/\text{mm}$) and theoretical resolution ($\Delta\lambda/\lambda$) for a 1200 lines/mm grating as a function of wavelength.

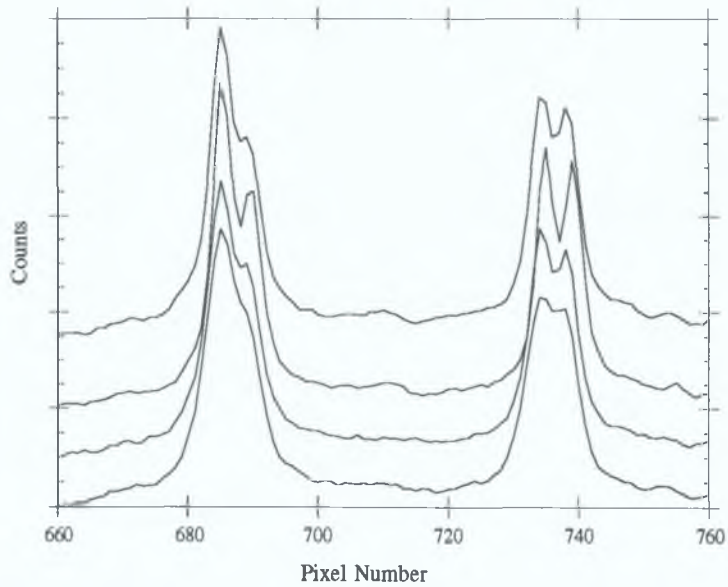


Figure 2.21. Spectrum of Al VII emission lines (10 μm entrance slit) showing dependence of resolving power with position of detector on the Rowland Circle.

At about midway through this range, approximately 260 \AA , there are some closely spaced Al VII emission lines. The plasma was generated by focusing the output of the Q-switched YAG laser on spectroscopically pure aluminium. The reciprocal dispersion at 260 \AA is 0.9925 \AA/mm for this grating/Rowland circle configuration. As mentioned in the previous section, the detector presents 40 mm of coverage at the circle, through the demagnification introduced by the fibre optic taper each pixel (25 \mu m diameter) of the PDA, corresponds to a spatial sampling width of 40 \mu m on the Rowland circle. In terms of wavelength, at 260 \AA each pixel should correspond to 0.0397 \AA . The Al VII doublet feature has a wavelength separation of 0.171 \AA and should therefore be a considerable test of the resolving power of the system.

An initial examination of the emission spectrum (the lowermost curve in figure 2.21) in the region of this doublet feature (at pixel no. 735) proved quite disappointing. A single broad peak with very little evidence of splitting was observed. Two possible sources of resolution degradation were examined. Firstly the voltage between the exit face of the MCP and the phosphor was increased to help reduce the spread of the emergent electron bunches. The divergence of the electron beam is caused by space-charge repulsion and by the random nonaxial velocity components of the electrons as they exit the channels. This resulted in a minor improvement in performance but also in an increased probability of arcing across the detector. Secondly and more fruitfully, we traversed the detector across the Rowland circle assuming that some degree of misalignment had occurred. The effect is well illustrated in figure 2.21 where the improvement in resolution is obvious as the detector is moved in 0.01 inch increments through the point of best focus.

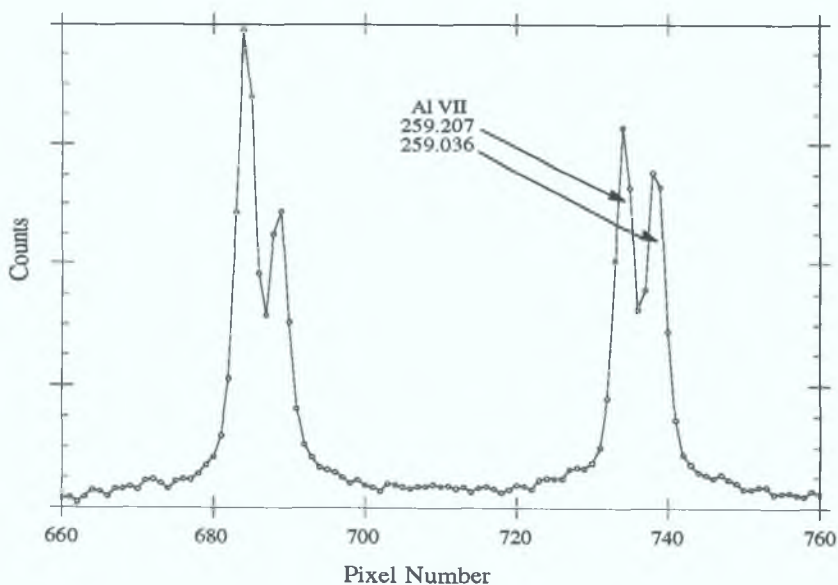


Figure 2.22 Spectrum at optimised focal position on the Rowland circle where the Al VII doublet at 260 \AA is clearly resolved.

The spectrum shown in figure 2.22 was recorded at the optimised detector position and is the result of 3 accumulated laser shots, at an MCP voltage of -0.930 kV and phosphor-MCP voltage of 4.5 kV. The doublet lines are separated by $259.207 - 259.036 = 0.171 \text{ \AA}$, while each pixel on the detector should correspond to 0.0397 \AA , therefore the number of pixels between the centres of the lines should be between 4 and 5 but closer to 4. Each data point, indicated by an open circle, in figure 2.22 corresponds to a single pixel of information and by inspection one observes that there are 5 pixels separating the features. This slight loss in resolution is most probably linked to the size of the gap between the MCP and the phosphor. The dependence of the diameter (ϕ) of the electron-bunch spot on the phosphor to the MCP-phosphor voltage V_{ph} and gap distance (s) is given to a good approximation by, $\phi = s[V_{\text{ph}}]^{-1/2}$ (Cromer *et al.* 1985). Clearly optimum resolution occurs at the smallest s compatible with maintaining a breakdown-free gap while also maintaining an adequate phosphor gain.

(ii) Calibration Procedure.

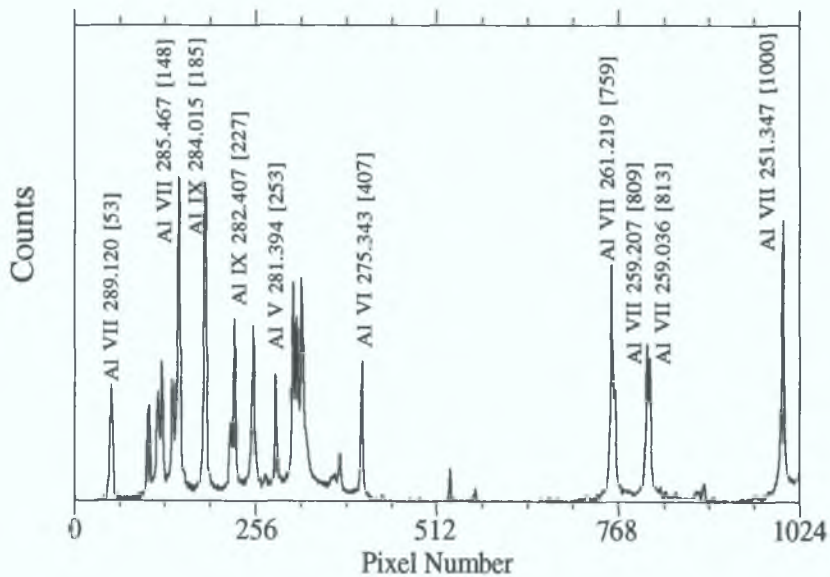


Figure 2.23. Reference emission spectrum, counts vs pixel number, of a laser produced Al plasma.

The spectral data produced by the detector is averaged and stored in an ASCII file, dimensions one column by 1024 rows. Each row entry corresponds to one pixel of information. In order to calibrate the entire spectral window of interest it is necessary to record a reference spectrum containing well known reference lines. This is normally achieved by recording the emission spectrum of a laser produced plasma. A

bipartheid target has been installed in the target chamber, which enables the reference target to be moved into position on the optical axis, without breaking the vacuum. Figure 2.23 shows an Al emission spectrum recorded at a counter reading (approximate chordal distance in inches from grating normal to the centre of detector array) of 24", accumulated over 5 laser shots. Emission lines from excited atoms four to eight times ionized are present in the spectrum. Wavelengths for the reference lines are derived from tables, mainly from Kelly (1987). The numbers shown in parenthesis are the corresponding pixel values at the centre of the reference lines.

In the situation where there happens to be very few Al reference lines available for a particular window, other targets such as silicon and aluminium oxide have proven very useful. In particular aluminium oxide, being a ceramic shows very little damage from laser ablation and yields strong ionic oxygen emission lines, the wavelengths of which are well known. The first step in converting all the pixel values into wavelengths is to ascertain the mathematical relationship between the pixel values of the known reference lines and their specific wavelengths. A second or third order polynomial least squared curve fit is applied to a plot of wavelength versus pixel number (figure 2.24).

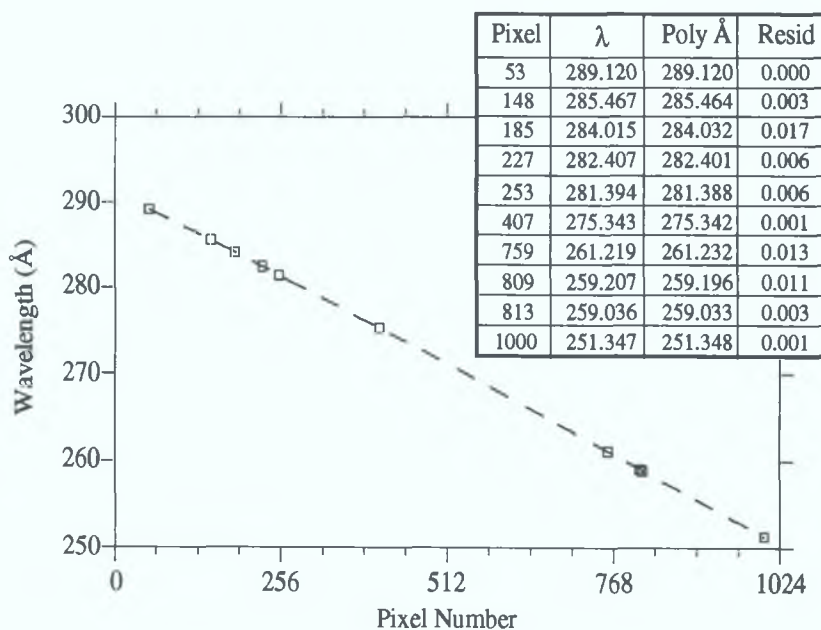


Figure 2.24. Plot showing curve fit, using a third order polynomial, of pixel number to wavelength.

The numerical coefficients of the best fit polynomial are stored in memory and this expression can be applied to the original pixel values, shown as column 'Poly Å' in figure 2.24, to determine how closely the curve fit describes the original data. In this case the residual is less than 0.017 Å which is well below the detector sampling

interval of approximately 0.04 \AA . Thus the wavelength calibration is accurate to less than one pixel. The stored polynomial expression can then be applied to the entire data set (1024 points), interpolating between the measured points, converting the complete window into wavelength or energy units. In the case where the spectrum of interest is not contained within the limits of one MCP coverage then the array is incremented, usually in one inch steps, to cover the complete spectrum. The overlapping wavelength scales are then used to merge their respective spectral information.

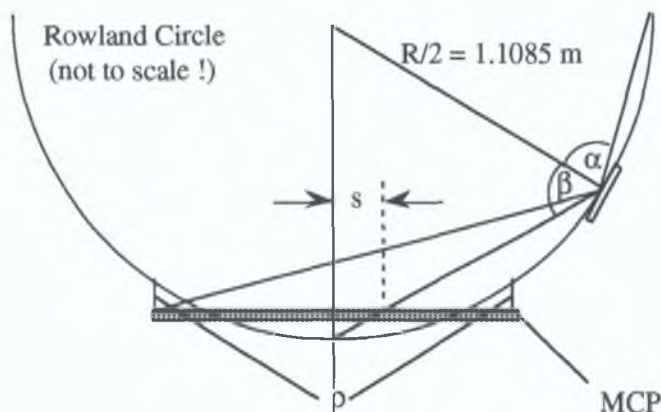


Figure 2.25. Exaggerated illustration showing the effect of placing a flat detector in the curved focal plane of a Rowland circle grazing incidence spectrometer.

This method of calibration avoids the errors involved in relying purely on knowing the chordal distance from the grating normal to the approximate centre of the array. The MCP is a flat field detector and is positioned tangentially to the curved focal plane of the concave grating. This resulting effect is shown in an exaggerated form in figure 2.25. In the two worst scenarios the detector can be oriented such that the point of tangency, or focus, is exactly in the centre, or at either extremities of the array. In the optimum position the detector is situated such that there are two points on the focal plane. The average perpendicular distance, ρ , between the MCP, centre and ends, and the Rowland circle is therefore minimised. But as can be observed from figure 2.25 the chordal distance, or equivalently the angle of diffraction β , does not correspond to the centre wavelength as measured by the detector. The wavelength defined by β , appears to the short wavelength side of the centre of the array and is shifted by a linear distance s . This shifting becomes more pronounced as β increases, $s = \rho [\tan \beta]$. The width of each pixel at the Rowland circle is 40 \mu m and ρ is approximately 10 \mu m , therefore at about $\beta = 76^\circ$ a shift of one pixel is introduced. By calibrating each window of capture individually, this effect can be accounted for.

2.3. References

Beutler H. G., J. Opt. Soc. A., **35**, 311, (1945).

Callcott T. A., Ederer D. L. and Arakawa E. T., Nucl. Inst. and Meths. in Phys. Res. A266, North-Holland, Amsterdam, 578, (1988).

Cromer C. L., Bridges J. M., Roberts J. R. and Lucatorto T. B., Appl. Opt., Vol. **24**, 2996, (1985).

Hopkins R. B., M.Sc. Thesis, Dublin City University (1992).

Lucatorto T. B., McIlrath T. J. and Roberts J. R., Opt. Soc. Am., **18**, 2505, (1979)

Mack J. E., Stehn J. R. and Edlén B., J. Opt. Soc. Am., **22**, 245, (1932).

Namioka T., J. Opt. Soc. A., **49**, 446, (1959).

Schäfer F. P., Smidt W. and Volze J., Appl. Phys. Lett., **9**, 306, (1966).

Sorokin P. P. and Lankard J. R., IBM J. Res. Dev., **10**, 306, (1966).

Shaw M., M.Sc. Thesis, Dublin City University, *in progress*, (1994).

Wiza J. L. (and references therein), Nucl. Inst. and Meths, Vol. **162**, 587, (1979).

2.4.1 General References

Chambers A., Fitch R. K. and Halliday B. S., “ Basic Vacuum Technology “, Adam Hilger, (1989).

Kelly R. L., “ Atomic and ionic spectrum lines below 2000 angstroms: Hydrogen through Krypton “, Part I (H-Cr), Part II (Mn-Kr)and Part III (Finding List), J. Physical & Chem. Ref. Data, Vol. **16**, supplement No. 1, (1987)

McPherson TM , “ Instruction Manual for 2.2 Metre Grazing Incidence Vacuum UV Monochromator “, (1992).

Michette A. G., “ Optical Systems for Soft X-rays “, Plenum Press, New York, (1986).

Samson J. A., “ Techniques of Vacuum Ultraviolet Spectroscopy “, Wiley & Sons (1967).

Svanberg S., “ Atomic and Molecular Spectroscopy “, Springer-Verlag, Berlin-Heidelberg, (1991).

Watson J., “ Optoelectronics “, Tutorial Guides in Electronic Engineering, Van Nostrand Reinhold (UK), (1988).

Chapter 3
Application of DLP Spectrometer Facility
to XUV Photoabsorption Studies

3.1 Introduction.

Following the description, in chapter two, of the functional aspects of the DLP XUV spectrometer facility this chapter describes the types of experiments which have been undertaken in order to investigate the capabilities of the combination of the DLP technique and the multi-channel photoelectric detection system. The experiments and results shown here represent just a sample of the numerous spectroscopic investigations which have been performed during the relatively short period of time that this facility has been operational. To this end, the emphasis has been placed on the various types of XUV photoabsorption experiments which are feasible with this setup. Where possible comparisons have been drawn with benchmark experiments performed using complementary techniques. Indeed, in some cases extensions of existing data from the literature have been achieved.

In any photoabsorption experiment the reproducibility of the continuum source, in terms of intensity and spectral integrity, is of the utmost importance. As a prelude to the description of the various photoabsorption studies, the characterisation of the laser produced plasma backlighting continuum source is outlined. Using this source initial photoabsorption experiments were carried out on stable species in solid and gas phase. The suitability of the DLP technique for measuring the inner shell photoabsorption spectra of neutral metal vapours, further touched upon in later chapters, is illustrated using the highly refractory elements of the first row transition metal series.

The major impact made by this technique in recent years has been through the measurement of the XUV photoabsorption spectra of free metal ions, both along isoelectronic and isonuclear sequences. Alkaline earth elements, such as calcium and barium have been the subject of numerous investigations in the light of their positions in transition regions of the Periodic Table and ease of vapourization. In particular the sensitivity of outer orbital behaviour to changes in the valence shell occupancy has stimulated the need to develop new techniques elucidating the inner shell spectra of valence excited and ionized species. These new techniques have provided an appropriate background with which the results obtained using this facility have been compared. In addition, new photoabsorption results in the energy region corresponding to 3p electron excitation, are presented for singly and doubly ionized calcium and a tentative analysis of the strongest features of the spectra, based on existing calculations and our own multi configuration Hartree-Fock calculations, is proposed.

3.2. Suitability of Experimental System for Photoabsorption Studies of Thin Films, Gases, and Free Metal Atoms in the XUV.

3.2.1. Characterisation of Backlighting Continuum Source.

In a typical DLP photoabsorption experiment a laser generated tungsten, or tantalum, plasma is used as the continuum backlighting source. Tungsten is a preferred target material due to its broad range of almost completely line free continuum emission in the XUV (25-180 eV) and its relatively low ablation rate. The continuum emission spectrum (I_0), in the absence of the absorbing column, is accumulated and averaged over a number of laser shots (usually from 10 to 20 shots, to improve the signal to noise ratio). The number of laser shots accumulated depends on the intensity of the continuum signal in the spectral region of interest. Figure 3.1 shows some typical XUV emission spectra of a Yag laser generated tungsten plasma in three different energy regions. Each spectrum has been accumulated over 20 shots using a 10 μm entrance slit and a 1200 lines/mm grating. The signature of these spectra are in very good agreement with the photoelectric measurements of Bridges *et al.* (1986).

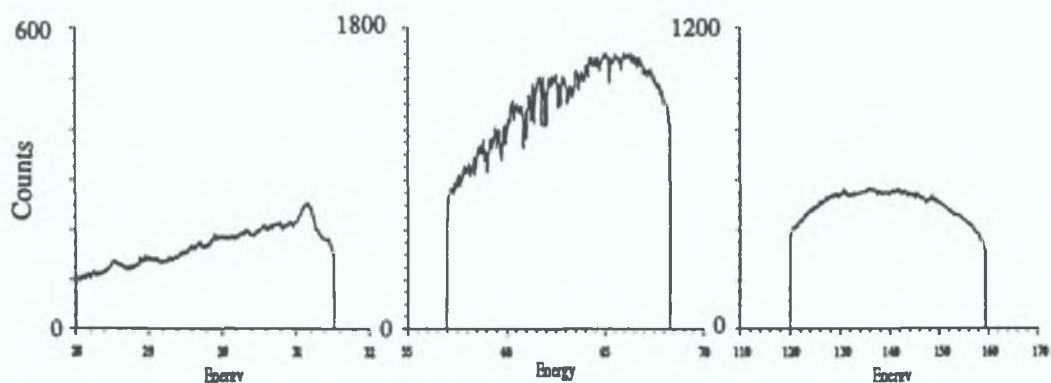


Figure 3.1. XUV emission spectra of a Yag laser generated tungsten plasma in three different photon energy regions, 28-32 eV, 55-70 eV and 120-170 eV.

The transmitted signal in the presence of an absorbing sample (I) is monitored shot to shot and also accumulated and averaged. The continuum signal is then again measured to check that there has been no fall off in intensity during the absorption measurement. The relative absorption can then be determined by calculating $\text{Ln}(I_0/I) = \sigma n l$, where σ is the total cross section, n is the number density of the species

of interest and l is the length of the absorbing column. It is extremely important therefore, that the shot to shot reproducibility of the continuum source is stable with respect to intensity. Figure 3.2 shows the ratio of two continuum spectra recorded at two different detector positions on the Rowland circle before and after a photoabsorption measurement. The lower of the two divided spectra corresponds to the

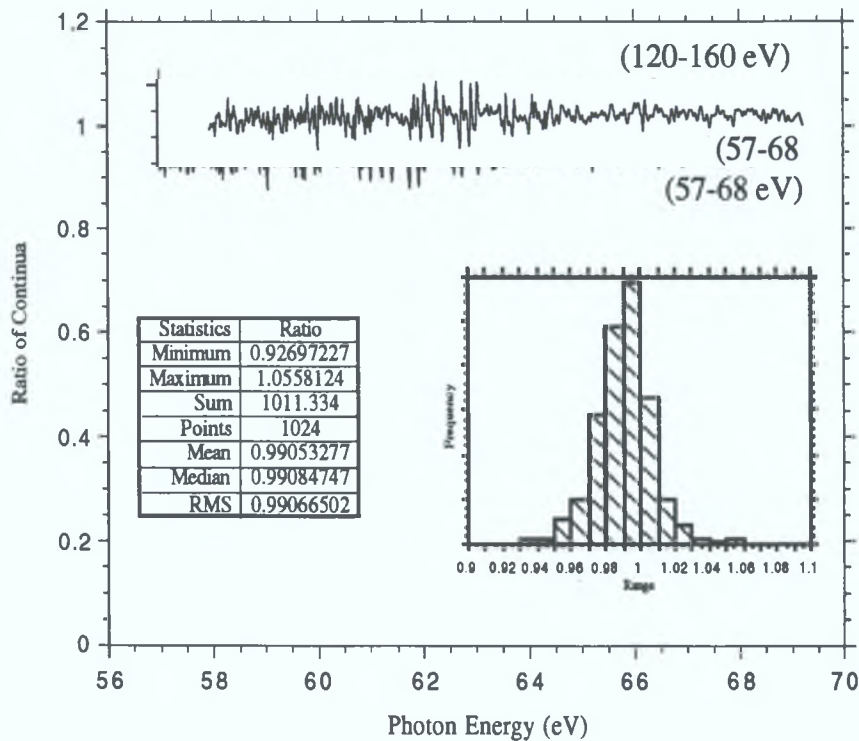


Figure 3.2. Statistics of the ratio of two laser generated W continuum emitting plasmas, each of which is the result of the accumulation of 20 laser shots and using a $10\ \mu\text{m}$ entrance slit.

ratio of two continua taken at the same detector position as the emission spectrum shown in the middle of figure 3.1. Each spectrum is the result of the accumulation of 20 laser shots using a $10\ \mu\text{m}$ entrance slit. There are some self absorption features present in this energy region but as can be observed from the ratio of the emission spectra, their positions and intensities are stable and so tend to divide out. The statistics of the data show that the mean value of the ratio is 0.99 and the standard deviation is 0.016; see figure 3.2. The reproducibility of the backlighting continuum is therefore better than 2% in this typical experiment. It should be stressed that this ratio represents the worst case scenario and the divided spectrum shown in the upper part of figure 3.2 is a more typical result of the ratio of two continuum spectra. This spectrum has been slightly shifted above unity to illustrate the uniformity more clearly. This ratio

was generated by dividing two emission spectra taken in the energy region of 120 to 160 eV which corresponds to the same energy region as the emission spectrum shown on the far right of figure 3.1.

3.2.2. Thin Film Photoabsorption Measurements in the XUV.

Thin films produced in a vacuum are rarely as dense as the material in the bulk. When synthesis is done by vacuum deposition, most metals have a density around 90% of theoretical, whereas many compounds such as fluorides have densities as low as 50% of theoretical. To accurately predict filter performance, density factors based on

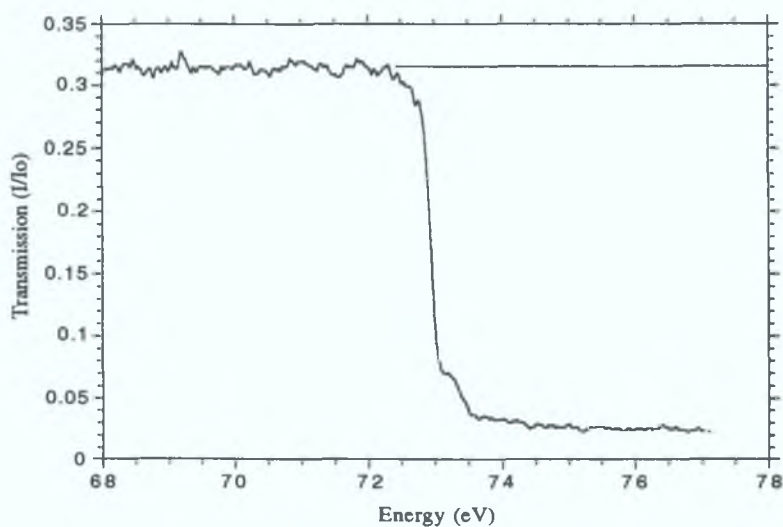


Figure 3.3. Spectral transmission characteristics of a 2000 Å thick Al foil, measured using a laser plasma backlighting source.

experimental measurements must be used (Powell *et al.* 1990). Filter performance for compounds can be predicted by assuming that the filter is made up of the individual elements taken in proportion to the percentage by weight of each element present. The transmittance of each element is determined separately and the individual transmittances are multiplied to get a composite transmittance. The results of these predictions are, however, not always reliable because of interactions that can occur between atoms within the compound.

During the process of determining a suitable filter for the XUV region, to reduce the effects of scattered light and second order interference, the transmittance of Al foils of varying thickness was measured using a laser plasma as a continuum source. Al is one of the best and most frequently used filter materials. It is relatively durable and is

easier to process than many other filter materials. It has a wide band pass (from 15 to 73 eV) and is excellent for visible light rejection. (The Al filters used here were fabricated at HASYLAB in Hamburg). The foils were supported on a copper mesh and inserted between the source and the toroidal mirror chamber. The transmission curve of a 2000 Å thick Al foil is shown in figure 3.3. The $L_{II,III}$ edge at 73 eV is clearly evident. The transmittance above 74 eV is reduced to about 0.025 which is less than 10% of that below the edge, which puts an upper limit on the background scattering contribution in this spectrum. From Powell *et al.* (1990), the absorption coefficient μ is approximately $5 \mu\text{m}^{-1}$ below the edge for Al. Therefore, from $I/I_0 = \text{Exp} [-\mu x]$ where x is the thickness of the absorber in μm , the transmittance below the edge for a $0.2 \mu\text{m}$ foil should be about 0.37. The transmittance of the copper mesh is about 85% and thus when the theoretical Al transmittance value is corrected due to the effects of the mesh, ($0.37 \times 0.85 = 0.31$) good agreement is achieved between theory and experiment: see figure 3.3. The success of these measurements displays the capability of the experimental system to accurately measure the photoabsorption characteristics of thin films in the XUV region of the spectrum.

3.2.3. XUV Photoabsorption Spectrum of Helium.

The measurement of the XUV photoabsorption spectrum of helium provides an important test of both the resolution and dynamic range of the system. The experiment was performed by first evacuating the target chamber to remove any residual gases. The target chamber was then vacuum isolated by closing the gate valve between the chamber and its turbo pumping system. Helium was admitted into the target chamber by means of an adjustable fine leak needle valve, to a positive pressure of about 0.2 mbar. The length of the absorbing column is defined approximately by the distance from the continuum source to the GCA ($\approx 25 \text{ cm}$). The relative absorption due to the presence of helium gas could therefore be measured in the usual way by recording the emission of the laser plasma continuum, i.e. $\text{Ln}(I/I_0) = \sigma n l$.

The spectrum shown in the inset of figure 3.4 was recorded in the photon energy range corresponding to the first ionization potential of helium. The modulation in the cross section at the K edge has been measured (Samson, 1967) and corresponds to a value of approximately 7.4 megabarn ($7.4 \times 10^{-18} \text{ cm}^2$). Using the ideal gas equation, $PV = nRT$, where P is pressure in Atm, V is volume in litres, n is the number of moles R is the universal gas constant and T is temperature in degrees Kelvin one can calculate the number density of helium atoms in the absorbing column. For a pressure of 0.2 mbar this corresponds to a number density of $4.9 \times 10^{15} \text{ cm}^{-3}$. The

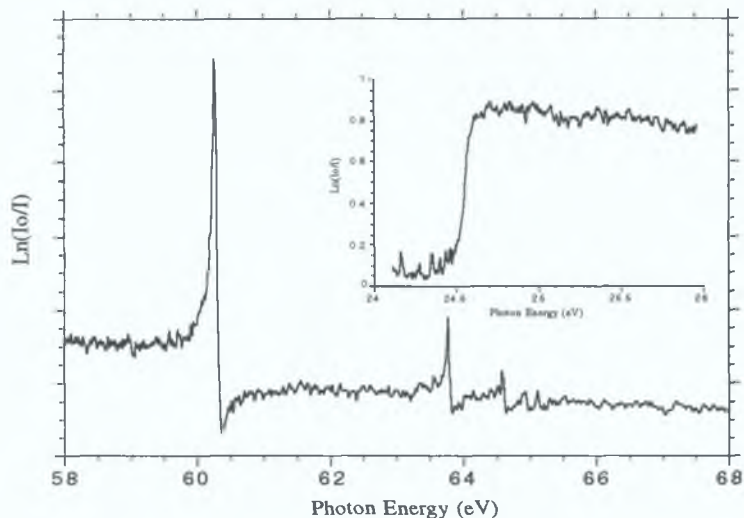


Figure 3.4. Photoabsorption spectra of He in the photon energy regions corresponding to direct photoionization (inset), and double electron excitation.

product of the number density, the column length (in cm) and the cross section (in cm^2) should therefore yield the modulation in $\text{Ln}(I_o/I)$, i.e $4.9 \times 10^{15} \times 25 \times 7.4 \times 10^{-18} = 0.9$. From the inset of figure 3.4 a modulation of 0.8 can be estimated. The difference between the two values is most probably due to the inherent error in the pressure measurement which for a Pirani gauge, in this pressure region, is quoted by Balzers to be 10-15%.

One of the most important examples of the application of synchrotron radiation to the field of atomic spectroscopy was the first experiment performed at the National Bureau of Standards in Washington. This involved the use by Madden and Codling (1963) of the continuum nature of the radiation to obtain the spectrum of helium in the region of 60 eV. At this energy two competing processes are possible. Direct photoionization can occur with the outgoing photoelectron gaining in kinetic energy the value of which is equal to the photon energy minus the binding energy of the initial state of the electron. However, an alternative process can occur whereby both 1s electrons are excited simultaneously to the 2s2p excited state. In fact, a whole series of excitation states exists converging to the $n=2$ state of He^+ . When such two-electron , or doubly excited, states are excited, their lifetimes are very short, typically 10^{-13} - 10^{-14} s.

The asymmetric nature of the resonances is due to the interaction between the excited state and the underlying direct photoionization continuum producing an interference effect in the cross section. This series is shown in the energy region 58 to

68 eV in figure 3.28, where up to the fifth member is clearly resolved. The width of the resonances and the strength of the higher members of the series provide a considerable test of the resolution and dynamic range, respectively, of the system. After deconvolution, Fano parameters of resonance width $\Gamma = 0.034$ and profile index $q = -2.88$, were obtained for the main $2s2p\ ^1P$ doubly excited resonance. These values compare well with the values reported by Madden and Codling (1963): 0.038 and -2.8, Morgan and Ederer (1984): 0.038 and -2.6, and Kossmann *et al.* (1988): 0.038 and -2.75, for the resonance width and profile index respectively.

The insensitivity of the laser plasma continuum source to ambient pressure, coupled with the GCA differential pressure barrier, and both the linearity and dynamic range of the photoelectric detection system, renders this type of experiment possible. The photoabsorption spectrum of xenon, in the region of the 4d 'Giant resonance' was also investigated using this technique and good qualitative agreement was observed with existing spectra in the literature. A prototype pulsed gas jet system was installed for tests by a group from University College Cork. Positioned between the source and the GCA, this device fires a pulse of gas across the optical axis at high pressure and the source is fired before the gas has time to expand into the low pressure environment. With such a sample injector system it should be possible to expand the range of gaseous compounds available for photoabsorption studies in this region of the spectrum.

3.2.4. Inner-Shell Photoabsorption Spectra of the First Row Transition Metals; Comparison with Synchrotron Data.

In order to demonstrate the suitability of the experimental system for photoabsorption studies of free metal atoms in the XUV, a series of experiments were carried out along the 3d transition metal sequence. The inner-shell spectra of the open 3d metal atoms pose a formidable challenge to experiment and theory. The coupling of the 3d electrons with core holes and the strong interaction with the underlying continua give rise to very complex photoabsorption spectra. These metals are highly refractory and hence the high temperatures required for creation of the metal vapour columns and the aggressiveness of the liquid metals in combination with the vacuum requirements of XUV optics, cause the great difficulties encountered in conventional XUV photoabsorption spectroscopic techniques. The inner shell series was recorded initially on photographic plates, but the reliable determination of relative cross sections is severely hampered by the limited response of photographic registration. A summary of the results recorded during a systematic study of the 3p absorption spectra from Ti to

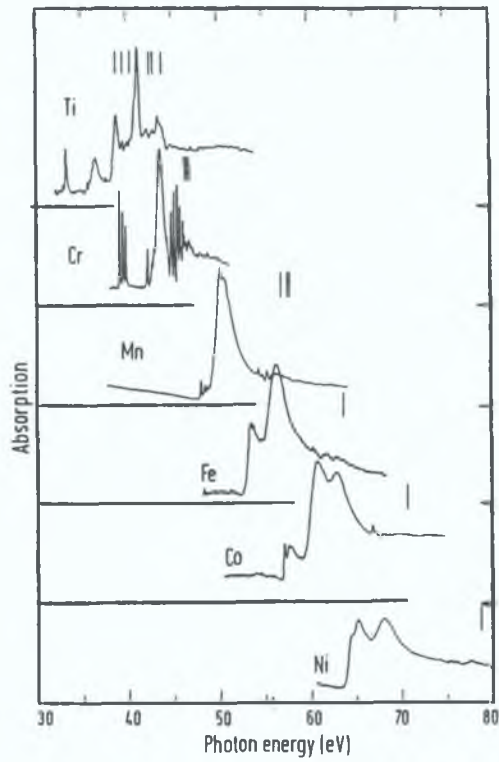


Figure 3.5a. 3d Transition metal sequence (after Meyer *et al.* 1987)

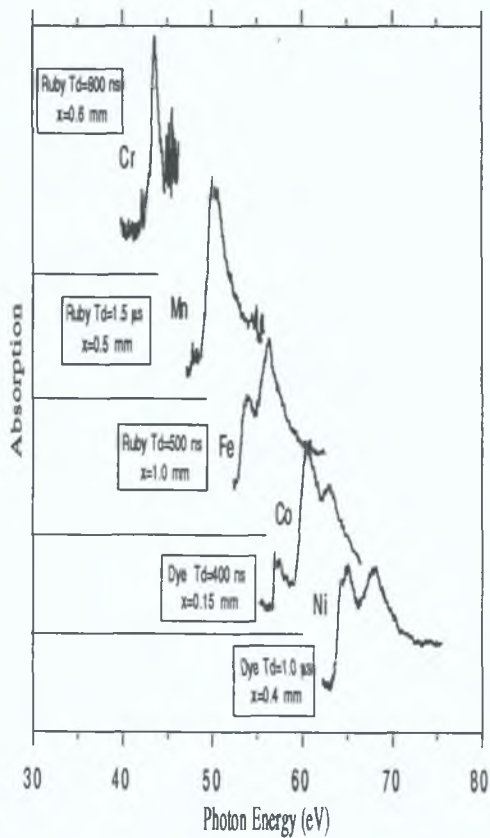


Figure 3.5b. 3d Transition Metal sequence, recorded using the DLP technique.

Ni by Meyer *et al.* (1986) using photoelectric detection is shown in figure 3.5a. These measurements were obtained by passing monochromatic synchrotron radiation, using a toroidal grating monochromator (TGM), through a metal vapour column maintained inside a resistively heated tubular furnace. The spectra were recorded in the photon energy range 30-80 eV, which corresponds to electron excitation from the 3p subshell of the type $3p^6 3d^n 4s^2 \rightarrow 3p^5 3d^{n+1} 4s^2$. The vertical bars in figure 3.5a mark the positions of the 3p ionization limits determined from absorption, photoelectron and ejected electron spectra.

Dramatic changes in the spectra are evident along the sequence. Mn, Fe, Co and Ni show very broad and asymmetric absorption maxima superimposed on the direct 3d photoionization background. Cr is the only element of the series which displays a set of well developed Rydberg series. A large fraction of the oscillator strength for transitions from the 3p subshell is concentrated in $3p^6 3d^n \rightarrow 3p^5 3d^{n+1}$ transitions which give rise to the dominant resonances. These states readily autoionize into the $3p^6 3d^{n-1} \epsilon f$ continuum channel. Interference between the discrete core excited states and the ϵf ionization continuum is responsible for the asymmetric lines shapes. In fact, each discrete state can interact with several continua but it has been shown that the main resonance lines from Cr to Ni could be well approximated by a superposition of Fano profiles sitting on a constant background continuum.

Using the DLP technique, where the absorbing column is created by laser ablation of spectroscopically pure transition metal targets, the same 3p absorption sequence was investigated. Figure 3.5b indicates the type of laser used to generate the absorbing sample, the inter-laser time delay (T_d) between backlighting continuum and sample plasma and the distance in mm (x) from the front surface of the absorber target to the optical axis of the system. In general the high refractory nature of these metals necessitated the use of the Q-switched ruby laser, focused in line configuration with relatively large inter-laser time delays and probed between 0.5 and 1.0 mm from the surface. Alternatively the use of the dye laser, focused to a spot, at relatively short inter-laser time delays while probing close to the target surface, was employed. The main 3p resonances of the resulting spectra were also parameterised as a superposition of Fano type profiles and the associated coefficients are shown in table 3.1 for inter comparison with those of Köberle, Kurig and Meyer *et al.*, where $E(\text{eV})$ is the resonance energy position, $\Gamma(\text{eV})$ is the full width at half maximum and q is the profile index, or asymmetry parameter.

Atom	3p excitation	<u>K.K&M</u>			<u>DLP Experiment</u>		
		E(eV)	Γ (eV)	q	E(eV)	Γ (eV)	q
Cr	$3p^6 3d^5 4s^1 \ ^7S - 3p^5 3d^6 4s^1 \ ^7P$	43.5±0.1	0.76±0.1	3.1±0.5	43.5	1.1	3.9
Mn	$3p^6 3d^5 4s^2 \ ^6S - 3p^5 3d^6 4s^2 \ ^6P$	50.1±0.1	1.4±0.1	3.0±0.5	50.2	1.9	3.2
	$- 3p^5 3d^6 4s^2 \ ^4L$	50.7±0.1	0.4±0.1	3.1±0.5			
Fe	$3p^6 3d^6 4s^2 \ ^4F - 3p^5 3d^7 4s^2 \ ^5F$	53.3±0.1	1.1±0.2	3.0±0.5	53.4	1.4	3.3
	$- 3p^5 3d^6 4s^2 \ ^5D$	56.1±0.1	3.1±0.2	3.5±0.5	56.0	3.3	4.1
Co	$3p^6 3d^7 4s^2 \ ^4F - 3p^5 3d^8 4s^2 \ ^4F$	60.4±0.1	3.2±0.2	3.3±0.5	60.5	3.1	3.6
Ni	$3p^6 3d^8 4s^2 \ ^3F - 3p^5 3d^9 4s^2 \ ^3P$	67.7±0.1	3.7±0.5	3.2±0.5	67.8	3.6	3.6

Table 3.1. Value of Fano coefficients for parameterisation of $3p \rightarrow 3d$ resonances of the transition metal series.

From figures 3.5a and 3.5b it can be observed that, in general, there is reasonable agreement obtained between the two techniques. The fitting of a Fano type profile to the main $3p \rightarrow 3d$ resonance of chromium is complicated by the close proximity of a well developed Rydberg series. In general the value of the width and the profile index obtained from the curve fitting procedure, has been found to be dependent on the size of the energy window used to define the limits of the curve fitting region. For the case of Mn, our curve fitting routine was unable to separate the two Fano resonances as determined from the synchrotron measurements. Treating the Mn $3p \rightarrow 3d$ resonance as one peak yields a total width comparable to the sum of the widths of the resolved components. These results serve to illustrate the versatility and complementary nature of this experimental setup, combined with the DLP technique, and its application to the measurement of the photoabsorption spectra of refractory metals in the XUV.

3.3. XUV Photoabsorption of Free Ions: Photoabsorption Studies in the Transition Regions of the Periodic Table.

3.3.1. Xenon Isoelectronic Sequence.

Over 60 years ago, Enrico Fermi used the Thomas-Fermi statistical model of the atom to predict a collapse of the $4f$ orbital for atomic numbers between 55 and 60, and thereby explained the formation of the first rare earth series of elements. In 1941, Maria Meyer used the same model to predict the onset of a second rare earth series associated with the orbital collapse of the $5f$ electron for atomic numbers between 86 and 91. She also showed that the abrupt changes in the character of the $4f$ electrons can be explained in terms of the f electron effective potential which, in these regions of the periodic table, consist of two wells separated by a positive centrifugal barrier. The outer well is dominated by the long range Coulomb potential and behaves asymptotically as $-1/r$ for neutral atoms (Cheng and Fischer, 1983). It is broad and shallow and can support an infinite Rydberg series of nf bound states. The inner well, on the other hand, is much narrower and deepens with increasing nuclear charge Z . For lighter atoms, it is not deep enough to support any bound state and all nf wave functions reside in the outer well. The first bound state of the inner well appears near $Z=58$ (Cerium) leading to the sudden collapse of the $4f$ wave functions from the outer into the inner well. This sudden collapse can also be ‘stimulated’ by altering the occupancy of the valence orbitals, through for example molecular bonding or ionization, affecting the close balance between the attractive atomic central potential and the repulsive centrifugal barrier. Thus, the evolution of this collapse within a given element can be investigated by studying the inner shell absorption spectra of its ions. This has been already achieved by Lucatorto *et al.* (1981) who studied the $4d$ photoabsorption spectra of Ba, Ba^+ and Ba^{++} (isoelectronic with xenon) and the associated $4f$ wave function collapse along this isonuclear sequence using the technique of RLDI (Resonant Laser Driven Ionization). In order to illustrate and compare the capability of the DLP technique to measure the photoabsorption spectrum of free ions, we revisited this part of the periodic table to investigate the $4d$ spectra of the xenon isoelectronic sequence.

The $4d$ -subshell absorption spectrum of Xe I has been studied extensively by many workers (Codling and Madden 1964, Ederer 1964, and Haensel *et al.* 1969). The most striking feature of the spectrum is the ‘delayed onset’ of continuous

absorption whereby the photoionization cross section rises from a low value directly above the 4d ionization thresholds, at about 70 eV, to a maximum about 40 eV above threshold; see figure 3.6. Using the independent particle model, Cooper (1964), explained this anomalous behaviour in terms of the exclusion of bound and low energy continuum f electrons from the atomic core by the centrifugal barrier, of the form $l(l+1)/r^2$, for f electrons. The result of which, is that only the $4d \rightarrow np$ transitions are observed below the 4d ionization thresholds for Xenon. In a similar fashion to the experiments using helium gas, described previously using this system, the target chamber was filled with xenon and the backlighting tungsten continuum plasma was generated in the presence (I) and absence (I_0) of xenon. Figure 3.7 shows the photoabsorption spectrum of xenon, $\ln(I_0/I)$, in the region of the $4d \rightarrow np$ series. These transitions appear as two relatively weak series of lines running up to the ${}^2D_{5/2}$ and ${}^2D_{3/2}$ limits of Xe^+ at approximately 67.5 and 69.5 eV respectively. It is not until the continuum f electrons acquire sufficient kinetic energy to penetrate the centrifugal barrier that the $4d \rightarrow f$ oscillator strength begins to rise.

Stimulated by the observation of the anomalous spectral signature of the xenon 4d ‘giant resonance’, a number of experiments were carried out on the lanthanide metals by Zimkina *et al.* (1967). Strong 4d subshell resonances were observed and attributed as essentially atomic $4d^{10}4f^n \rightarrow 4d^94f^{n+1}$ transitions. It was not, however, at that time technically feasible to demonstrate the atomic character of the 4d-resonances. The 4d photoabsorption spectrum of atomic barium was recorded by Connerade and Mansfield (1974) and Rabe *et al.* (1974), at about the same time. The results of this work show that the 4d spectrum of atomic barium has the same general shape as that of xenon, displaying delayed onset of continuous absorption and a ‘giant resonance’, almost 30 eV in width, above the 4d thresholds. In the energy region corresponding to $4d \rightarrow np$ excitation, below the 4d thresholds, there are marked differences however. The well developed Rydberg structure present in the xenon spectrum, shown in figure 3.7, is no longer evident in the case of barium. This is due to the collapse of the 4f wave function in the presence of the core hole for barium, which reduces the central field sufficiently for orbital contraction to occur in the $4d^94f6s^2$ configuration. Since the inner well of the effective potential is now deep enough to hold a collapsed 4f orbital, the overlap between the 4d and 4f orbital should increase dramatically, while those between the 4d and higher nf orbitals remains small because the potential barrier still prevents low energy f wave functions from entering the inner region. Thus, the 4d absorption spectrum of atomic barium should show strong absorption lines from the $4d \rightarrow 4f$ transitions in addition to delayed onset. This collapse of the 4f wave

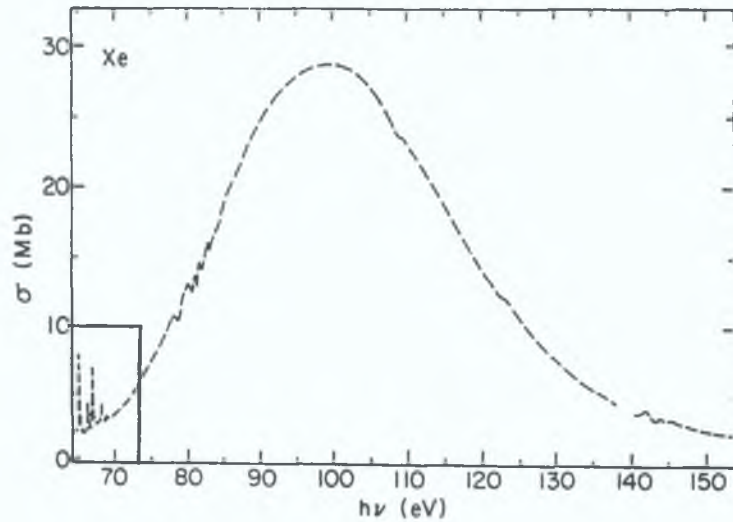


Figure 3.6. Photoabsorption spectrum of Xenon in the region of the 4d 'giant resonance' (after Haensel *et al.* 1969)

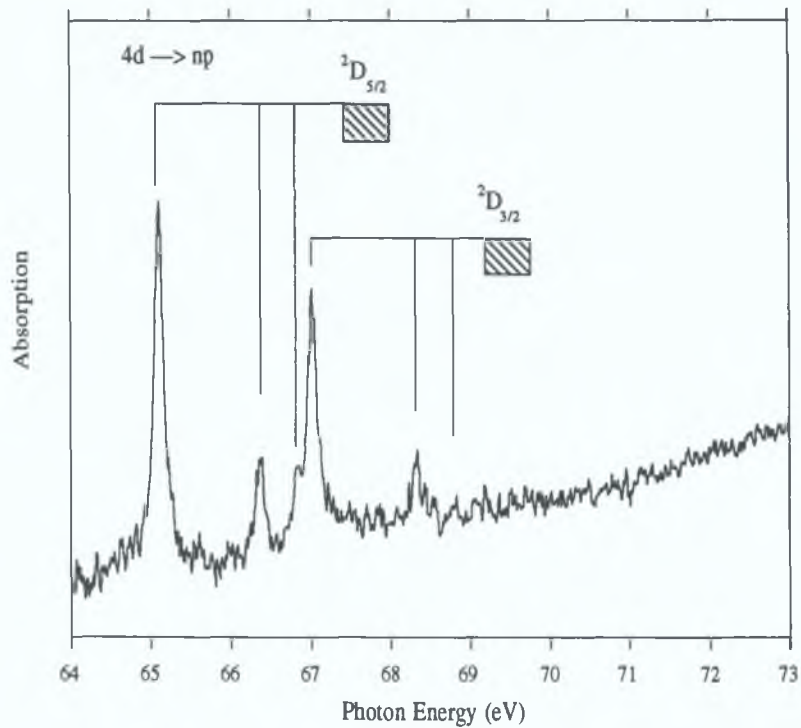


Figure 3.7. Photoabsorption spectrum of xenon in the region immediately below the 4d threshold showing the 4d \rightarrow np series and their corresponding limits. This spectrum was measured by backfilling the target chamber with xenon to a positive pressure of 0.1 mbar, yielding an absorbing column length of approximately 25 cm. This absorbing column was then backlit with a tungsten XUV continuum emitting laser produced plasma.

function has been shown to be term dependent (Cheng and Fischer 1983) and the absence of the strong $4f\ ^1P$ below the $4d$ threshold in neutral barium, see uppermost spectrum in figure 3.8a, is generally explained as due to the raising of the $4f\ ^1P$ discrete level into the f continuum as a result of strong exchange effects (Dehmer *et al.* 1971). The 3P and $^3D\ 4f$ states, are not strongly effected by exchange interaction with the open core and appear as relatively weak lines below the $4d$ thresholds. These states are however very localised and lie in close proximity to the core, explaining their persistence in the $4d$ spectrum of the solid, this is not however the case for the np states. As mentioned previously, the further collapse of the $4f\ ^1P$ orbital can be stimulated by lowering the potential barrier between the inner and outer wells. This can be achieved by removing the valence electrons, thus experiments were initiated involving the investigation of the $4d$ photoabsorption spectra of singly and doubly ionized barium.

Experiments involving the measurement of the photoabsorption of free ions pose considerable difficulties, due to the transient nature of such species and the need to create an adequate column density for absorption. The laser based technique of RLDI (Resonant Laser Driven Ionization) has proven itself to be one of the most successful approaches developed in recent years. The technique involves tuning a dye laser to the first optical resonance transition of a metal, the vapour of which is contained in a conventional heat pipe. The interaction of this tuned radiation leads to almost 100% ionization within $1.5\ \mu\text{s}$ of laser initiation. By suitable timing of an XUV pulse, the absorption spectra of various mixtures of ground, excited and ionized free atoms can be obtained.

Lucatorto *et al.* (1981) used the technique of RLDI, combined with photographic registration, to investigate the $4d$ subshell photoabsorption spectra of the Ba, Ba^+ and Ba^{2+} isonuclear sequence. The use of two independently tuned dye lasers was necessary to first ionize the neutral barium vapour and then to further ionize the Ba^+ . Analysis of this $4d$ sequence revealed a spectacular change in spectral signature due to the manifestation of orbital contraction phenomena in the $4f$ transition region. The $4d\text{---}4f$ 'giant resonance' of barium undergoes a radical change of character as the valence electrons are removed: see figure 3.8a. The broad resonance of Ba, located above the $4d$ ionization limits changes to a familiar discrete Rydberg type spectrum, running up to the various $4d$ ionization limits of Ba^{2+} . The appearance of many discrete lines was unexpected. It was assumed that the potential barrier should still prevent higher nf wave functions from entering the inner well. Accordingly there should be either only one strong resonance line from the $4d\ \text{---}\ 4f\ ^1P$ transition or

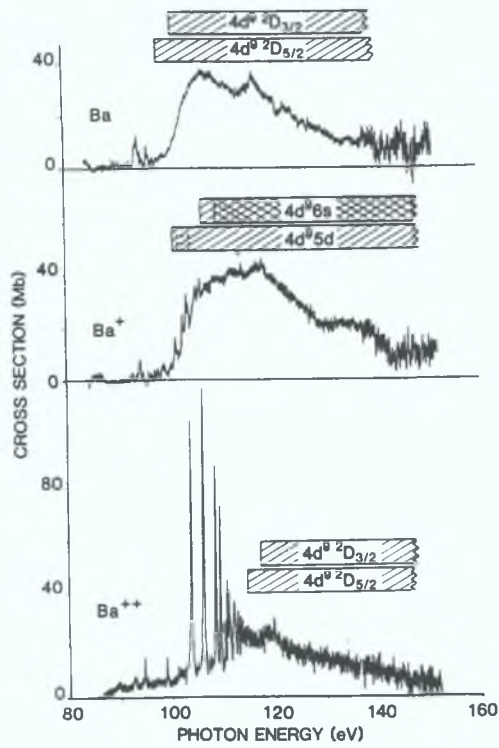


Figure 3.8a. Photoabsorption spectra of Ba, Ba⁺ and Ba²⁺ in the region of the 4d giant resonance, measured using the RLDI technique (after Lucatorto *et al.* 1981).

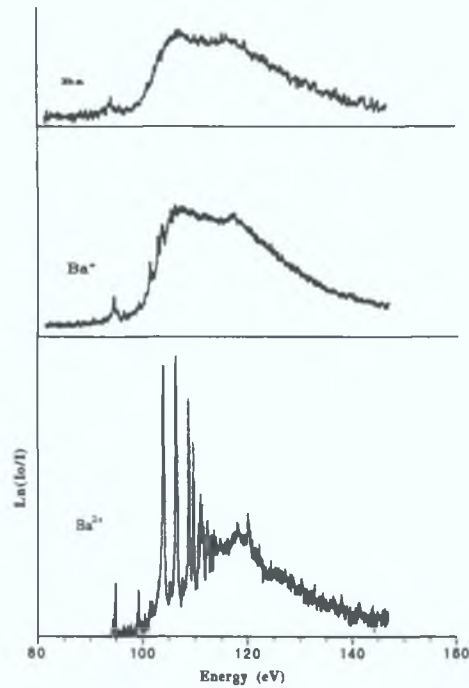


Figure 3.8b. Photoabsorption spectra of Ba, Ba⁺ and Ba²⁺ in the region of the 4d giant resonance measured using the DLP technique.

none at all if the $4f$ level is raised into the continuum. Connerade and Mansfield (1982), suggested that the $4f^1P$ level in Ba^{2+} suffers a “Collapse of the second kind” and that the nf wave functions are hybridised having comparable amplitude in the inner and outer wells, yielding strong absorption from the $4d \rightarrow nf^1P$ transitions. The success of the RLDI technique stimulated publications of various theoretical approaches, using both the independent electron and many body models.

The Ba isonuclear sequence was reinvestigated using the DLP technique, the results of which are shown for comparison in figure 3.8b. The photoabsorption spectra of the various ion stages were obtained by varying the inter-laser time delay, between the continuum probe XUV pulse and the laser generated absorbing column, and by adjusting the spatial position of the surface of the barium target with respect to the optical axis of the spectrometer/toroidal mirror ensemble. In addition, the spectrum of neutral barium was obtained by using the dye laser to generate the absorbing column whereas the spectra of Ba^+ and Ba^{2+} necessitated the use of the Q-Switched ruby laser, the shorter pulse width of which tends to produce ionized species.

As can be observed from the comparison of figures 3.8a and 3.8b, in general good agreement, in terms of resonance energies and widths, with the RLDI experiment exists. Some subtle differences in the general shape of the spectra, especially in the high energy, or tail off, region of the giant resonances of Ba and Ba^+ , is probably due to the former use of photographic registration. Another possibility for the observed differences, in the tail off region, is the fact that a BRV spark source was used as a backlighting continuum which may have produced some source features in this energy region. In comparing the RLDI and DLP spectra for Ba^{2+} one observes a difference between the ratio of continuum to discrete absorption between the two spectra. This is probably due to the fact that the discrete features are quite narrow and the folded instrument response has not been removed from the DLP spectrum. The resulting enhancement in the discrete features would certainly lead to an increase in their relative intensity compared to the level of continuum absorption. In addition, the ionic purity of the DLP spectra has been subsequently improved through an extended set of measurements by Köble *et al.* (1994) along the xenon isoelectronic sequence.

As mentioned in chapter one, the main limitation of the RLDI technique is that it is only applicable to those elements for which an adequate column density can be maintained. Further, the ultimate charge state of the sample column is set by the operational limitations of the short wavelength range of the dye laser tuned to the resonance transition, which rapidly moves into the VUV with increasing ion stage. It was this second limiting factor which prevented the extension of the investigation of the $4d$ photoabsorption behaviour along the xenon isoelectronic sequence to the La^{3+}

ion using the RLDI technique. This situation was, however, rectified through the work of Hansen *et al.* (1989) who used a ‘single laser’ version of the DLP technique to record the XUV photoabsorption spectrum of a lanthanum laser produced plasma in the region of 4d excitation. The ion density in the absorbing column was quite low due to the fact that the single laser was optically divided to generate both the backlighting continuum and the absorbing plume. The lack of temporal and spatial control over the absorption process also added to the difficulties encountered in trying to separate the

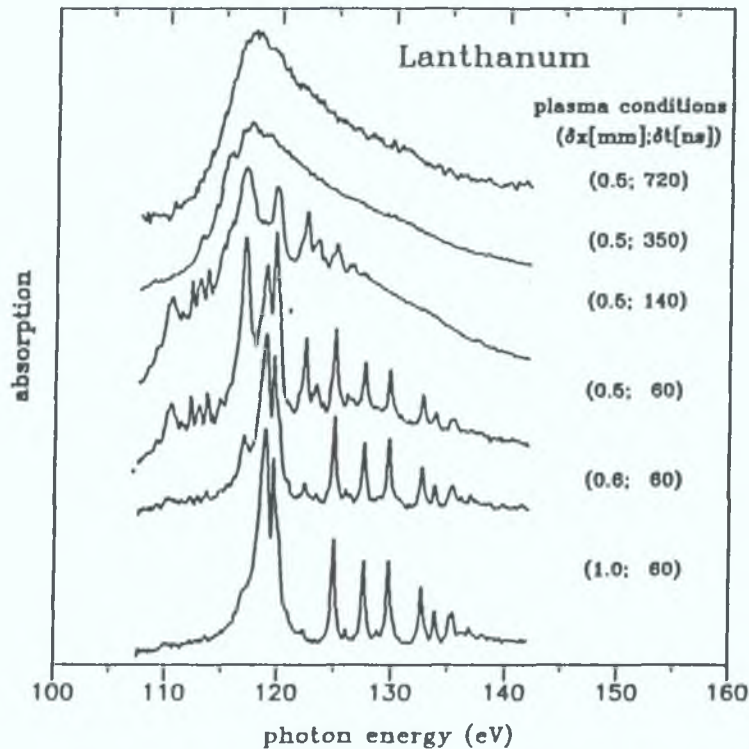


Figure 3.9. Photoabsorption spectra, in the region of 4d excitation, of a lanthanum plasma under different experimental conditions Δx , Δt . The transition from the ‘giant resonance’ profile of atomic La to the discrete type spectrum of La^{3+} is well illustrated. The strongest line of the spectrum, at 118 eV is associated with the $4d^9 4f^1 P$ state of La^{3+} (after Köble *et al.* 1994).

different ion stages in the lanthanum plasma. The observed spectrum revealed some weak evidence of discrete Rydberg type structure associated with nf wave function collapse, but the predicted dominant $4d^9 4f^1 P$ resonance was conspicuous by its absence.

Exploiting the advantages offered by the present experimental system, such as multi-laser capability which increases the power output available for the generation of the absorbing plume, temporal and spatial control over the probe continuum beam and the increased dynamic range of the photoelectric detection system compared to photographic registration the 4d photoabsorption spectrum of La^{3+} was reinvestigated. Using this experimental system the Xe isoelectronic sequence has been extended from Ba^{2+} to La^{3+} by Köble *et al.* (1994) with considerable success. The 4d spectrum of La^{3+} is shown in figure 3.9. The same transition from giant resonance to a discrete type spectrum, where most of the oscillator strength is concentrated in the 4d—4f resonance, has been observed. This particular series of experiments has shown that the system is capable of reproducibly recording the inner shell spectra of free ions and that the DLP technique is a versatile and unique method of overcoming the ion stage limitations of the RLDI approach.

3.3.2. Calcium and its Ions in the XUV.

(i) Neutral Calcium.

Calcium $[\text{Ar}] 4s^2$ is the third member of the alkaline earth series after beryllium and magnesium. The simple atomic structure of the alkaline earths having closed subshells, and the ease with which they can be vapourized are the main reasons that these elements have been favourite candidates for photoionization experiments. In particular calcium plays an important role in both experimental and theoretical studies of inner shell excitation. The main reason is the near degeneracy of the 4s with the 3d levels in the presence of a core hole, which gives rise to strong inter-configurational mixing (Mansfield 1987) with the result of pronounced many electron effects.

The properties of the 3d orbitals are closely connected with the position of Ca ($Z=20$) in the Periodic Table near the transition metal series from scandium to nickel ($Z=21-28$) where the 3d subshell becomes successively filled up. Calcium shows similar orbital behaviour to another alkaline earth element, barium $[\text{Xe}] 4s^2$ ($Z=56$) discussed in the previous section. In excited Ca states the 3d electrons move in an effective bi-well potential which is created through the dynamic competition between the attractive Coulomb interaction of the many electron system and the repulsive centrifugal forces, proportional to $l(l+1)/r^2$. The localisation of the 3d electrons from

the outer well, with its hydrogenic character to the inner well, near the core region, is critically dependent on small changes in this effective potential. The collapse of the 3d orbital into the core region has a strong effect on the photoabsorption process of the 3p subshell. Whereas for uncollapsed 3d orbitals the small overlap between 3p and 3d results in dominating continuum transitions $3p \rightarrow \epsilon d$, for collapsed 3d orbitals the main part of the oscillator strength is channelled into discrete transitions $3p \rightarrow 3d$. The “soft” outermost $4s^2$ valence shell tends to collapse and “shatter” upon core ionization and gives rise to a very rich satellite spectrum (Bizau *et al.* 1987). The softness of the $4s^2$ shell is due to low-lying empty 3d levels. In the presence of a core hole these 3d levels become core-like and move down into the vicinity of the 4s level. As a consequence the $3p^5 4s^2$, $3p^5 4s 3d$ and $3p^5 3d^2$ configurations become nearly degenerate and sometimes strongly mixed leading to pronounced satellite structure revealed by ‘shake’ processes in the energy region of the main $3p^5 4s^2$ photoelectron lines.

3d orbital collapse in this transition region of the Periodic Table ($Z=18-20$) was initially investigated through measurements of the 2p subshell photoabsorption spectra of argon ($Z=18$) by Nakamura *et al.* (1968). For argon, where the 3d orbital remains uncollapsed, most of the $2p \rightarrow d$ oscillator strength resides in the continuum. This contrasts with the situation regarding the 2p spectrum of potassium ($Z=19$) and calcium, measured by Manfield (1975) and (1976) respectively, where as the 3d wave function collapses in the presence of the 2p core hole, the $2p \rightarrow d$ oscillator strength is taken from the continuum and appears in very strong $2p \rightarrow 3d$ transitions. Also, prominent $2p \rightarrow nd$ series are observed even after the 3d wave function has collapsed into the inner well. Thus, although nd ($n > 3$) states are eigen states of the outer well they still have sufficient core penetration to produce $2p \rightarrow nd$ transitions.

Mansfield and Newsom (1977) reported the first observation of the 3p subshell photoabsorption spectrum of atomic calcium. The Ca I spectrum was measured between 10 and 40 eV revealing at least 125 new lines. The experimental arrangement comprised of a BRV vacuum spark continuum source, a 3 m normal incidence spectrograph with photographic registration and a resistively heated furnace with a metal vapour containment system. A comprehensive and detailed interpretation of the gross features of the spectrum was achieved by comparison with Hartree-Fock calculations of configurations which can be reached by single or multi-electron excitations from the ground state $3p^6 4s^2 \ ^1S$. The spectrum is dominated by the single electron transition $3p^6 4s^2 \ ^1S \rightarrow 3p^5 4s^2 3d \ ^1P$ at 31.4 eV. This transition is favoured by the large overlap of the 3p orbital with the collapsed core-like 3d orbital. Figure 3.10, above, shows the photoabsorption spectrum, of neutral calcium measured using

the DLP XUV spectrometer system in the energy region corresponding to 3p electron excitation. A dye laser, in line focus configuration, was used to generate the absorbing plasma. The strongest feature in the spectrum is the 3p \rightarrow 3d 1P ‘giant resonance’ at

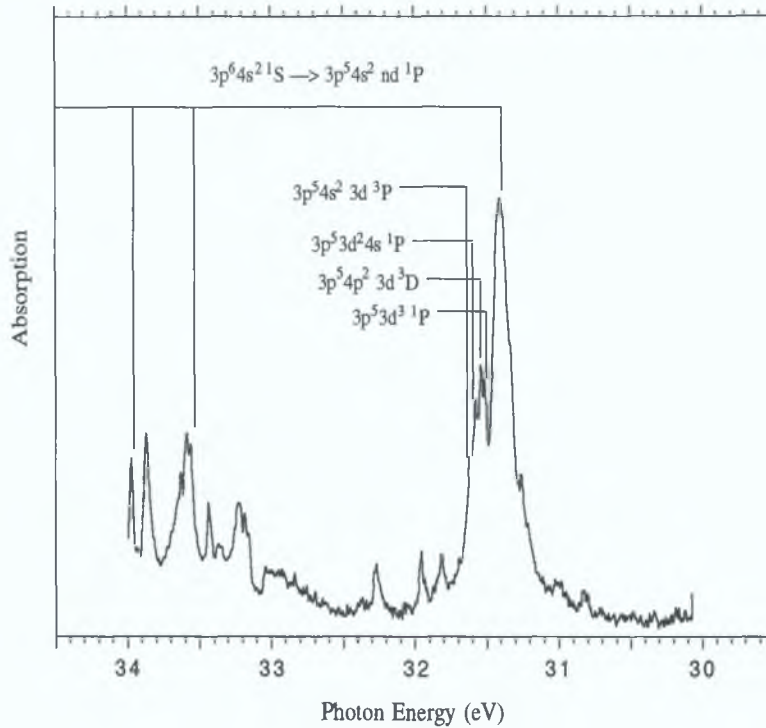


Figure 3.10. 3p photoabsorption spectrum of atomic calcium measured using the DLP technique with parameters, $\Delta t = 3.0 \mu s$, $\Delta x = 2.0 \text{ mm}$. This spectrum corresponds to one capture region of the MCP along the Rowland circle of the spectrometer and results from the accumulation of 20 laser shots with a spectrometer entrance slit of width $20 \mu m$.

31.4 eV. Some strong multi-electron transitions are also shown, the spectral assignments of which are given by Mansfield and Newsome (1977), demonstrating the significant role played by electron-electron correlation effects in the energy region of 3p excitation for this element.

As mentioned above, the original 3p spectrum of Ca I as measured by Mansfield and Newsome (1977) was recorded on photographic plates the transmission of which are replicated as densitometer traces in their paper. They also recorded their spectra at various column densities to enhance the weaker spectral features just below the 3p thresholds, while saturating the absorption due to resonance features. It is difficult therefore, to make a direct comparison with our multi-channel photoelectric absorption measurements. Sato *et al.* (1985), have measured the photoion yield, after XUV photoexcitation and ionization, of atomic calcium in this energy region using a

time-of-flight mass spectrometer. Their results show that a large amount of Ca^{2+} photoions are produced in the energy region below the 3p thresholds arising from the two step process $3p^5 4s^2 nl \rightarrow \text{Ca}^+ 3p^5 3d 4s + e_1 \rightarrow \text{Ca}^{2+} 3p^6 + e_1 + e_2$. On crossing

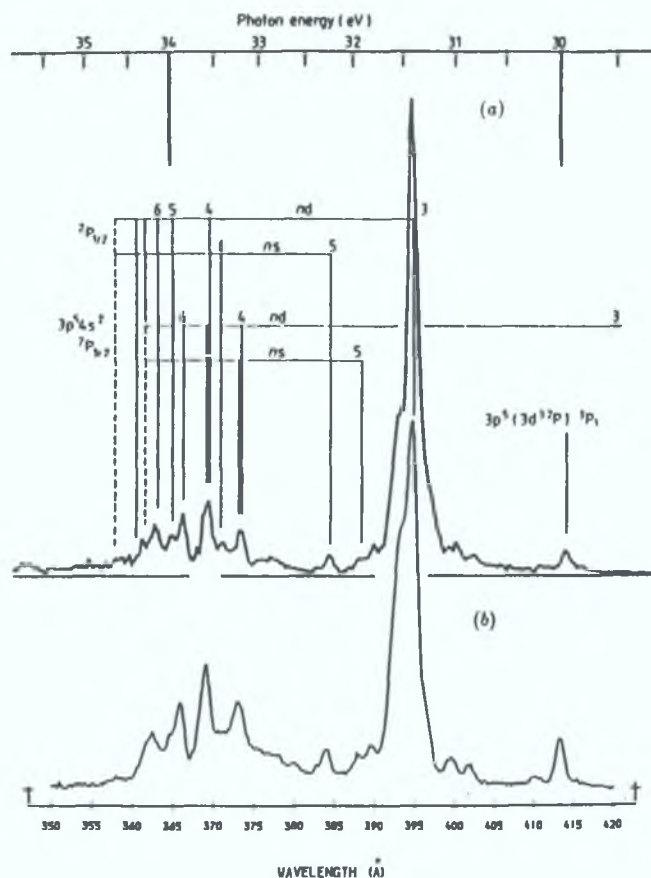
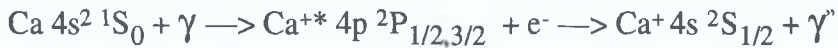


Figure 3.11. (a) Ca^+ photoion yield spectrum measured by Sato *et al.* (1985). Four series are indicated which converge to the $3p^5 4s^2 2P_{3/2,1/2}$ limits of Ca^+ assigned by Mansfield and Newsome (1977). (b) Measurement of the fluorescence intensity of the Ca^+ ($4^2P \rightarrow 4^2S$) transition as a function of wavelength by Hamdy *et al.* (1991).

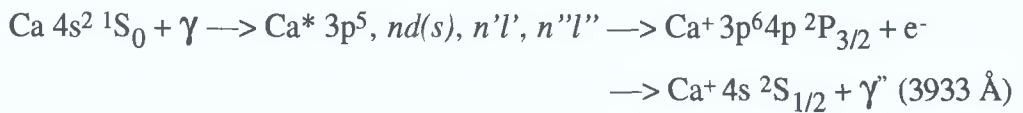
the 3p thresholds, between 34 and 35 eV, the ratio $\text{Ca}^{2+}/\text{Ca}^+$ rises to approximately 5. Above threshold the production of Ca^{2+} proceeds via the two step mechanism of direct 3p ionization and subsequent Auger decay of the Ca^+ photoion, i.e. $\text{Ca}^+ 3p^5 4s^2 \rightarrow \text{Ca}^{2+} 3p^6 + e$ (Sonntag and Zimmermann 1992). Figure 3.11 (a) shows the corresponding Ca^+ photoion yield spectrum.

Techniques such as photoion, photoelectron and fluorescence spectroscopy can be used to separate the individual ionization channels involved in the photoionization process. In addition, if the angular distribution of the ejected photoelectrons is measured, e.g. Baier *et al.* (1992) and Ueda *et al.* (1993), with respect to a symmetry

axis of the experimental geometry, information can be obtained about the angular momentum of the orbitals concerned. When the photoion is left in an excited state another refinement is possible by measurement of both the intensity and polarisation of the fluorescence radiation emitted when the ion decays, revealing information about the population of the magnetic sublevels in the final excited state and the alignment of the excited ion. Shown in figure 3.11 (b) is the fluorescence intensity of the $\text{Ca}^+ (4^2\text{P} \rightarrow 4^2\text{S})$ transition as a function of photon energy incident on ground state Ca atoms recorded by Hamdy *et al.* (1991). Interestingly their original intention had been to study the direct ionization and excitation process,



where γ represents the incoming photon and γ'' the fluorescent photon emitted as the ion decays. However, this process was found to have a very low cross section but a Many Body Perturbation Theory (MBPT) calculation by Altun and Kelly (1985), indicated a much larger cross section for ionization and excitation of Ca into the $4p \ ^2\text{P}$ state of Ca^+ by correlation with excitation of the 3p electrons via the 3p — 3d ‘giant resonance’, i.e.



Bizau *et al.* (1987), in their extensive photoelectron measurements in the energy region of 27 to 40 eV have measured the Constant Ionic State Spectrum (CISS) of the $\text{Ca}^+ 3p^6 4p$ satellite line, yielding its partial cross section contribution. The relative variation in peak intensity across this spectrum is generally in good agreement with the data of Hamdy *et al.* (1991) shown in figure 3.11 (b).

(ii) Singly Ionized Calcium.

As in the case of barium, the desire to study orbital collapse and its dependence on the effective potential ‘seen’ by the contracting orbital, provided stimulus for the investigation of the inner shell spectra of excited state calcium, Ca^* , and singly ionized calcium, Ca^+ . By exciting or removing a 4s valence electron slight modifications in the effective potential can be achieved. In general the wave function of the excited outer electron extends over a radius which is much larger than for an atom in the ground

state. Therefore, in the photoionization of an excited atom, the atomic potential is probed over a larger spatial range. The excited state can be prepared with a well defined set of quantum numbers and the photoionization dynamics of these precisely defined states can be studied as a function of incident photon energy (Wuilleumier *et al.* 1991). In 1973 McIlrath and Carlsen published a paper describing the production of large numbers ($\approx 10^{16} \text{ cm}^{-2}$) of calcium atoms in a selected excited state by laser optical pumping. A dye laser was tuned to 6572.8 \AA and used to excite the calcium atoms, contained in a furnace, into the $4s4p \text{ }^3\text{P}$ lowest triplet level. Immediately after excitation of the calcium by the laser pulse, a fast flash lamp ($\approx 4 \text{ }\mu\text{s}$) was fired and the absorption spectrum from the excited state was recorded photographically. This work demonstrated, for the first time, the feasibility of optical pumping of free metal atoms by coherent light.

After the success of the RLDI technique in measuring the photoabsorption spectrum of the free ions of barium (Lucatorto *et al.* 1981) and lithium (McIlrath and Lucatorto 1977), Sonntag *et al.* (1986) applied the technique to the measurement of the $3p$ subshell spectrum of Ca^* and Ca^+ . They used a similar experimental setup to the original RLDI arrangement, the main differences being the employment of a samarium laser plasma continuum source and multi-channel photoelectric registration (Cromer *et al.* 1985). The optical resonance line of calcium, $3p^64s^2 \text{ }^1\text{S} \rightarrow 3p^64s4p \text{ }^1\text{P}$, at about 4227 \AA and therefore not readily accessible to high energy, long pulsed dye lasers. Instead they pumped the intercombination line, $3p^64s^2 \text{ }^1\text{S} \rightarrow 3p^64s4p \text{ }^3\text{P}$ at 6572.8 \AA which has an oscillator strength almost 10^{-5} times smaller than the resonance line.

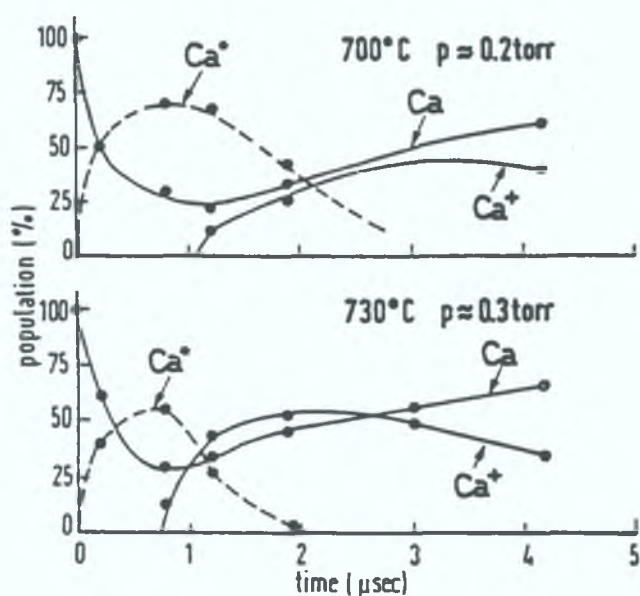


Figure 3.12 Temporal evolution of the relative populations of Ca , Ca^* and Ca^+ at two different heat pipe temperatures. (after Sonntag *et al.* 1986).

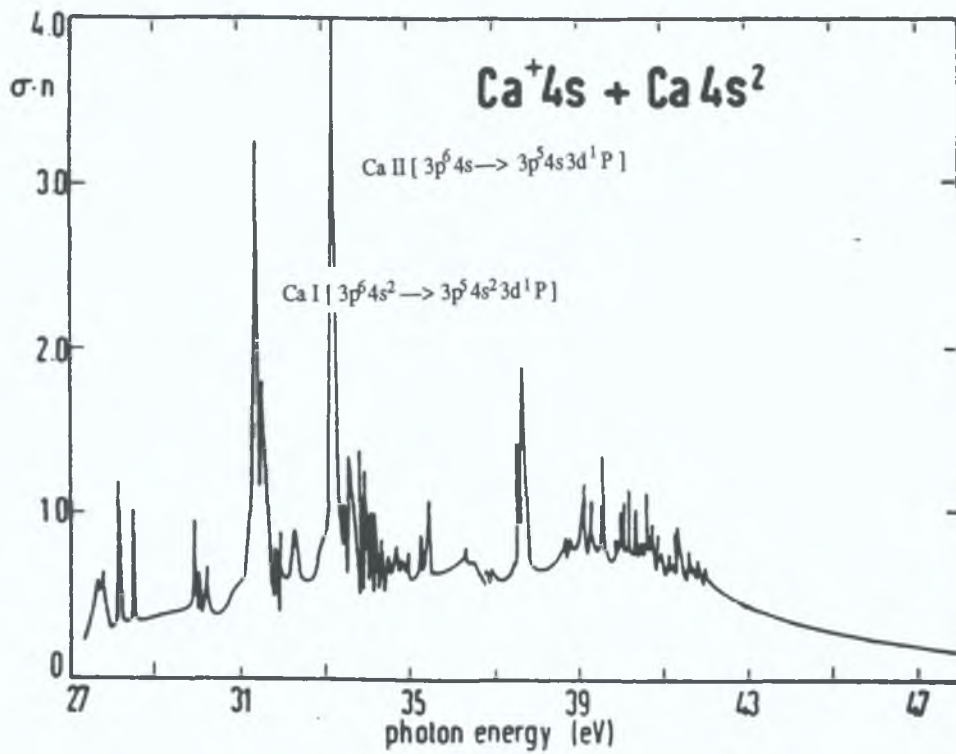


Figure 3.13. Photoabsorption due to a mixture of Ca and Ca⁺ in the region of 3p excitations using the RLDI technique (after Sonntag *et al.* 1986).

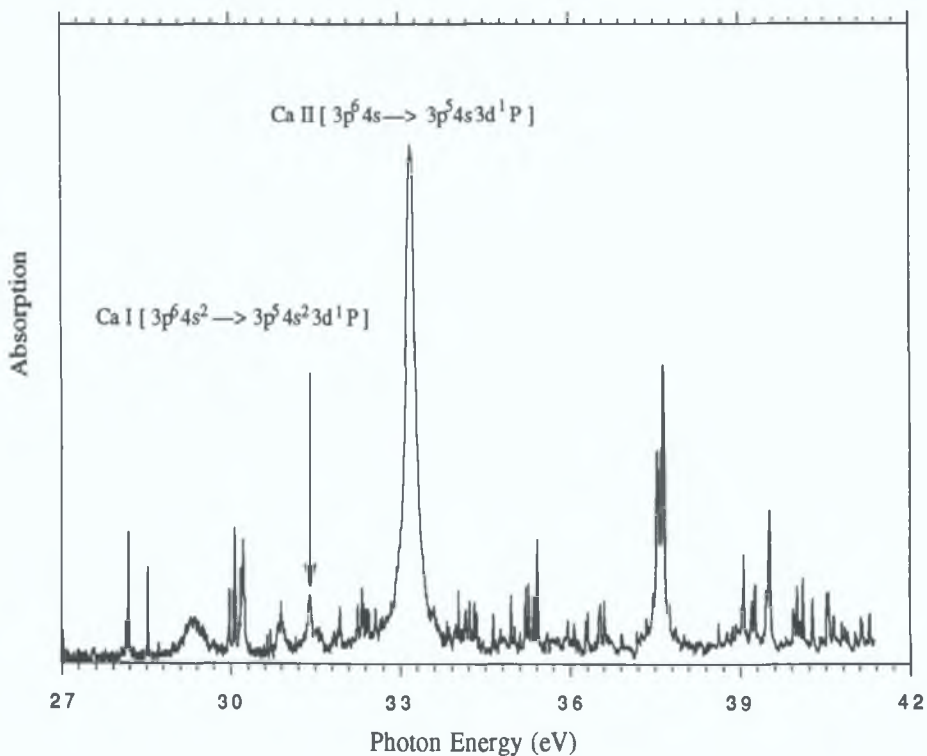


Figure 3.14. Photoabsorption spectrum of Ca⁺ in the region of 3p excitation measured using the DLP technique with $\Delta t = 600$ ns and $\Delta x = 4.0$ mm.

Their results showed that it was only possible to generate, at maximum a population ratio of 50% for singly ionized atoms. This is in marked contrast to the situation for barium and lithium, where it proved possible to ionize 100% of the neutral atoms when the dye laser was tuned to the resonance line of the element concerned. Figure 3.12 shows the relative populations of Ca, Ca* and Ca⁺ at different furnace temperatures as a function of inter-laser time delay. Comparing the behaviour at 700° C with that at 730° C one can see that the higher Ca number density at 730° C results in a faster deexcitation of the laser excited Ca metastable state, and a more efficient conversion of the excitation to ionization. This vapour density dependence is clear evidence for the collisional nature of the ionization mechanism behind the resonantly driven process. The study of this ionization process through optical pumping of the low lying triplet state in Ca, still attracts considerable attention both with pulsed (Khan *et al.* 1990) and CW dye lasers (Khan and Kuhaili 1993).

As mentioned already, in this particular set of RLDI experiments, a samarium laser produced plasma was used to backlight the calcium vapour. By proper temporal synchronisation of this continuum emitting plasma with respect to the dye pumping laser the inner shell photoabsorption spectrum of calcium in various mixtures of ground, excited and ionic states was probed. Figure 3.13 shows the photoabsorption spectrum corresponding to the conditions of maximum column density of Ca⁺ in the energy region of 3p electron excitation. However the optical pumping limitations of the RLDI technique, for the case of calcium, which lead to incomplete ion stage separation are clearly evident. The 3p — 3d giant resonance of neutral calcium centred at 31.4 eV has a peak cross section of about 100 Mb, and remains very strong in this spectrum. The 3p resonance line of Ca⁺, 3p⁶4s —> 3p⁵4s3d, occurs at 33.2 eV above the ground state of the ion, and appears as the strongest line in the spectrum superimposed on the background absorption due to calcium neutral. Both lines are located well above the first ionization potential of the species concerned and are subsequently broadened by the Coster-Kronig decay of the 3p hole. The two lines at approximately 28 eV arise due to 3p excitations of the form, Ca⁺ 3p⁶4s ²S_{1/2} —> 3p⁵4s² ²P_{3/2,1/2}. The 3p spectrum spectrum as measured using the RLDI technique can be compared to figure 3.14 which shows the photoabsorption spectrum of a calcium laser produced plasma in the energy region of 3p excitation. A ruby laser in line focus configuration was used to generate the absorbing plasma. The absorbing plasma conditions were optimised such that attenuation due to the 3p resonance feature of Ca I was at a minimum. The 3p resonance lines of Ca and Ca⁺ are flagged in figure 3.14. Clearly a considerable improvement in spectral purity over the corresponding RLDI spectrum has been achieved. It is also obvious that there are extra absorption features revealed by the DLP

spectrum, the origin of which will be discussed below in relation to important pioneering experiments undertaken on this atomic system through techniques based on the merging of ion beams with synchrotron radiation.

The first measurement of the absolute cross section for the photoionization of a positive ion was achieved by Lyon *et al.* (1986) using an apparatus in which the beams of ground state positive ions and energy-resolved radiation from the Daresbury Synchrotron source were merged. A schematic drawing of the experimental setup is shown in figure 3.15. Ground state positive ions, produced in a surface ionization source (S) were mass analysed by a magnet M1, and collimated by a pair of slits (C) into a beam 2 mm wide, and 3 mm high. The ions were then merged with the chopped VUV photon beam in the biased cylinder (I) producing an interaction zone some 12 cm in length. The singly ionized atoms were collected at C1 whilst the doubly charged ions were individually detected at D. The ion beams were separated by a second magnet M2 and the photon flux from the storage ring was monitored by a photodiode (PD).

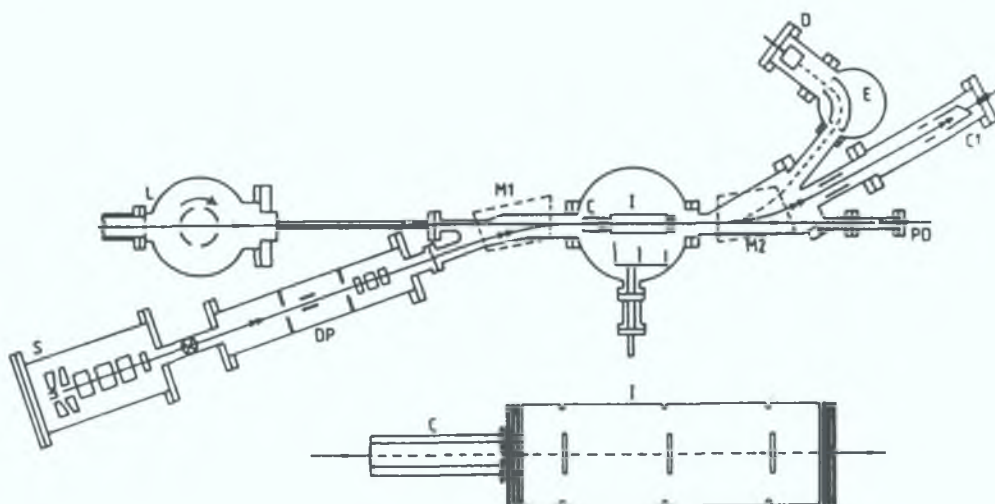


Figure 3.15. Schematic drawing of first experimental arrangement used to measure the absolute cross section of positive ions, by merging beams of ground state ions and synchrotron light. The inset shows the collimator and biased cylinder used to steer the ion beam in the interaction zone (after Lyon *et al.* 1986).

Lyon *et al.* (1986) initially used this experimental setup to measure the absolute photoionization cross section of Ba^+ ions in the energy region 16.0-29.5 eV corresponding to 5p electron excitation, by recording the number of Ba^{++} produced after inner shell excitation and ionization with synchrotron light. Approximately 75 peaks were resolved, the largest of which corresponding to cross sections greater than 3000 Mb. The same apparatus was employed to measure the absolute photoionization

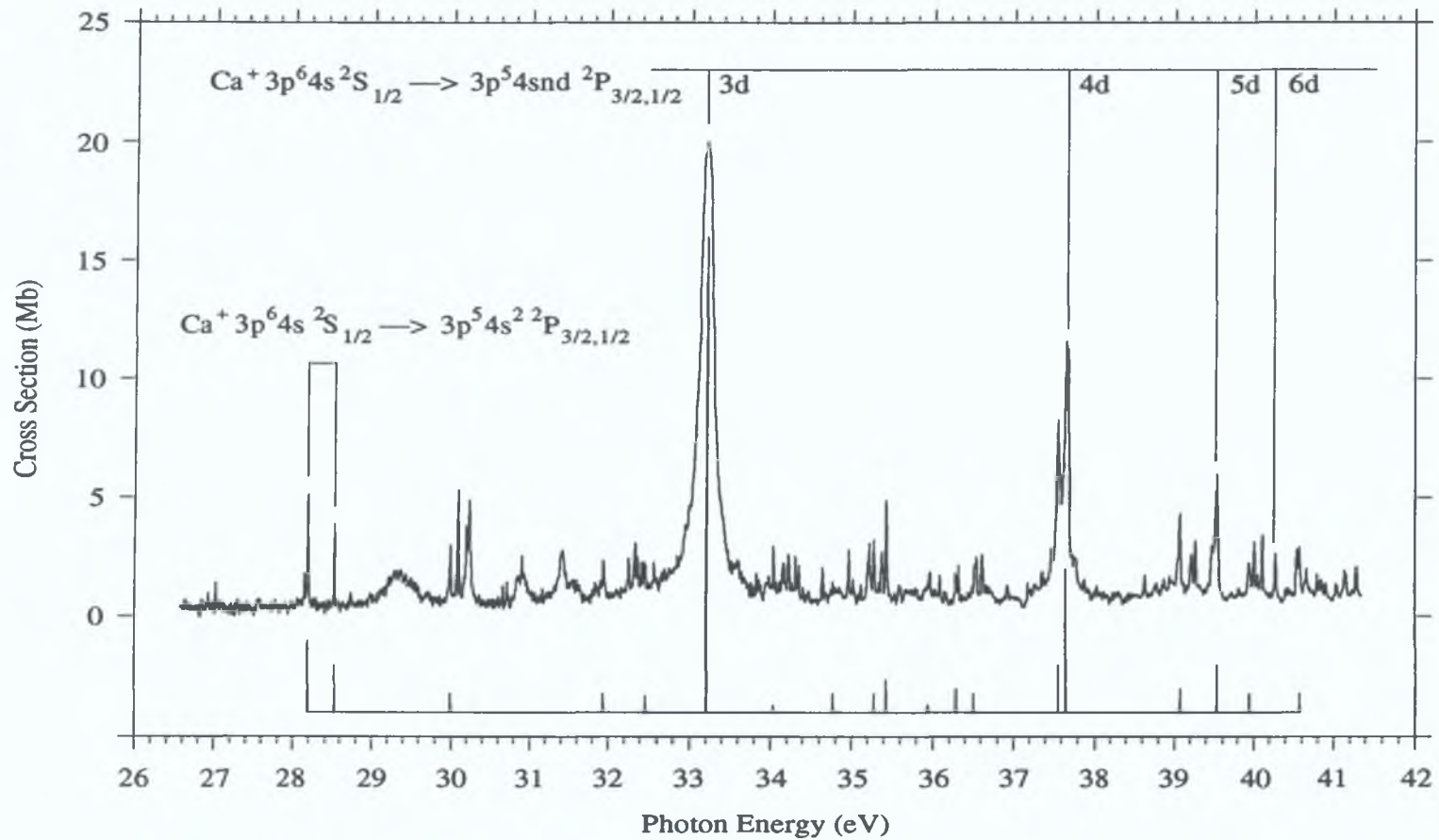


Figure 3.16. Comparison of Synchrotron crossed ion beam experiment and data on the 3p absorption spectrum of Ca⁺ as measured using the DLP technique. The stick plot indicates the relative intensities of the spectral features observed by Lyon *et al.* (1987b).

cross section of Ca^+ ions (Lyon *et al.* 1987), in the energy region of 26.0-43.0 eV corresponding to excitations from the 3p subshell. The Ca^+ measurements proved to be more difficult than those for Ba^+ because the cross sections of the absorption features tend to be smaller. In addition the 3p resonances of Ca^+ occur at higher energies, than the 5p resonances of Ba^+ , where there was a lower available flux of resolved radiation. In order to detect the weaker resonances it was therefore necessary to increase the width of the monochromator slits to increase the number of photoions produced. The resolution ($E/\Delta E$) subsequently varied from about 2000 for the strongest features, such as the 3p — 3d ‘giant resonance’ of Ca^+ , to approximately 400 for the weaker features. A summary of the observed features is shown as a stick plot in the lower half of figure 3.16 for comparison with the DLP results. One can observe that the relative intensity of the strongest features is in excellent agreement with the DLP results, but because the weaker features generally have narrow profiles they appear much reduced in intensity in the spectrum of Lyon *et al.* (1987), due to the resolution degradation necessary for their observation. In contrast, the resolution across the DLP spectrum has a much smaller variation from about 2500 to 2100 and is hence a more accurate reflection of the relative intensity variation. The DLP spectrum has been normalised to the peak cross section of the 3p — 3d ‘giant resonance’ of approximately 2000 Mb.

Quite recently Bizau *et al.* (1991) and (1992), demonstrated for the first time the feasibility of using the technique of photoelectron spectroscopy to study the photoionization of a positively charged ion beam with synchrotron radiation. The experimental difficulties presented by such measurements are considerable for a number of reasons. The low density of ions focussed in the small source volume of an electron analyser ($\approx 10^8$ ions cm^{-2} which 3 to 4 orders of magnitude smaller than the density available in the more standard investigation of neutral species) makes it extremely difficult to observe the ejected electrons. In addition, the transmission of an electron spectrometer is about 1%, as compared to nearly 100% in the case of ion spectrometry, while the length of the interaction region in both cases is about 1 cm and 10 cm respectively. For these reasons it was decided to study a resonant photoionization process since photoionization cross sections are greatly enhanced by the existence of an intermediate excited autoionizing state. The Ca^+ 3p — 3d ‘giant resonance’, was therefore an ideal choice because the energy position and very substantial cross section (≥ 2000 Mb) were well known from the data of Lyon *et al.* (1987) and Sonntag *et al.* (1986). Also the excitation energy of this resonance occurs in the tuning range of the undulator insertion device, at Super ACO, allowing the

photon flux at the 3p —3d resonance energy, to be optimised by changing the gap between the bending magnets. The singly charged calcium ions are produced in a plasma discharge ion source, then extracted and analysed before being made collinear with the axis of the Cylindrical Mirror electron Analyser (CMA). The ion beam propagates in the opposite direction to the monochromatised radiation from the undulator: see figure 3.17, and is focused in the source volume of the CMA by 3

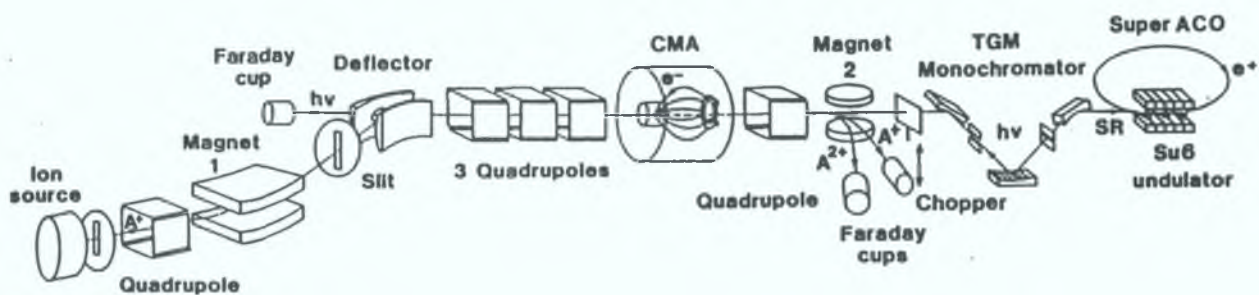


Figure 3.17. Schematic diagram of first experimental setup used to measure the photoelectron spectrum of a positively charged ion beam (after Bizau *et al.* 1991).

electrostatic quadrupoles. The electrons detected after the resonant photoionization process, described by,

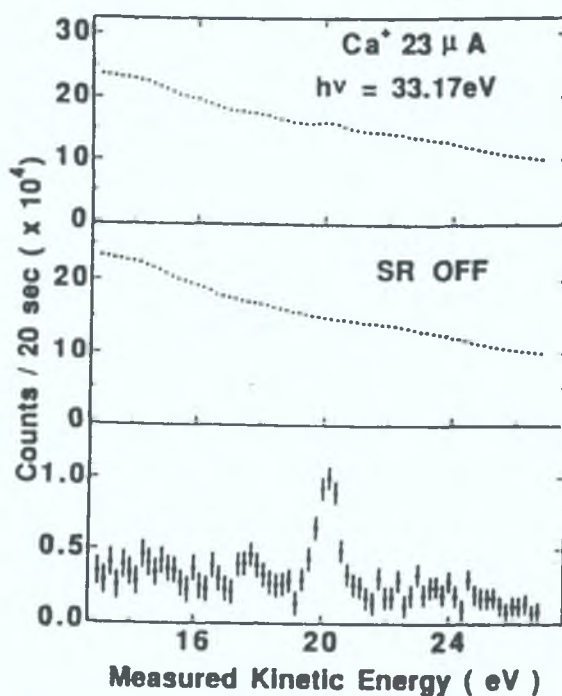
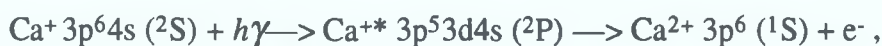


Figure 3.18. Photoelectron spectrum measured due to resonant photoionization of the Ca^+ ion beam, top, without synchrotron light, middle, and bottom, after subtraction of these two signals (after Bizau *et al.* 1992).

should have a kinetic energy of $33.20 - I_p \text{ Ca}^+ (11.87) = 21.33 \text{ eV}$. Figure 3.18 shows the measured kinetic energy of the electrons detected both with an incident photon energy of 33.17 eV (33.20 eV in the ions frame) and in the absence of synchrotron light. The large background electron signal is due to collisional ionization between the Ca^+ ion beam and the molecules of the residual gas in the CMA. Upon subtraction of this background a small modulation in the kinetic energy spectrum is observed revealing the resonant photoionization of the calcium ions. However the detection of features with lower cross sections will require an improved ion source to increase the available ion flux, reduction of the residual pressure to lower the background signal and a higher photon flux to increase the counting rates.

Shown over leaf, in table 3.2, is a summary of the most prominent features observed in the DLP spectrum of Ca^+ , in the region of 3p excitation. Included for comparison are the resonances detected using various other techniques. Pejcev *et al.* (1978) measured the High Resolution Ejected Electron (HR-EE) spectrum of atomic calcium. The incident electron energies were varied from 30 to 500 eV and 165 autoionizing levels of both Ca I and Ca II were recorded. The interpretation of these results is complicated by the fact that both parity allowed and parity forbidden states are populated by low energy electron impact. Mansfield and Ottley (1979) have attempted to analyse the ejected electron spectrum by performing single configurational Hartree-Fock calculations in the energy region corresponding to 3p electron excitation. The results of this analysis has also been used by Bizau *et al.* (1987) as an aid to the identification of the source of the Auger electrons which they detected after Ca I 3p ionization with synchrotron radiation. The transition energy values shown in table 3.2, corresponding to their photoelectron work have been calculated by simply adding the ionization potential of Ca^+ (11.87 eV) to the Auger kinetic energies assuming the final state in the decay process $\text{Ca}^+ 3p^5 nl n'l' \rightarrow \text{Ca}^{2+} 3p^6$, is achieved through the ejection of a 4s valence electron. The merged ion beam data of Lyon *et al.* (1987), has very recently been the subject of an analysis by Ivanov *et al.* (1993) who calculated the photoionization cross sections of the 4s,3p and 3s subshells of Ca^+ using a non relativistic, spin polarized version of the Random Phase Approximation with Exchange. Values for the oscillator strengths and energy positions for the main single electron transitions were obtained and this information was used to identify the most prominent features in the experimental spectrum of Lyon *et al.* (1987). The assignments given in table 3.2 are most reliable for the 3p \rightarrow 4s and 3d resonance features of Ca^+ , the other assignments should be treated as being very tentative.

The two narrow lines at 28.20 and 28.54 eV are generally accepted to be due to

<u>This Work</u> DLP	Lyon Ion+Sr	Bizau(Calc) PE	Sonntag RLDI	Pejcev(Calc) HR-EE	Assignment
26.84				26.86	CaII
26.92				26.95	CaII 3p ⁵ (3d ² ¹ D) ² P _{1/2}
27.02	27.06			27.04	CaII 3p ⁵ (3d ² ¹ D) ² P _{3/2}
28.20	28.20	28.20	28.21	28.20	CaII 3p ⁵ 4s ² ² P _{3/2}
28.54	28.55	28.51	28.55	28.54	CaII 3p ⁵ 4s ² ² P _{1/2}
29.99	30.00	30.01		30.00	CaII 3p ⁵ (3d ² ¹ S) ² P _{3/2}
30.22	30.30	30.28			CaII 3p ⁵ (3d ² ¹ S) ² P _{1/2}
31.41			31.40		CaI 3p ⁵ 4s ² 3d ¹ P
31.93	31.90				CaII 3p ⁵ (3d ² ³ P)
32.25					
32.33					
32.42	32.40				
32.57		32.57			
33.21	33.21		33.21	33.38	CaII 3p ⁵ 4s3d ² P _{3/2}
34.04	34.00	34.98			CaII 3p ⁵ 3d4p
34.15					
34.22					
34.30					
34.35					
34.67					CaIII 3p ⁵ 3d ¹ P
34.96					
35.22					
35.28					
35.37					
35.42		35.46			CaII 3p ⁵ 4p ²
36.32		36.36			
36.54					
36.61		36.66			CaII 3p ⁵ 4s5s
37.55	37.5				CaII 3p ⁵ 4s4d ² D
37.65	37.65				CaII 3p ⁵ 4s4d ² P
39.53					CaII 3p ⁵ 4s5d ² P
40.12	40.10				CaII 3p ⁵ 4s6d ² P
40.66	40.77				CaII 3p ⁵ 4s7d ² P

Table 3.2. Comparison of strongest features observed in the DLP spectrum with features observed using complementary spectroscopic techniques. All values are given in eV and derived from the spectrum shown in figure 3.16

the $3p \rightarrow 4s \ ^2P_{3/2,1/2}$ transitions into the half filled $4s$ valence shell and are in excellent agreement with the series limits $3p^5 4s^2 \ ^2P_{3/2,1/2}$ (34.313 and 34.658 eV) calculated by Mansfield and Newsom (1977) from their extensive experimental measurements on neutral calcium. Interestingly the three weak features in the DLP spectrum, centred at about 26.8 eV., while absent from the data of the merged ion beam experiment, are in reasonable agreement with three similarly weak features observed in the ejected electron spectrum of Pejcev *et al.* (1978). Mansfield and Newsom (1977) have calculated an energy of 33.519 eV for the $3p^5 3d^2 \ ^2P$ configuration of Ca^+ . When the ionization potential of Ca neutral (6.11 eV) is subtracted from this, a value of 27.409 is obtained. This is a little higher than the experimental value, but there appears to be no other structure present in this energy region, which is in agreement with the conclusions of Ivanov *et al.* (1993). In addition Ivanov predicts a second peak due to the spin orbit splitting of the 2P term which remained unobserved in the data of Lyon *et al.* (1987). The assignments for these transitions, given in table 3.2, are derived from a further calculation of the ejected electron spectrum by Mansfield (1980). Doubly excited transitions of the same type, $3p^6 4s \ ^2S \rightarrow 3p^5 3d^2 \ ^2P$, are in evidence at around 30 eV but with increased oscillator strength and in again in reasonable agreement with the $3p^5 (3d^2 \ ^1S) \ ^2P_{3/2}$ series limit tentatively identified by Mansfield and Newsom for neutral calcium.

The strongest line in the DLP spectrum, is of course the $\text{Ca}^+ 3p - 3d$ 'giant resonance' at 33.21 eV which appears weak and misassigned in the photoelectron data of Bizau *et al.* (1987). The Auger lines corresponding to the decay of the $3p^5 4s^2$ levels of Ca^+ to $\text{Ca}^{2+} 3p^6$, appear strongest in the photoelectron spectrum because they represent the photoionization process whereby the valence shell remains undisturbed. The kinetic energy of the outgoing electrons remains constant, at $28.20 - 11.87 = 16.33$ eV for the $^2P_{3/2}$ initial state, for example. To observe the Auger decay of the $\text{Ca}^+ 3p^5 3d 4s$ state requires a photon of at least $(33.21 + 6.11) = 39.72$ eV in energy. The kinetic energy of the outgoing Auger electron corresponding to this Ca^+ initial state should therefore be $(33.21 - 11.87) = 21.34$ eV. In the electron distribution curve, corresponding to an incident photon energy of 47.32 eV, there are in fact two electron lines situated in the appropriate relative energy positions of 21.4 and 7.9 eV. The latter energy is the kinetic energy of the photoionized $3p$ electron from calcium neutral, ie $47.32 - 6.11 - 33.21 = 8.0$ eV. The initial Ca^+ excited state is however assigned as $\text{Ca}^+ 3p^5 4s 4p$ in disagreement with the above argument.

There are two absorption features in the energy region of the $\text{Ca}^+ 3p - 3d$ 'giant

resonance' which should be mentioned. At 31.41 eV is the 3p — 3d resonance line of neutral calcium. The very weak line at 34.67 eV is the 3p — 3d resonance line of doubly ionized calcium. The small contribution of these two lines, considering their relatively large oscillator strengths, serve to illustrate the high degree of purity of the DLP spectrum.

Mansfield and Newsom (1977), calculate an energy of 40.6 eV for the $3p^54p^2$ level of Ca^+ , which after the subtraction of the ionization potential of Ca neutral would place this level at about 34.5 eV above the ground state energy of Ca^+ . Further calculations by Mansfield (1980) predict many resonances corresponding to the $3p^54p^2$ level of Ca^+ in the energy region 35 to 37 eV. There is also evidence of these features in the photoion data of the merged ion beam experiment but because of the low resolution level many of the individual narrower resonances are smeared together. Many of these levels will be of 2P in nature and will therefore interact strongly with the main 3p — 3d 2P 'giant resonance' (Ivanov *et al.* 1993) making reliable assignment very difficult. Between 36 and 37 eV is the predicted energy position of the second member of the $3p^64s \rightarrow 3p^54sns$ series. The higher members of the $3p^54snd$ series are indicated in figure 3.16. A more detailed analysis of this high resolution photoabsorption data will require a very comprehensive set of configuration interaction calculations to unravel the rich and complex satellite structure associated with the important influence of many electron effects for this ionic system.

(iii) Argon-like Calcium.

In order to extend the 3p photoabsorption measurements along the calcium isonuclear sequence to Ca^{2+} , an initial set of survey experiments were carried out in the energy region of 30 to 55 eV. While recording the photoabsorption spectrum of Ca^+ , a ruby laser in line focus configuration was used to generate the absorbing plasma and the optimum DLP condition were found to be at an inter-laser time delay of 600 ns and at a spatial position 4 mm away from the target surface. To generate an absorbing plume containing a high density of Ca^{2+} ions, the ruby laser was, again, used this time focused to a spot approximately 0.75 mm in diameter. Using an inter-laser time delay of 50 ns and probing the plasma 0.5 mm away from the target surface, the spectrum in figure 3.19 was recorded. Some contamination from Ca^{3+} ions is evident in this spectrum, the strongest lines occur in a complex array between 36 and 38 eV. The stick plot in the lower part of figure 3.19 indicates the energy positions and relative

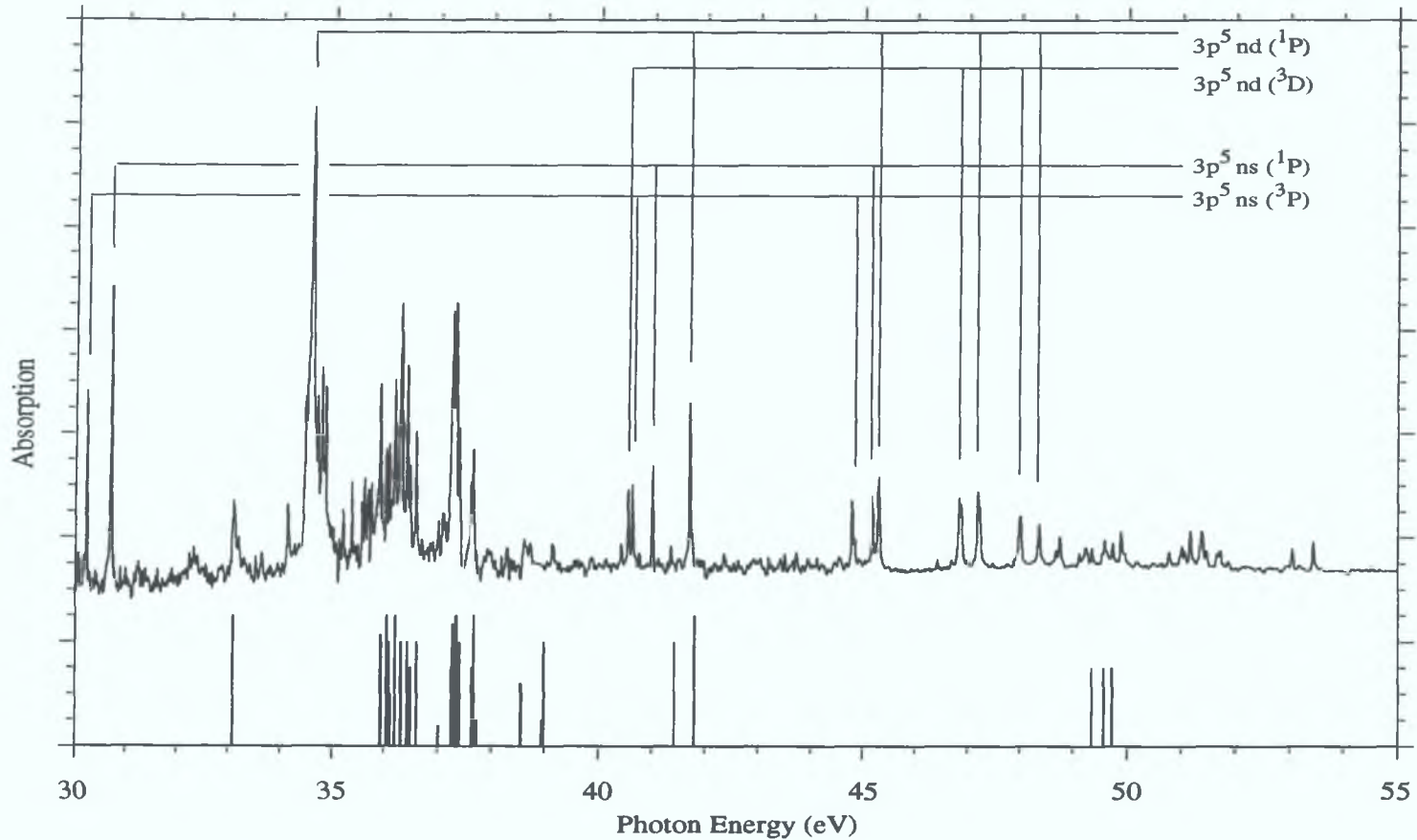


Figure 3.19. Photoabsorption spectrum of a calcium laser produced plasma in the energy region corresponding to 3p subshell excitation. DLP conditions were $\Delta t = 50$ ns, $\Delta x = 0.5$ mm, using a ruby laser in spot focus configuration. The stick plot corresponds to the energy positions and intensities of known emission lines from excited Ca^{3+} .

Energy eV _(Cowan)	<i>gf</i>	Assignment	E _(observed)	E _(observed) -E _(Cowan)
30.184	0.087	3p ⁵ 4s (3P)	30.220	0.0359
30.597	0.536	3p ⁵ 4s (1P)	30.600	0.0030
34.987	4.240	3p ⁵ 3d (1P)	34.610	-0.3770
40.587	0.025	3p ⁵ 4d (3D)	40.540	-0.0470
40.652	0.057	3p ⁵ 5s (3P)	40.620	-0.0320
40.941	0.084	3p ⁵ 5s (1P)	41.000	-0.0589
41.992	0.981	3p ⁵ 4d (1P)	41.700	-0.2920
44.687	0.039	3p ⁵ 6s (3P)		
44.758	0.018	3p ⁵ 5d (3D)	44.760	0.0019
44.986	0.040	3p ⁵ 6s (1P)	45.160	0.1740
45.341	0.326	3p ⁵ 5d (1P)	45.380	0.0390
46.703	0.020	3p ⁵ 7s (1P)		
46.792	0.036	3p ⁵ 6d (3D)	46.800	0.0079
47.006	0.015	3p ⁵ 7s (3P)		
47.144	0.120	3p ⁵ 6d (1P)	47.200	0.0560
47.856	0.012	3p ⁵ 8s (1P)		
47.938	0.040	3p ⁵ 7d (3D)	47.980	0.0420
48.162	0.009	3p ⁵ 8s (3P)		
48.222	0.052	3p ⁵ 7d (1P)	48.350	0.1280
48.578	0.008	3p ⁵ 9s (1P)		
48.651	0.045	3p ⁵ 8d (3D)	48.740	0.0890
48.885	0.006	3p ⁵ 9s (3P)		
48.910	0.018	3p ⁵ 8d (1P)	49.100	0.1900
49.060	0.005	3p ⁵ 10s (1P)		
49.132	0.050	3p ⁵ 9d (3D)	49.220	0.0879
49.370	0.008	3p ⁵ 10s (3P)		
49.501	0.086	3p ⁵ 10d (3D)		
49.749	0.057	3p ⁵ 10d (1P)		

Table 3.3. Summary of observed and calculated single electron transitions in argon-like Ca²⁺ in the energy region corresponding to 3p excitation.

intensities of known emission lines from excited Ca^{3+} listed in Kelly's tables (1987). The higher series members of this array are also present at about 49.5 eV and above. The pair of lines present above the 3p threshold of Ca^{2+} (50.9 eV), at approximately 53.5 eV arise due to excitations from the 3s subshell and correspond to the $3s3p^64p\ ^3P$ and 1P states. The 1P line is the stronger of the two and has been observed in absorption in a high voltage spark spectrum by Kastner *et al.* (1977).

The 3p photoabsorption spectrum of Ca^{2+} bears considerable resemblance to the 3p spectrum of Ca^+ , shown in figure 3.16. The spin orbit split 4s lines again lie about 4 eV below the main $3p^53d$ line. As in the case of Ca^+ the 3p — 3d line remains the strongest feature in the spectrum, however the 4s lines have gained in relative intensity indicating a more even distribution of oscillator strength across the spectrum. Ignoring the contribution from Ca^{3+} , the spectrum has relatively few absorption features compared to Ca^+ . All the resonances must be attributed to single electron transitions since of course they all lie below the first ionization limit at 51 eV.

Table 3.3 lists the observed energies, in eV, of the strongest features in the DLP spectrum shown in figure 3.19 corresponding to single electron transitions from $\text{Ca}^{2+} 3s^23p^6\ ^1S_0$. The spectrum is dominated by the 3p — nd and $(n+1)s$ transitions. The calculations shown in the first column were performed using the Cowan suite of codes (Cowan 1981) and are based on the Hartree-Fock Multi-Configurational method. The composition of the ground state was assumed to be purely $3p^6\ ^1S_0$ in nature. The relatively large oscillator strengths associated with the intercombination transitions indicates the pronounced level of configuration mixing, resulting in a rapid departure from pure LS coupling with increasing energy. The fifth column describes the absolute difference in energy between the observed and calculated structure. There is generally very good agreement between the calculated and observed features except most notably in the cases where an $nd\ ^1P$ state lies close in energy to an $(n+1)s\ ^1P$ state revealing strong evidence of discrete-discrete configuration interaction.

As mentioned above, in the DLP spectrum shown in figure 3.19 there is a significant contribution of absorption from Ca^{3+} ions between 35 and 38 eV and in the vicinity of the 3p thresholds at approximately 51 eV. In order to facilitate the process of spectral assignment, especially in the region of the higher series members of the $3pnd$ and ns excited states, another DLP spectrum was recorded in the energy region of 44 to 52 eV. A slightly longer inter-laser time delay of 80 ns was used and the absorbing calcium plasma was probed 0.75 mm from the target surface. These optimal conditions were obtained by monitoring the absorption contribution from the higher

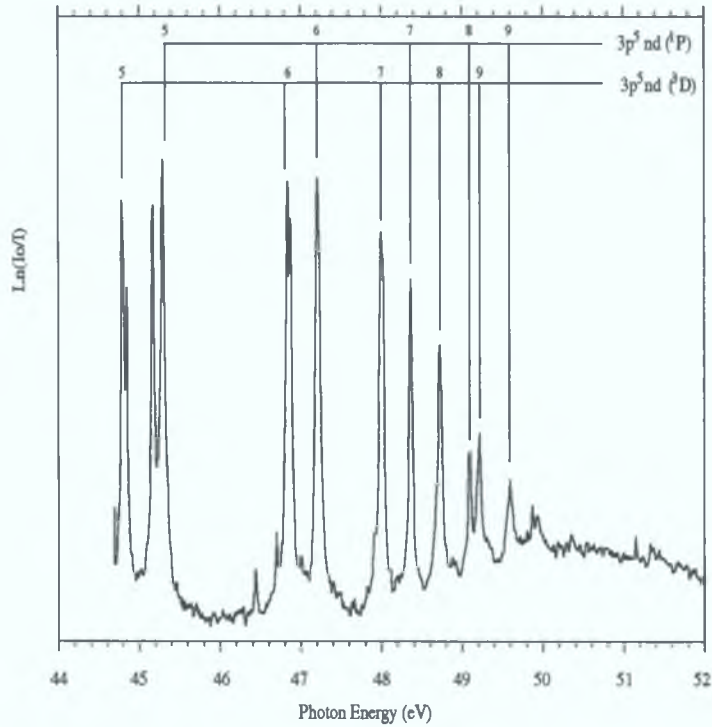


Figure 3.20. Photoabsorption spectrum of a calcium laser produced plasma in the region of the $3p$ thresholds of Ca^{2+} with DLP conditions of $\Delta t = 80 \text{ ns}$ and $\Delta x = 0.75 \text{ mm}$.

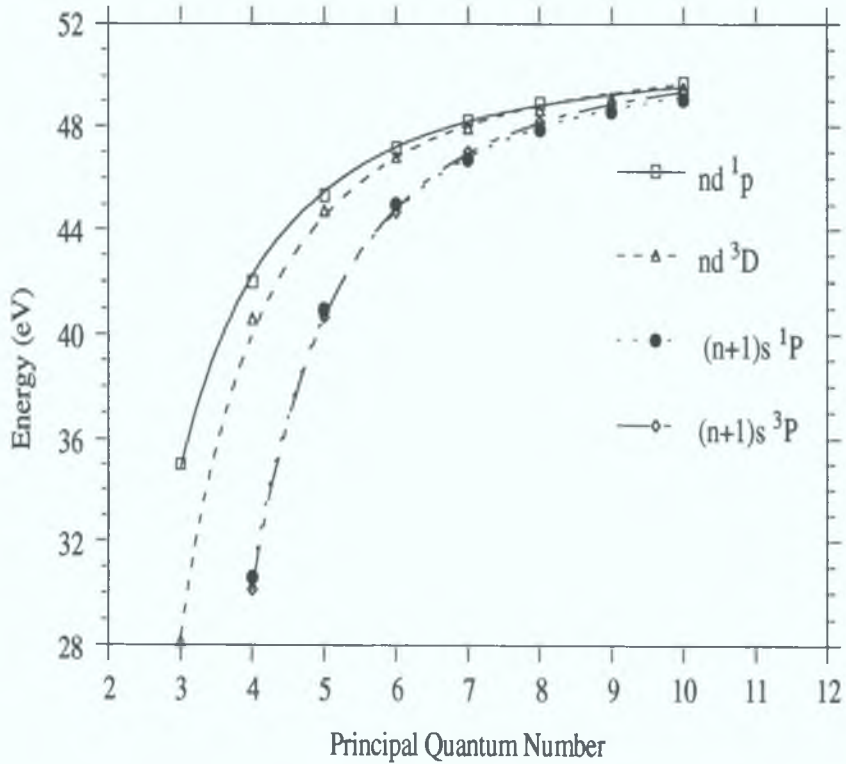


Figure 3.21. Plot of energy versus the excited configuration principal quantum number for the nd and $(n + 1)s$ series of Ca^{2+} based on the HF-CI calculations.

series members of the 3p excited states of Ca³⁺ in the region of the 3p thresholds of Ca²⁺. This spectrum is shown in figure 3.20 and corresponds to one capture region of the MCP along the Rowland circle. The relative intensities of the absorption lines remain the same as those observed in figure 3.19, also the degree of contamination from Ca³⁺ is extremely small in comparison.

The spectral assignment indicated in figure 3.20 is based on the calculated energy level positions and the relative oscillator strengths shown in table 3.3. Finally, in order to gain some further insight into the outer orbital behaviour along this isonuclear sequence the average quantum defects along the *nd* and (*n* + 1) series were calculated using a Rydberg formula, both using the calculated and observed energy positions of the absorption lines. Figure 3.21 shows the curvefits using the formula

$$E_n = I_p - Z^2R/(n - \delta)^2$$

to the MCHF calculated resonance energy positions, where E_n , I_p , Z , R , n and δ , are the excitation energy, energy position of the series limit, spectrum number, Rydberg constant, principal quantum number of the excited state and the average quantum defect which should be constant along the series. This quantum defect analysis also provides a check on the validity of the derived classification. For the *nd* ¹P and ³D series the average quantum defect, δ , was calculated to be 0.232 and 0.68 respectively from the MCHF data. From the observed series δ was calculated to be 0.275 and 0.568, yielding values of 50.939 and 50.954 for the respective series limits, the former of which is in excellent agreement with the lowest 3p threshold at 50.91 eV. Due to the weakness of the higher members of the *ns* ³P series it only proved possible to derive an average quantum defect for the *ns* ¹P series. From the MCHF data the theoretical value for δ *ns* ¹P is 1.536 compared to the observed δ of 1.55 yielding a value of 51.08 for the lower 3p threshold. The much larger value of average quantum defect for the *ns* series reflects the increased core penetration of the *ns* orbitals, which suggests the further contraction of the outer orbitals due to the removal of both 4s valence electrons. This is consistent with the observed substantial increase in strength of the 4s lines relative to the main 3d line in the Ca²⁺ spectrum, compared to the situation in Ca⁺ where the 3p — 3d ‘giant resonance’ completely dominates the measured spectrum.

In conclusion, we have measured the photoabsorption spectra of neutral calcium, singly ionized and doubly ionized calcium, in the photon energy range corresponding to electron excitation from the 3p subshell. This has been achieved using the DLP technique combined with multi-laser plasma generation and multi-channel photoelectric

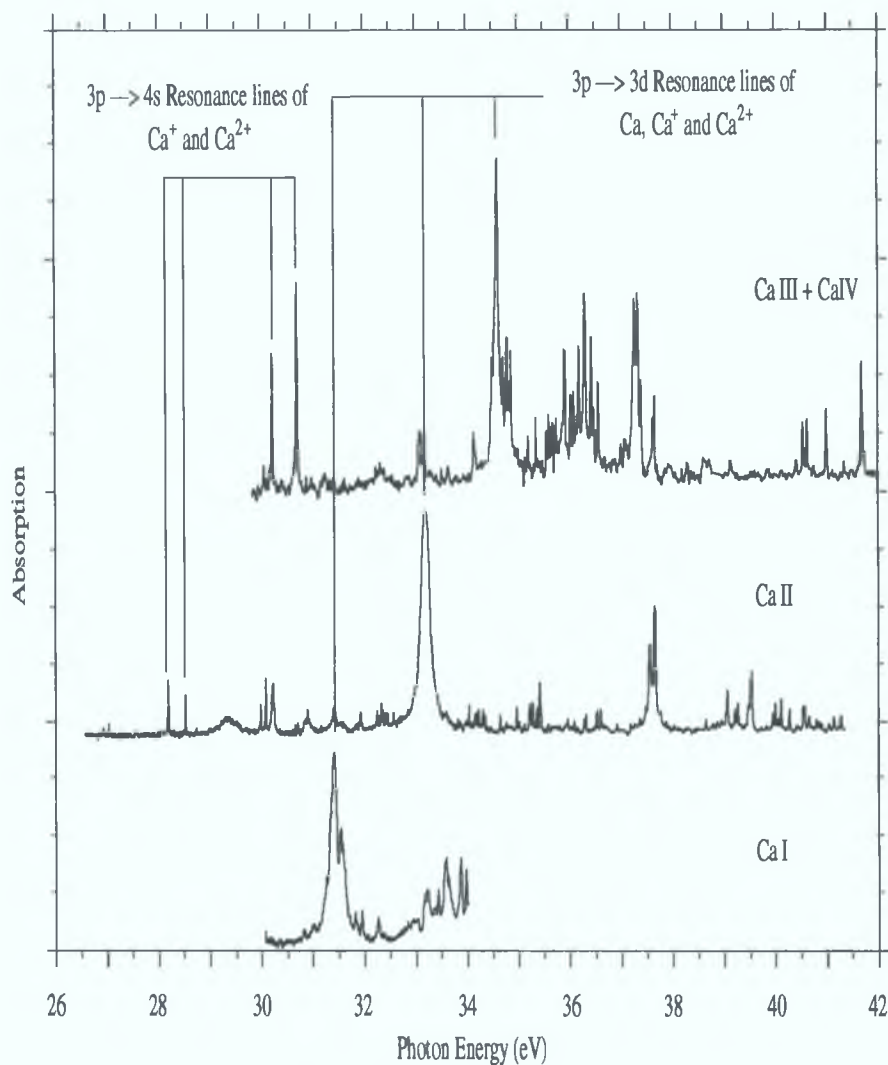


Figure 3.22. Summary of photoabsorption spectra of atomic calcium and its ions in the energy region corresponding to electron excitation from the 3p subshell. The absorbing plasma conditions were $\Delta t = 3.0 \mu\text{s}$, $\Delta x = 2.0 \text{ mm}$ for Ca I, $\Delta t = 0.6 \mu\text{s}$, $\Delta x = 4.0 \text{ mm}$ for Ca II, and $\Delta t = 0.05 \mu\text{s}$ and $\Delta x = 0.5 \text{ mm}$ for Ca III + Ca IV (further optimised to $\Delta t = 0.08 \mu\text{s}$ and $\Delta x = 0.75 \text{ mm}$ in the region of the higher Rydberg members of the Ca III $3pnd$ series; see figure 3.20)

detection. Also the advantages offered by the present experimental setup in terms of control of temporal and spatial probing of the absorbing plume has yielded the possibility of recording very pure ion stage separation, in comparison to other available techniques such as RDLI for example; see figure 3.13. Figure 3.22 summarises the photoabsorption spectra of atomic calcium and its ions, in the energy region of the 3p — 3d ‘giant resonance, recorded in this set of experiments.

The DLP spectrum of neutral calcium was recorded using a dye laser in line focus configuration, to produce the absorbing column, and displays practically no contribution from the next ion stage and is dominated by the main 3p — 3d resonance at 31.4 eV. The relative variation in intensity of the absorption features across the spectrum is a more accurate reflection of the true variation, compared to the photographic measurements by Mansfield and Newsom (1977). The Ca⁺ spectrum was recorded using the Q-switched ruby laser, also in line focus configuration. Again, this spectrum corresponds to absorption from almost pure ground state singly ionized calcium, and is dominated by the main Ca⁺ 3p — 3d resonance at 33.2 eV. Our experience, in general with other elements, e.g. Mosnier *et al.* (1994), is that excited state contributions occur at plasma conditions favouring the production of the next higher ion stage and at spatial positions close (< 0.2 mm) to the absorber target surface. At the plasma conditions used to record the Ca⁺ spectrum, i.e. $\Delta t = 600$ ns and $\Delta x = 4.0$ mm, one would therefore not expect to observe core excitation from any optically or collisionally excited states. The observed spectrum shows good agreement with the absolute photoionization cross section measurements of Ca⁺, measured by Lyon *et al.* (1987) and reveals more underlying structure due to an improved level of resolution and an increase in ion density in the interaction zone.

The photoabsorption spectrum of argon-like Ca²⁺ displays an interesting redistribution of spectral intensity compared to Ca⁺. The 3p — 4s resonance lines, split by the spin orbit interaction of the core, gain appreciably in oscillator strength relative to the main 3p — 3d resonance at 34.61 eV, see figure 3.22. This gain in oscillator strength is associated with a further contraction of the 4s orbital resulting in increased core penetration and overlap with the 3p orbital. This orbital contraction is reflected by the anomalously high value of the average quantum defect for the *ns* Rydberg series. The spectral purity of the Ca²⁺ data has been further improved, in the energy region of the higher members of the 3*pn*d Rydberg series, by increasing the inter-laser time from 50 to 80 ns and by probing the absorbing plume some 0.75 mm from the target surface, see figure 3.20.

3.4. References.

Altun Z. and Kelly H. P., Phys. Rev. A., **31**, 3711, (1985).

Baier S., Fiedler W., Müller B. R., Schulze M., Zimmermann P., Meyer M., Pahler M., Prescher Th., von Raven E., Richter M., Rüder J. and Sonntag B., J. Phys. B: At. Mol. Phys., **25**, 1471, (1992).

Bizau J. M., Gérard P., Wuilleumier F. J. and Wendin G., Phys. Rev. A., **36**, 1220, (1987).

Bizau J. M., Cubaynes D., Richter M., Wuilleumier F. J., Obert J., Putaux J. C., Morgan T. J., Källne E., Sorensen S. and Damany A., Phys. Rev. Lett., **67**, 576, (1991).

Bizau J. M., Cubaynes D., Richter M., Wuilleumier F. J., Obert J., Putaux J. C., Rev. Sci. Instrum., **63**, 1, (1992).

Bridges J. M., Cromer C. L. and McIlrath T., Appl. Opt., Vol. **25**, No. 13, (1986).

Cheng K. T. and Fischer C. F., Phys. Rev. A., **25**, 2811, (1983).

Clark C. W. and Lucatorro T. B., "Giant Resonances in Atoms, Molecules and Solids", Ed. Connerade J. P., Plenum Press, New York, p137, (1987).

Codling K. and Madden R. P., Appl. Opt., **4**, 1431, (1965).

Connerade J. P. and Mansfield M. W. D., Proc. R. Soc. Lon. A., **341**, 267, (1974).

Cowan R. D., "Theory of Atomic Structure and Spectra", (Berkeley, CA: University of California Press), (1981).

Cromer C. L., Bridges J. M., Roberts J. R. and Lucatorro T. B., Appl. Opt., **24**, 2996, (1985).

Dehmer L., Starace A. F., Fano U., Sugar J. and Cooper J. W., Phys. Rev. Lett., **13**, 1521, (1971).

Ederer D. L., Phys. Rev. Lett., **13**, 760, (1964).

Haensel R., Keitel G., Schreiber P. and Kunz C., Phys. Rev., **188**, 135, (1969).

Hansen J. E., Brilly J., Kennedy E. T. and O'Sullivan, Phys. Rev. Lett., **63**, 1934, (1989).

Hamdy H., Beyer H-J., West J. B. and Kleinpoppen H., J. Phys. B: At. Mol. Phys., **24**, 4957, (1991).

Ivanov V. K. and West J. B., J. Phys. B: At. Mol. Phys., **26**, 2099, (1993).

Kastner S. O., Crooker A. M., Behring W. E. and Cohen L., Phys. Rev. A., **16**, 577, (1977).

Kelly R. L., " Atomic and ionic spectrum lines below 2000 angstroms: Hydrogen through Krypton ", Part I (H-Cr), Part II (Mn-Kr) and Part III (Finding List), J. Physical & Chem. Ref. Data, Vol. **16**, supplement No. 1, (1987)

Khan M. A. and Al-Kuhaili M. F., J. Phys. B: At. Mol. Phys., **26**, 393, (1993).

Khan M. A., Khawaja E. E. and Al-Juwair H. A., J. Phys. B: At. Mol. Phys., **23**, L533, (1990).

Köberle H., Diplomarbeit, Universität Hamburg, Int. Bericht Desy F41, HASYLAB 86-03, (1986).

Köble U., Kiernan L. M., Costello J. T., Mosnier J-P., Kennedy E. T., Ivanov V. K., Kupchenko V. A. and Shendrik M. S., *submitted to Phys. Rev. A.* (1994).

Kossmann H., Krässig B. and Schmidt V., J. Phys. B: Atm. Mol. Opt. Phys., **21**, 1489, (1988).

Kurig T., Diplomarbeit, Universität Hamburg, Int. Bericht Desy F41, HASYLAB 86-04, (1986).

Lucatorto T. B., McIlrath T. J. and Roberts J. R., Appl. Opt., Vol. **18**, No. 14 , (1979).

Lucatorto T. B., McIlrath T. J., Sugar J. and Younger S. M., Phys. Rev. Lett., **47**, 1124, (1981).

Lyon I. C., Peart B., Dolder K. and West J. B., J. Phys. B: At. Mol. Phys., **20**, 1471, (1987).

Lyon I. C., Peart B., West J. B. and Dolder K., *J. Phys. B: At. Mol. Phys.*, **19**, 4137, (1986).

Madden R. P. and Codling K., *Phys. Rev. Lett.*, **10**, 516, (1963).

Mansfield M. W. D., *Proc. R. Soc. Lond.*, **A346**, 555, (1975).

Mansfield M. W. D., *Proc. R. Soc. Lond.*, **A348**, 143, (1976).

Mansfield M. W. D., “Giant Resonances in Atoms, Molecules and Solids”, ed. Connerade J. P., (Plenum), New York, (1987).

Mansfield M. W. D., *Hartree-Fock with Exchange calculations performed in 1980, relayed in a private communication 1993*.

Mansfield M. W. D. and Newsom G. H., *Proc. R. Soc. Lond.*, **A357**, 143, (1977).

Mansfield M. W. D. and Ottley T. W., *Proc. R. Soc. Lond.*, **A365**, 413, (1978)

Meyer M., Prescher Th., von Raven E., Richter M., Schmidt E., Sonntag B. F. and Wetzel H. E., *Z. Phys. D.*, **2**, 347, (1986).

Meyer M., Prescher Th., von Raven E., Richter M., Schmidt E., Sonntag B. F. and Wetzel H. E., “Giant Resonances in Atoms, Molecules and Solids”, ed. Connerade (Plenum), New York, (1987).

Morgan H. D. and Ederer D. L., *Phys. Rev. A.*, **29**, 1901, (1984).

Mosnier J-P., Costello J. T., Kennedy E. T., Kiernan L. and Sayyad H. H., *Phys. Rev. A.*, *in press* (1994).

McIlrath T. J. and Carlsen J. L., *J. Phys. B: Atom. Molec. Phys.*, **6**, 697, (1973).

McIlrath T. J. and Lucatorto T. B., *Phys. Rev. Lett.*, **38**, 1390, (1977).

Nakamura M., Sasamuma M., Sato S., Watanabe M., Yahmashita H., Iguchi Y., Ejiri A., Nakai s., Yamaguchi S., Sagawa T, Nakai Y. and Oshio T., *Phys. Rev. Lett.*, **21**, 1303, (1968).

Pejcev V., Ottley T. W., Rassi D. and Ross K. J., *J. Phys. B: At. Mol. Phys.*, **11**, 531, (1978).

Powell F R , Vedder P W , Lindblom J F and Powell S F , Opt Eng , Vol 29, No 6, (1990).

Rabe P , Radler K and Wolff H W , 9th international conference on Vacuum Ultraviolet Radiation Physics, Hamburg, (1974)

Samson J. A , “ Techniques of Vacuum Ultraviolet Spectroscopy “, Wiley & Sons (1967)

Sato Y , Hayaishi T , Itikawa Y , Itoh Y , Murakami J , Nagata T , Sasaki T , Sonntag B , Yagishita A and Yoshino M , J Phys B At Mol Phys , 18, 225, (1985)

Sonntag B and Zimmermann P , Rep Prog Phys , 55, 911, (1992)

Sonntag B F , Cromer C L , Bridges J M , McIlrath T J and Lucatorto T B , AIP Conf Proc , 147, 412, (1986)

Tondello G , Optica ACTA, Vol 20, No 3, 357, (1979)

Ueda K , West J B , Ross K J , Hamdy H , Beyer H J and Kleinpöppen, *submitted to Phys Rev A June, 1993*

Wuilleumier F J , Cubaynes D and Bizau J M , “ Atomic and Molecular Physics Third US-Mexico Symposium ”, eds Cisneros C , Alvarez I and Morgan T J (World Scientific Publishing Company Singapore), p474, (1991)

Zimkina T M , Fomichev V A , Gribovskii S A and Zhukova I I , Sov Phys -Solid State, 9, 1128, (1967)

Chapter 4

Photoabsorption Spectrum of Atomic
Zinc and its Ions (Zn^{n+} $n=1,2,3$), in the
Region of 3p Electron Excitation.

4.1. Introduction.

The main aim of this chapter is to describe the photoabsorption spectra of atomic zinc and its ions in the photon energy region corresponding to excitation from the 3p subshell, recorded using the dual laser plasma technique coupled with photoelectric registration.

In their comprehensive review of the XUV spectroscopy of metal atoms, Sonntag and Zimmermann (1992), show that for the 3d transition metals, as long as the 3d shell is unfilled, the lowest members of the Rydberg series of 3p core excited states autoionize into the $4s^{-1}$ and $3d^{-1}$ valence and subvalence channels. This produces strong broad absorption features with varying degrees of asymmetry along the transition metal sequence (see figure 3.5a). Following on from nickel, along the sequence there are the noble metals the first of which is copper, with ground state $3p^6 3d^{10} 4s^2 \ ^1S_0$. Because the 3d subshell is full only the weaker $3p \rightarrow ns$ ($n \geq 4$) transitions are expected to give rise to absorption features in the energy region corresponding to 3p electron excitation. The profile of the $3p \rightarrow 4s$ resonances in the total and partial cross sections is determined by the probabilities for autoionization or Auger decay, e.g. super Coster-Kronig processes, of the resonances.

For atomic zinc, ground state $3p^6 3d^{10} 4s^2 \ ^1S_0$ the 4s shell is full and as a consequence the photoabsorption spectra along this isonuclear sequence, in the region of 3p excitation, should yield dramatically contrasting spectral signatures, ranging from the situation for Zn I where excitations $3p \rightarrow 5s$ are strongest, to Zn IV where the 3d shell is open and transitions of the type $3p \rightarrow 3d$ predominate. A series of survey experiments were first carried out, varying inter-laser time delay, laser irradiance and absorbing plasma spatial position before optimisation of the absorbing plasma conditions to maximise the purity of the absorption spectra for each ion stage along the isonuclear sequence. Photoabsorption results are presented for Zn I, II, III and IV, also included are *ab initio* Hartree-Fock calculations using the Cowan code (1981) which is used to determine the expected trends in transition energies and line intensities along the isonuclear sequence.

4.2. Review of Work to Date on Subvalence Excitations of Atomic Zinc.

4.2.1. Excitation from 3d Subshell.

Beutler and Guggenheimer (1933) were the first to investigate the absorption spectrum of atomic Zn below 900 Å. They observed five Rydberg series of absorption lines converging on the $3d^9 4s^2 \ ^2D_{3/2,5/2}$ levels of Zn II and identified them as excitations of a 3d-subshell electron to np and nf states. In their analysis of this spectrum they assumed that the 4s valence subshell remains undisturbed. Garton and Connerade (1969) repeated Beutler and Guggenheimer's measurements with greater resolution and an increased length of absorption column. They were able to extend substantially the number of observed transitions and also revised Beutler and Guggenheimer's analysis, showing in particular that the JK coupling scheme is more appropriate to this spectrum than the LS scheme used by Beutler and Guggenheimer.

Absolute photoionization cross section measurements in the range 790 to 1320 Å were reported by Marr and Austin (1969) who measured photoionization cross sections for both the continuum and the more intense $3d^{10} 4s^2 \ ^1S_0 \rightarrow 3d^9 4s^2 \ np \ (J=1)$ resonances. This provided impetus for calculations using many-body perturbation theory by Fliflet and Kelly (1974) who reproduced the main features of Marr and Austin's data .

Although Beutler and Guggenheimer were aware, from a consideration of the zinc spark spectrum (Zn II), of the possibility of resonances due to the simultaneous excitation of the two valence electrons in this energy region, they found no experimental evidence for such a process. Double excitations in Zn I were not detected by Garton and Connerade (1969). This failure to observe double electron resonances was attributed to the nature of the background continuum sources and to the low zinc vapour pressures used. Mansfield and Connerade (1978), using the featureless background continuum provided by the 500 MeV Bonn synchrotron, reported the observation of more than 120 Zn I two electron resonances. They measured the absorption spectrum of Zn I between 400 and 1000 Å, dividing the lines broadly into two distinct groups. One group at longer wavelength (900-990 Å), due to the simultaneous excitation of the two valence electrons, and a shorter wavelength group (420-610 Å), attributed to the simultaneous excitation of one valence and one subvalence subshell electron.

Back *et al.* (1981) reported the ejected-electron spectrum of zinc vapour, arising from autoionising transitions excited by electron impact. They were able to identify most ejected electron lines by comparison with the autoionising spectrum of Zn I as revealed in the vacuum ultraviolet photoabsorption measurements. These photoabsorption experiments were limited to the autoionising levels of Zn I which could be excited by absorption of a photon from the ground state, i.e J=1 levels of odd-parity configurations. In the experiments of Back *et al.*, a number of additional lines appeared which were attributed to autoionization of 'optically forbidden' Zn I levels. Mansfield (1981) in his analysis of these features used *ab initio* Hartree-Fock programs to calculate the even-parity configurations. Peart *et al.* (1987) measured the absolute photoionisation cross section of singly ionised zinc atoms (Zn II) in the energy range 21.7 to 27.9 eV, above the 4s thresholds. They made the remark that there seemed to be no calculations or measurements of autoionization structures in Zn II with which to compare their results, apart from the study of electron impact ionization of Zn⁺ by Rogers *et al.* (1982), which was recorded at somewhat lower energies. Cowan and Wilson (1988) replied by providing *ab initio* calculations of the positions of core-excited level structures of the type 3d⁹4s np,mf .

Most recently Svensson *et al.* (1993), reported the measurement of the valence photoelectron spectrum of atomic zinc using monochromatised synchrotron radiation. The photoelectron spectra were recorded at photon energies in excess of the double ionization threshold of neutral zinc (27.35 eV). In addition to the main 3d⁻¹ and 4s⁻¹ photolines, shake up (3d⁹4s(n + 1)s) and conjugate shake up (3d⁹nsnp and (n + 1)p) satellite lines were observed. The conjugate shake up process results in an ionic excited state of ²D or ²P character. In the latter case the state can couple to the underlying double ionization continua 3p⁶3d¹⁰ εl ε'l' ²P causing an asymmetric profile to be observed in their photoelectron spectra. In the light of this interaction between the process of direct double ionization and the populating of an ionic excited state, lying just above the shake off threshold, the authors conclude that such interactions affect the normal partitioning in excess energy between the two outgoing electrons.

4.2.2. Excitation from 3s Subshell.

Structure in the Zn I absorption spectrum associated with the excitation of the 3s subshell was first observed by Connerade and Mansfield (1974). In their paper they reported 3s structure between 70 and 105 Å in Zn vapour observed using the continuous radiation of the Bonn synchrotron as the background source. They interpret

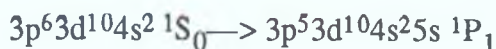
this structure in terms of a series of upper levels of the configuration, $3s3p^64s^2 nl$ converging on the $3s\ ^2S_{1/2}$ limit. In their tabulation of X-ray atomic energy levels, Bearden and Burr (1967) predicted absorption edges at $135.9\text{ eV } \Delta E \pm 1.1\text{ eV}$ (3s) and at $86.6\text{ eV } \Delta E \pm 0.6\text{ eV}$ (3p), although it is not quite clear whether the predictions apply to the atom in the vapour or in the solid owing to the mixture of data in their interpolation. Lotz (1970) attempted to correct Bearden and Burr's tables and lists binding energies for free atoms. For Zn I, Lotz gives 141 eV and 94 eV (M2), 91 eV (M3) $\Delta E \pm 2\text{ eV}$ in each case. Connerade and Mansfield (1974) performed a Hartree-Fock calculation with the computer code of Froese Fischer and yielded a wavelength of 87.5 \AA for the $3s \rightarrow 4p$ transition against an experimental wavelength of about 88.6 \AA . On calculating the 3s limit they placed it at 85.3 \AA - almost exactly the experimental value.

As mentioned before, Fliflet and Kelly (1974) using MBPT reproduced the main features of Marr and Austin's photoabsorption measurements in the 3d region. Fliflet and Kelly (1976), again using MBPT extended their results to 1000 eV by calculating the photoionisation cross sections of the 3p and 3s subshells, and quoted electron removal energies of 87.1 and 137 eV for the 3p and 3s subshells respectively, while failing to make reference to the experimental determination of 3s limit at 145.3 eV by Connerade and Mansfield two years previously.

4.2.3. Excitation from 3p Subshell.

To date there has been no attempt to measure the 3p photoabsorption spectrum of atomic zinc. As mentioned above, Connerade and Mansfield (1974) recorded the 3s photoabsorption spectrum but did not extend their measurements to longer wavelengths to investigate the 3p absorption spectrum. In a recent discussion with Connerade (1993), he cited three main reasons, firstly the fall-off in synchrotron intensity and grating efficiency towards longer wavelengths, secondly grating order sorting problems in this region and finally the inherent weak nature of the 3p inner shell transitions.

The energy position of the $3p \rightarrow 5s$ resonance transition has been the subject of a number of conflicting calculations. In their 1978 paper, Mansfield and Connerade, report that their Hartree-Fock calculations place the lowest energy Zn I 3p subshell transitions,



at about 95 eV. Using the MBPT approach, Fliflet and Kelly (1976) calculated that the $3p \rightarrow 5s$ resonance line should be located at 83.7 eV.

In a very recent series of experiments, Adam *et al.* (1994) at the Super ACO synchrotron facility in Paris, have located the energy positions of the $3p^5 3d^{10} 4s^2 ns$ (and nd) core excited states in the 91-99 eV region. These measurements were achieved by exciting the M shell of atomic zinc in the 80-110 eV photon energy range with synchrotron radiation and by using photoelectron and photoion detection to determine the decay kinetics of the 3p core holes. Adam *et al.* (1994) have also performed *ab initio* calculations using intermediate coupling, where the ground state is assumed to be well described by the $3p^6 3d^{10} 4s^2 (1S)$ configuration, which display good quantitative agreement with their experimental results. The importance and relevance of these complementary measurements will be discussed in further detail, in the context of the high resolution photoabsorption data obtained independently using the DLP technique.

Before proceeding directly to the description of the measurement of the photoabsorption spectra of atomic zinc and its ions in the region of 3p excitation, it is worthwhile to outline the predicted behaviour of electron excitation from the 3p subshell along this isonuclear sequence. A series of *ab initio* Hartree-Fock calculations were performed using the Cowan suite of codes (Cowan 1981) to determine the approximate transition energies and relative oscillator strengths of the main 3p resonances for each ion stage. The results of these calculations are summarised in figures 4.1 and 4.2. The stick plot shown in the lower half of figure 4.1 shows the predicted *gf* values and relative energy positions of the 3p resonances. In each case the calculated absolute transition energies have been reduced by 2.9 eV. This constant shift yields very good agreement in terms of correspondence of excitation energies, between the observed and calculated spectra.

Because the measured spectra represent the relative absorption cross section the *gf* values have been normalised to the respective intensities of the main 3p resonance line in each spectrum. One should also note that the photoabsorption spectra have been scaled by various factors (shown on each spectrum) to show the structure more clearly.

Figure 4.2 shows the energy level structure of this isonuclear sequence in both the valence and subvalence regimes. The upper half of figure 4.2 shows the calculated relative positions of the onset of 3p excitation above the ground states of each ion. The numbers beneath the calculated 3p excitations refer to appropriately labelled transition energies given in subsequent tables. The lower half of the figure has been constructed from the excitation energies of 3d and 4s transitions listed in Moore's tables (1958) and shows the ionization potential of each ion stage up to Zn^{3+} . Also shown are the lowest

excited state levels, in the case of each ion, whereby core excitation of a 3p electron can take place to an open 4s or 3d shell.

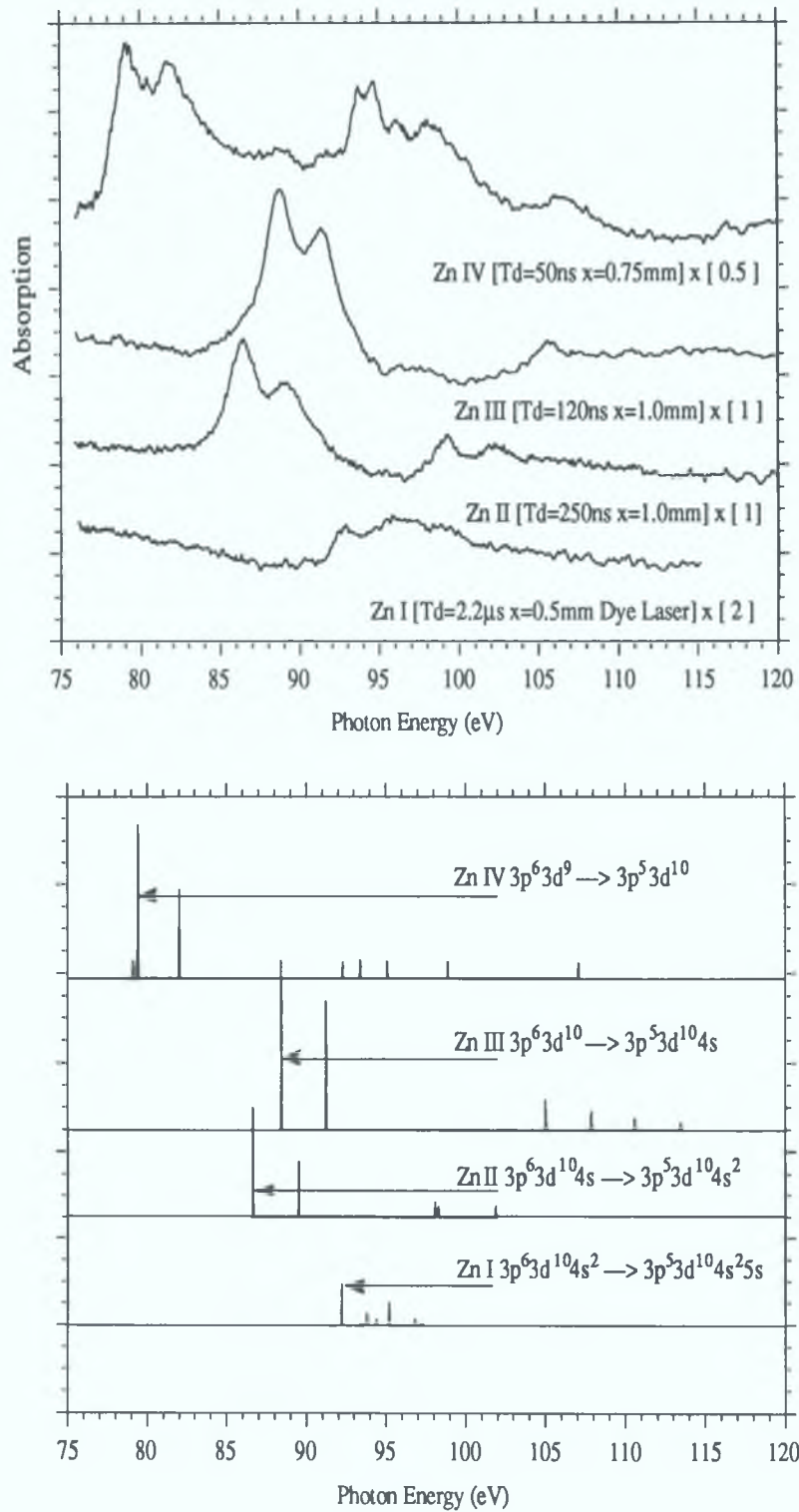


Figure 4.1. Comparison of observed spectra with the calculated transition energies and oscillator strengths.

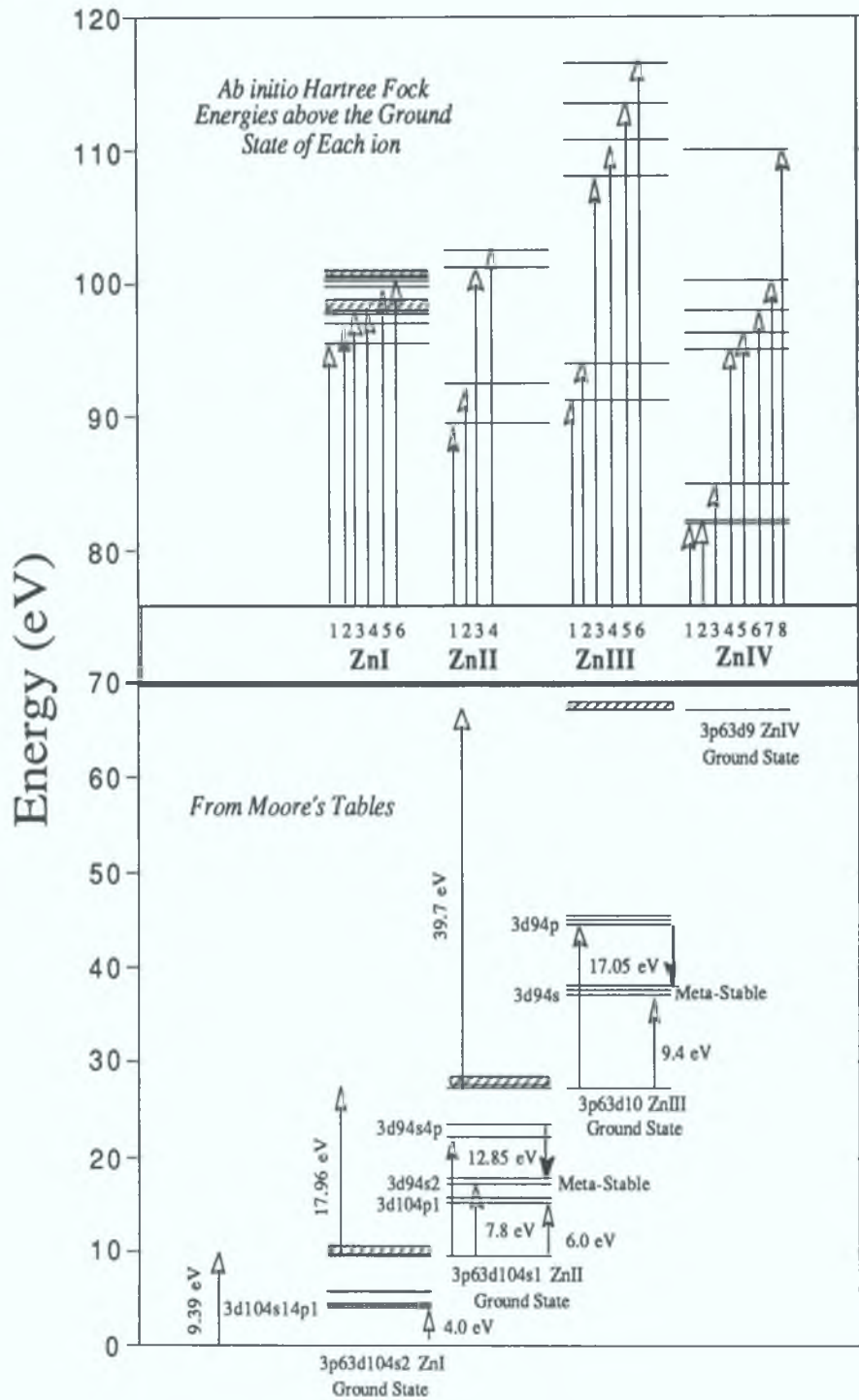


Figure 4.2. Energy level diagram, in the valence (lower half) from Moore (1958) and subvalence energy regions, with respect to the ground state of each ion.

4.3. Photoabsorption Spectrum Of Zn I, in the Region of 3p Excitation.

In order to determine the appropriate absorbing plasma conditions to yield the neutral zinc spectrum, i.e. laser power density, inter-laser time delay (T_d) and distance from the surface of the absorber target to the optical axis (Δx), initially the spectrum was examined in the energy region of 3s excitation, already measured by Connerade and Mansfield (1974). Figure 4.3 shows the photoabsorption spectrum of Zn I in the 3s region (before and after smoothing performed with a moving average type filter) as determined by using the DLP technique.

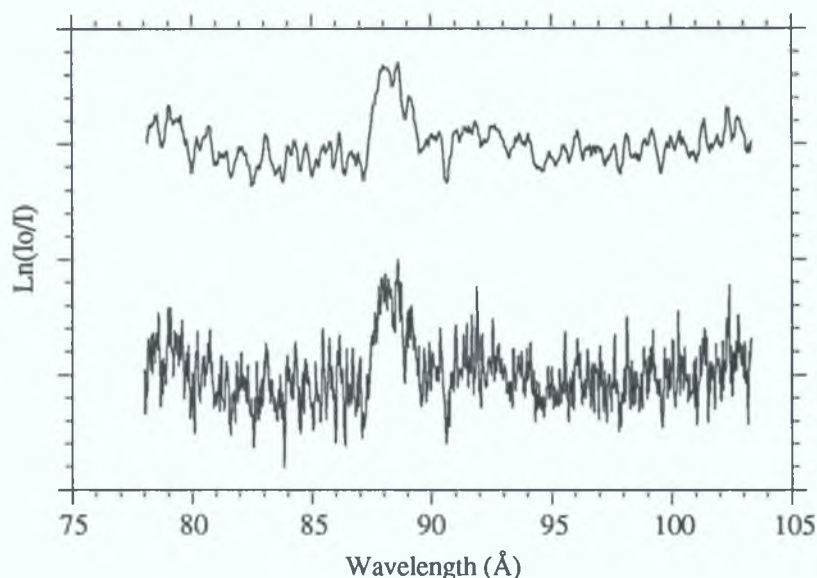


Figure 4.3. 3s photoabsorption spectrum of Zn I ($T_d=2.2 \mu s$, $\Delta x=0.5 \text{ mm}$).

The broad weak structure in the centre of the spectrum can be attributed to the $3s^2 3p^6 3d^{10} 4s^2 \rightarrow 3s 3p^6 3d^{10} 4s^2 4p$ core excited resonance transition (Connerade and Mansfield $88.6 \pm 0.5 \text{ \AA}$). The wide breadth of the feature may be interpreted as a consequence of the very fast decay of the 3s hole through super Coster-Kronig recombination processes. An unscaled Cowan code calculation predicts the oscillator strength for the 5p member of the series to be almost a factor of ten smaller than for the resonance $3s \rightarrow 4p$ transition. This would place the expected feature within the noise level of the data and, coupled with broadening effects, may explain why the 5p transition is not observed.

Having determined the most appropriate plasma conditions necessary to obtain the photoabsorption spectrum of Zn I in the 3s region, by first finding the optimum inter laser time delay and absorbing plasma spatial position, photoabsorption experiments were performed in the region of the 3p resonance. Using a Dye laser in line focus configuration, length of absorbing column 15 mm approximately, the spectrum in figure 4.4 was recorded.

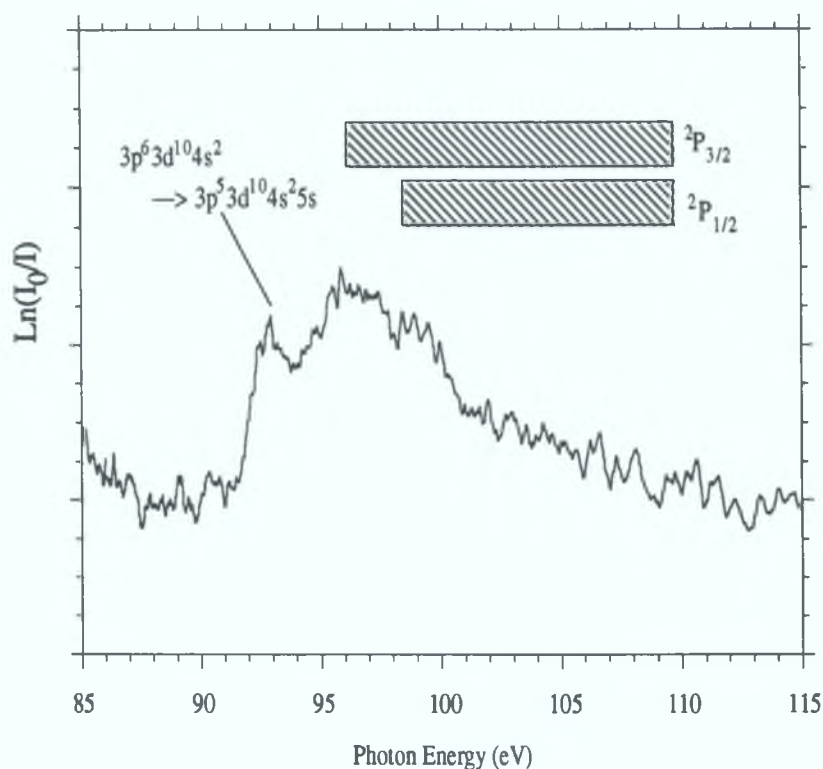


Figure 4.4. Photoabsorption spectrum of Zn I, in the 85-115 eV energy region, where the absorbing plasma was generated using a dye laser focused to a line, at an inter-laser time delay of 2.2 μ s and probed 0.5 mm from the target surface.

Our experimental data shows, as expected, some weak modulations superimposed on the continuous 3d absorption background. Table 4.1 in conjunction with the calculated energy level diagram - figure 4.3, summarises the observed and calculated features for absorption from ground state Zn I. The 3p transitions indicated numerically from 1 to 6 above the ground state level of Zn I correspond to the configurations labelled 1 to 6 in table 4.1. Coster-Kronig decay processes produce a large broadening of the 3p core excited states which form a series of overlapping states running up to two closely spaced limits, $2P_{3/2}$ and $2P_{1/2}$, of Zn II at 96.1 and 98.9 eV (Adam 1994) respectively. Due to the number, breadth and weak intensity of these features only the 3p \rightarrow 5s resonance line appears to be resolvable. Only the $3p^5 ns$

transitions have been included in the table as these have much more oscillator strength associated with them than the $3p^5nd$ resonances. This is consistent with the rule that the oscillator strength of $l \rightarrow l+1$ transition is primarily in the continuum whereas $l \rightarrow l-1$ transitions have less continuum oscillator strength (Fliflet 1976)

Configuration	E_{Obs} (eV)	Γ (eV)	E_{Cowan} (eV)	E_{Adam} (eV)	gf
Zn I— $3p^63d^104s^2$ 1S_0					
1 $3p^53d^104s^25s$ 1P_1	93.08	2.2 ± 0.2	95.1	93.18	0.0091
2 $3p^53d^104s^25s$ 3P_1			98.1	95.98	0.0049
3 $3p^53d^104s^26s$ 1P_1			96.7	94.76	0.0027
4 $3p^53d^104s^26s$ 3P_1			99.7	97.56	0.0014
5 $3p^53d^104s^27s$ 1P_1			97.3	95.32	0.0012
6 $3p^53d^104s^27s$ 3P_1			100.2	98.13	0.0006

Table 4.1 $3p \rightarrow ns$ resonances of atomic zinc

Using a synchrotron crossed atomic beam experimental system, Adam *et al* (1994) have measured the PES (Photoelectron Emission Spectrum) and the double and single photoionization yield of atomic zinc in the photon energy region of $3p$ excitation and ionization. The monochromatic XUV light (bandwidth ≈ 0.1 to 0.3 eV) was focused onto the interaction zone approximately 10 mm from the exit nozzle of a resistively heated graphite cell. The ions were extracted from the interaction zone and detected with a time-of-flight mass spectrometer. Collecting the outgoing ions Zn^n allows for the determination of the cross sections $\sigma_{\text{ion}}(Zn^n)$ for the production of ions with charge n . In the XUV, autoionization and Auger decay are predominant over fluorescent decay and therefore the relation,

$$\sigma_a = \sum_n \sigma_{\text{ion}}(Zn^n) \quad (4.1)$$

holds very well. These cross sections should not be confused with the normal one or two electron photoionization cross sections $\sigma(Zn^+)$ and $\sigma(Zn^{++})$ describing the probability for the direct emission of one electron,



or two electrons,



by one incident photon. If, for example, the singly charged core excited ions decay via the Auger transition,



the photoionization cross section $\sigma(\text{Zn}^+)$ is equal to the cross section $\sigma_{\text{ion}}(\text{Zn}^{++})$ describing the probability for creating a doubly charged ion. To a good approximation the relation,

$$\sigma_a = \sigma(\text{Zn}^+) + \sigma(\text{Zn}^{++}) \quad (4.5)$$

is valid. Deviations only occur for excitations into discrete states which decay via fluorescence emission. Therefore in this energy region the total ion yield, for doubly and singly charged zinc ions after photon excitation, should be approximately the same as the total cross section as measured in our photoabsorption experiment. Curve a, in

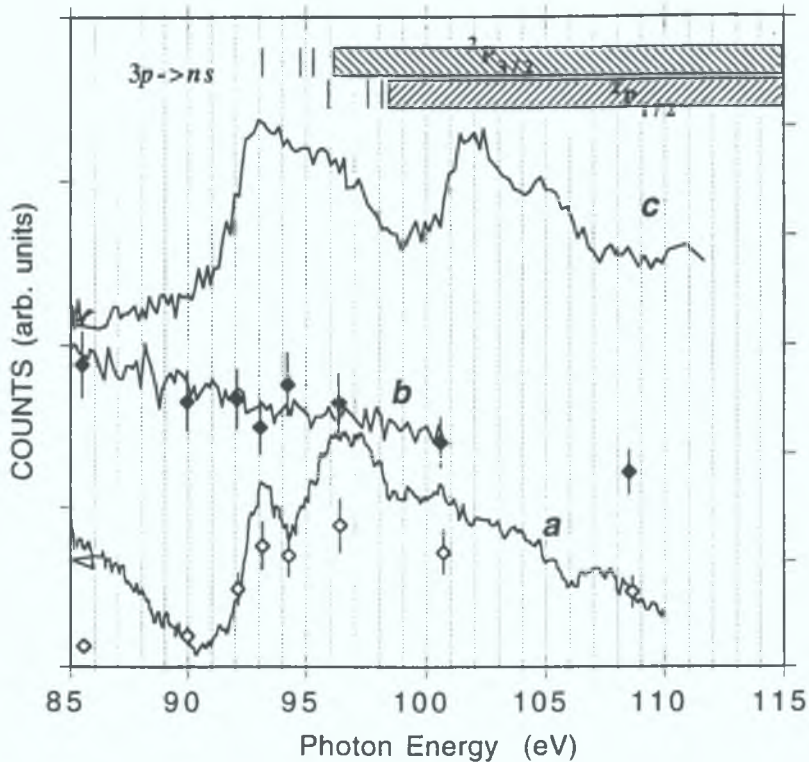
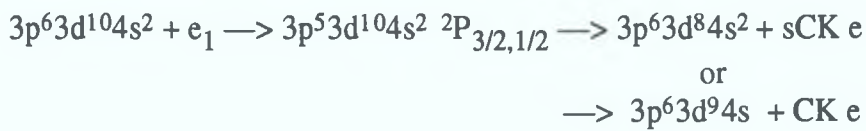


Figure 4.5. Curve a: total ion yield; curve b: Constant Ionic State Spectrum of the $3d^{-1}$ photoline ; curve c : Constant Kinetic Energy Spectrum recorded at 5.6 ± 0.35 eV electron energy. The tick marks indicate the resonance energies of $3p \rightarrow ns$. The hatched horizontal bars locate the continua with $3p^{-1} ({}^2P_{3/2,1/2})\epsilon l$ configurations (after Adam *et al.* 1994).

figure 4.5 is the total ion yield, corresponding to expression (4.5) as measured by Adam *et al.* (1994), and shows evidence of resonant processes for atomic Zn in the 80 to 115 eV photon energy range. The enhancement in the total ion yield centred at 93 eV is entirely due to a corresponding increase in the number of Zn^{2+} ions detected at that energy. This is due to the preferential decay of the core excited states $3p^5 3d^{10} 4s^2 ns$ and nd , to doubly charged ions. The large enhancement centred around 96 eV may be explained by the contributions of 1P and 3P excited states corresponding to a $3p \rightarrow ns$ ($n \geq 6$) electronic transition, but also by the contribution of the $3p^{-1} \ ^2P_{3/2}$ partial photoionization cross section since the threshold of this ionic state is located at approximately 96.1 eV. Comparison of the total ion yield curve with the $3p$ photoabsorption data, measured using the DLP technique, figure 4.4, reveals very good agreement between the two complementary techniques.

Mehlhorn *et al.* (1977), have measured the decay of the $3p$ core hole, created through the process of electron impact ionization, i.e.



for atomic zinc. Figure 4.6 shows the measured electron energy distribution curve after

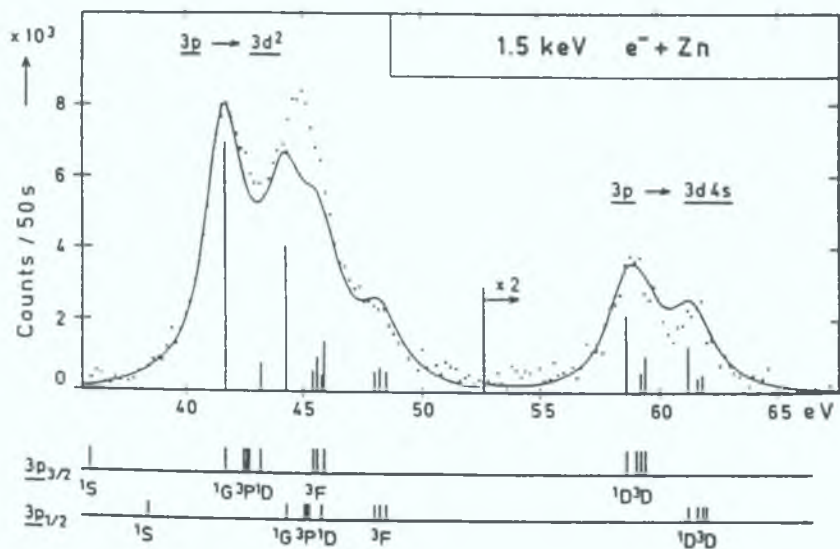


Figure 4.6. Measured electron energy distribution curve after impact ionization of free zinc atoms using 1.5 keV electrons. The stick plot indicates the theoretical relative intensity contributions of each decay channel. The solid line is the theoretical spectrum assuming a level width of $\Gamma(^2P_{1/2}) = \Gamma(^2P_{3/2}) = 2.1 \pm 0.2$ eV, (after Mehlhorn *et al.* 1977).

impact ionization using 1.5 keV electrons. Coster-Kronig (CK) and super Coster-Kronig (sCK) transitions are of special importance because of their much larger transition probabilities compared to Auger transitions. Assuming Lorentzian line shapes for the individual components contributing to the total spectrum, the best fit to the experimental intensity distribution (solid line in figure 4.6) yielded a level width $\Gamma(^2P_{1/2}) = \Gamma(^2P_{3/2}) = 2.1 \pm 0.2$ eV, which agrees very well with the width obtained for the 1P level from the DLP photoabsorption results. In addition, Mehlhorn *et al.* (1977) showed that this level width is in good agreement with the solid state value indicating that the total transition rate changes only very little between the free Zn atoms and the Zn atoms in the solid state.

4.4. Photoabsorption Spectrum Of Zn II, in the Region of 3p Excitation.

Singly ionized zinc, Zn II, is the isoelectronic equivalent of Cu I having a ground state configuration of $3p^6 3d^{10} 4s^1 \ ^2S_{1/2}$, where one of the valence 4s electrons has been removed. In the case of Zn I the outer shell is closed and the first allowed

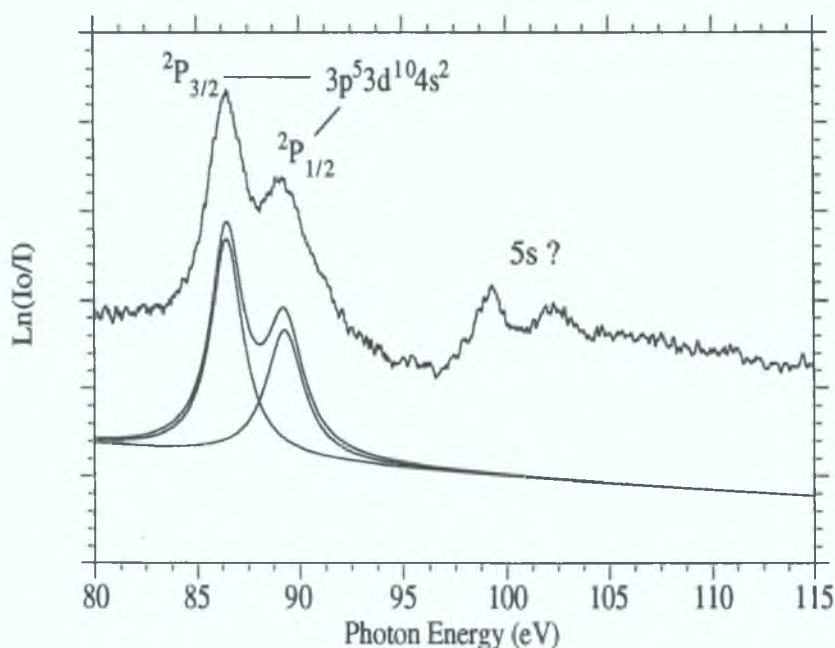


Figure 4.7. Photoabsorption spectrum, upper curve, of singly ionized zinc in the energy region of 3p excitation. The lower curve is the superposition of two Lorentzian profiles resolved into their respective peaks describing the main $3p \rightarrow 4s, ^2P_{3/2}, ^2P_{1/2}$ resonance transition.

excitation from the 3p shell is to the 5s level, whereas in the case of Zn II the first allowed transition is to the 4s level. Therefore, from table 4.2, one would expect to observe a significant increase in oscillator strength for the resonance transition $3p \rightarrow 4s$, which should be composed of two peaks due to spin orbit interaction within the excited state configuration. In order to create an absorbing column of Zn II the Dye laser was replaced by a Q-switched ruby laser and the plasma temporal and spatial conditions optimised to $T_d = 250$ ns and $\Delta x = 1.0$ mm.

Bruhn *et al.* (1979) have measured, photographically, the photoabsorption spectrum of atomic copper in the region of 3p excitation, from 60 to 85 eV approximately. The copper vapour was contained in a heat pipe and a synchrotron source was used to backlight the sample cell. The measured spectrum is shown in figure 4.8 and displays two broad predominating symmetric peaks superimposed on the monotonically decreasing background of the $3d\epsilon f$ continua. This spectrum bears striking resemblance to the 3p spectrum of Zn II, figure 4.7, as measured using the DLP technique.

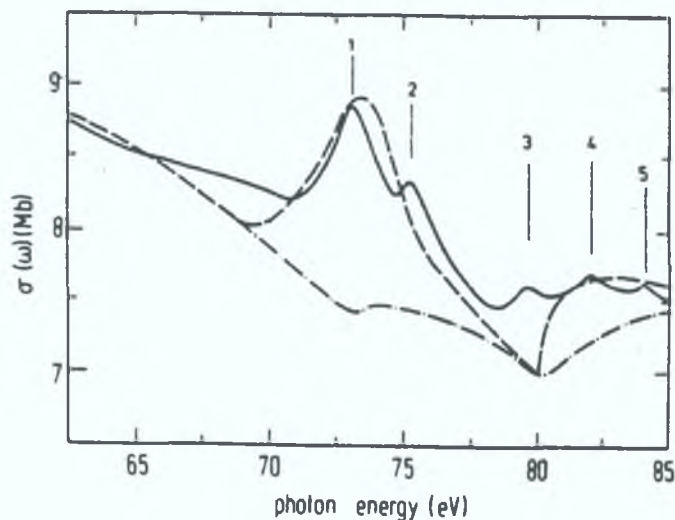


Figure 4.8. Relative copper vapour absorption spectrum in the 3p excitation region (Bruhn *et al.* 1979). Calculated total photoabsorption cross section including Auger decay of the 3p hole (—) and 3d partial cross section (---) (Zangwill and Soven 1981). The absolute cross section only refers to the calculated spectra (after Sonntag and Zimmermann 1992).

Interaction between the $3p \rightarrow 4s$ discrete transition and the $3d \rightarrow \epsilon l$ continuum in Zn II, is weaker than the interaction between the $3p \rightarrow 3d$ resonance and 3d continuum in the open 3d shell transition metals, refer to figure 3.5a, where this

interference in the cross section can give rise to asymmetric line shapes. Indeed, Köberle (1985) and Kurig (1985) showed that the photoabsorption spectra of the atoms Cr to Ni could be well approximated by a superposition of Fano profiles sitting on a constant background. The weaker interaction of the 3p → 4s level results in a more symmetric type profile superimposed on the monotonically decreasing background of the 3d continuum. Thus, for Zn II the main resonance profiles could be best described by two Lorentzian curves positioned at 86.45 and 89.27 eV, of FWHM 1.9 and 2.1 eV respectively, sitting on an monotonically decreasing background, curve fitted with the expression,

$$\sigma_{\text{total}} = A E^{(-B)} + \sum_{i=1 \text{ to } 2} C_i (1/(1+(((E-E_{0i})/\Gamma_i/2)^2)))$$

where Γ_i and E_{0i} are the full width at half maximum and centre energy position of the resonance respectively and σ_{total} is the total absorption in the energy window of interest: see lower curve in figure 4.7.

With the removal of one of the 4s electrons, Cowan code calculations indicate that the onset of 3p absorption,



in Zn II should be about 6 eV below the onset of 3p absorption in Zn I, relative to the ground states of each ion stage, with the $^2\text{P}_{3/2}$, $^2\text{P}_{1/2}$ components having a spin orbit splitting of about 2.9 eV. From the limits of the 3p → ns series in Zn I, i.e. $3p^5 3d^{10} 4s^2 \text{ } ^2\text{P}_{3/2,1/2}$, determined to be at approximately 96.1 and 98.7 eV respectively by Adam *et al.* (1994), the energies of the 3p → 4s $^2\text{P}_{3/2,1/2}$ transitions of Zn II can be calculated by simply subtracting the first ionization potential of Zn I (9.4 eV) from the values of the series limits. This would place the 3p core excited states, Zn II $3p^5 3d^{10} 4s^2 \text{ } ^2\text{P}_{3/2,1/2}$ at approximately 86.7 and 89.3 eV above the ground state of the ion. Table 4.2 summarises the results of calculations on ground state absorption of Zn II, indicating the positions and widths of the $^2\text{P}_{3/2}$, $^2\text{P}_{1/2}$ resonance lines as determined by the above curve fit procedure. Good agreement is observed between the calculated and experimental value for the spin orbit splitting of the resonance line. The ratio of the oscillator strengths between the $^2\text{P}_{3/2}$ and $^2\text{P}_{1/2}$ components is calculated to be 0.52, close to the statistically weighted ratio of 2:1. Since the natural widths of the lines are approximately equal and the instrumental broadening is negligible compared to the Auger width, the amplitudes of the curvefitted Lorentzian profiles should be proportional to their *gf* values. From the curve fit data, the ratio of the amplitudes of

the peaks is 0.60 and is, therefore, in reasonable agreement with the calculated ratio.

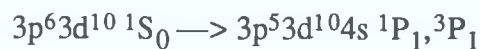
Configuration	E_{Obs} (eV)	Γ (eV)	E_{Cowan} (eV)	E_{MCDF} (eV)	gf
Zn II-- $3p^63d^{10}4s^1\ ^2S_{1/2}$					
1 $3p^53d^{10}4s^2\ ^2P_{3/2}$	86.45	1.9 ± 0.3	89.5	87.0	0.1449
2 $3p^53d^{10}4s^2\ ^2P_{1/2}$	89.27	2.1 ± 0.3	92.4	90.2	0.0745
3 $3p^53d^{10}4s5s\ ^2P_{3/2}$	99.00		101.2		0.0150
4 $3p^53d^{10}4s5s\ ^4P_{3/2}$	102.0		104.8		0.0154

Table 4.2. $3p \rightarrow ns$ resonances of singly ionized zinc, the nd resonances have been found to have negligible oscillator strength in comparison, and so have been omitted.

It should be noted from the valence section of the energy level diagram, figure 4.2, that the first optically excited state, $3d^{10}4p$ of Zn II is about 6 eV above the ground state and that the first state where there is a hole in the 3d shell, which is parity forbidden, occurs about 7.8 eV above the ground state, hence the high purity of the ground state spectrum observed.

4.5. Photoabsorption Spectrum Of Zn III, in the Region of 3p Excitation.

Zn III has a closed shell configuration in its ground state of, $3p^63d^{10}\ ^1S_0$ where both of the 4s valence electrons have been removed. Our Cowan code calculations predict that the onset of 3p absorption in Zn III,



should be approximately 2 eV above the onset in Zn II, with respect to their ground states: refer to figure 4.3, and that the spin orbit splitting between the 1P_1 and 3P_1 components should be 2.8 eV. Having optimised the plasma conditions in the absorbing column, using the ruby laser, to $T_d = 120$ ns and $\Delta x = 1.0$ mm the absorption spectrum of Zn III was recorded: see figure 4.9.

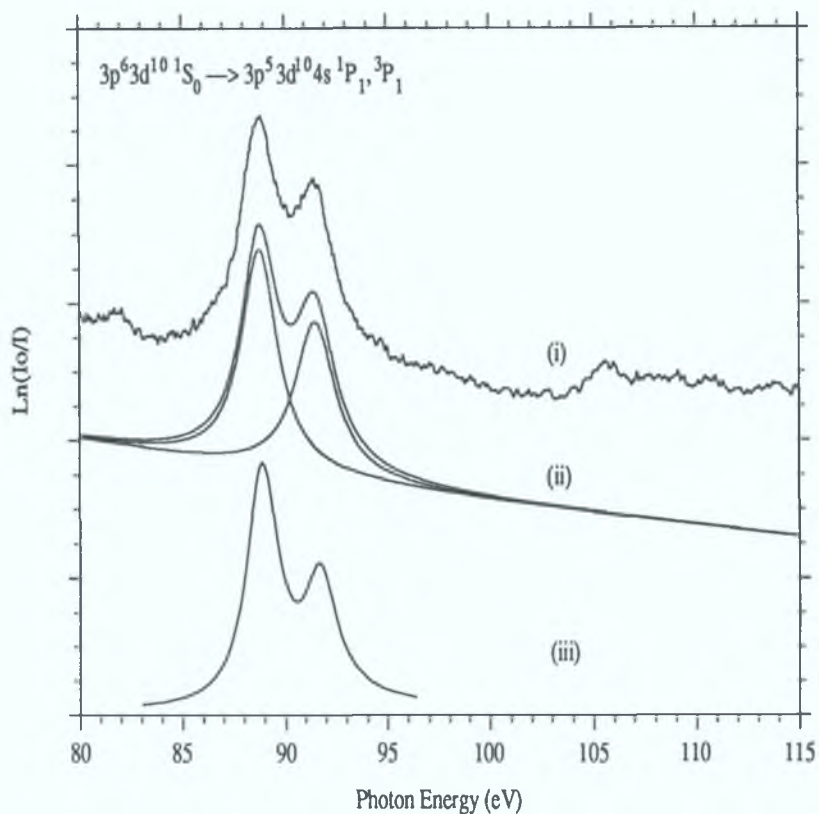


Figure 4.9. Curve (i): photoabsorption spectrum of Zn III from 80-115 eV, (ii) Lorentzian curve fit to main resonance transition $3p \rightarrow 4s$, showing components of superposition, (iii) RPAE calculation of total cross section in the region of the $3p$ resonance (after Ivanov 1993).

The same curve fitting routine was applied to this data where it was assumed that the two main peaks could be best described by Lorentzian curves superimposed on a monotonically decreasing background. Table 4.3 in conjunction with the energy level diagram, figure 4.2, summarises the results of calculations on ground state absorption of Zn III indicating the positions and widths of the 1P_1 , 3P_1 resonance lines as determined by the above curve fit procedure.

As in the case of Zn II, because the spin orbit components of the $3p \rightarrow 4s$ are approximately the same width, the ratio of the amplitudes of the resolved Lorentzian profiles should be proportional to the ratio of the gf values. From table 4.3 this ratio is about 0.75 which indicates that the high energy component of the main resonance, at 91.5 eV in Zn III, should be slightly larger than in Zn II. From the Lorentzian curve fit, curve (ii) in figure 4.9, the ratio of the amplitudes for Zn III is 0.71, which is in reasonable agreement with the ratio of the associated gf values. Curve (iii) in figure 4.9 is from a calculation by Ivanov (1993) using the RPAE (Random Phase Approximation with Exchange) method to determine the total cross section in the region of the $3p \rightarrow 4s$ main resonance.

Configuration	E_{Obs} (eV)	Γ (eV)	E_{Cowan} (eV)	Γ_{RPAE} (eV)	gf
Zn III-- $3p^63d^{10} 1S_0$					
1 $3p^53d^{10}4s 1P_1$	88.74	2.0 ± 0.3	91.3	1.8	0.1450
2 $3p^53d^{10}4s 3P_1$	91.49	2.1 ± 0.3	94.1	2.0	0.1096
3 $3p^53d^{10}5s 1P_1$	105.5		107.9		0.0258
4 $3p^53d^{10}5s 3P_1$			110.8		0.0159
5 $3p^53d^{10}6s 1P_1$			113.5		0.0094
6 $3p^53d^{10}6s 3P_1$			116.4		0.0064

Table 4.3 $3p \rightarrow ns$ resonances of doubly ionized zinc, the nd resonances have, again, been found to have negligible oscillator strength in comparison, and so have been omitted.

The absolute energies of the RPAE calculations have been shifted by +4 eV in figure 4.9 to bring them into line with the observed spectrum. The results of these calculations produce two broad symmetric peaks, split by 2.8 eV, where the total width of each peak consists of the sum of the autoionization and Auger widths. The main contribution to the width of the lines comes from the Auger contribution which is driven by the super Coster-Kronig decay kinetics of the 3p core hole. The calculated total width of the spin orbit components of the $3p \rightarrow 4s$ resonance transition, 1.8 and 2.0 eV respectively, are in very good agreement with the experimental values derived from the curvefitting routine. The photoabsorption spectrum, curve (i) in figure 4.9, reveals some weak absorption features around 82 eV. This structure appears as a result of some slight contamination from the next ion stage, Zn IV, the main resonance transition of which, $3p \rightarrow 3d$, has considerable oscillator strength and has been found to be located in this energy region.

4.6. Photoabsorption Spectrum Of Zn IV, in the Region of 3p Excitation.

In common with the open 3d shell transition metals (see figure 3.5a), the photoabsorption spectrum of Zn IV, ground state $3p^63d^9 2D_{5/2,3/2}$, in the 3p region should be dominated by the fact that a large fraction of the oscillator strength is concentrated in the $3p^63d^n \rightarrow 3p^53d^{n+1}$ transitions. These discrete states can then

readily autoionize into the $3p^6 3d^{n-1}ef$ continuum channel. Interaction between the $3p \rightarrow 3d$ core excited resonances and the underlying direct photoionization continua of the 3d shell produces broad asymmetric type resonance profiles. Cowan code *ab initio* calculations predict the onset of absorption from $3p \rightarrow 3d$ for Zn IV to occur about 9 eV below the energy position of the $3p \rightarrow 4s$ resonance in Zn III, relative to their respective ground states, and that the oscillator strength associated with these transitions should be dramatically larger with the opening of the 3d shell, see table 4.4. The uppermost curve in figure 4.10, was produced using a tightly focused ruby laser, $T_d = 50$ ns and $\Delta x = 0.75$ mm, to generate the optimised ionic absorption column and corresponds to three capture regions of the detector.

From figure 4.10 one observes a dramatic change in spectral signature associated with the $3p \rightarrow 3d$ resonance transition. This spectrum in the region 75 to 90 eV, shown as an inset in figure 4.10, has been curve fitted as superposition of two Fano type profiles offset on a constant background described by the relation,

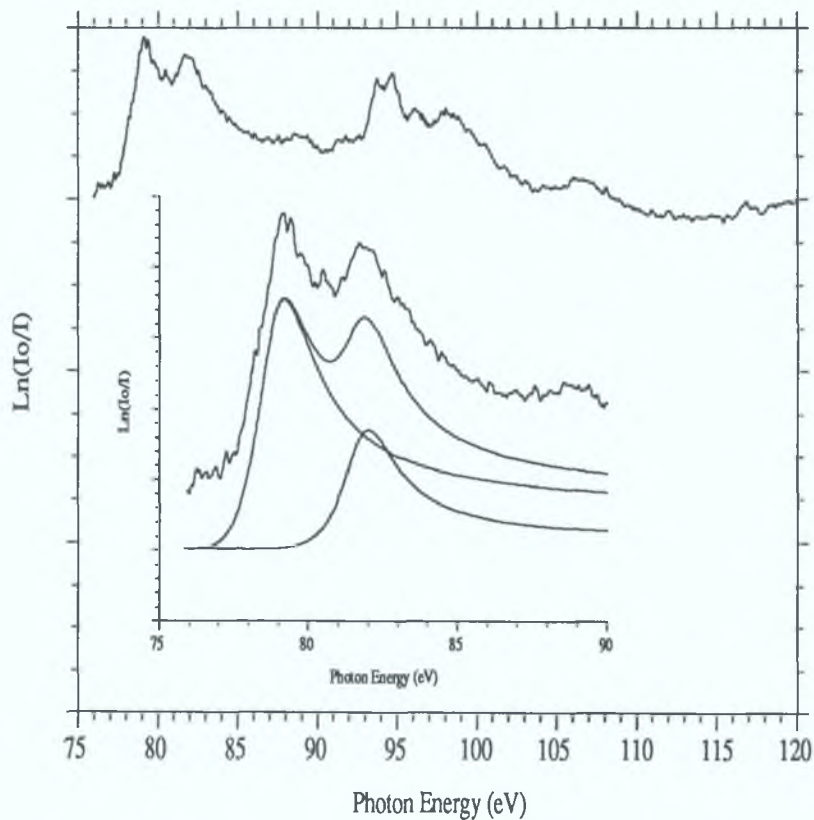


Figure 4.10. Photoabsorption spectrum of Zn IV from 75 to 120 eV, and inset, Fano curve fit applied to the resonance transition between 75 and 90 eV.

$$\sigma_{\text{total}} = \sigma_c + \sum_{i=1 \text{ to } 2} \frac{\sigma_i (q_i + \epsilon_i)^2}{1 + \epsilon_i^2}$$

$$\epsilon_i = (E - E_i)/(\Gamma_i/2)$$

where Γ_i and E_i are the width and the energy position of the resonance respectively, q_i is the asymmetry parameter and ϵ_i is the reduced energy in units of half width ($\Gamma_i/2$). The stronger interaction of continuum and discrete states compared to Zn II and Zn III is obvious in the change from symmetric to asymmetric type features. In the context of the 3d transition metal sequence, the 3p photoabsorption spectrum of Ni, with a ground state of $3p^63d^94s^2$, shows some similarity with the 3p spectrum of Zn IV especially in the main resonance energy region. The profile parameters associated with the Fano curve fit, i.e. resonance position, width and asymmetry parameters are included in table 4.4., along with a tentative assignment of some of the other features in the spectrum. The absorption structure between 93 and 97 eV is most likely associated with transitions of the type $3p \rightarrow 4s$.

Configuration	E_{Obs}	Γ	q	E_{Cowan}	E_{MCDF}	gf
Zn IV-- $3p^63d^9\ ^2D_{5/2(a)}$						
$3p^63d^9\ ^2D_{3/2(b)}$						
1(b) $3p^53d^{10}\ ^2P_{1/2}$	82.0					0.2780
2(a) $3p^53d^{10}\ ^2P_{3/2}$	78.72	2.3	2.4	82.3	82.8	2.5180
3(b) $3p^53d^{10}\ ^2P_{1/2}$	81.7	2.2	3.4	84.9	85.9	1.4470
4(b) $3p^53d^94s\ ^4F_{3/2}\ ?$	94.0			95.2		0.2530
5(b) $3p^53d^94s\ ^2F_{3/2}\ ?$	94.7			96.3		0.2932
6(b) $3p^53d^94s\ ^2F_{5/2}\ ?$				98.0		0.2779
7(a) $3p^53d^94s\ ^2D_{5/2}\ ?$	98.5			101.8		0.2675
8(a) $3p^53d^94s\ ^2F_{3/2}\ ?$	106.0			110.0		0.2465

Table 4.4. Tentative assignment of the 3p absorption spectrum of Zn IV.

4.7. Summary and Conclusions

Photoabsorption experiments have previously been performed on Zn vapour in the 3d and, to a lesser extent, 3s regions of the spectrum, using conventional heat pipe

technology to establish a stable vapour column coupled with a synchrotron source acting as a backlighting continuum. To date there appears to be no comprehensive calculations or experimental photoabsorption data available on core excited Zn in the 3p region. Using the DLP technique results were obtained for Zn I, II, III and IV in this region. The degree of purity of these spectra has been greatly enhanced by the fact that the valence and subvalence excited states of each ion stage are well separated in terms of energy from the ground state: refer to figure 4.2. These four ion stages produce spectra ranging from the very strong and complex open 3d shell transition metal like Zn IV to the relatively weak and simple closed 4s shell system of Zn I. The elucidation of the 3p photoabsorption spectrum of atomic zinc has subsequently been confirmed through the complementary techniques of photoion and photoelectron spectroscopy. Also, very recently Dunne *et al.* (1993) have measured, photographically, the photoabsorption spectrum of singly ionized gallium in the region of 3p excitation. The averaged densitometer traces of these plates show reasonable correspondence, in terms of overall spectra signature, with our DLP results for atomic zinc which is the isoelectronic equivalent of Ga⁺.

The degree of interaction between the discrete transitions from the 3p shell, of the type $3p \rightarrow ns, nd$ and the 3d continua, produced by the direct photoionisation process, $3d^n \rightarrow 3d^{n-1} \epsilon f$, is responsible for the variation in symmetry of the resonance profiles. The widths of the profiles can be interpreted as the result of various possible Auger decay channels most notably where electron-hole recombination in the 3p level results in the removal of a 3d electron. The main features of the spectra of Zn II, III and IV have been parametrised using a superposition of either Lorentzian or Fano type resonances sitting on an monotonically decreasing or constant background respectively.

On the subject of calculations it may be observed from the tables that the absolute energies of the various absorption features are offset by varying amounts from 2 to 3 eV with respect to the *ab initio* Hartree-Fock calculations. Ohno and Wendin (1977) have performed a many body calculation, based on the Random Phase Approximation, to determine the width and energy position of the $3p^5 3d^1 4s^2$ state of atomic zinc. Excellent agreement was found with the photoelectron data of Mehlhorn *et al.* (1977) by treating the primary electron ionization and Auger emission in a unified manner. Ohno and Wendin (1977) come to the conclusion that the $3p^{-1}$ level is strongly affected by super Coster-Kronig fluctuation and decay, giving rise to a $3p^{-1}$ level shift of 2-3 eV and a line width of 2.1 eV. They also predict that this energy shift can be accidentally accounted for, by performing relativistic self consistent field calculations through ground state correlation effects. Because the calculations performed here are of

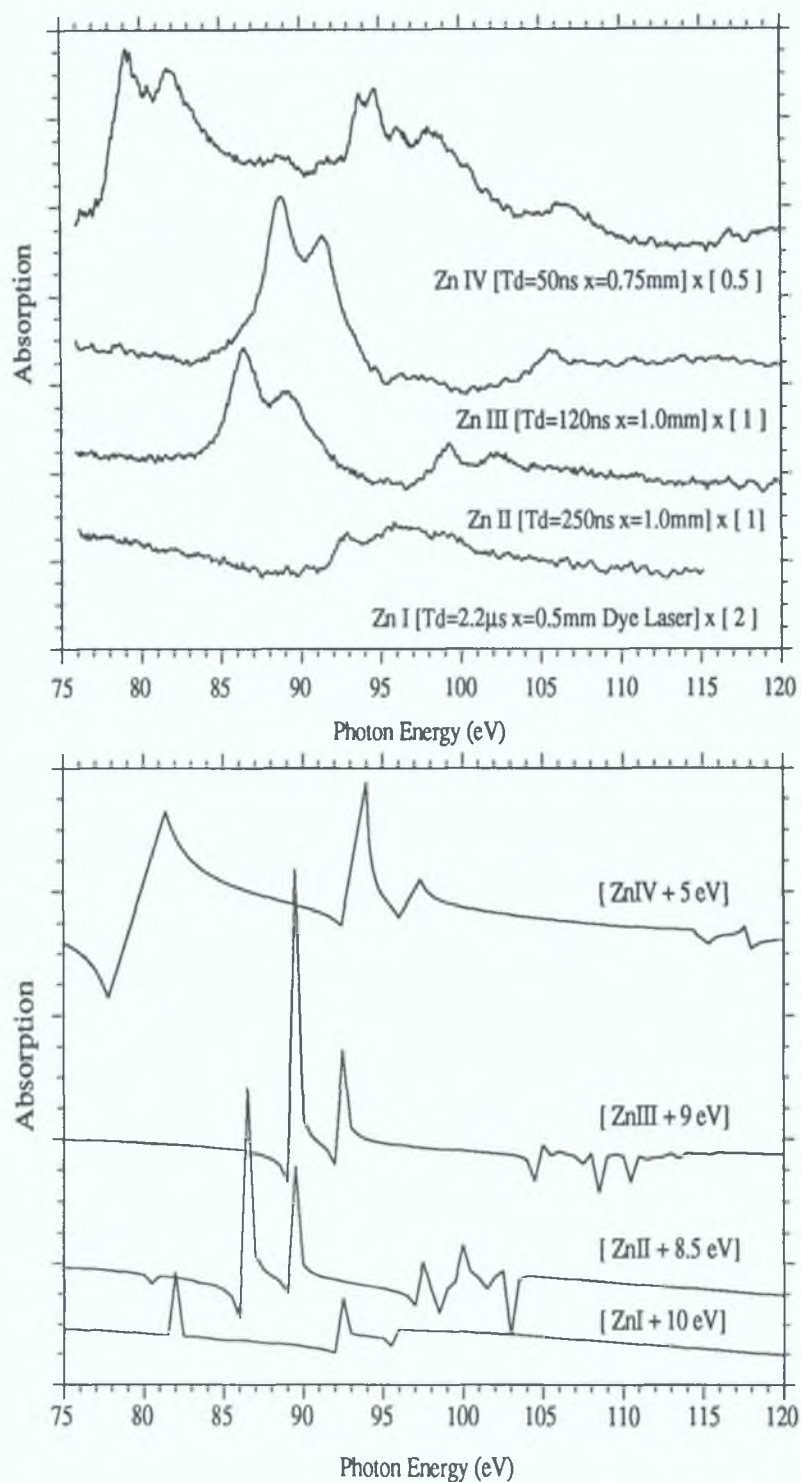


Figure 4.11. Summary of photoabsorption spectra of Zn I,II, III and IV indicating the optimised DLP conditions and the scaling factor for each plot, underneath is a summary of the TDLDA calculations of the total cross section in the energy region of 3p excitation - the energy scale of each plot has been shifted to bring the calculated spectrum in line with the observed.

the nonrelativistic self consistent field type, this may explain the near constant discrepancy of 3 eV between the observed and calculated energy positions of the 3p resonances. However, the Cowan code calculations reproduce the spin orbit energy splitting and the relative intensities in the observed spectra quite accurately. From comparison of the calculated energy level diagram, figure 4.2, and the summary of the DLP results, figure 4.1, the relative energy position for the onset of 3p absorption, above the ground state of each ion stage, is in very good agreement with experiment. The oscillator strength calculations show, as expected, that for the situation where the 3d shell is closed that the $3p^5ns$ resonances have much more oscillator strength than the $3p^5nd$ resonances.

Finally, the lower half of figure 4.11 shows the results of a TDLDA (Time Dependent Local Density Approximation) calculation, using the Zangwill code, of the total cross sections of Zn I, II, III, and IV in the energy region 75 to 120 eV compared to the experimental data. This program performs self consistent field calculations for atoms and ions in stationary states. It also calculates the response of an atom or ion to a weak external oscillating field taking account of the most important collective effects. The basic idea of TDLDA is, that an external field polarizes the electronic charge cloud of the atom, which gives rise to an induced field. Both external and induced field superimpose to give an effective driving field, to which the electrons respond independently (Köble *et al.* 1994). The cross section for photoabsorption can be obtained from the imaginary part of the polarizability of the electron density. The main output includes static and dynamic polarizabilities and photoabsorption and partial photoemission cross sections.

The overall shape of the spectra are well reproduced, with the individual energy shifting being indicated on each plot. In the case of Zn I the spectrum has been shifted so that the feature associated with excitation from the 3s shell is placed at 140 eV. The strong line at 82 eV in Zn I is unobserved in the experimental data. The TDLDA code only calculated transitions from the ground state so its origin can not be attributed to absorption from any valence or subvalence excited state. The absence of this feature indicates the need to perform a photoabsorption experiment with Zn I vapour in the 3p region using perhaps a low temperature heatpipe and a synchrotron as source of continuous radiation in the VUV to confirm that there are no absorption features from the 3p level below 93 eV.

4.8. References.

- Adam M. Y. A., Stranges S., de Simone M., Svensson S. and Combet-Farnoux F., *Phys. Rev. A.*, *accepted November 1993 , to be published 1994.*
- Back G. C., White M. D., Pejcev V. and Ross K. J., *J. Phys. B: At. Mol. Phys.*, **14**, 1497, (1981).
- Bearden J. A. and Burr A. F., *Rev. Mod. Phys.*, **39**, 125, (1967).
- Beutler H. and Guggenheimer K., *Z. Phys.*, **87**, 176, (1933).
- Bruhn R., Sonntag B. and Wolff H. W., *J. Phys. B: At. Mol. Phys.*, **12**, 203, (1979).
- Connerade J. P. and Mansfield M. W. D., *Proc. R. Soc. Lond. A.*, **339**, 533, (1974).
- Cowan R. D., “ The Theory of Atomic Structure and Spectra (Berkely: University of California Press), (1981).
- Cowan R. D. and Wilson M., *J. Phys. B: At. Mol. Phys.*, **21**, L275-L279, (1988).
- Dunne P., O’Sullivan G. and Ivanov V. K., *Phys. Rev. A.*, Vol. **48**, No. 6, (1993).
- Fliflet A. R. and Kelly H. P., *Phys. Rev. A.*, Vol. **10**, No. 2, 508, (1974).
- Fliflet A. R. and Kelly H. P., *Phys. Rev. A.*, Vol. **13**, No. 1, 312, (1976).
- Garton W. R. S. and Connerade J. P., *Astrophys. J.*, **155**, 667, (1969).
- Ivanov V. (*Private Communication*), (1993).
- Köberle H., Diplomarbeit, Universität Hamburg, Int. Bericht Desy F41, 86-03, (1985).
- Köble U., Kiernan L., Costello J. T., Mosnier J-P., Kennedy E. T., Ivanov V. K., Kupchenko V. A. and Shendrik M. S., *submitted to Phys. Rev. A.*
- Kurig T., Diplomarbeit, Universität Hamburg, Int. Bericht Desy F41, 86-04, (1985).

Lotz W , J Opt Soc Am , **60**, 206, (1970)

Mansfield M W D , J Phys B· At Mol Phys , **14**, 2781, (1981)

Mansfield M W D and Connerade J. P , Proc R Soc Lond A , **359**, 389, (1978).

Marr G V and Austin J M , J Phys B. At Mol Phys., **2**, 107, (1969)

Mehlhorn W., Breuckmann B and Hausamann D., Physica Scripta, **16**, 177, (1977).

Moore C E , “ Atomic Energy Levels”, edited b Edit Natl Bur Stand (US), Circ No 567 (US GPO, Washington, D C , 1958)

Ohno M and Wendin G , J Phys B Atom Molec Phys , **12**, 1305, (1979)

Pearl B , Lyon I C and Dolder K , J Phys B At Mol Phys , **20**, 5403, (1987).

Rogers W T , Stefani G , Camilloni R , Dunn G H , Msezane A Z and Henry R J W , Phys Rev A , **25**, 737, (1982)

Svensson S , Stranges S and Adam M Y , Phys Rev A , **48**, 3051, (1993)

Sonntag B F and Zimmermann P , Rep Prog Phys , 911, (1992)

Zangwill A and Liberman D A , Com Phys Comm (North Holland, Amsterdam), **32**, 63, (1984)

Zangwill A and Soven P , Phys Rev B , **24**, 4121, (1981)

Chapter 5
Photoabsorption Studies Along the
Lithium Isonuclear Sequence in the
Region of Single and Multiple K-Shell
Electron Excitation.

5.1 Introduction.

Inner-shell-vacancy states, the existence of which was known experimentally in the early 1930s, appear as discrete energy levels embedded in a continuum spectrum. They play an important role in various physical processes such as photoabsorption, electron scattering, and multielectron phenomena in ion-atom and atom-atom collisions. The investigation of these states both experimentally and theoretically has yielded important information on the effects of electron correlations in atomic systems. This in turn has led to the development of new theories, classification schemes, and the search for new quantum numbers to characterise these states (Conneely *et al.* 1992). In this regard Cooper *et al.* (1963), were the first to question the validity of the normal quantum mechanical assignment of the double K-shell electron transitions of helium. Since the $n = 2$ level of He^+ is degenerate ($2s$ and $2p$), two separate He series might be expected to converge to this limit, namely $2snp$ and $2pns$. These series have a common lowest level with $n = 2$. The observation of a single series (Madden and Codling 1963; see figure 3.4) indicated that the classification, $2snp$ and $2pns$ does not constitute an appropriate zero-order approximation. Cooper *et al.* (1963) therefore proposed new zero-order states ($2n \pm$) where the $+(-)$ quantum number corresponds to radial motions of the two electrons in and out of phase with one another and that the $2s2p$ state belongs to the $+$ classification. They also predicted the future observation of weak and very narrow $(-)$ levels.

Since the first observation, in photoabsorption, of doubly excited states in helium in the early 1960s (Madden and Codling 1963), great progress has been made in understanding the nature of electron-electron correlation in doubly excited states. Doubly excited helium is the archetypical example for autoionizing phenomena, since it represents the most fundamental autoionizing atomic system, which is - due to its relative simplicity - also readily accessible to theoretical treatment - the Coulombic three body problem (Zhou *et al.* 1993). With improving performance of synchrotron sources and monochromators, a great deal of experimental effort has been devoted to precision measurements of photoionization cross sections in the vicinity of autoionizing doubly excited states.

Upon excitation of both K-shell electrons to states below the $n=2$ threshold of He^+ , final states with six different symmetries ($^1S^e$, $^3S^e$, $^1P^o$, $^3P^o$, $^1D^o$, $^3D^o$) can be populated, each containing up to three Rydberg series. In photoexcitation, the dipole-selection rule allows only $^1P^o$ final states, which reduces the number of observable

Rydberg series to three, i.e. $2snp\ ^1P^o$ ($sp,2n^+$), $2pns\ ^1P^o$ ($sp,2n^-$) and $2pnd\ ^1P^o$. The resolution of experimental measurement has been lowered to 0.004 eV, e.g. Domke *et al.* (1991 and 1992), stimulating a renewed interest in these resonances, and subsequently revealing details of high lying members of doubly excited state series, $2snp$ and $2pns$, and also uncovering weak resonances, $2pnd$ $n=3-6$, which had not been observed before. This series of results complete the identification of the simplest double excitation states of He, accessible by photoexcitation below the $n=2$ ionization threshold. They have also helped to clarify a theoretical controversy regarding the correct energies of these states and provided a means to check the quality of the existing atomic multiconfigurational calculations for He.

In a similar sense to helium being the simplest closed shell atom, lithium is the simplest open-shell many electron system besides hydrogen. This makes lithium an excellent choice to study, particularly because the effects of electron correlation on the photoionization process can be quite large, since one third of the electronic charge is removed upon ionization (Langer *et al.* 1991). On moving from helium to lithium the addition of a single electron makes possible the formation of triply excited states (Conneely *et al.* 1992), in which all three electrons reside in the $n=2$ subshell leaving a doubly vacancy in the K-shell. Such multiply excited species can be considered an ideal planetary or ‘hollow atom’ and represents a model system for the study of electron correlation in a three electron atom - the Coulombic four body problem. Further, while helium exhibits only direct double photoionization (Schwartzkopf *et al.* 1993), i.e. $He + h\nu \rightarrow He^{2+} + 2e^-$, lithium offers the potential for the study of both direct and resonant ($Li + h\nu \rightarrow Li^{***} \rightarrow Li^{2+} + 2e^-$) double photoionization where Li^{***} corresponds to a triply excited (or double K-shell vacancy) state. Hence a strong case exist for the initiation of studies into the photoabsorption spectrum of atomic lithium at energies corresponding to the simultaneous photoexcitation of both K-shell electrons.

5.2. Collisional Experiments on Multiply Core Excited States in the Lithium Isonuclear Sequence.

As in the early studies of doubly excited autoionizing resonances in helium, by Silvermann *et al.* (1959,1964), first experiments on doubly core excited states in three electron atomic systems were exclusively collisional in nature. The first observation of triply excited states in three electron systems was in an electron scattering experiment, $e^- + He$, by Kuyatt *et al.* (1965). These resonances were identified by Fano and

Cooper (1965) as being due to the decay of the $2s^2 2p\ ^2P$ and $2s2p^2\ ^2D$ states of He⁻. There have been numerous collisional experiments carried out on lithium and its ions, most prolifically in the mid to late 1970's, with the intention of investigating the multiple core excited states, both optically allowed and parity forbidden levels, the most significant of which are outlined below. Mannervik (1989) has reviewed the work carried out on two, three and four-electron systems, concentrating on optical emission spectroscopy. Particular emphasis is placed on core excited "bound" states, i.e. states which are not allowed to decay by Coulomb autoionization which means that the state will decay radiatively.

The first evidence for the formation of doubly core excited neutral lithium emerged from the beam-foil experiments of Bruch *et al.* (1975). The beam-foil interaction mechanism was successfully shown to populate highly excited states in lithium by passing 300 keV Li⁺ ions through, approximately 300 Å thick, carbon foils. These multiply excited Li I^{**}, Li I^{***}, and Li II^{**} states, emerging from the back surface of the foil, having energies in excess of the first ionization limit, then decay via Coulomb autoionization provided the parity, spin, and orbital angular momenta of the initial and final states are unchanged. The prompt electron spectra and the delayed spectra from long lived metastable states can be observed in the same experiment by moving the foil in and out of the focus of an electron spectrometer along the beam axis. However, due to kinematic broadening effects and to uncertainties in the velocity determination of the projectile beam, this method yielded results with greater than 0.1 eV uncertainty. By passing a 70 keV lithium beam through a thin He gas target, Pegg *et al.* (1975) achieved higher resolution, but owing to electron spin conservation no evidence of the formation of quartet states was found in Li⁺ + He collisions. Ziem *et al.* (1975) report the first measurements of autoionizing states produced by H⁺ and He⁺ impact on an atomic Li vapour target. The use of a vapour target further reduced the effects of kinematic line broadening and some of the core excited levels were measured to within ± 0.01 eV. They also reported the first observation of the $1s2s2p\ ^4P^o$ quartet metastable state at 57.385 eV above the Li I ground state. In addition, the excitation energies of the $2s^2\ ^1S$, $2s2p\ ^3P$ and $2s2p\ ^1P$ doubly excited states of, Helium-like, Li II were determined at, 142.26 ± 0.03 , 147.02 ± 0.03 and 150.31 ± 0.03 eV respectively, above the ground state of the singly charged Lithium ion. Rødbro *et al.* (1979), recorded the ejected-electron spectra of singly and doubly core excited states strongly populated in 100 to 500 keV Li⁺ single collisions with He and CH₄, confirming the assignments of Ziem and his co-workers and further extending the number of resonances observed. The large body of data accumulated on multiple core

excited states in atomic lithium and its ions, through collisional experiments, provided an impetus for a number of theoretical studies which appeared during this period (Ahmed and Lipsky 1975, Safronova and Senashenko 1978, Nicolaides and Beck 1977, Simons *et al.* 1979 and Chung 1982) the latter paper providing the most complete analysis of the Rødbro *et al.* (1979) data, to date.

Agentoft *et al.* (1984) observed for the first time the radiative decay of $2p^3 (^4S) \rightarrow 1s2p^2 (^4P)$ at 145.02 \AA while the lifetime of this state was later measured

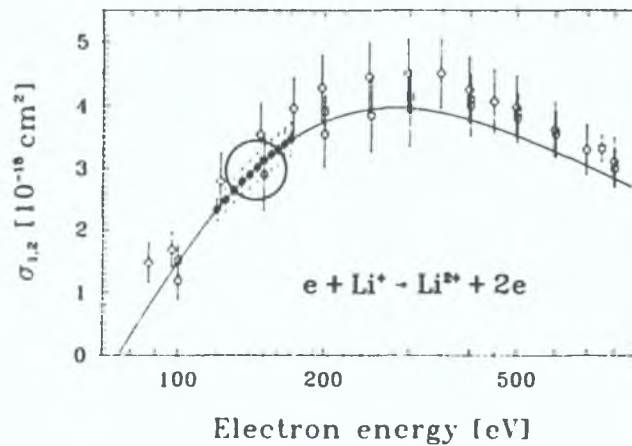


Figure 5.1a. Measured cross section for electron impact ionization of Li^+ ions, the encircled area indicates the energy region corresponding to resonant ionization of Li^+ due to electron capture. (after Müller *et al.* 1989).

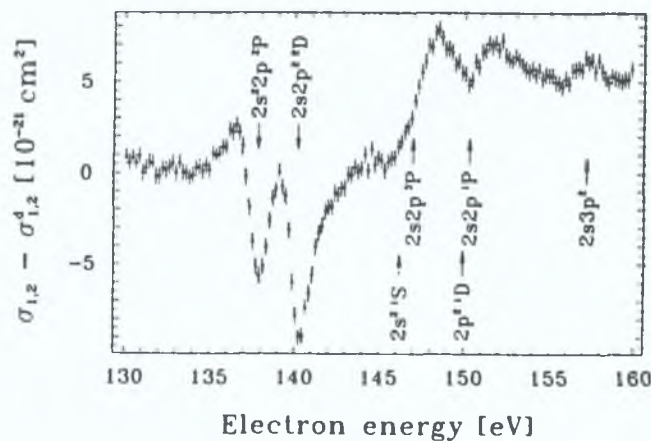


Figure 5.1b. Expanded view of energy region encircled in figure 5.1a. The direct photoionization background, $\sigma_{1,2}^d$ has been subtracted to reveal the resonant ionization structure. (after Müller *et al.* 1989).

by Mannervik *et al.* (1989). The $1s2p^2$ ($^2P^e$) state is metastable against autoionization and has been observed to decay radiatively to $1s^22p$ ($^2P^o$) at 207.46 Å by Buchet *et al.* (1973) and more recently by Träbert *et al.* (1985). Harris (1980) proposed a 207 Å laser in neutral lithium based on this transition.

The most recent study of the $1s^22s$ ($^2S^e$) \longleftrightarrow $2s^22p$ ($^2P^o$) and $1s^22p$ ($^2P^o$) \longleftrightarrow $2s2p^2$ ($^2D^e$) double K-shell vacancy excited states of lithium has been reported by Müller *et al.* (1989) in an electron + Li^+ impact ionization experiment. Non resonant double excitation with subsequent autoionization,



was found at electron energies above a threshold of 146 eV. Below this energy a resonant process was observed involving correlated double excitation simultaneous with the capture of the incident electron and subsequent deexcitation of the triply excited state by emission of two correlated electrons. The result is a doubly ionized ion, i.e.



The cross section for direct ionization in the 140 eV region is ≈ 3 MB (see figure 5.1a), while the resonant process is three orders of magnitude lower, $\approx 5 \rightarrow 10$ kB (see figure 5.1b). A key feature of this experiment is the high dynamic range detection required to observe these extremely weak resonances in the presence of a non resonant background signal three orders of magnitude greater. These results will be discussed in relation to the photoabsorption data recorded using the DLP technique.

The technique of photoabsorption spectroscopy has the dual advantage of generally higher resolution and spectra of less complexity due to the presence of only electric dipole allowed transitions from a known ground state. Exploiting the versatility of the DLP technique, coupled with advantage of high dynamic range photoelectric registration, we have measured for the first time the photoabsorption spectrum of atomic lithium, at energies (approx. 140 eV) corresponding to the simultaneous excitation of both K-shell electrons. This series of experiments, outlined and reviewed in the context of other photoabsorption studies which provide benchmarks in the field, represent the first step in photoionization studies of this fundamental atomic system, in which the motion of all three electrons in the Coulombic field of the nucleus is so highly correlated (Kiernan *et al.* 1994).

5.3. Previous Photoabsorption Measurements of the K-shell Spectra of Atomic Lithium and its Ions.

Dave Ederer and his colleagues (1970, 1971), at the National Bureau of Standards, were the first to measure the K-shell photoabsorption spectrum, using a synchrotron background source and a vapour furnace, of atomic lithium. Resonant structure was observed for incident photons in the energy range 50-70 eV. These resonances, more than 50 eV above the first ionization potential, were attributed to the excitation of a K-shell electron $1s2snl$, or the simultaneous excitation of a K-shell electron and an outer electron to final states of the type $1s2pns$ or $1snln'l'$. Due to the

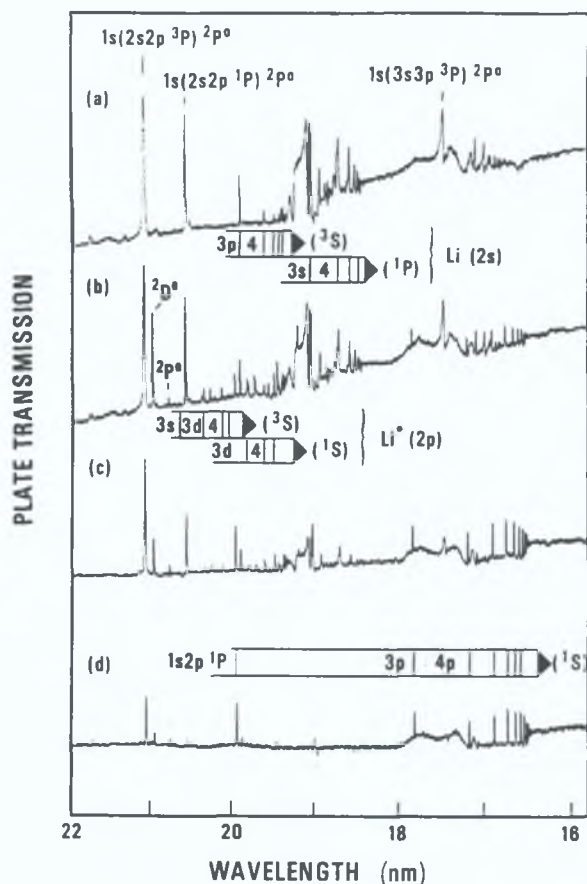


Figure 5.2. Densitometer tracings from photographic plates, of spectra taken (a) before laser initiation, (b) 200 ns, (c) 400 ns and (d) 600 ns after laser initiation using the technique of RLDI. The spectra describe K-shell excitations from ground state Li I, valence excited Li*, and ground state Li+. The broad persistent structure from 17-18 nm is a source feature. (after McIlrath and Lucatorto 1977).

fact that close to the onset, the K-shell absorption cross section exhibits a complex resonance structure due to the narrowly spaced limits $1s2s\ ^1,3S$ and $1s2p\ ^1,3P$ of the Li^+ ion core (Mehlmann *et al.* 1978), only two Rydberg series were positively identified, $1s2snp$ and $1s2pns$ converging on the $1s2s\ ^3S$ (64.4 eV) and $1s2p\ ^1P$ (67.5 eV) limits of Li II respectively. Using the technique of flash-pyrolysis, Cantú *et al.* (1977), remeasured the K-shell photoabsorption spectrum of atomic lithium and proposed tentative spectral assignment of the two series not previously labelled by Ederer *et al.* (1970). This technique also enabled the measurement of the K-shell photoabsorption spectrum of singly ionized lithium in the energy region 57-78 eV. Resonances were observed, and identified, corresponding to the principal series of Li^+ , $1s^2\ ^1S^e \rightarrow 1snp\ ^1P^o$ $2 \leq n \leq 14$.

Using the laser based technique of RLDI (Resonant Laser Driven Ionization), McIlrath and Lucatorto (1977) reported the first observation of the even-parity core excited resonances of atomic lithium. A pulsed 1-MW dye laser (pulse width approx. 800 ns) tuned to the $1s^22s\ ^2S^e \rightarrow 1s^22p\ ^2P^o$ optical transition at 670.8 nm was used to populate the odd parity excited states. Core excitation to the even parity states, was achieved by suitable timing of the dye laser pulse with respect to a triggered vacuum spark XUV continuum probe pulse. Over twenty lines representing absorption resonances from the $1s^22p\ ^2P^o$ levels were observed. It was also found that at about

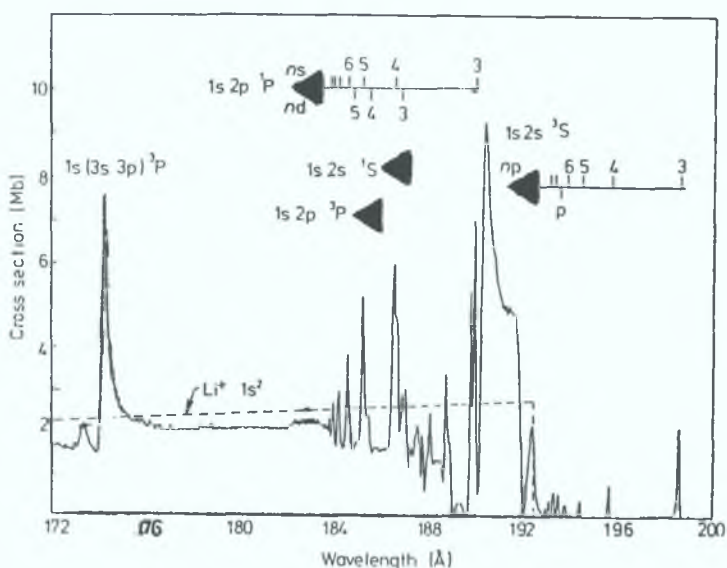


Figure 5.3. Absorption cross section of lithium from 172 to 200 Å, showing the four series limits and series, converging to the $1s2s\ ^3S$ and $1s2p\ ^1P$ limits are shown at the top of the figure (after Mehlmann *et al.* 1978).

600 ns after laser initiation almost 100% ionization of the lithium vapour could be obtained, enabling the K-shell spectrum of Li⁺ to be recorded, see figure 5.2.

Mehlmann *et al.* (1978) reported the first measurement of the absolute absorption cross section in the K-edge region of lithium vapour: see figure 5.3. The temperature profile of the heat pipe, used to contain the lithium vapour, was accurately measured via ten thermocouples welded to the external wall of the heat pipe. From known lithium vapour pressure data the pressure distribution along the absorption column, and thus the number of lithium atoms present in the absorbing path could be calculated. The absolute accuracy of the measured photoionization cross section was reported to be better than 15%. These measurements revealed that a large fraction of the total oscillator strength for K-shell photoionization is contained in the region immediately above the 1s2s ³S threshold and implied that photoionization leaving the ion in 1s3s (shake-up) and 1s3p (conjugate shake-up) final states has a non negligible contribution in this energy region. In 1982 Mehlmann *et al.* extended these photoabsorption measurements by recording the spectrum of atomic lithium from 175-110 Å revealing details on the structure of the doubly excited resonances immediately below the 1s3l and 1s4l limits of the Li⁺ ion, the first member of which, 1s(3s3p) ³P, is shown at 174.3 Å in figure 5.3.

As outlined in the previous section, early collisional experiments on lithium and its ions only enabled the observation of the decay products resulting from a myriad of excited states. Carroll and Kennedy (1977) were the first to measure the photoabsorption spectrum of singly ionized lithium in the energy region corresponding to double K-shell excitation. This type of experiment was realised only after the development of laser produced plasmas both as XUV light sources and also as high density sources of ions for photoabsorption studies. This pioneering work, based on an early form of the DLP technique (see figure 1.13), provided an important extension of the helium-like doubly excited series 2snp ¹P. The first three members of the 1s² → 2snp ¹P series were identified and Fano parameters E₀, Γ and q, (energy position, width and profile index of resonance respectively) were obtained for the n=2 member of the series. Also the principal series 1s² → 1snp ¹P and its adjoining ²S ep photoionization continuum were observed. In their analysis of the photographically recorded photoabsorption data, Carroll and Kennedy (1977) derived an analytical expression for the convolution of the spectrometer instrument function, determined from densitometer scans of sharp atomic lines, with the theoretical, Fano (1961), resonance profile,

$$\sigma = \sigma_0 [(q + \epsilon)^2 / (1 + \epsilon^2)] \quad (5.3)$$

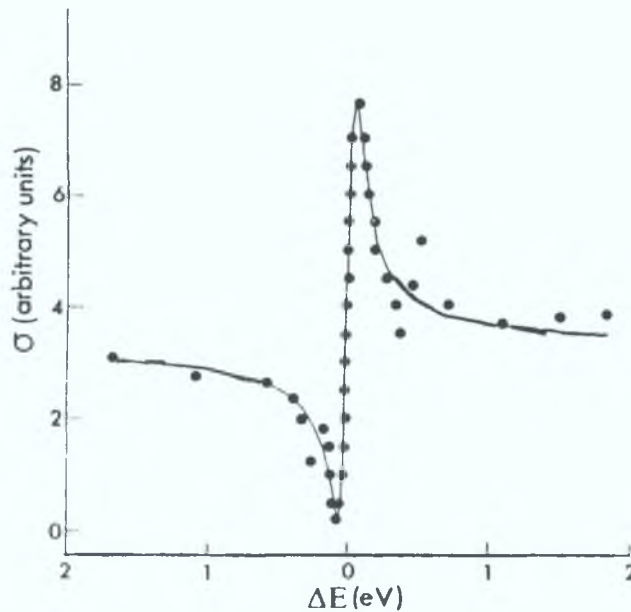


Figure 5.4. $1s^2 \ ^1S \rightarrow 2s2p \ ^1P$ resonance of Li^+ . The points are derived from a densitometer trace of a photographic plate. The solid line represents a curve fit to the data assuming a convolution of a known instrument function and a Fano type resonance profile. (after Carroll and Kennedy, 1977).

where ε is reduced energy in units of half width, $\varepsilon = (E - E_0)/(\Gamma/2)$. This convolved analytical expression was applied through a least squared fitting routine to a set of averaged experimental data, in this way the profile parameters could be extracted without having to initially remove the folded instrument function (Kennedy 1977). Figure 5.4 shows a least squared curve fit to a typical set of experimental data in the energy region of the $1s^2 \ ^1S \rightarrow 2snp \ ^1P$ resonance, assuming a triangular instrumental function with full width at half-maximum of 0.08 eV. The helium-like series was later extended to doubly ionized beryllium using a modified version of the DLP technique by Jannitti *et al.* (1984).

5.4. Optimisation Requirements of Experimental Technique to Observe Double K-Shell Resonances.

The work of Carroll and Costello (1986), and Costello *et al.* (1991), demonstrated for the first time the effectiveness of the DLP technique as a suitable means of observing the XUV photoabsorption spectra of highly refractory neutral

metal atoms, such as thorium and chromium, prepared in their respective ground states. In general the spectral signature of absorption features measured were of considerable oscillator strength and also the comparatively large width of the resonances presented no real difficulties in terms of instrumental resolution degradation. The extension of the application of this technique to the measurement of the triply excited, $1s^22s ({}^2S^e) \rightarrow 2s^22p ({}^2P^o)$, resonance of atomic lithium represents a considerable experimental challenge considering the very weak and narrow character of the expected feature. In general any photoabsorption experiment designed to observe this resonance would require, (i) high optical resolution, (ii) a wide dynamic detection range and (iii) an adequate column density in the absorbing sample.

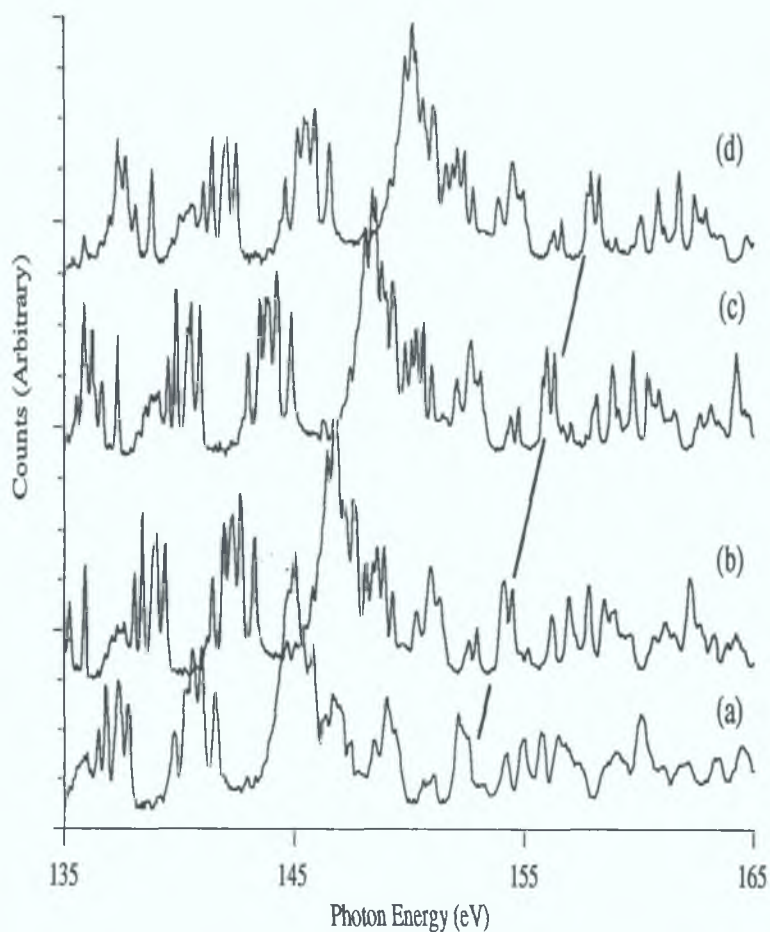


Figure 5.5. Optimisation of spectrometer focusing in the energy region 135-165 eV by traversing the detector perpendicular to the point of tangency with the Rowland circle. (a) -0.0125", (b) initial position 0.0", (c) +0.0125" and (d) +0.0250".

In the present experimental system, requirement (i) is limited by the spectrometer optics and ultimately by the spatial sampling period of the MCP-PDA detection system at the focus of the Rowland circle. As already outlined in section 2.1.9 part (i), the best resolution of the spectrometer detection system, $(E/\Delta E)$, at approximately 140 eV is ≈ 1200 before deconvolution techniques are applied. To ensure, in so far as possible, that this optimum resolution was achieved, the spectrometer focusing was investigated by recording groups of closely spaced sharp emission lines, originating from the same ion stage, from aluminium and silicon laser produced plasmas in the 130-160 eV energy region. The detector was traversed across the Rowland circle in a direction perpendicular to the point of tangency, in steps of 0.0125 inches. Spectrometer focusing was found to be the dominant factor in resolution degradation. Using an entrance slit width of 10 μm , the focusing optimisation using an aluminium plasma is shown in figure 5.5, where position (c) was found to have the best focus.

In regard to requirement (ii), the dynamic range of the detection system ultimately determines the smallest observable variation in intensity. This limit of discrimination is set by the digitisation process of the analog signal from the PDA detector which is executed by the camera controller card in the OMA interface. The voltage signal from each signal is converted to an eleven bit number which corresponds to a maximum signal of approximately 2000 counts. The camera head is Peltier cooled to $+5^\circ\text{C}$ and has a measured dark noise signal of less than one count.

In order to produce an adequate column density the absorbing plasmas were generated by focusing the laser output into a long line focus parallel to the optical axis of the system. Plasmas up to 22 mm in length were generated using a cylindrical type lens and represented the longest line plasmas we have used to date. In order to probe the most appropriate DLP experimental conditions, such laser type, power density, inter-laser time delay and the spatial position of the plasma relative to the optical axis of the system, to maximise the purity of ion stage and number density of absorbing atoms in the sample plasma a series of survey experiments were carried out. In order to assess the suitability of the system for measuring relatively narrow (compared to the resolution limit at that energy) and weak photo absorption features, we first measured the $1s^2 (^1S^e) \rightarrow 2s2p (^1P^o)$, doubly core excited resonance of Li^+ originally recorded photographically, using the single laser DLP technique, by Carroll and Kennedy (1977).

5.5. Measurement of the Doubly core excited $1s^2(^1S^e) \rightarrow 2s2p(^1P^o)$ Resonance of Singly Ionized Lithium.

The observation of the doubly excited helium-like series, provided a benchmark for the measurement capability of the facility. In this series of experiments the transient Li^+ absorbing column was created by the laser ablation of a spectroscopically pure lithium metal target using a Q-switched ruby laser (1.5 J in 30 ns) in line focus configuration (15 mm long, 0.5 mm wide) using a cylindrical lens, at an irradiance of $\approx 6 \times 10^7 \text{ W cm}^{-2}$. The metal target was cleaved in atmosphere and precleaned, under vacuum in the target chamber, by firing 20 to 30 defocused Q-switched ruby shots onto the surface. The synchronised backlighting continuum emitting plasma was generated by tightly focusing the output of a Q-switched Nd:Yag laser (1 J in 15 ns) onto the surface of a cylindrical tungsten target. Again, the tungsten target was precleaned by firing 5 to 10 laser shots before the continuum emission spectrum (I_0) was recorded. Initially we recorded the single electron K-shell spectrum in the region of the principal series $1s^2(^1S^e) \rightarrow 1snp(^1P^o)$, up to the $1s\ \epsilon p(^2S)$ limit, a typical photoabsorption spectrum ($\text{Ln}(I_0/I)$ vs Photon energy) in the energy region 58-78 eV is shown in figure 5.6. This spectrum should be compared with the RLDI data recorded by McIlrath and Lucatorto (1977); figure 5.2 (d), and shows a high degree of Li^+ purity. Indeed, the percentage contribution of absorption from neutral lithium is extremely small, indicated in figure 5.6 by the weakness of the normally dominant neutral lithium $1s2s2p$ resonance line at approximately 59 eV.

By varying the inter-laser time delay and the spatial position of the lithium target with respect to the optical axis of the system, defined by the position of maximum detected intensity of the continuum plasma, the relative purity of the ion stage present in the absorbing plasma can be recorded. The error in the time delay is approximately ± 20 ns (determined by the combination of the continuum probe pulse and by the jitter in the electronic delay circuits) while the spatial resolution in the plane of the slit (determined by the spectrometer/toroidal mirror coupling optics) is better than 100 μm . For each absorbing plasma spatial position, incremented in 0.25 mm steps away from the optical axis, the inter-laser time delay was scanned from 0-500 ns in steps of approximately 50 ns. From the resulting photoabsorption data the area under the resonance line, $1s^2(^1S) \rightarrow 1s2p(^1P)$, for each combination of temporal and spatial coordinates, was calculated by summing the individual pixel absorption values defined

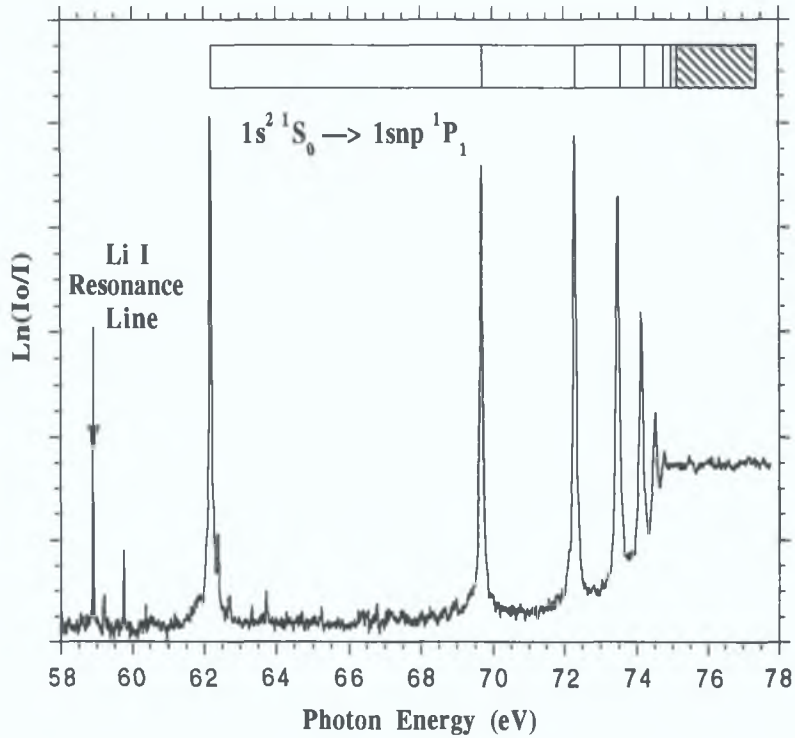


Figure 5.6. Photoabsorption spectrum of Li^+ corresponding to single $1s$ electron excitation where the purity of the spectrum is demonstrated by the weakness of the main $1s^2 2s ({}^2S) \rightarrow 1s[2s2p({}^3P)] ({}^2P)$ resonance transition in neutral lithium at 59 eV.

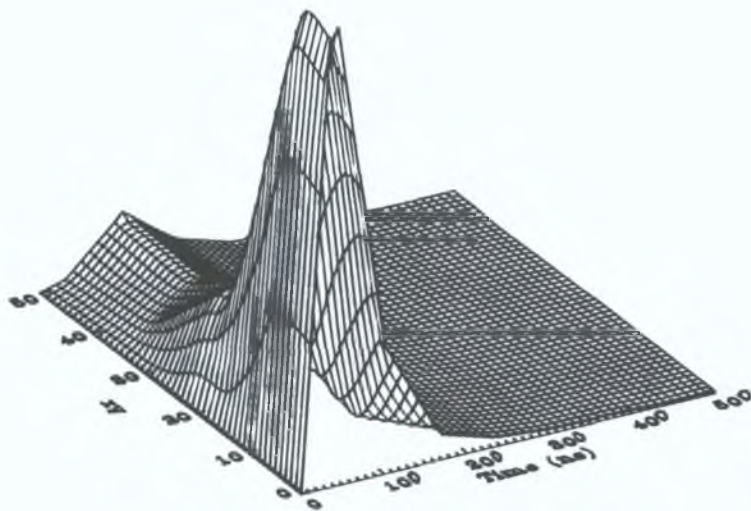


Figure 5.7. Temporal and spatial dependence of photoabsorption due to Li^+ , where the Δx is the spatial position, in mm, of the target with respect to the optical axis of the system and time is the inter-laser time delay in ns.

by the profile. The results of this work permitted the construction of a three dimensional map of the temporal and spatial evolution of Li^+ in the laser generated absorbing plasma which is shown in figure 5.7.

As can be seen from figure 5.7, there is very little absorption due to Li^+ after 200 ns even close to the target surface. There is also a rapid fall off in absorption between 1.0 and 2.0 mm away from the surface due to the expansion of the ablated material. Coincident with the measured diminution in absorption from Li^+ a slight increase in absorption from Li neutral, outside of the time space region bounded by the main peak in figure 5.7, was observed, yielding some evidence of recombination processes. This Li neutral absorption dependence has not been included in figure 5.7 for reasons of clarity. From this temporal and spatial map the appropriate time and space coordinates for maximum absorption from Li^+ were determined to be approximately 100 ns, between the laser optical pulses, and 0.75 mm from the target surface, respectively. These parameters were also verified by monitoring the maximum jump in photoabsorption in the vicinity of the K-edge at approximately 76 eV.

Having optimised the absorption due to Li^+ , initially in the region of the K-edge, the photoabsorption spectrum, covering the expected energy position of the $1s^2 ({}^1S) \rightarrow 2s2p ({}^1P)$ doubly excited resonance, was measured; see figure 5.8. This

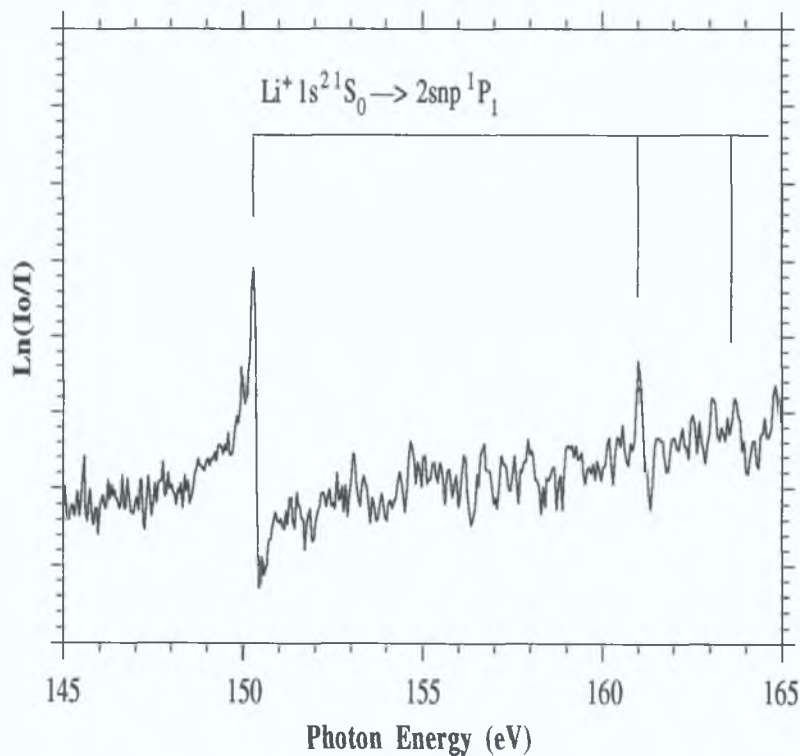


Figure 5.8. Photoabsorption spectrum of singly ionized lithium in the energy region, 145 to 165 eV, corresponding to double K-shell electron excitation.

resonance line is located more than 70 eV above the first ionization limit of Li^+ . The asymmetric nature of the resonance is clearly evident from figure 5.9, which shows the main resonance in the energy region of 149 to 152 eV. The interaction of the quasi-bound $2s2p$ (1P) state with the underlying direct $1s\epsilon p$ photoionization continuum; refer to energy level diagram-figure 5.10, is responsible for the asymmetric modulation in the relative absorption data. The data was recorded with a $10\ \mu\text{m}$ entrance slit and a 1200 lines/mm grating, and results from the accumulation of 3 sets of 25 laser shots taken independently in single shot accumulation mode. The reproducibility of data is demonstrated by the good signal to noise ratio maintained across the spectrum. Each

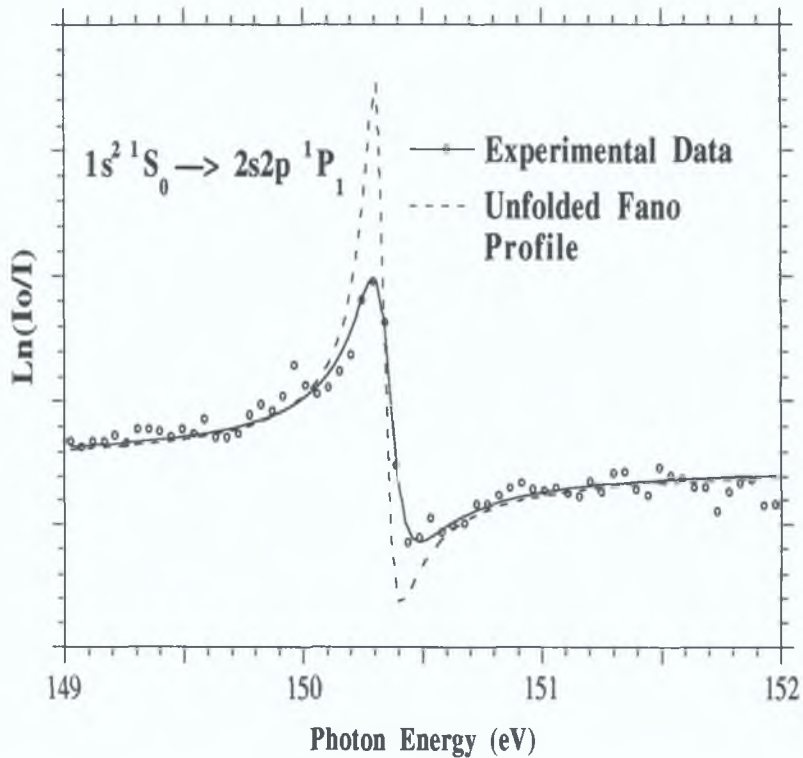


Figure 5.9. Photoabsorption spectrum of singly ionized lithium in the vicinity of the $1s^2 2s$ (1S) \rightarrow $2s2p$ (1P) doubly excited transition. The smooth curve is obtained by fitting the Fano profile formula to the raw experimental data while the dashed curve represents the corresponding least squared fit following the removal of instrument broadening.

open circle corresponds to one pixel of information. The full curve was obtained by fitting a Fano profile formula, see equation (5.3), to the raw experimental data and is meant to provide a guide to the eye only. Using a commercially available deconvolution package, based on the maximum likelihood technique, the instrument broadening was removed from the raw spectrum. The instrument response function was found to be best described by a Gaussian profile of width 3.4 pixels. The

significant enhancement of the doubly excited resonance illustrates the overwhelming influence of instrumental broadening. The Fano profile formula was then applied to the restored data and the extracted parameters are shown in table 5.10. Good agreement is obtained, within the limits of experimental error, with the values reported by Carroll and Kennedy (1977).

Fano Parameters	E_0 (eV)	Γ (eV)	q
Observed	150.28 ± 0.05	0.090 ± 0.030	-1.8 ± 0.4
Carroll & Kennedy	150.29 ± 0.05	0.075 ± 0.025	-1.5 ± 0.3
			- 0.5

Table 5.1. Comparison of observed Fano parameters, describing the doubly excited Li^+ resonance, with those obtained by Carroll and Kennedy (1977).

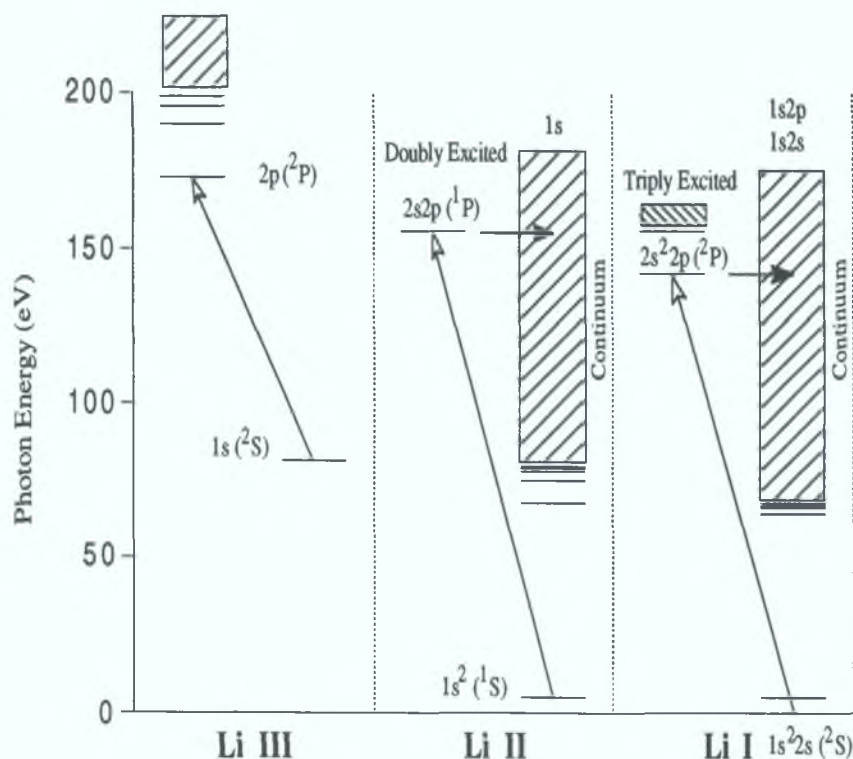


Figure 5.10. Energy level diagram summarising the K-shell excitations, both single and multiple, of Li III, Li II and Li I. Also shown are the direct underlying photoionization continua which interact with the quasi bound doubly and triply excited autoionizing states of Li II and Li I respectively. The odd parity core singly, doubly and triply excited states are shown connected to their respective Li III, Li II and Li I ground states.

The close interrelation of the three atomic systems Li^{2+} , Li^+ and neutral Li is well illustrated by the energy level diagram, figure 5.10, which summarises the main K-shell excitations of interest in this work. The limit of the doubly excited series $2pns$ of Li^{2+} , for example corresponds to the same energy position, above the ground state of neutral Li, as the Lyman- α transition, $1s (^2S) \rightarrow 2p (^2P)$, in Li III. The limit of the principal series, $1s^2 (^1S) \rightarrow 1snp (^1P)$, of Li^+ corresponds to the ground state energy position of the Li^{2+} . Also the limit of the triply excited series $2s2pns$, in neutral Li, will be defined by the exact excitation energy of the doubly excited state $2s2p$ in Li^+ plus the ground state energy of Li^+ . In each case the transition in the ion of the higher charge state will also act as the series limit for a Rydberg progression for the lower charge state ion (Mannervik *et al.* 1989).

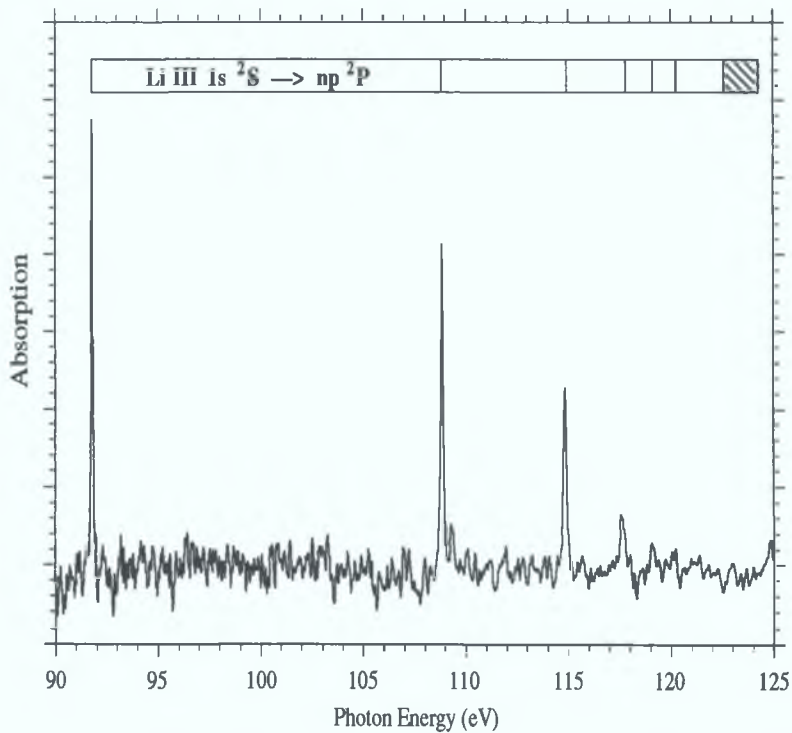


Figure 5.11. Photoabsorption spectrum of Hydrogen-like lithium, showing the principal series, $1s \rightarrow np$.

Before moving on to the measurement of the K-shell excitations of neutral lithium the principal series of Li^{2+} was recorded in photoabsorption and is shown in figure 5.11. The absorbing plasma was generated by focusing the Q-switched output of the ruby laser to a spot ≈ 0.75 mm in diameter using a 10 cm focal length spherical lens. A more tightly focused beam only resulted in unwanted emission from the fore plasma. This series has been observed in emission, of course, and is well described by

a simple hydrogenic Rydberg formula adjusted for the mass of the lithium nucleus. This photoabsorption spectrum completes the measurement of the K-shell excitations, from the ground state, of lithium's singly and doubly ionized species.

5.6. Measurement of the Triply Excited $1s^2 2s$ ($2S^e$) \rightarrow $2s^2 2p$ ($1P^o$) Resonance of Neutral Lithium.

The energy spectrum of atomic systems having three electrons such as neutral lithium, and lithium-like ions, can be divided into three groups of levels. The first group, converging on the $1s^2$ ($1S^e$) ground state of the corresponding two electron residual ion, consists of levels with a filled K-shell together with an excited electron. They are the ground state and singly excited states $1s^2 nl$ ($2l$) with parity $(-1)^l$. The second group is composed of levels for which there is only one K-shell electron. The terminology for these states is not uniform (Conneely 1992). Either of two electrons can decay down to fill the $1s$ vacancy. Hence, in analogy with two electron systems, such as helium and Li^+ , they are often referred to as doubly excited states. The other term used to describe inner-shell-vacancy states is taken from the Auger effect for many electron systems, where it is referred to as a single-inner-shell-vacancy state. The third spectral group consists of double K-shell vacancy states with no electrons in the $1s$ shell. These are also described as triply excited states, such as $Li^{***} (nl, n'l', n''l'')$, $n, n', n'' \geq 2$ (e.g. Kiernan *et al.* 1994).

The Lyman- α transition, $1s \rightarrow 2p$ in Li III, has a 'satellite' in the Li II* spectrum corresponding to the $1s2p \rightarrow 2p2p$ transition (Mannervik *et al.* 1989). Using a similar analogy, the triply excited resonance transition, $1s^2 2s$ ($2S^e$) \rightarrow $2s^2 2p$ ($2P$) of neutral lithium can be considered a 'satellite' to the Li^+ doubly excited resonance transition $1s^2 \rightarrow 2s2p$ and as such is expected to be very much weaker. From the experience gained, in the optimisation procedure of maximising the number density and purity of absorbing species in the fore plasma, while trying to observe the doubly excited Li^+ resonance, the ruby—target interaction mechanism was considered unsuitable for generating an adequate column density of neutral lithium atoms. Further, as outlined in the previous work of Costello *et al.* (1991) using the DLP technique, the use of long pulse dye lasers to generate the absorbing column yields a generally 'cooler' type of plasma consisting almost exclusively of neutral species prepared in the ground state. Thus, for this series of experiments a flash lamp pulsed dye laser (≈ 2.5 J in $1 \mu s$, broadband), the operation of which was outlined in chapter 2, was used to

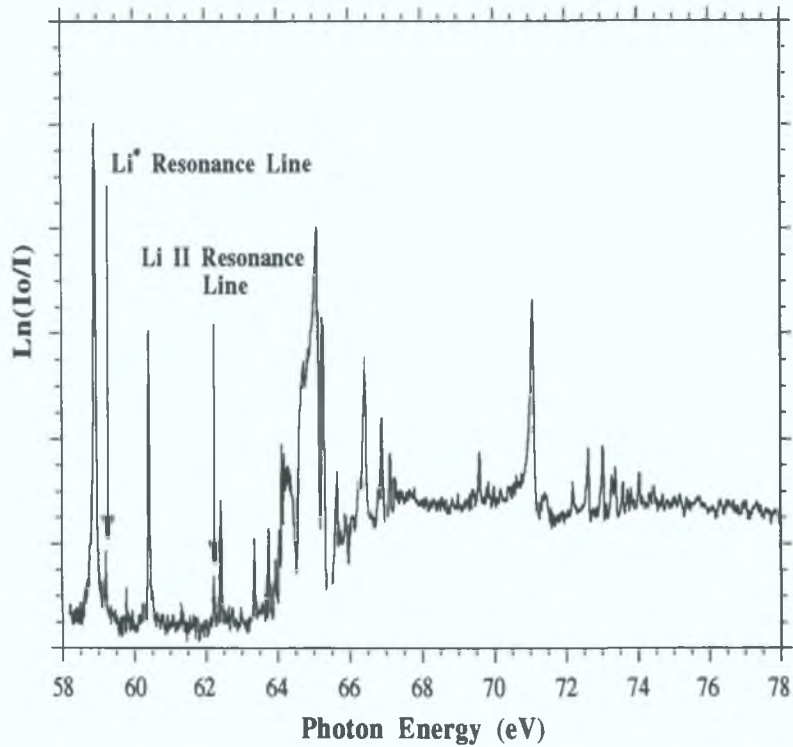


Figure 5.12. K-shell photoabsorption spectrum of the dye laser produced lithium plasma at an inter-laser delay of 800 ns corresponding to maximum ground state neutral lithium. Indicated on the plot are the strongest lines of valence excited Li and Li⁺ in this energy region.

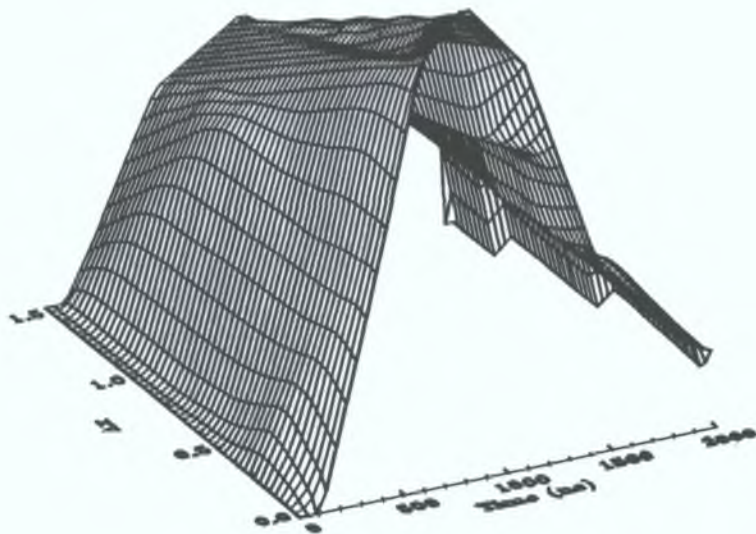


Figure 5.13. Temporal and spatial dependence of photoabsorption due to neutral lithium, where the Δx is the spatial position, in mm, of the target with respect to the optical axis of the system and time is the inter-laser time delay in ns.

generate the absorbing column.

As in the case of Li^+ we first investigated the K-shell spectrum of neutral lithium in the energy region corresponding to single 1s electron excitation, between 58 and 78 eV, with the intention of maximising absorption due to Li I in the vicinity of the K-edge at about 68 eV. Figure 5.12 shows a typical photoabsorption spectrum recorded with a tungsten continuum backlighting plasma, 0.5 mm away from the lithium target surface and at an inter-laser time delay of 800 ns. The dye laser was focused to a line, 22 mm long (parallel to the optical axis of the system) x 1 mm wide, corresponding to an irradiance of approximately $1 \times 10^6 \text{ W/cm}^2$. The photoabsorption spectrum shown in figure 5.12 should be compared with the RLDI data (recorded using photographic registration) of McIlrath and Lucatorto (1977); see figure 5.2 (a), and the absolute cross section measurements of Mehlmann *et al.* (1978) (recorded using photoelectric registration); see figure 5.3. Some contribution from optically excited lithium and singly ionized lithium can be observed with the K-shell core excited resonance being flagged in the case of each species. The relative weakness of both lines is a good measure of the purity of the ground state neutral lithium in the absorbing sample.

In a similar fashion to the approach taken with Li^+ , the time-space dependence of absorption due to ground state neutral lithium was investigated. By probing the dye laser generated fore plasma at various spatial positions with respect to the optical axis of the system and at different inter-laser time delays the contour plot in figure 5.13 was constructed. The temporal and spatial evolution of this type of laser generated plasma deviates considerably from the behaviour of the ruby generated plasma; see figure 5.7. For photoabsorption due to Li^+ , one observes a marked degree of localisation in time and space corresponding to maximum number density in the absorbing column. As is clear from figure 5.13 neutral species dominate about 0.75-1.0 μs after the peak of the dye laser optical pulse and at spatial positions close to the target surface. A sharp fall off in lithium neutral vapour density for inter-laser time delays in excess of 1 μs is observed as the expanding vapour rarifies. The small contribution from absorption due to Li^+ indicates that the lithium neutral vapour is created mostly by direct laser evaporation and to a very small extent by recombination processes. From the RLDI data of McIlrath and Lucatorto (1977), the relative population of valence excited lithium ($1s^2 2p$) to ground state lithium is estimated to be less than 10 %. From the absolute photoionization cross section of Li in this energy region (Mehlmann *et al.* 1978) we estimate the average lithium vapour density, at the optimised space-time coordinates, to be $\approx 5 \times 10^{17} \text{ atoms cm}^{-3}$.

In addition to the different plasma temporal and spatial characteristics observed while using the Q-switched ruby and dye lasers to generate the absorbing column, some experimental difficulties were encountered which should be mentioned. The rate of ablation of target material was found to be significantly greater while using the dye laser. This is probably due to two factors, firstly the much longer optical pulse length (1.0 μs compared to 30 ns) and secondly the increased length of the absorbing plasma (22 mm compared to 15 mm). This necessitated frequent replacement of the vacuum windows, which became rapidly coated on the inner surface, reducing the intensity of laser light reaching the target. The increased ablation rate also produced deep scarring of the target surface. To avoid consequent drift of the plasma away from the optical

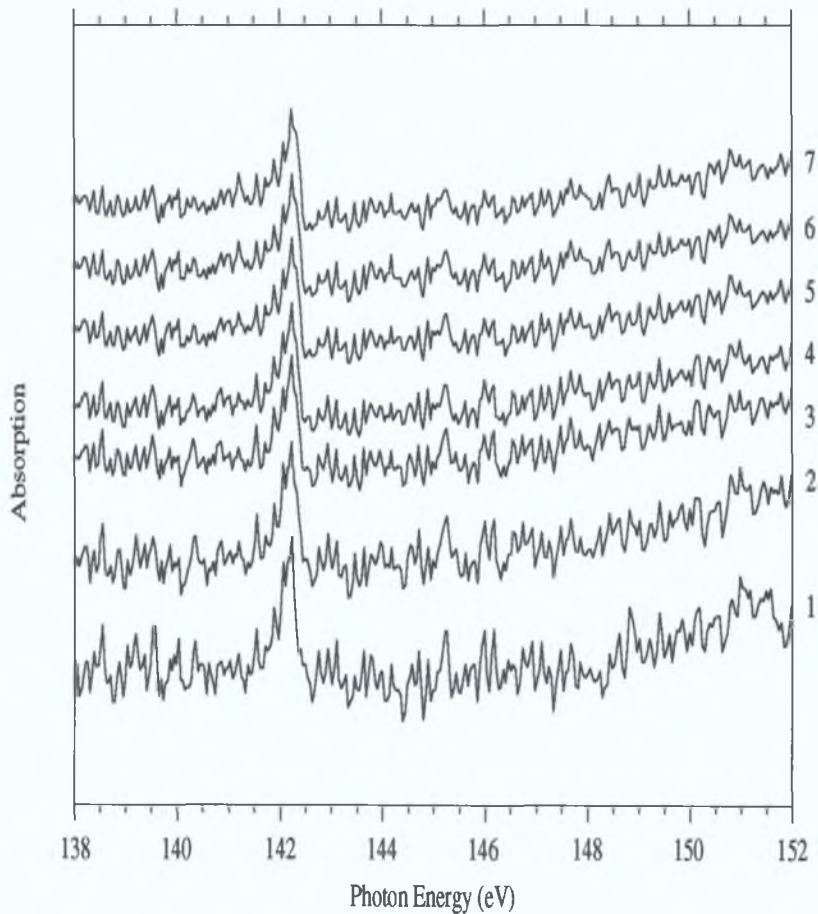


Figure 5.14. Photoabsorption spectrum of atomic lithium in the energy region, 138-152 eV, corresponding to double K-shell excitation. Plot sequence 1 to 7 illustrates the result of accumulation of sets of different experimental runs. Plot 7 corresponds to the addition of the entire set of 21 files each of which is generated by calculating $\text{Ln}(I_0/I)$ from 25 I_0 (continuum) and 25 I (absorption signal) shots, while running in single shot accumulation mode.

axis of the system, target damage was monitored regularly. During target replacement the lithium metal was cleaved in atmosphere, having been stored under vacuum, and

precleaned before each absorption experiment by firing the defocused output of the ruby laser 10-20 times onto the surface *in vacuo*. At no stage were any characteristic emission lines observed which would indicate any contamination due to oxidation. The output intensity of the ruby laser is reasonably constant with time, this however is not the case with the dye laser. After about 300-400 laser shots the output intensity tends to decrease rapidly, due to degradation of the lasing medium, resulting in a lower column density in the absorbing plasma. Thus the dye solution had to be replaced on a regular basis to maintain maximum output.

Having maximised the absorption due to neutral lithium in the vicinity of the K-edge, the optimised conditions were applied in the photon energy region corresponding to the simultaneous excitation and photoionization of both K-shell electrons. Figure 5.14 reveals the evidence of resonant processes in the energy region 138-152 eV. Because of the inherent weakness of the triply excited resonance, centred between 142 and 143 eV, many laser scans were accumulated to improve the signal to noise ratio. Spectrum 1 in figure 5.14 results from the accumulation of 3 sets of 25 scans.

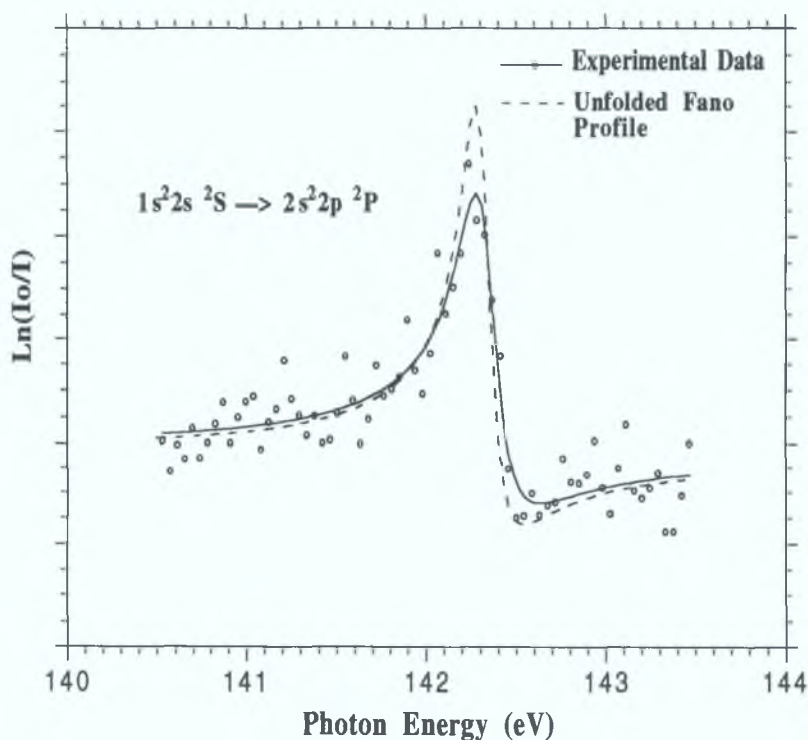


Figure 5.15. Photoabsorption spectrum of atomic lithium in the energy window of the main $1s^2 2s (^2S^e) \rightarrow 2s^2 2p (^2P^o)$ transition. The broken curve represents a Fano profile fit to the restored data following removal of instrument broadening.

Spectrum 2 corresponds to 3 independent sets of 25 scans added to the data of spectrum 1, and so on up to spectrum 7, which corresponds to the accumulation of about 525 scans. The modulation in absorption due to the triply excited resonance $1s^22s\ (^2S) \rightarrow 2s^22p\ (^2P^o)$ is approximately 3% and demonstrates clearly the difficulty in observing this feature in photoabsorption.

The photoabsorption spectrum, corresponding to spectrum 7 in figure 5.14, in the vicinity of the triply excited resonance, from 140-144 eV, is shown in figure 5.15. The solid line, in figure 5.15, is a curve fit to the raw data and clearly emphasises the asymmetric Fano type characteristics of the resonance. The instrument broadening was removed from the data, in a similar fashion to Li^+ , and the resulting curve fit to the restored data is shown as a broken curve. In order to estimate the experimental width of the $2s^22p\ (^2P^o)$ state a Fano (Fano 1961) profile formula describing the interaction of a single discrete state with many continua was applied. This formula is similar to the single discrete-single continuum channel case; see equation (5.3), e.g. helium doubly excited state, apart from the inclusion of a smoothly varying background σ_b ,

$$\sigma = \sigma_b + \sigma_0 [(q + \epsilon)^2 / (1 + \epsilon^2)] \quad (5.4)$$

This formula should be applicable, as our autoionization rate calculations using the Cowan (Cowan 1981) suite of codes, show that the decay rate of the $2s^22p\ (^2P^o)$ state is not strongly affected by discrete-discrete configuration interaction (CI) (Costello 1993) and to a good approximation the resonance can be considered as a single discrete state coupled to many continuum channels. The width obtained post deconvolution is less than 25% narrower than that obtained from the raw experimental data and is to be contrasted with the Li^+ case, where the instrumental broadening approximately doubles the width of the doubly excited $2s2p\ (^1P_1)$ state; see figure 5.9. The extracted Fano parameters E_0 , Γ , and q are shown in table 5.2 in conjunction with available calculations and measured parameters derived from previous collisional experiments existing in the literature.

As mentioned previously, Bruch *et al.* (1975) measured the ejected electron spectrum resulting from the decay of triply excited states of neutral lithium produced through the beam-foil interaction mechanism. The $2s^22p\ ^2P$ triply excited state can decay, via Coulomb autoionization, to two lower ionic excited states, ie $Li^+ 1s2s\ ^1S$ or $1s2s\ ^3S$. Two ejected electrons should therefore be detected reflecting the energy

Fano Parameters	E_0 (eV)	Γ (eV)	q
Observed	142.32 ± 0.05	0.20 ± 0.04	-2.2 ± 0.6
Other Experiments			
Bruch (1975)*	142.61	—	—
Rødbro (1979)*	142.19 ± 0.1 (142.54 ± 0.1)	—	—
Müller (1989)	143.09 ± 0.1	1.2	—
Calculations			
HF-CI	141.90	0.21	—
Chung (1982)	142.26	—	—
Simons (1979)	142.66	0.13	—
Safronova (1978)	141.81	0.24	—
Nicolaidis (1977)	141.70	—	—
Ahmed (1975)	142.61	—	—

Table 5.2. Comparison of computed and measured Fano parameters for the $1s^22s$ ($^2S^e$) \rightarrow $2s^22p$ ($^2P^o$) transition of atomic lithium, the transition energies marked with an asterisk have been computed from the quoted experimental free electron energies.

separation of the $1s2s$ 1S and 3S limits of neutral lithium, i.e. $66.31(^1S) - 64.41(^3S) = 1.9$ eV. The energy values for both limits are derived from the high resolution photoelectron measurements of Langer *et al.* (1991). Bruch *et al.* (1975) reported two electron lines at 76.3 and 78.2 eV corresponding to decay to the lower states of $1s2s$ 1S and 3S respectively. These two electron lines have the appropriate energy interval of 1.9 eV, and by adding the energy level of the 1S and 3S limits above the ground state of lithium neutral one can calculate that the initial excited state, $2s^22p$ 2P should be at 142.61, as shown in table 5.2. Rødbro *et al.* (1979) measured the ejected electron spectrum of triply excited lithium using the collisional excitation process whereby a

Li⁺ ion beam was impacted on gaseous targets. In contrast to Bruch *et al.* (1975), they report two electron lines at 75.88 and 78.13 eV with an energy interval of 2.25 eV. Using these free electron energies the initial 2s²2p ²P state, therefore, has two possible energy positions of 142.19 or 142.54 eV, as shown in table 5.2. The second line at 142.54 eV corresponds to decay to the final ionic state of 1s2s ³S and overlaps with another line, associated with Li⁺, in their ejected electron spectrum. This would seem to indicate that the former calculated value of 142.19 eV is more reliable since the associated electron line is well separated in energy from any other spectral features.

Müller *et al.* (1989), have measured the direct and resonant production of Li²⁺ through electron impact ionization and resonant electron capture, into the intermediate 2s²2p ²P triply excited state, of a Li⁺ ion beam. In their experiment they collected the Li²⁺ product ions at incident electron energies corresponding to both interaction processes. The cross section for direct impact ionization is shown in figure 5.1a. The cross section for resonant electron capture is three orders of magnitude lower and figure 5.1b shows the subtraction of the direct ionization cross section from the resonant cross section. The shapes of the resonances clearly indicate strong interference of the resonant channel with the nonresonant direct ionization channel.

The triply excited resonance, 1s²2s(²S) → 2s²2p(²P), according to our photoabsorption measurements, is located at 142.32 ± 0.05 eV and is in excellent agreement with the most recent computed value, using a saddle point technique of 142.26 eV given by Chung (1982). The calculation of the autoionization width of the 2s²2p(²P) state has been reported by Safronova and Senashenko (1978) who obtained a value of 0.24 eV using a 1/Z expansion and Simons *et al.* (1979), whose value of 0.14 results from the application of Many Body Perturbation Theory. Using the Cowan code three separate autoionization rate calculations, were carried out, including three continuum configurations (1s2sεp, 1s2sεs and 1s2pεd) coupled with either one (2s²2p), two (2s²2p + 2p³) or twenty five discrete configurations (Costello 1993). All the orbitals of which were computed variationally. The results of these calculations yielded values of 0.18, 0.22 and 0.21 respectively for the width of the 2s²2p (²P₀) state compared to the measured value of 0.20 ± 0.04. This value is also in good agreement with that of Safronova and Shenashenko (1978) but not with that of Simons *et al.* (1979) To the best of our knowledge there is no published theoretical value for the profile index q, for comparison with experiment.

In conclusion, the doubly excited series 2snp of helium-like lithium has been observed, for the first time with photoelectric registration and, within the limits of experimental error, the Fano parameters of the main doubly excited resonance were

found to agree with those measured previously using the DLP technique by Carroll and Kennedy (1977) Also measured, for the first time, was the fundamentally important photoabsorption spectrum of triply excited neutral lithium, where all three electrons reside in the same $n=2$ shell The position, width and profile index of the main $1s^22s$ ($^2S^e$) \rightarrow $2s^22p$ ($^2P^o$) resonance were obtained. This was achieved by exploiting the versatility of the DLP technique and by working at the operational limits, in terms of resolution and dynamic range, of our spectrometer detection system Simple HF calculations predict a substantial number of other weak triply excited resonances many of which have a width comparable to or less than that of our instrumental width Hence further experiments on this fundamental atomic system will require high resolving power spectrometers, coupled to high photon flux sources with high dynamic range detection to resolve the supernumerary triply excited resonances which characterise the atomic lithium spectrum at excitations energies above 140 eV. In order to obtain detailed information on the dynamics of resonant double photoionization in three electron systems, angle resolved photoelectron spectroscopy on ground and laser excited/aligned lithium, e.g. Pahler *et al* (1992), at photon energies corresponding to triple excitation will be required

5.7 References.

Agentoft M., Andersen T and Chung K. T., J. Phys. B: At. Mol. Phys., **17**, L433, (1984).

Ahmed M. and Lipsky L., Phys. Rev. A., **12**, 1176, (1975).

Bruch R., Paul G., Andrä J. and Lipsky L., Phys. Rev. A., **12**, 1808, (1975).

Cantú A. M., Parkinson W. H., Tondello G. and Tozzi G. P., J. Opt. Soc. Am., **67**, No. 8, (1977).

Carroll P. K. and Costello J. T., Phys. Rev. Lett., **57**, 1581, (1986).

Carroll P. K. and Kennedy E. T., Phys. Rev. Lett., **38**, 1036, (1977).

Chung K. T., Phys. Rev. A., **25**, 1596, (1982).

Conneely M. J., Lipsky L. and Russek A., Phys. Rev. A., **46**, 4012, (1992).

Cooper J. W., Fano U. and Prats F., Phys. Rev. Letts., **10**, 518, (1963).

Costello J. T., Kennedy E. T., Sonntag B. F. and Clark C. W., Phys. Rev. A., **43**, 1441, (1991).

Costello J. T., *Private Communication* (1993).

Cowan R. D., “ The Theory of Atomic Structure and Atomic Spectra “, Univ. of California - Berkeley Press, (1981).

Domke M., Remmers G. and Kaindl G., Phys. Rev. Lett., **66**, 1306, (1991).

Domke M., Remmers G. and Kaindl G., Phys. Rev. Lett., **69**, 1171, (1992).

Ederer D. L., Lucatoro T. and Madden R. P., Phys. Rev. Lett., **25**, 1537, (1970).

Ederer D. L., Lucatoro T. and Madden R. P., J. de Physique, Colloque C4, supplément n° 10, Tome 32, C-85, (1971).

- Fano U, Phys. Rev., **124**, 1866, (1961).
- Fano U. and Cooper J. W., Phys. Rev., **138**, A400, (1965).
- Harris S. E., Opt. Lett., **5**, 1, (1980).
- Jannitti E., Nicolosi P. and Tondello G., Opt. Commun., **50**, 225, (1984).
- Kennedy E. T., PhD Thesis, National University of Ireland, (1977).
- Kiernan L. M., Kennedy E. T., Mosnier J-P. and Costello J. T., *submitted to Phys. Rev. Lett. December 1993*.
- Kuyatt C. E., Simpson J. A. and Mielczarek S. R., Phys. Rev., **138**, A385, (1965).
- Langer B., Viefhaus J., Hemmers O., Menzel A., Wehlitz R. and Becker U., Phys. Rev. A., **43**, 1652, (1991).
- Madden R. P. and Codling K., Phys. Rev. Lett., **10**, 516, (1963).
- Mannervik S., Physica Scripta, **40**, 28, (1989).
- Mannervik S., Short R. T., Sonnek D., Träbert E., Möllner G., Lodwig V. Heckmann P. H. Blanke J. H. and Brand K., Phys. Rev. A., **39**, 3964, (1989).
- McIlrath T. J. and Lucatorto T. B., Phys. Rev. Lett., **38**, 1390, (1977).
- Mehlmann G., Cooper J. W. and Saloman E. B., Phys. Rev. A., **25**, 2113, (1982).
- Mehlmann G., Ederer D. L., Saloman E. B. and Cooper J. W., J. Phys. B: At. Mol. Phys., **11**, No.22, L689, (1978).
- Müller A., Hofmann G., Weissbecker B., Stenke M., Tinschert K., Wagner M. and Salzborn E., Phys. Rev. Lett., **63**, 758, (1989).
- Nicolaides C. A. and Beck D. R., J. Chem. Phys., **66**, 1982, (1977).
- Pahler M., Lorentz C., Von Raven E., Sonntag B. F., Baier S., Müller B. R., Schulze M., Zimmermann P. and Kabachnik N. M., Phys. Rev. Lett., **68**, 2285, (1992).

Pegg D J , Haselton H H , Thoe R S , Griffin P M , Brown M. D and Sellin I A , Phys Lett , **50A**, 447, (1975)

Røbro M , Bruch R and Bisgaard P , J Phys B At Mol Phys , **12**, 2413, (1979)

Safronova U. I and Senashenko V S., J Phys B At Mol. Phys , **11**, 2623, (1978)

Schwarzkopf O , Krassig , Elmiger J and Schmidt V , Phys Rev. Lett , **70**, 3008, (1993)

Shore B , J Opt Soc Am , **57**, 881, (1967)

Silvermann S M and Lassetre E. N , Ohio Univ Res Foundation, 1953-1958, Report No. 9, p12, (1959)

Silvermann S M and Lassetre E N , J Chem Phys., **40**, 1265, (1964)

Simons R L., Kelly H P and Bruch R., Phys Rev A , **19**, 682, (1979)

Trabert E , Blanke J H , Hucke R and Heckmann P H , Physica Scripta, **31**, 130, (1985).

Zhou B , Lin C. D , Tang J-Z., Watanabe S and Matsuzawa M , *submitted to Phys Rev A , June 1993.*

Ziem P , Bruch R. and Stolterfoht N , J. Phys. B At Mol Phys , **8**, L480, (1975)

Chapter 6

Summary and Conclusions

The primary objective of this final chapter is to briefly summarise what has been achieved to date and to make conclusions regarding the degree of success that has been attained. In addition some suggestions for future experimental work, which would represent an extension of the existing thesis are outlined.

6.1. Summary and Conclusions.

Through the course of this work a facility with multi-channel photoelectric detection has been developed, which is based on the use of laser plasmas as both light sources and absorbing media. The system is capable of measuring the photoemission and photoabsorption spectra of atoms, excited atoms and ions in the XUV region of the spectrum. The individual components which have been integrated together to form this system have been described in detail in chapter two. The key performance characteristics of the system are,

- (i) Wide energy range coverage (20-250 eV).
- (ii) Shot to shot monitoring of the inter-laser time delay and relative intensity of each laser output pulse.
- (iii) Selectivity of ion stage via three laser system.
- (iv) Single shot sensitivity.
- (v) High resolution.
- (vi) Multi-channel detection.
- (vii) Good reproducibility.
- (viii) Measurement of relative photoabsorption cross section ($-\ln(I/I_0)$)
- (ix) Ease of operation.

The operational energy range of the system is determined by the type of grating in use and the available length of bellows connecting the detector chamber to the main grating chamber. There are three kinematically mounted gratings available for use with this spectrometer which have 600, 1200 and 2400 lines per mm rulings. These yield

energy ranges of 10-90 eV, 20-180 eV and 40-360 eV respectively, for an angle of incidence of 84°. The ultimate choice of grating is usually a trade off between required resolution and the available continuum photon flux. With the 1200 lines/mm grating currently in place and the limitation of the toroidal mirror grazing angle the practical energy range is between 20 and 180 eV.

A significant improvement over previous DLP arrangements is the ability to monitor the shot to shot stability of the inter-laser time delay and the relative intensity of the laser pulses. The video output from the PDA can also be monitored simultaneously shot to shot. The two digitising oscilloscopes used for this purpose are normally co-located with the PC which is responsible for firing the lasers and controlling the accumulation of data from the detector. In this way the user can interactively prevent rogue data from being accidentally accumulated with otherwise valid data.

The multi-laser aspect of the facility, coupled with the ability to electronically vary the inter-laser time delay (± 10 ns), the spatial position of the absorbing plasma (± 50 μm) and the power density incident on the target has greatly enhanced the capacity to probe and select the ionization stage of interest in the absorbing plasma. In general, the use of the long pulse duration dye laser has been found to yield a relatively cool absorbing plasma suitable for the study of neutral or singly ionized species. The Q-switched ruby laser enables higher ionization stages to be studied. Use of cylindrical optics to produce a line focus configuration can substantially increase the effective absorption column.

The incorporation of a gold coated toroidal mirror in the system to efficiently couple the XUV light into the spectrometer has dramatically reduced the number of laser shots required to obtain a spectrum. Using previous DLP arrangements without such a mirror, it was found necessary to accumulate, in some cases, hundreds of laser shots to produce an adequate blackening on photographic plates. Using the present system an absorption spectrum, with a good signal to noise ratio, can be obtained with the accumulation of typically 10 to 20 laser shots depending of course on the strength of the features concerned. It has also proven possible, where the absorption features concerned are of considerable intensity, to record single shot spectra to investigate the inter-relationship of lines associated with the same ion stage. In this way, from the collective behaviour of certain lines, it is possible to identify features originating from the same ion stage while changing absorbing plasma conditions.

The resolution of the system depends on the grating in use and the energy region of interest. For all the spectra illustrated in this thesis a 1200 lines per mm grating was used. The resolution limit is ultimately set by the spatial sampling period of the detector along the Rowland circle. Assuming a minimum separation of three pixels, a resolution

of between approximately 1000 at 180 eV and 2500 at 20 eV, should be available using a 1200 lines per mm grating. Post data processing utilities offer the possibility of applying several methods of resolution enhancement from a known instrument response function.

The multi-channel detection system covers 40 mm of the focal curve at the Rowland circle. This represents an energy interval of, for example, approximately 30 eV at a central detector position of 100 eV. The width of the energy window decreases as the detector is moved further away from the grating along the Rowland circle. The use of such a multi-channel detection system increases the rate of accumulation of spectral data over conventional scanning slit spectrometers.

The reproducibility of the laser plasma continuum light source has been measured to be, on average, better than 3%. This is mainly due to two factors. Firstly the full output of a single dedicated laser (Nd:YAG), the intensity of which is extremely reproducible from shot to shot, is used to generate the continuum backlighting plasma. Secondly, the target material used for the most part was tungsten which is very durable and has a very low ablation rate, resulting in a much reduced risk of occlusion of the source due to surface damage. By simply recording the accumulated continuum emission from the backlighting plasma in the absence (I_0) and presence (I) of an absorbing species the relative photoabsorption spectrum, $-\ln(I_0/I)$, can be computed.

Probably one of the most attractive features of the present system is its simplicity and relative ease of operation. It is possible for one person to operate the entire system. To date, the facility has been used by a number of visiting scientists, from University College Cork and Universität Hamburg, with considerable success. The grazing incidence spectrometer and toroidal mirror chamber are maintained under high vacuum at all times and thus when a change of target material is required, the system down time is typically less than five minutes, due to the small pumping volume and independent venting capability of the target chamber. In addition, the amount of target material used up in a typical photoabsorption experiment, is minute compared to what might be needed to create an adequate vapour density in a heat pipe or furnace. The various vacuum components, manufactured inhouse, have been terminated with standard ISO ports facilitating any future modifications or inclusions to the system.

During the characterisation process a program of XUV photoemission and photoabsorption experiments were undertaken to determine the performance of the overall system in terms of resolution, calibration and suitability for the measurement of relative photoabsorption cross sections of both atoms, free and in a solid matrix, and ions. These experiments included the measurement of the photoabsorption characteristics of thin films, inert gases, atomic vapours of refractory metals and trends along isoelectronic and isonuclear sequences in transition regions of the Periodic Table.

The wide range of experiments undertaken, with practically no alteration of the system, serves to illustrate the inherent versatility of the present facility. The data obtained along the calcium isonuclear sequence upon comparison with the results of previous RLDI and synchrotron/ion beam experiments serves to illustrate the potential role of the DLP facility in providing reliable atomic and ionic photoabsorption data.

The first observation of the photoabsorption spectra of atomic zinc and its ions (Zn^{n+} ; $n=1,2,3$) in the energy region corresponding to electron excitation from the 3p subshell, has been obtained. In contrast to the transition metals preceding zinc, where the open 3d subshell produces strong and broad 3p — 3d resonances, relatively weak absorption structures are observed corresponding to 3p — ns transitions, for the situation where the 3d shell is closed (i.e. Zn, Zn^+ and Zn^{2+}). The large width of the resonances is primarily due to the predominant decay of the 3p hole through super Coster-Kronig and Coster-Kronig processes. The observed 3p — ns resonances have a symmetric profile reflecting the weak interaction between the direct 3d photoionization continuum and the ns discrete states. For the situation where the 3d shell is opened (i.e. Zn^{3+}), however, a dramatic change in spectral signature is in evidence, corresponding to the 3p — 3d resonance transitions. In addition to an observed increase in intensity, the 3p — 3d resonance is asymmetric in character suggesting strong interaction of the core excited state with the underlying continuum. Simple Hartree-Fock calculations reproduce the observed trends, in oscillator strengths and relative excitation energies along this isonuclear sequence. Some calculations, based on the collective models of the Random Phase Approximation with Exchange and the Time Dependent Local Density Approximation, are also included which show reasonable agreement with the observed spectral signatures.

Finally, results are presented regarding photoabsorption studies undertaken along the important lithium isonuclear sequence in the region of single and multiple K-shell electron excitation. The first photoelectric measurement of the helium-like $Li^+ 2snp$ doubly excited series has been obtained. The absorbing column of Li^+ was first optimised by extensive measurements of the temporal and spatial evolution of a ruby laser produced lithium plasma in line focus configuration. Fano parameters for the main $2s2p \ ^1P$ doubly excited resonance, were extracted having first removed the folded instrument response function from the raw spectral data. Good agreement was observed, within the limits of experimental error, with the resonance parameters obtained previously using photographic registration. Working at the operational limits in terms of resolving power and dynamic range of the present system, we have observed, for the first time, evidence of a photon-induced triply excited state in atomic

lithium. The same procedure employed to optimise the Li^+ ion density in the absorbing plasma, where the temporal and spatial evolution of the plasma was mapped out, was used in the case of neutral lithium. A dye laser in line focus configuration generated the absorbing plasma. The length of the absorbing column needed to generate an adequate density of atomic lithium represents, by far, the longest plasma ever used in this setup. The extracted energy position and width of the $2s^22p$ triply excited state, are in good agreement with our multi configuration Hartree-Fock calculations and with the most recent available calculations in the literature. This experiment represents the first step in the photoionization studies of this fundamental atomic system in which the motion of the three electrons in the field of the nucleus is so highly correlated. It is hoped that this work will act as a stimulus for further experimental work and calculations on resonant double photoionization of atomic lithium.

6.2. Suggestions for Future Work.

This thesis underlines the ability of the DLP technique to record photoabsorption spectra of a wide variety of atoms and ions in spectral regions corresponding to inner shell excitations. The reliability of the data depends on the success in isolating an atomic or ionic species in a single known state. By exploiting the temporal and spatial behaviour of the absorbing plasma considerable progress can be made for atoms or ions which have clear spectral signatures and energy levels structures which favour ease of separation. However, the much preferred experimental option would be to develop an independent means of characterisation of the absorbing plasma plume. One such technique would be to probe the absorbing column simultaneously in the valence energy regime. The energy transitions (and often absolute cross sections) are generally well known for valence electron excitations..

The DCU Laser Plasma Group has already acquired a 1 m normal incidence spectrometer for this purpose. The energy range of this spectrometer covers from approximately 5 to 40 eV, and will enable the measurement of cross sections in the valence excitation regime. It is intended to install a gated VUV array detection system similar to the multi-channel device already in operation in the grazing incidence spectrometer, to provide simultaneous dual energy range monitoring of the absorbing plasma. This will enable critical cross checking of the absorbing species by observation of known valence transitions. This cross checking in different spectral regions will be essential to obtain reliable cross sections for case of atomic and ionic species which are not easily separable by observation of their XUV spectra alone.

It is envisaged that a second focusing optic, such as an off axis parabolic mirror,

will be inserted between the existing target chamber and toroidal mirror chamber. This mirror will operate at a much reduced angle of incidence compared to the toroidal mirror because of the improved reflectivity at longer wavelengths. The mirror will probably be designed with a small hole through the centre to allow the XUV light to pass through and onto the toroidal mirror, at the same time coupling the VUV light efficiently into the normal incidence spectrometer. Considerable modifications to the software controlling the existing data acquisition process and to the timing circuits will also be required to successfully operate both multi-channel detection systems simultaneously.

There are a wealth of possible extensions that could be made to the spectroscopic investigations already outlined in this thesis. All the existing spectra could be improved by gathering more photoabsorption data to improve the statistics of some of the weaker features present. In the case of the calcium isonuclear sequence, extensive calculations are required to unravel the rich satellite structure which characterises the Ca^+ 3p photoabsorption spectrum. The degree of ion stage separation between Ca^{2+} and Ca^{3+} , in the region of the 3p — 3d main resonance could also be improved upon. It would also be interesting to record the 3p spectrum of argon-like calcium above the 3p thresholds to investigate the possibility of multiple electron excitations.

Absolute photoionization cross section data exists for Zn^+ in the region of 3d electron excitation. Unfortunately this energy region proved to be just outside the energy range set by the 1200 lines per mm grating. Using the 600 lines per mm grating it would be possible to measure the 3d spectrum of Zn^+ for comparison with the absolute cross section data. Using the same optimised absorbing plasma conditions in the region of 3p excitation one would be able put the Zn^+ photoabsorption data on an absolute scale. Prof. M.Y. Adam of LURE, in Paris, has expressed considerable interest in the results obtained for the free ions of zinc. She has proposed an experiment to measure, using photoelectron spectroscopy, the decay of the 3p hole produced through the interaction of synchrotron light with a beam of molecules such as ZnCl_2 and ZnBr_2 . Because of the strong electron affinity of the the halogen elements for the two 4s valence electrons and the intrinsic atomic character of the 3p excitations, it is quite possible that the zinc atoms in these molecules will exhibit some semi ionic properties. The inter comparison of the spectra of free atom and the molecule would yield important information about the type of bonding which exists within the molecule.

As mentioned already the triply excited resonance of atomic lithium has been observed while operating at the limits of the present system resolution and dynamic range. In order to investigate further the predicted weak and narrow supernumerary

structure in the energy region of the main $2s^22p$ triply excited resonance it will be necessary to increase the absorbing column density, the resolution and the dynamic range of the detection system. Such an experimental system is under construction for use this autumn, by Prof. B. F. Sonntag and his group at the DESY synchrotron in Hamburg. The resolution of the toroidal grating monochromator in use on this particular beam line, which is positioned directly after an undulator insertion device, is about 5000 and represents an almost five fold increase in performance. The intense photon flux available from the undulator will provide a bright backlighting continuum source producing high counting rates. Both photoabsorption and photoion experiments are planned. The photoion measurements will provide more detailed information on the decay kinetics of these triply excited states leading to improved understanding of the resonant double photoionization process. In the future, it should also prove possible to measure the even parity triply excited states, such as $2s2p^2$ by initial excitation to the valence excited state, $1s^22p$, using a tunable dye laser.

Appendix A
System Mechanical Drawings

Legend

A2: Schematic side view of total system showing the relative heights of various components with respect to the optical axis of the system.

A3: Support frame for electrical cables and cooling lines which clamps around the top of the detector UHV chamber.

A4: Support frame for toroidal mirror chamber.

A5: Cylindrical section of toroidal mirror chamber which bolts onto the entrance slit assembly of the grazing incidence spectrometer.

A6: Side view of cubic section of toroidal mirror chamber.

A7: Underneath of Dn 63 pumping flange for toroidal mirror chamber.

A8: Top side of Dn 63 pumping flange for toroidal mirror chamber.

A9: Flange with angled Dn 40 pumping port for toroidal mirror chamber.

A10: Toroidal mirror mount and base plate.

A11: Example of alignment template with angled 1.0 mm at 16° to define the optical axis of the system.

A12: Dimensioned plan view from the toroidal mirror chamber to laser plasma target chamber.

A13: Glass Capillary Array holder fitted in a standard Dn 40 port.

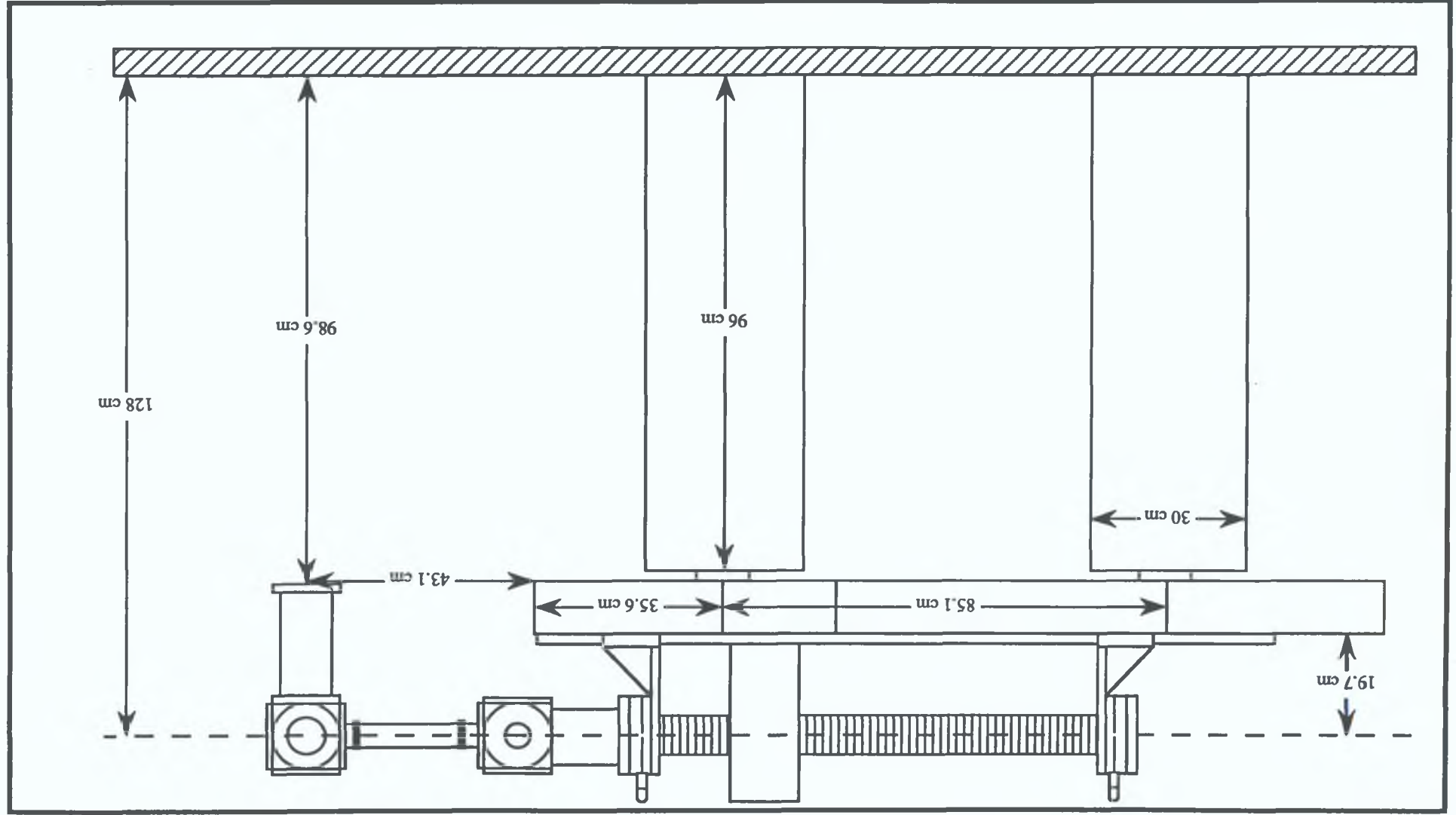
A14: Side view of cubic laser plasma target chamber.

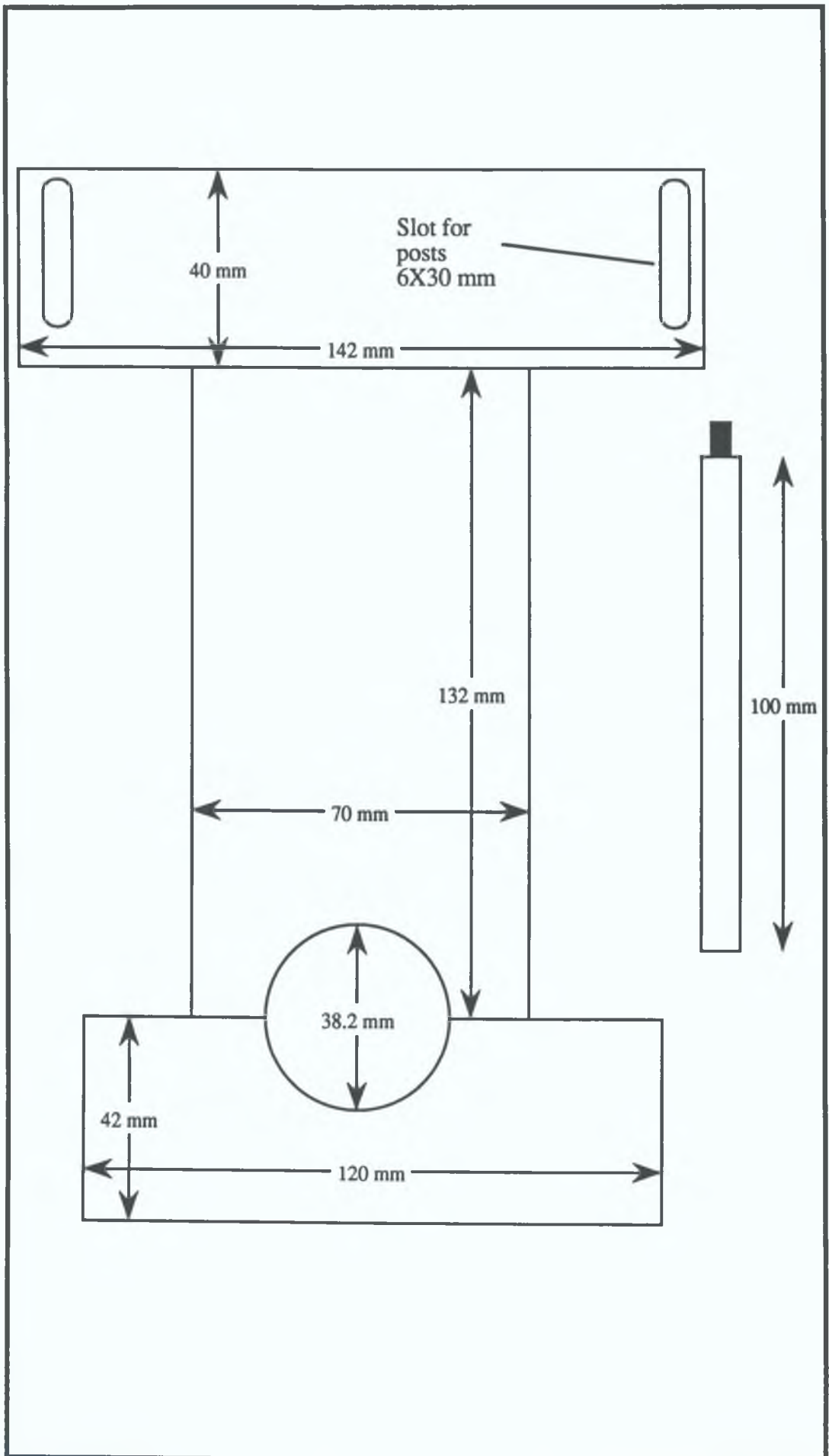
A15: Support column for target chamber cube.

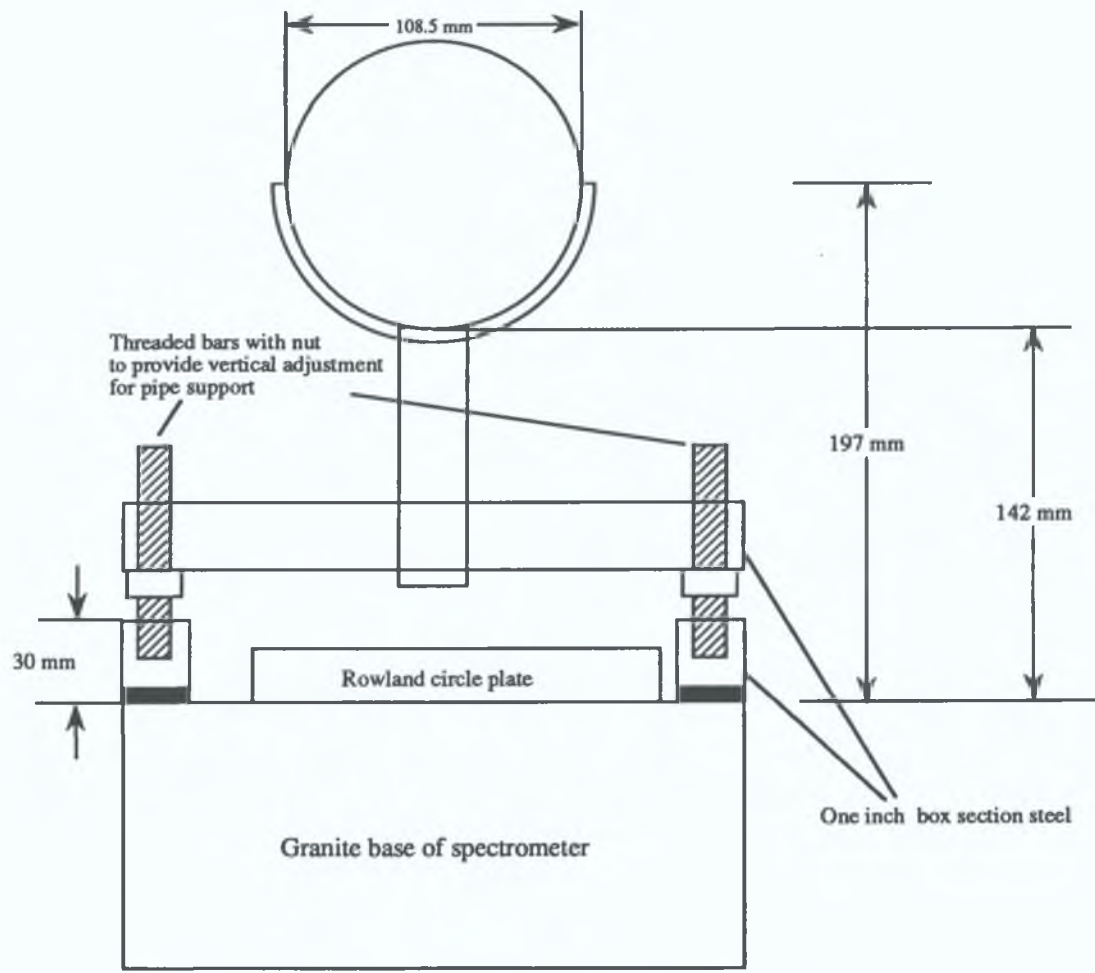
A16: Target chamber protective inner sleeve.

A17: Movable continuum target holder.

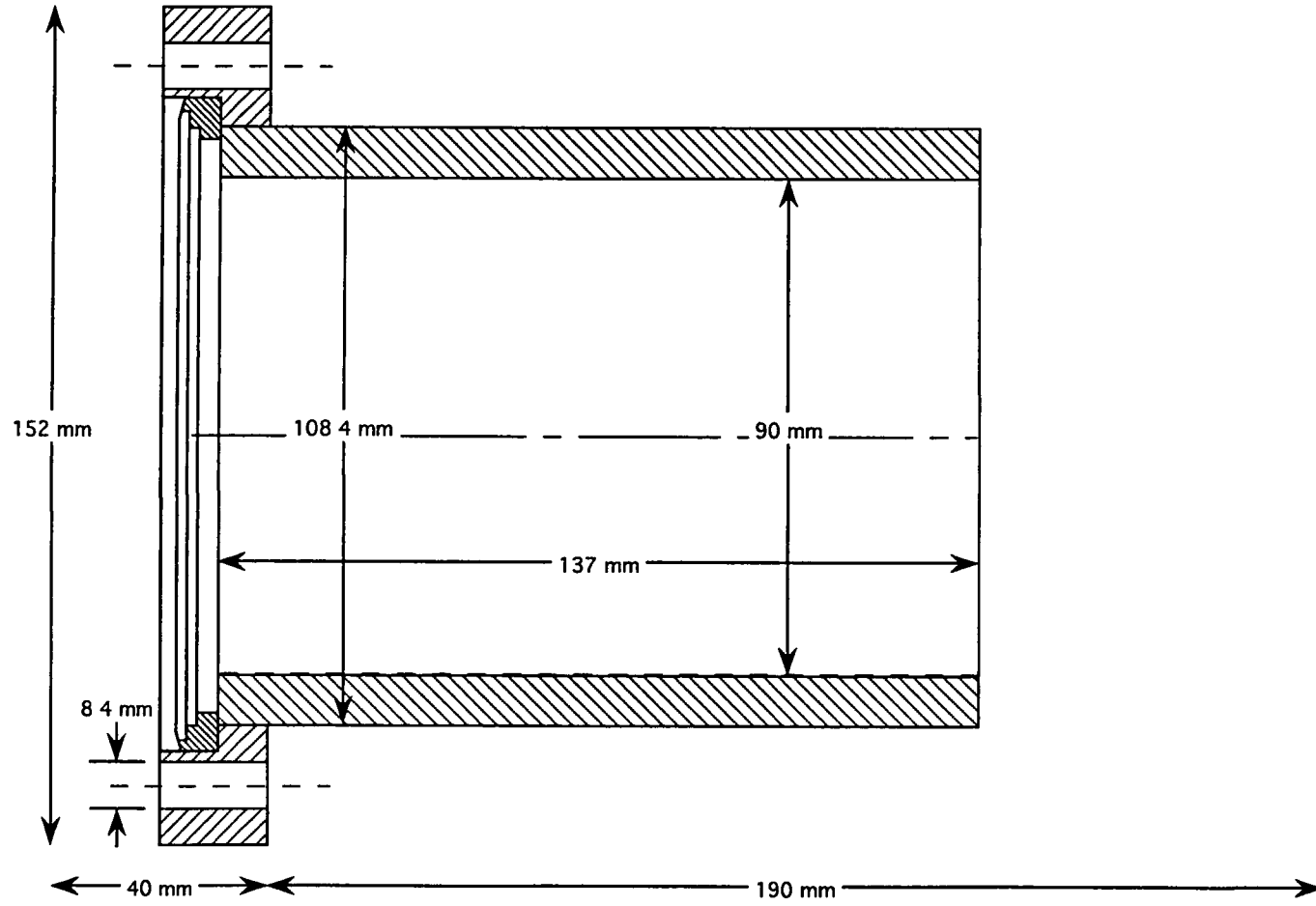
A18: Base plate for laser focusing optics which clamps around the support column.

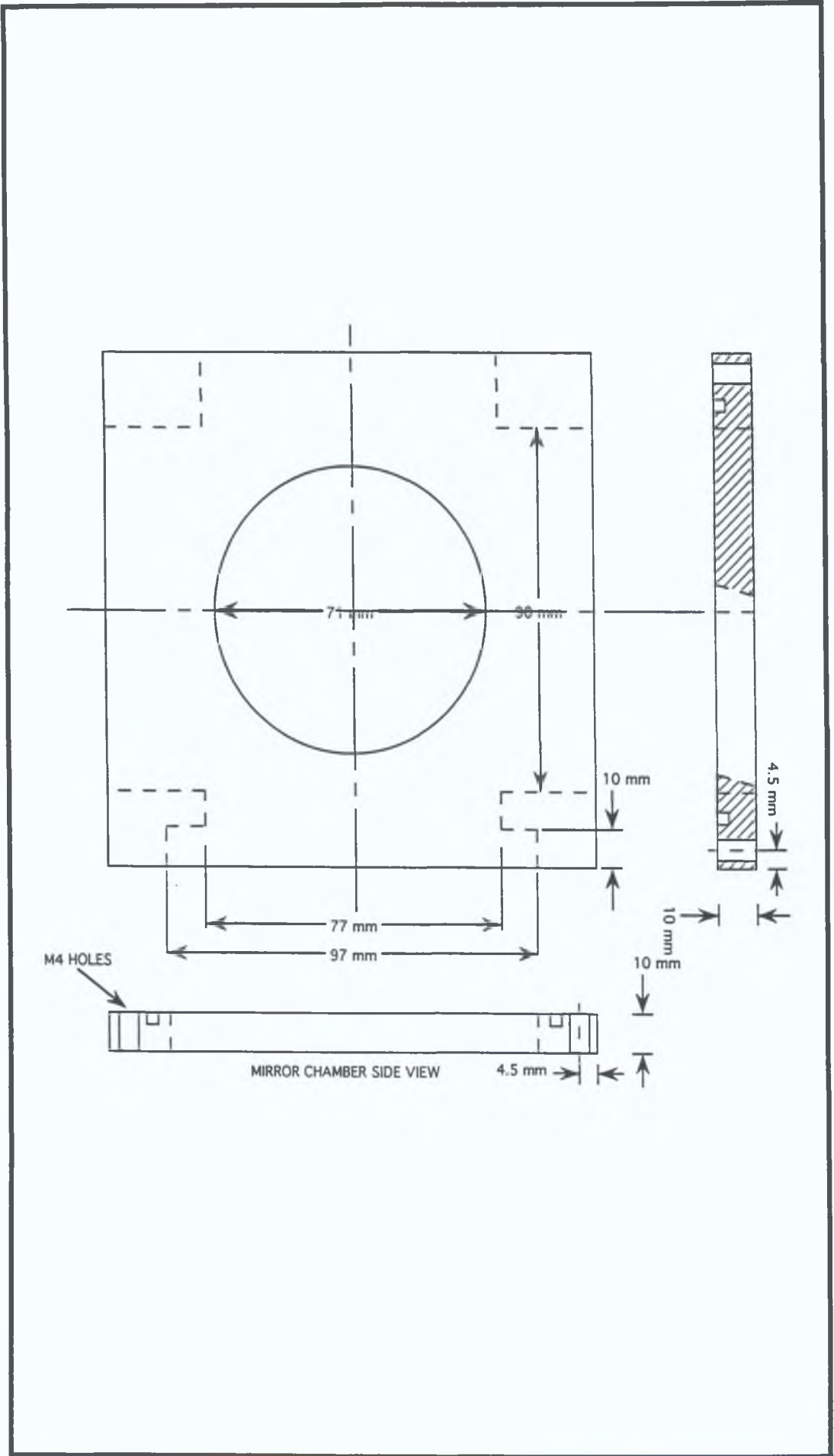


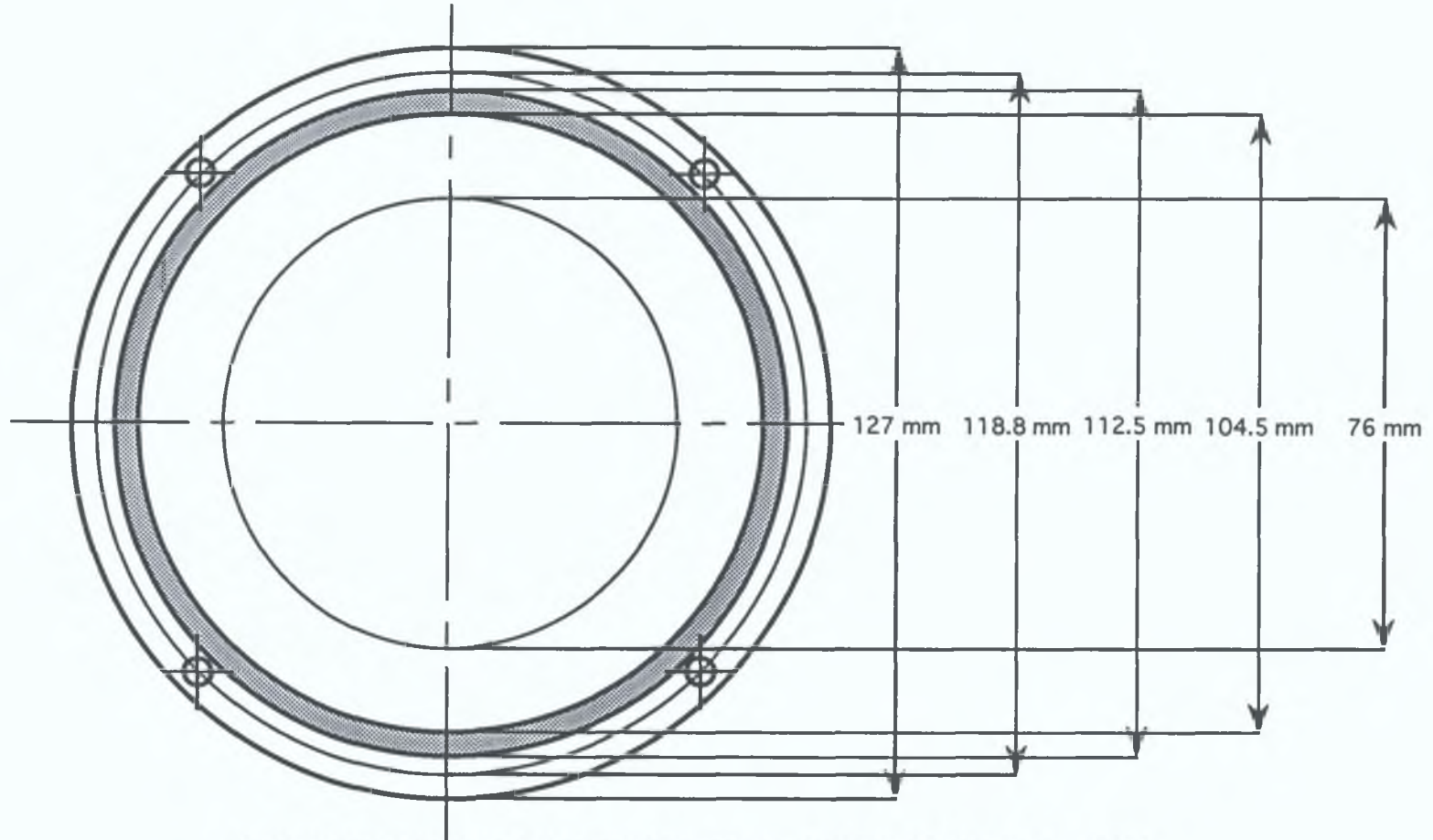




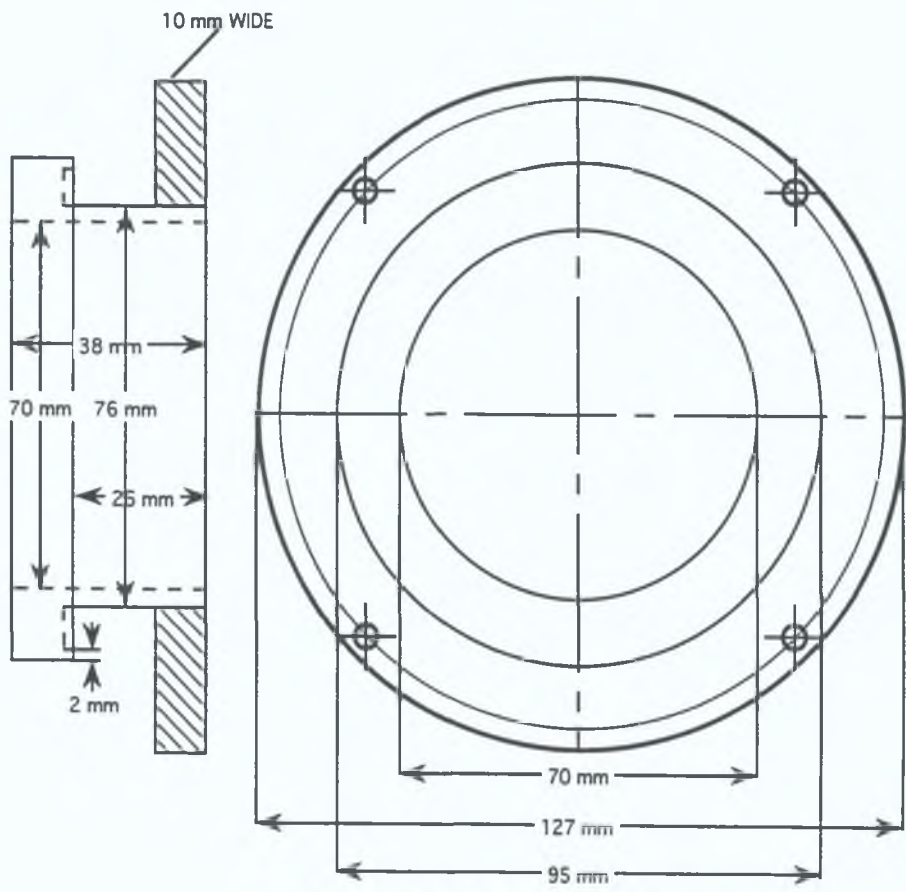
CF 100 SPECTROMETER SIDE



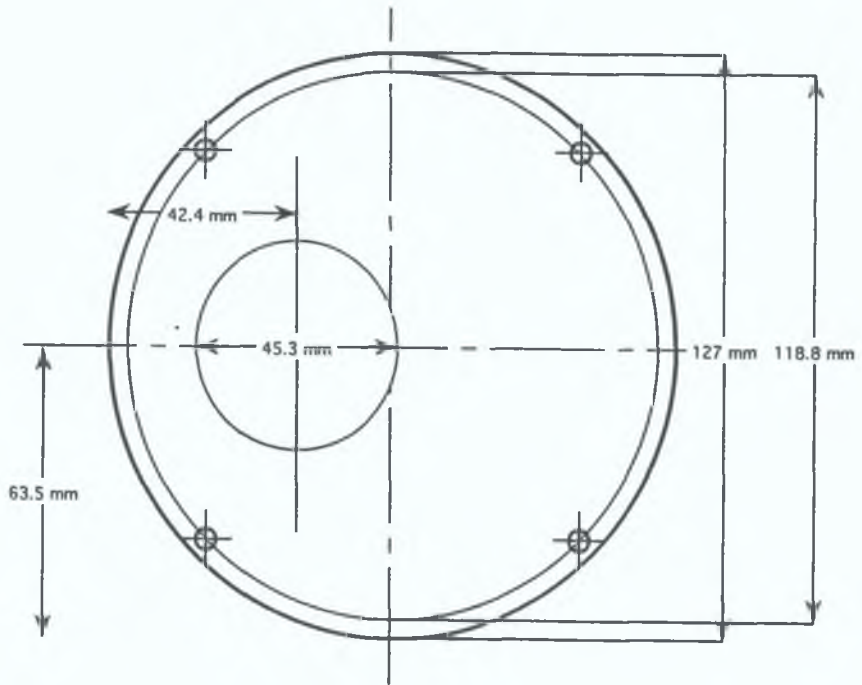




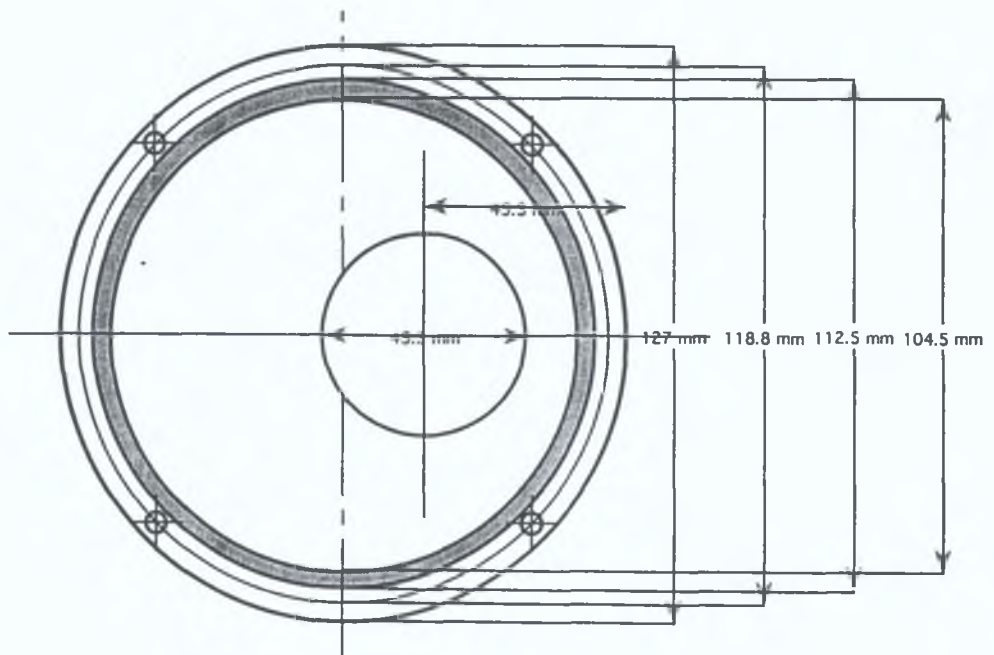
[FLANGE WITH DN 63 PORT FOR PUMPING (inside view) O RING GROOVE IS 2 mm DEEP]



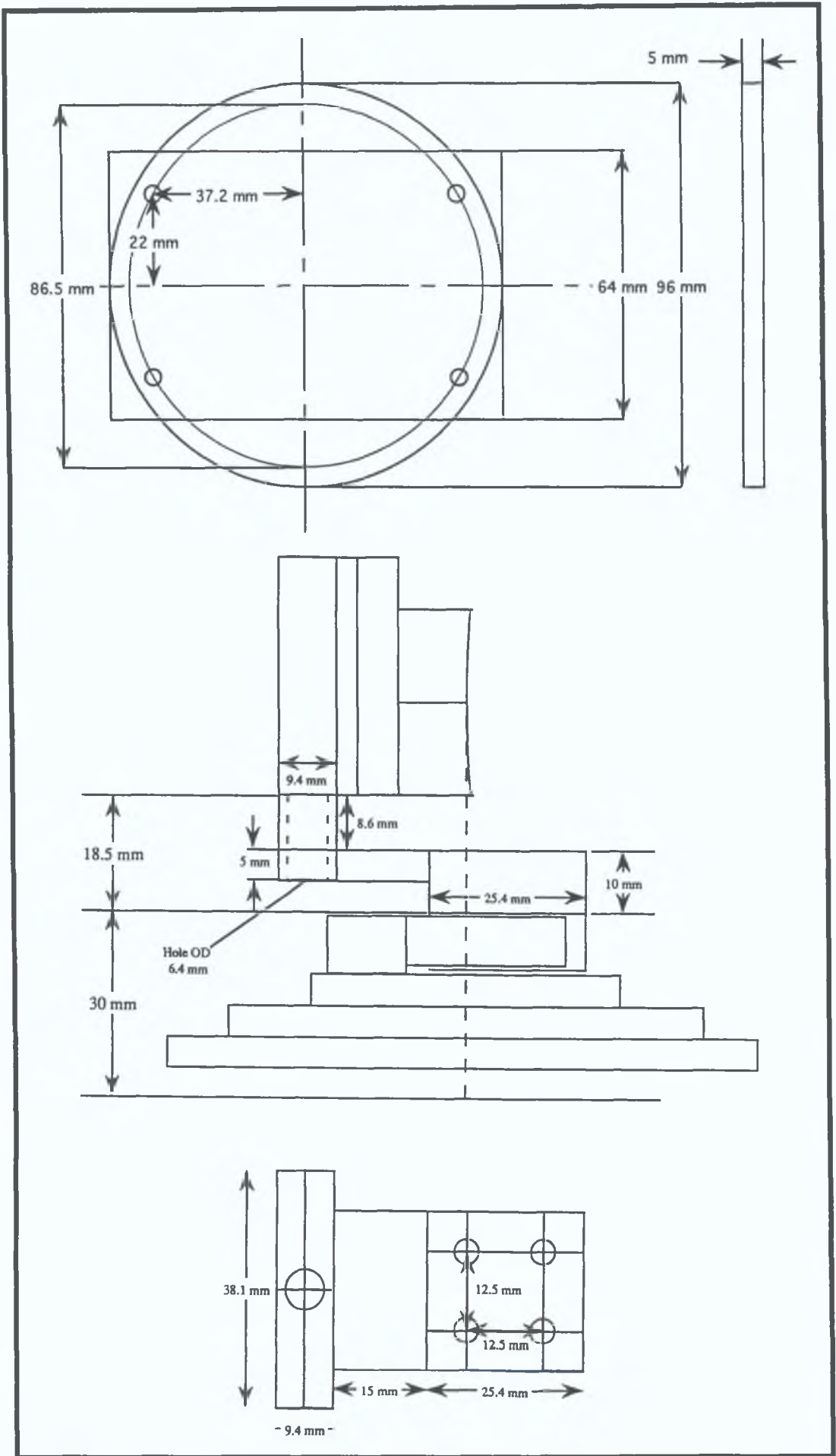
[FLANGE WITH DN 63 PORT FOR PUMPING (outside view)]

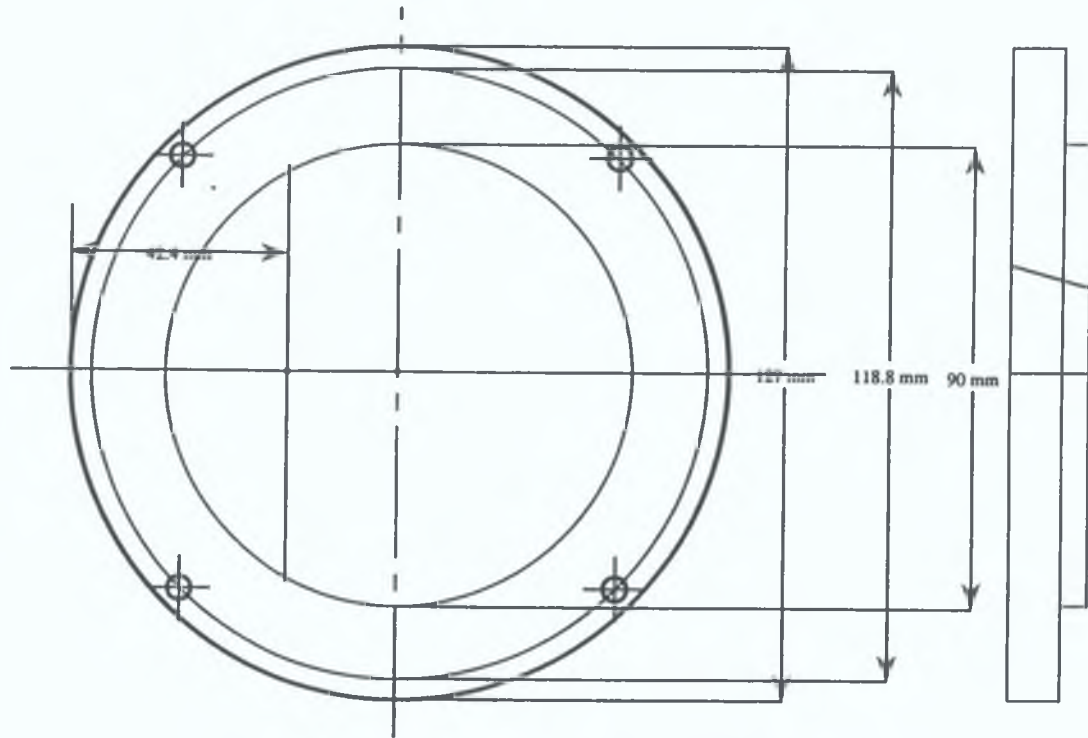


OUTSIDE VIEW OF PLATE WITH ANGLED OPENING FOR
DN40 PIPE DIAM 45.3 mm WITH 4X4 HOLES



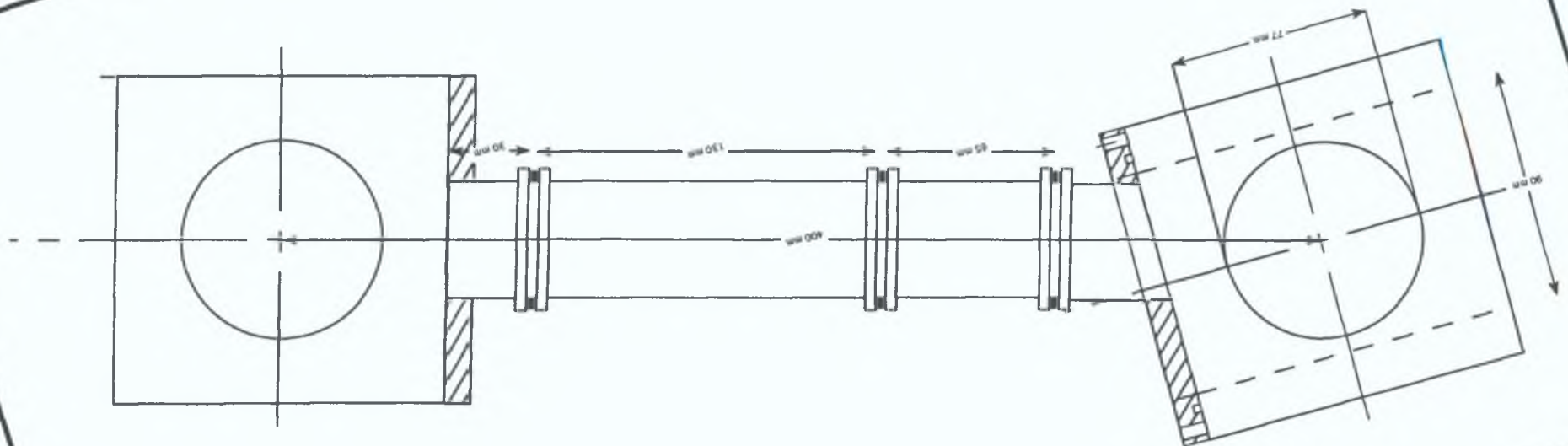
INNER SIDE OF PLATE WITH ANGLED DN40 PIPE

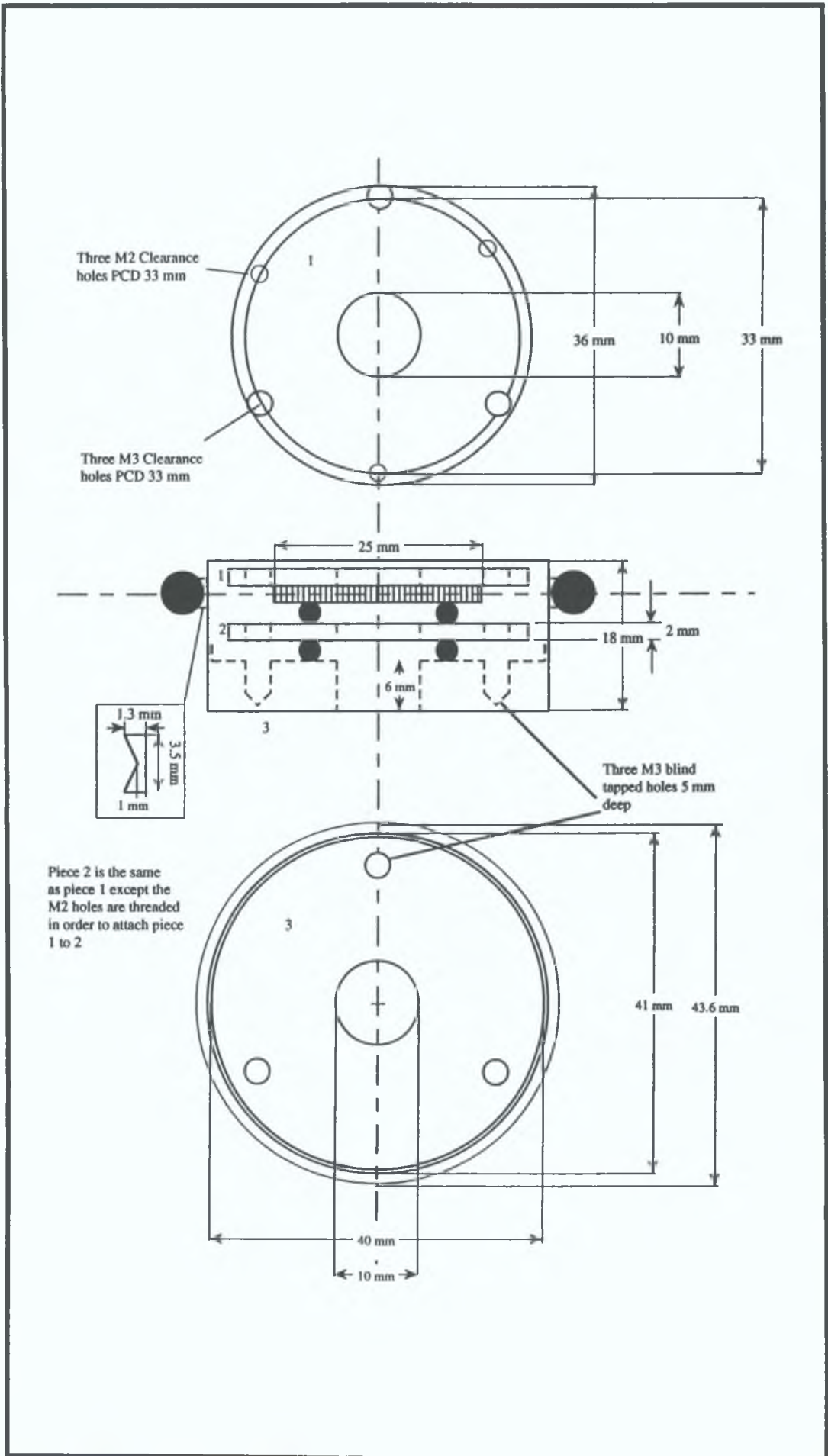


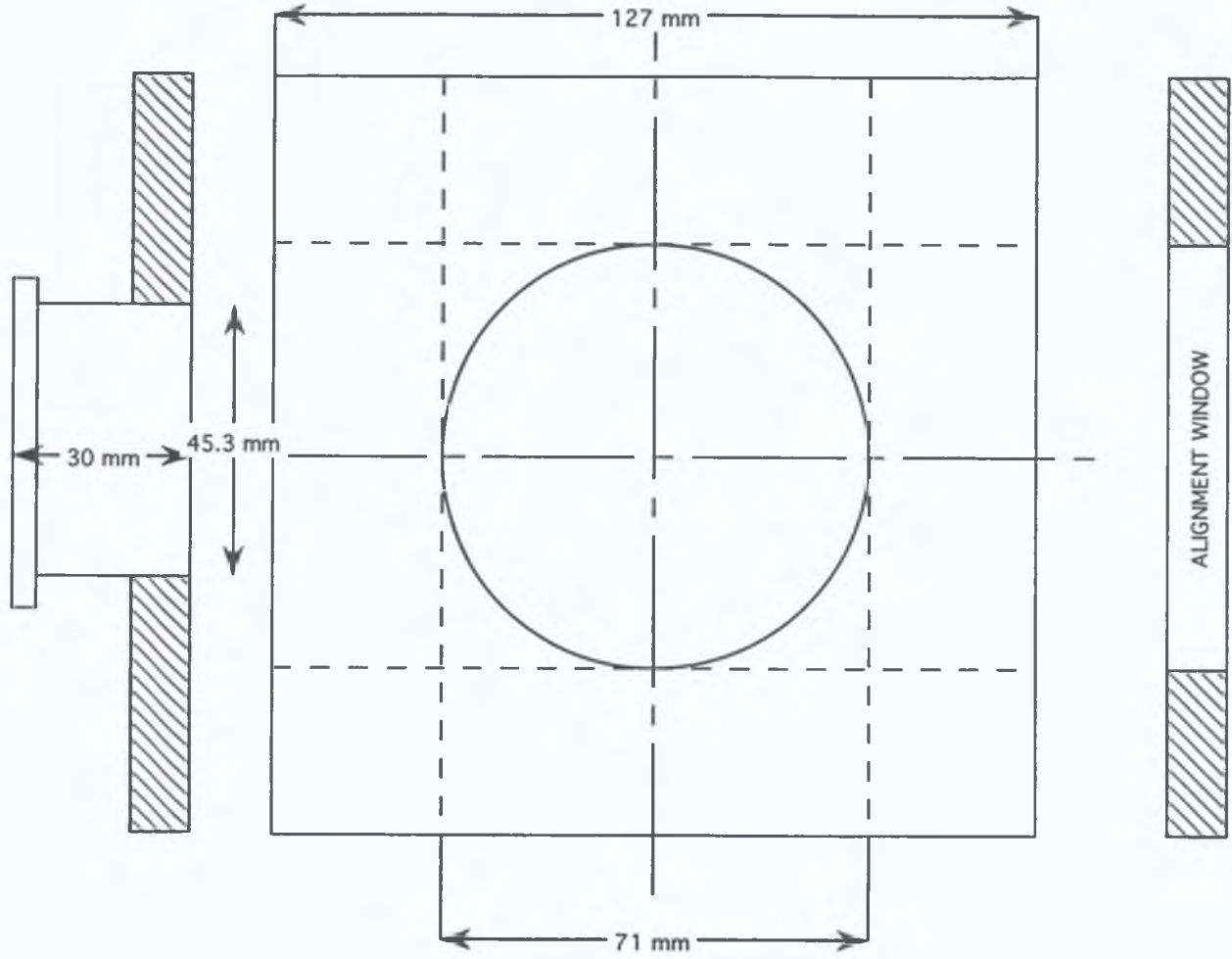


INNER SIDE OF TEMPLATE WITH ANGLED 1mm HOLE AT 16 DEGREES

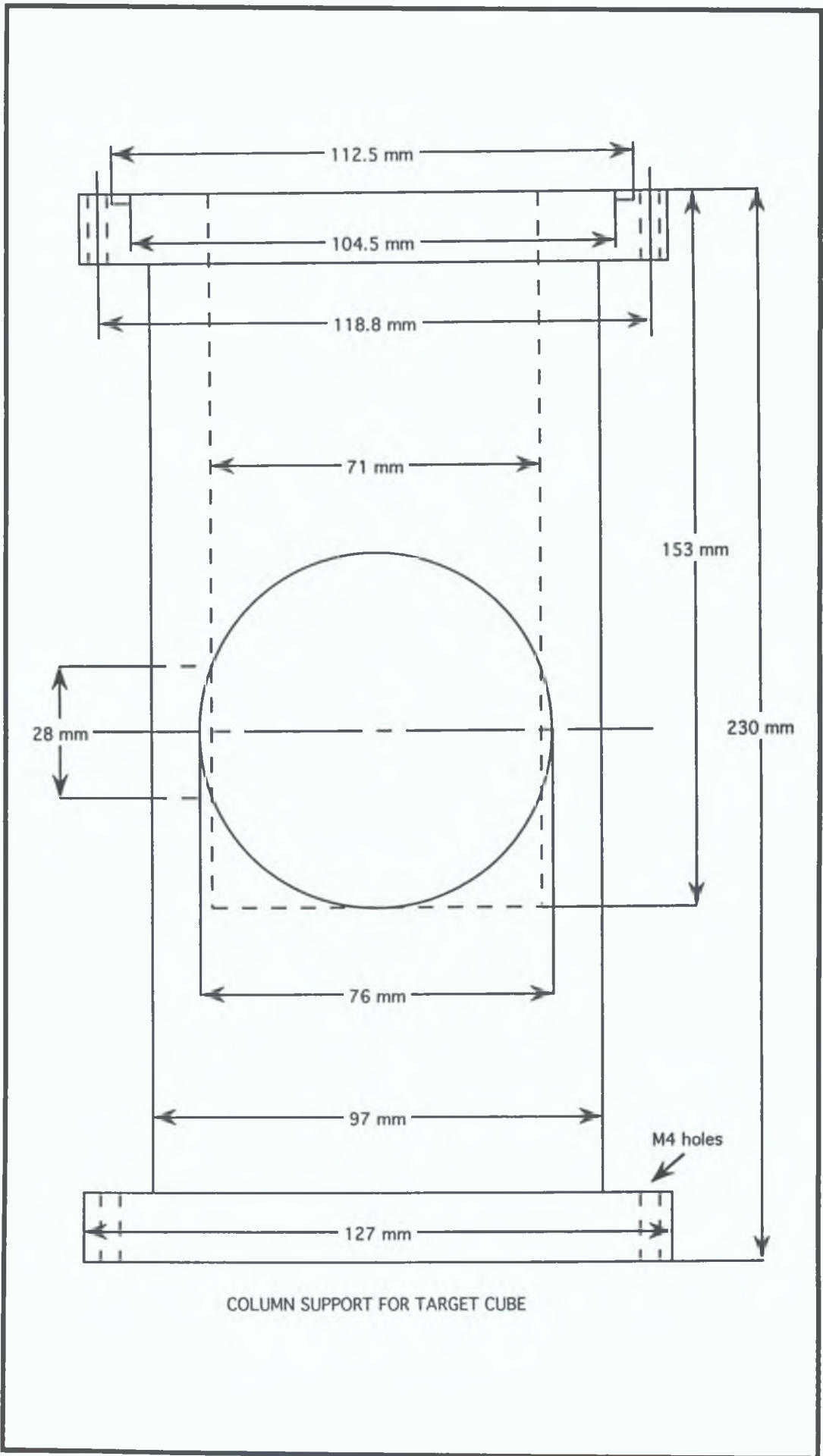
- A12 -

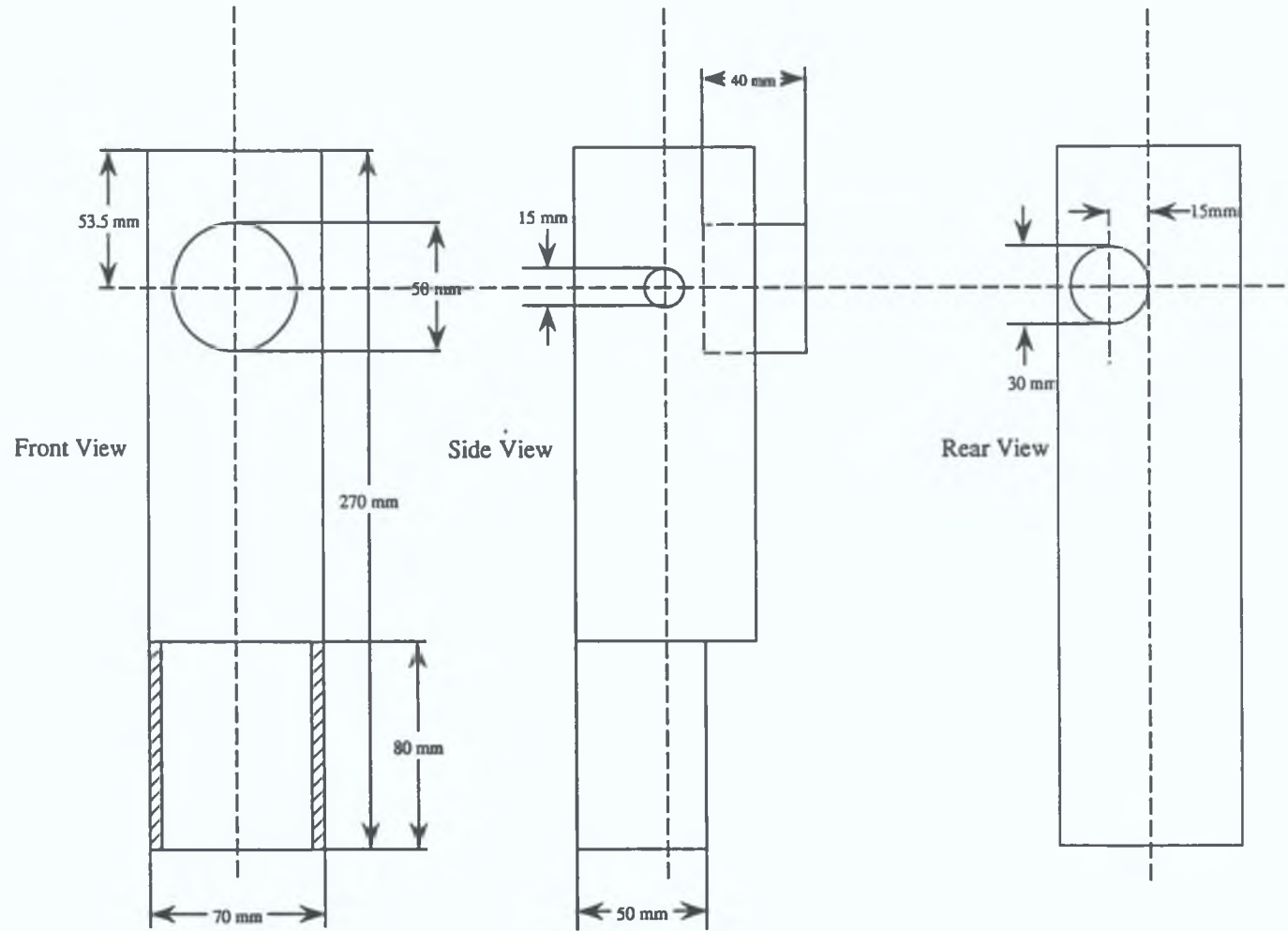


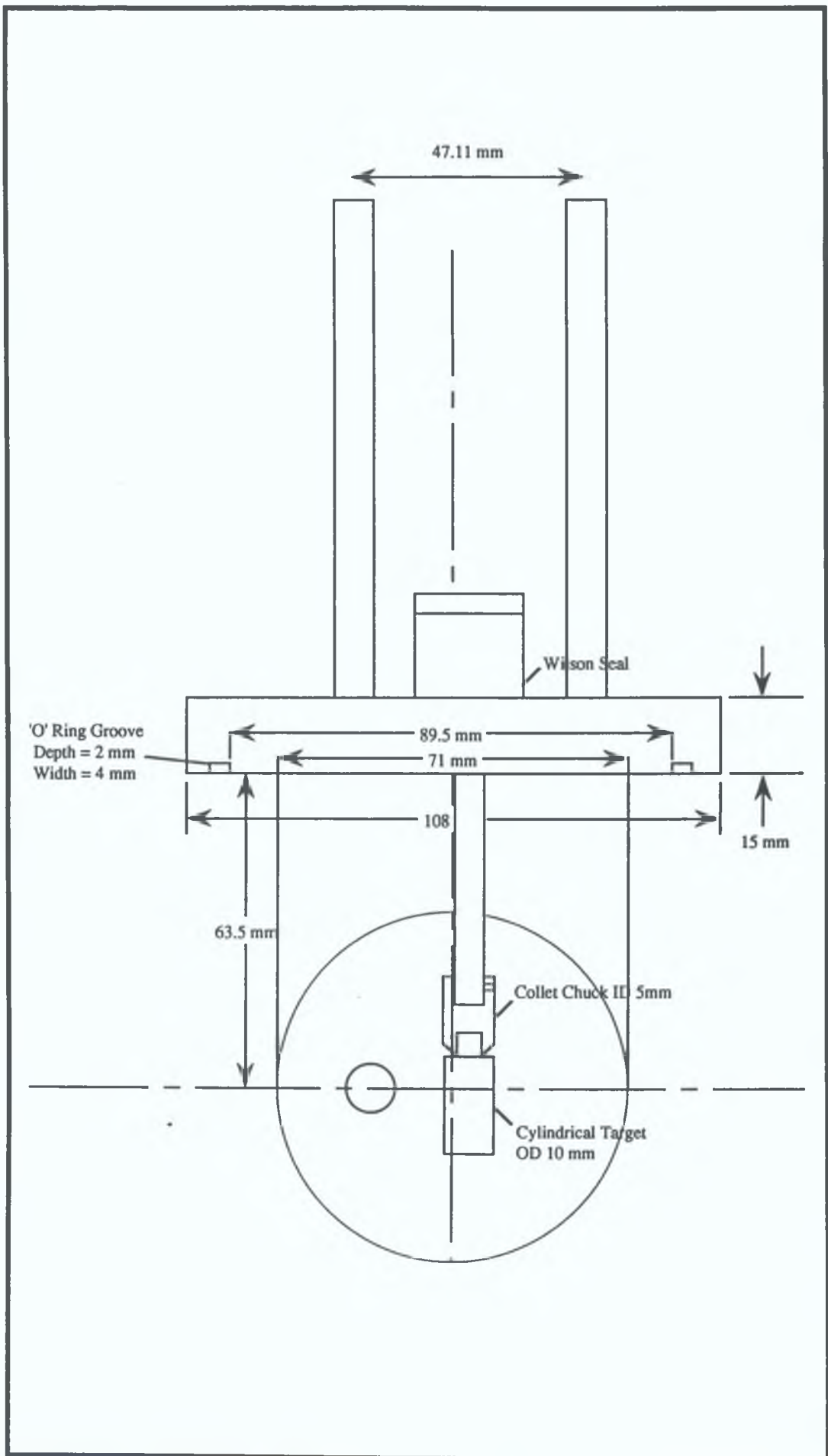


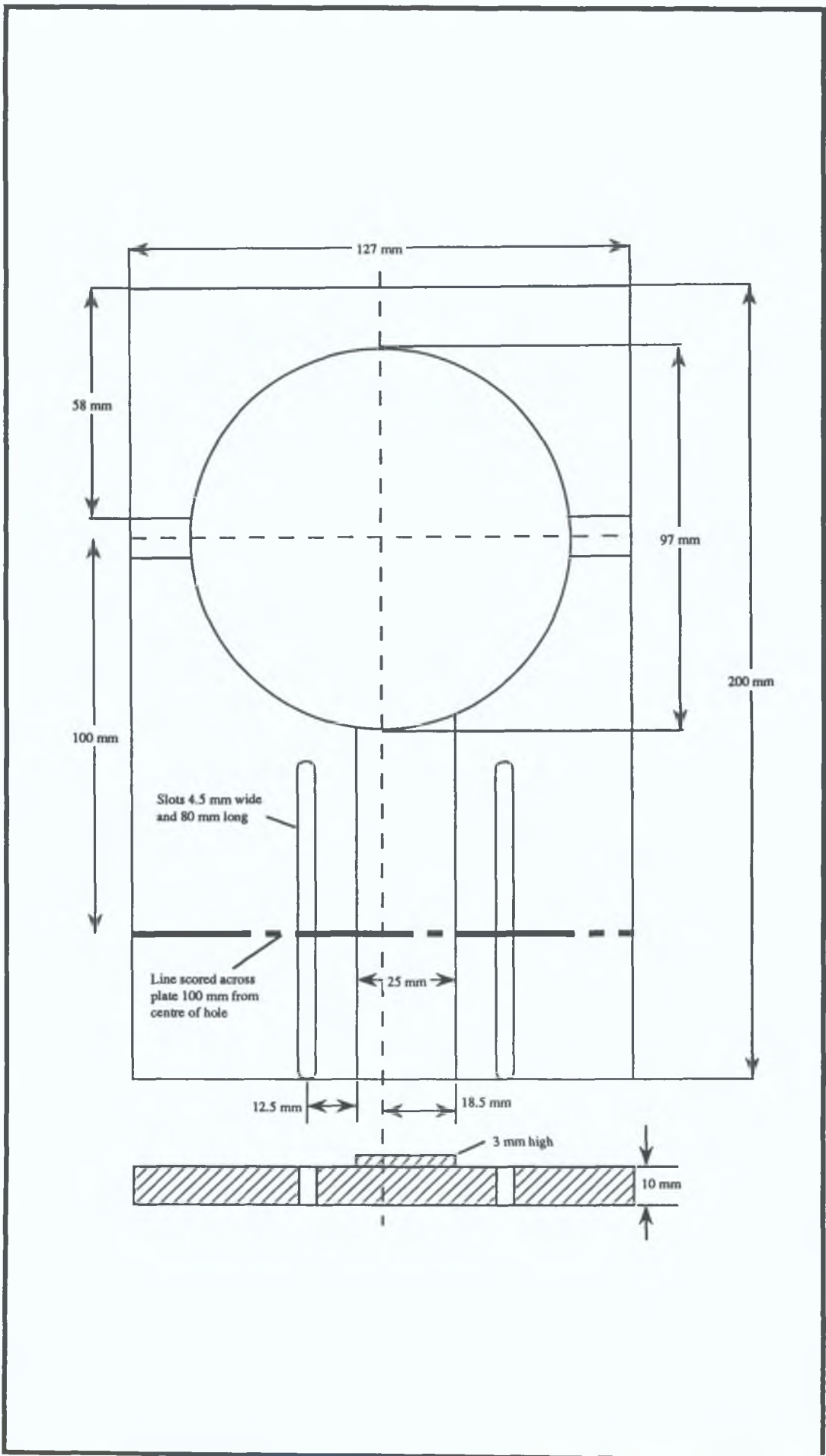


LASER TARGET CUBE (side view)









Acknowledgements

I wish to extend my sincere thanks to Prof Eugene Kennedy for providing me with the opportunity to undertake this research at Dublin City University. His enthusiasm, which was maintained throughout the completion of this work, and positive attitude towards the "try it and see" approach were very much appreciated

I am indebted to Dr. John Costello for his time and help with the analysis of the results outlined in chapter 5. I would also like to thank Dr Jean-Paul Mosnier for numerous helpful and always stimulating discussions

During my period as a postgraduate student with the School of Physical Sciences at Dublin City University I received the chance to work at the DESY and BESSY synchrotron facilities in Hamburg and Berlin respectively To this end I wish to thank Prof Bernd Sonntag, Prof Peter Zimmermann and their postgraduate students for their assistance and hospitality Also many thanks to Prof Marie-Yvonne Adam, Prof Mike Mansfield and Prof Vadim Ivanov for their communication of experimental results and calculations prior to publication

To all the postgrads in the Laser Plasma Group at DCU — thank you. In particular I would to express my gratitude to Ulrich and Hassan for bringing N123 to life

The precise and speedy machining work of Des Lavelle and Cian Merne facilitated the timely and smooth integration of the experimental system The assistance of the other technical staff of the DCU School of Physical Sciences is also appreciated

The unquestioning support and encouragement of my family and friends throughout my years at university will never be forgotten

Last but by no means least, I wish to thank Fiona for her infinite patience and invaluable pep talks just when I needed them most Her immeasurable contribution is very much appreciated